

NASA NAG5-900

**Studies of the Net Surface Radiative Flux
from Satellite Radiances during FIFE**

-Final Report-

*GRANT
IM-43-CR
p. 146*

Principal Investigator
Robert Frouin
California Space Institute
Scripps Institution of Oceanography
La Jolla, California 92093-0221

(NASA-CR-193150) STUDIES OF THE
NET SURFACE RADIATIVE FLUX FROM
SATELLITE RADIANCES DURING FIFE
Final Report (Scripps Institution
of Oceanography) 146 p

N94-10953
--THRU--
N94-10955
Unclas

G3/43 0167945

June 14, 1993

During the years of our First ISLSCP Field Experiment (FIFE) investigation "*Studies of the Net Surface Radiative Flux from Satellite Radiances during FIFE*" (NAG5-900), our efforts have focused on radiative transfer model validation, calibration of VISSR and AVHRR solar channels, development and refinement of algorithms to estimate downward solar (shortwave) and terrestrial (longwave) irradiances at the surface, including photosynthetically available radiation (PAR) and surface albedo, verification of these algorithms using in situ measurements, production of maps of shortwave irradiance, surface albedo, and related products (e.g., cloud albedo, fractional cloud cover), analysis of the temporal variability (diurnal, seasonal) of shortwave irradiance over the FIFE site, development of a spectroscopy technique to estimate atmospheric total water vapor amount, and study of optimum linear combinations of visible and near-infrared reflectances for estimating the fraction of PAR absorbed by plants. Among these activities, the last two and the one concerning PAR estimation from space were not part of our original technical plan, but they appeared interesting to undertake since they were addressing FIFE issues. Most of our investigation's objectives have been accomplished, but we have not been successful in achieving useful accuracies on estimates of downward longwave irradiance, and we have done too little work on the longwave radiation lost by the surface. The satellite sensors available, unfortunately, did not appear sufficiently sensitive to the key parameters governing the variability of the longwave fluxes, making ill-conditioned and, therefore, arduous the inverse problem. The scientific results of the investigation are summarized below.

1. Radiative Transfer Model Validation

The radiative transfer models of Tanré et al. (1985) and Morcrette (1984), or simplified schemes based on these models, are used in our algorithms to estimate surface radiation fluxes from satellite radiances. Although these models have been verified against exact calculations or line-by-line models, they have not been validated against in situ measurements. During FIFE, concomitant radiosonde observations, sky photographs, aerosol turbidity, and radiation measurements were made, offering the opportunity to compare model outputs to surface-measured fluxes. The comparisons were made in clear sky conditions since the available data did not permit adequate characterization of some important cloud parameters. The results are described in Frouin et al. (1990; see Appendix 1). Figures 1 and 2, which display scatter plots of calculated versus measured fluxes, summarize the results. The agreement is good between calculated and measured fluxes, with correlation coefficients above 0.98 and standard deviations of 23.2 Wm^{-2} (2.7%) and 13.0 Wm^{-2} (3.7%) for shortwave and longwave irradiances, respectively. The model of Tanré et al. (1985) overestimated shortwave irradiance by 13.2 Wm^{-2} on average, whereas the model of Morcrette (1984) underestimated

longwave irradiance by 7.4 Wm^{-2} . If significant, these biases may compensate partially when computing the radiation budget at the surface. On longer time scales (e.g., daily, monthly) more characteristic of climate studies, we expect the standard deviations to be greatly reduced. These results demonstrate the suitability of the models of Tanré et al. (1985) and Morcrette (1984) for radiation budget studies, at least in clear sky conditions.

2. Calibration of VISSR and AVHRR Solar Channels

We have performed a sensitivity study of the net shortwave irradiance at the surface to calibration (Gautier and Frouin, 1988; see Appendix 2). This study has shown that, in overcast conditions, a 10% loss in sensor sensitivity (increase in gain) translates into uncertainties of up to -70 Wm^{-2} on instantaneous values and of up to -15 Wm^{-2} on monthly averages. In tropical regions, the monthly-averaged uncertainty is typically -14 Wm^{-2} (Figure 3). This uncertainty appears as a bias with a sign opposite to that of the calibration bias; in other words a positive bias on calibration induces a negative bias on net shortwave irradiance (cloud albedo is overestimated).

VISSR and AVHRR calibration was achieved by applying the indirect method described in Frouin and Gautier (1987). This method, which uses space and the White Sands Monument area in New Mexico as calibration targets, computes the radiance measured at satellite altitude using the model of Tanré et al. (1985). The relevant atmospheric characteristics are estimated from either climatological data (aerosol size-frequency distribution and refractive index) or observations at nearby meteorological stations (water vapor amount and aerosol loading). Figure 4 shows the GOES-6 VISSR calibration gain (relates count-squared to reflectance) obtained (open circles) and how it compares with values reported by other investigators (the compilation was made by Whitlock et al., 1990). Some erratic fluctuations are observed from one gain estimate to the next, in some instances reaching 10%. Changes of such amplitude, however, are at the limit of the uncertainty level. In addition to the relatively high-frequency fluctuations, the gain exhibits low-frequency variations, with minimum values in spring and early summer. From July to December 1987, the gain increased by approximately 36%. Compared to the prelaunch gain, the gain at the end of 1987 reads higher by 64%.

3. Algorithm Development, Refinement, and Validation

3.1 Downward Shortwave Irradiance, Including PAR, and Surface Albedo

We have applied the satellite method of Gautier et al. (1980) to GOES-6 VISSR data acquired during FIFE. The version used accounts for aerosol scattering and absorption, which was accomplished based on the model of Tanré et al. (1985). The objective was to assess whether the method can provide quantitative information on the temporal variability of downward shortwave irradiance (or insolation) and PAR during the experiment. In the calculations, surface albedo at each observation time during the day was determined for each IFC from the

minimum brightness count over the entire IFC. We have indicated (Frouin and Gautier, 1990; see Appendix 3) how the Gautier et al. (1980) method can be modified to yield PAR estimates. In this case, cloud absorption vanishes in the model equations and clear sky PAR is computed using the coefficients given by Frouin et al. (1989). The computational procedure included checks of the satellite navigation and of the data quality, and calibration of the VISSR visible channel (see above). Appendix 4 summarizes the results obtained for the five IFCs. The satellite estimates of insolation and PAR were in good agreement with in situ measurements. During IFC-2, for instance, the correlation coefficients were above 0.95 with the standard errors of estimate of 21.6 Wm^{-2} (9%) and 8.2 Wm^{-2} (6.5%) for daily insolation and PAR, respectively (Figure 5). These errors are acceptable for climate studies. The satellite estimates also described well the diurnal variability of PAR and insolation (Figure 6). Using the ratio of PAR and insolation determined in situ with the satellite estimate of insolation, we obtained daily PAR values with a slightly higher r.m.s error than when PAR was directly estimated from the satellite data. This indicates that the large scale satellite climatologies of insolation now produced within the framework of ISCCP can be simply converted into useful climatologies of PAR for global studies of photosynthetic activity, although a more direct use of the satellite data would be optimum. The various techniques so far proposed to estimate PAR from satellite data, including the one of Frouin and Gautier (1990), are discussed in Frouin (1993) (Appendix 5).

3.2 Downward Longwave Irradiance

The net longwave irradiance flux at the surface, owing to its small variability, is less important than the shortwave one. It cannot be neglected, however, particularly in the presence of clouds that decrease surface insolation while increasing the downward component of the longwave flux. Several methods have been proposed to estimate the downward longwave flux at the surface from satellite measurements (see, for instance, Darnell et al., 1983; Frouin et al., 1988; Gupta, 1989). Although some of them have been used to generate global fields of net longwave flux, few validation studies have been made. We therefore investigated the performance of two of them (Frouin et al., 1988; Gupta, 1989) by comparing their outputs with carefully taken in situ measurements. Computations using the same atmospheric temperature and moisture profiles indicated that, for clear sky conditions, the two model outputs are correlated. The values obtained using Gupta's (1989) model are systematically higher by 15 Wm^{-2} . Since Frouin et al. (1988) uses Morcrette's (1984) model, and since this model slightly underestimates downward longwave irradiance (see section 1), we may conclude that the performance of the two models is similar, Gupta's (1989) model overestimating downward longwave irradiance in somewhat warm and humid atmospheres. Computations using vertical sounder (TOVS) data as input did not show good agreement with in situ measurements, especially in cloudy conditions (Figure 7). This was expected since other uncertainties are added: that of the retrieved profile itself and the uncertainty resulting from the distance between

the TOVS observations and the pyrgeometer measurements. Details of this study are given in Bréon et al. (1990; see Appendix 6).

3.3 Atmospheric Water Vapor Amount

We have shown (Frouin and Middleton, 1990; see Appendix 7) that viewing the earth's surface in two spectral channels, one narrow, the other wide, centered on the same wavelength at the water vapor absorption maximum near 940 nm yields accurate atmospheric total water vapor amounts independently of the surface reflectance properties (Figure 8). The concept was verified using concomitant SE-590 spectrometer and radiosonde data acquired during FIFE IFCs. Under varied geometries and atmospheric conditions, and for several surface targets, the relationship between radiance ratio in the narrow and wide spectral channels was stable, following an expected exponential law (Figure 9). The SE-590 instrument, however, did not view the surface from above the atmosphere or even above the boundary layer, where most of the water vapor is concentrated, and therefore did not permit verification of the technique in actual conditions of aircraft or satellite viewing. In such conditions, simple physics showed that the effect of photons backscattered by aerosols is to lower unacceptably the retrieved water vapor amount when the aerosols are located above the boundary layer. Airborne experiments, on the other hand, were carried out (Frouin et al., 1990; Appendix 8) and have demonstrated the suitability of the method over both land and sea.

3.4 Fraction of PAR Absorbed by Plants

Using the SAIL model (Verhoef, 1984), we have simulated for varied, yet realistic soil and canopy parameters, namely leaf optical properties, soil reflectance, Leaf Area Index (LAI), and Leaf Inclination Distribution Function (LIDF), above canopy visible and near-infrared reflectances and daily-averaged (weighted by incident radiation) fraction of PAR absorbed by plants, APAR. The objective was to find linear combinations of visible and near-infrared reflectances that improve the accuracy of APAR estimates when compared to that obtained using Normalized Difference Vegetation Index (NDVI). Figures 10 and 11 display some results (see, also Podaire et al., 1991; Appendix 9). The calculations were performed for LAIs of 0.01, 0.05, 0.1, 0.2, 0.5, 1, 2, and 5, erectophile, planophile, and spherophile canopies, soil reflectances of 0.1, 0.2, 0.3, and 0.4, and typical leaf optical properties. The soil reflectance was assumed white spectrally, and the various LIDFs were considered separately in the regressions. We see in Figure 10 (bottom) that the influence of the background on the daily-averaged APAR versus instantaneous relationships is substantial, especially at moderate LAIs, but is substantially reduced when using linear combinations of reflectances (Fig. 11, bottom). In this case, the points corresponding to a same LAI are generally more aligned with the best fit line. The result is a drastic improvement in the APAR residual error. For the geometries of Figures 10 (bottom) and 11 (bottom), the residual error is reduced from 0.064 to 0.029 (planophile case), 0.052 to 0.018 (spherophile case), and 0.049 to 0.013 (erectophile case). When using NDVI, the minimum residual error is obtained for nadir viewing (Figure 10, top), but when

using linear combinations it is generally preferable to view the target at 60° viewing zenith angle, although in the case of a planophile canopy any viewing geometry provides similar results (Figure 11, top). Analysis of quantum sensor and radiometer measurements collected during FIFE have corroborated that an optimized linear channel combination scheme is a potentially better predictor for APAR (Figure 12).

4. Effect of Broken Clouds on Shortwave Irradiance

In operational satellite algorithms to estimate surface shortwave irradiance, top-of-atmosphere reflectances are used to infer pixel-averaged cloud reflectance and, then, cloud transmittance (flux transmittance). Isotropy of the radiance reflected by the surface and clouds is generally assumed, and the clouds are considered plane-parallel. This approach suffers a number of limitations, basically linked to the anisotropy of the radiance field emerging from clouds. Broken clouds, in particular, can affect drastically the spatial distribution of surface shortwave irradiance, as illustrated in Figure 13, which contrasts the situations on August 4, 1989 a clear day, and August 8, 1989, a partially cloudy day, at site 16.

On August 8, cumulus clouds started to develop around 11:30 local time, were fully developed by early afternoon, and disappeared around 16:00 local time, which manifested in short periods of alternate high and low irradiance values. The high values largely exceeded those observed at the same time on August 4, by as much as 130 Wm^{-2} between 13:00 and 14:00 local time. The cloud field at 13:32 local time, as captured by Dr. Eloranta's lidar installed a few kilometers from the pyranometer, is displayed in Fig. 14.

Qualitatively, when there are no clouds (August 4), the pyranometer measures $E \cos \theta$ where E is the solar constant and θ is the sun zenith angle (we neglect in this discussion scattering and absorption by molecules and aerosols). When there are clouds (August 8), two cases are possible: the clouds obscure or do not obscure the sun. If the clouds obscure the sun, the pyranometer measures $E' < E \cos \theta$, and the shortwave flux is essentially diffuse. If the clouds do not obscure the sun, the pyranometer measures $E'' > E \cos \theta$, which is not surprising because to the direct shortwave flux is superimposed a diffuse flux from the clouds. In other words we expect $E'' = E \cos \theta + E'$ if we assume that the diffuse flux does not depend on the location of the clouds. Figure 16, however, suggests that the situation is more complex on August 8 since between 12:00 and 14:30 local time we estimate $E' = 270 \text{ Wm}^{-2}$ and $E'' - E \cos \theta = 130 \text{ Wm}^{-2}$ or about $E'/2$! Thus the excess flux when the sun is not obscured is not equal to the diffuse flux measured in the shade of the clouds.

To go further in this interpretation, consider spherical clouds of radius R and, for the sake of simplicity, neglect cloud-cloud interactions. In the case of an isolated cloud illuminated by a directional beam of irradiance E , Monte Carlo calculations show that the average backscattered radiance $L(\chi)$, where χ is scattering angle, is nearly isotropic for average optical thickness above 16. It

follows that $L=E/4$ since the cloud is conservative. Now suppose that we have N such clouds covering an area of surface S . The fractional cloud coverage is $n=N\pi R^2/S$. For any sun position (not too low above the horizon to avoid shade effects) the N clouds collect a flux $N\pi R^2 E$. Since they are Lambertian, they scatter half of this flux toward the ground. Thus the average diffuse reflectance at the surface is $N\pi R^2 E/2S$, that is $nE/2$. Assume that this diffuse irradiance is homogeneous spatially. Depending on whether the sun is obscured or not by a cloud, the model predicts that the pyranometer measures $nE/2$ or $nE/2+E\cos\theta$. An interesting aspect of the model is that E' does not depend on q , as observed in Figure 16. However, taking $nE/2=270 \text{ Wm}^{-2}$, $E\cos\theta=860 \text{ Wm}^{-2}$, $\theta=25^\circ$ at 14:00 local time gives $n=0.57$, which is not unreasonable, but too high (see Figure 14).

So far we have been able to explain qualitatively the measurements, but the model remains too simplistic. It appears that the clouds may not be thick enough to behave as Lambertian bodies. Therefore we shall write $E''=E\cos\theta+E_d$ with $E_d=130 \text{ Wm}^{-2}$ when the pyranometer is lit by the sun and $E'=E_d+E_1$ when the pyranometer is in the shade of a cloud, where E_1 is an excess flux that must be explained by the cloud transmittance (the clouds are not completely opaque). Let t denote the cloud optical thickness. Because of the diffraction peak of the phase function (where the light scattered is practically transmitted), we expect an effective transmittance equal to $\exp(-t/2)$. Assume that the light scattered (order 2 and higher orders) is isotropic. We have $E_1=E\cos\theta \exp(-t/2)$ and $E_d=nE[1-\exp(-t/2)]/2$. Using $E_1=140 \text{ Wm}^{-2}$ and $E\cos(25^\circ)=860 \text{ Wm}^{-2}$, we obtain $t=3.6$, which is reasonable (if the scattering coefficient is $0.5/\text{km}$, the cloud geometrical thickness is 72m). For the fractional cloud coverage, we obtain $n=0.33$, which is in better agreement with the observations.

A more specific calculation is necessary to justify the above explanation. Using sky photographs and lidar measurements, we can estimate the average dimension of the clouds, their average spacing, cloud base altitude and thickness. This information was fed into a Monte Carlo code that computed the spatial distribution of the cloud transmittance at the surface. Figure 15 gives the results obtained at 13:50 local time for cylindrical clouds of optical thickness 12. The cloud transmittance reaches values as high as 113% in the region not obscured by the clouds. Using a typical clear atmosphere and a cloud-level wind of 4ms^{-1} blowing from the North (as measured from Pr. Brutsaert's radiosondes), we were able to reproduce many features of the pyranometer trace (Figure 13), including the near-constant minimum values, the maximum values when the sun was not obscured, as well as the fine structure associated with the cloud edges and cloud shadowing (Figure 16).

5. Variability of Downward Shortwave Irradiance

High resolution (about 1.5 km) maps of hourly and daily surface solar irradiance over the FIFE site have been produced for all the IFCs (1 through 5). Maps of other useful parameters, namely equivalent cloudiness (one minus the

ratio of actual and clear sky irradiances), cloud albedo, clear sky irradiance, and surface albedo, have also been produced.

Since cloud-radiation interactions are important to weather and climatic prediction, we have examined the role of clouds in modulating insolation (Frouin and Gautier, 1990; see Appendix 3). The daily cloud forcing, or the difference between clear and actual sky conditions, reached about 75% of the clear sky insolation on some days (e.g., days 180 and 181). Minimum (or maximum) values occurred every 2 to 4 days, corresponding roughly to the time scales of mid-latitude atmospheric disturbances. Compared to the effect of changes in water vapor amount and aerosol type and amount, the cloud forcing largely dominates, by typically one order of magnitude. While developing satellite techniques to estimate insolation (or PAR), one should therefore concentrate on the role of clouds (determining accurately the governing cloud parameters) rather than on the influence of the clear atmosphere.

Correlation between cloud radiative forcing and fractional cloud coverage was also studied using sky camera data and meteorological reports (Bréon et al., 1990; see Appendix 10). Using the sky camera data, we found linear correlation coefficients of 0.62, 0.31, and 0.49 for shortwave, longwave, and net radiative forcings, respectively. Using the meteorological station data, we found lower correlation coefficients. These rather low values show that cloud amount is not the only parameter driving radiative forcing. A governing parameter for cloud forcing is liquid water content, but this parameter was not measured. The average diurnal cycle of the shortwave, longwave, and net cloud radiative forcings exhibited a definite diurnal cycle, with maximum values around local noon for the shortwave forcing, and minimum values at the same time for the longwave and net forcings. These cycles, if confirmed by other observations, should be taken into account when evaluating radiation budgets from heliosynchronous satellites.

6. References

- Bréon, F.-M., R. Frouin and C. Gautier, 1990: Satellite estimates of downwelling longwave irradiance at the surface during FIFE. Proc. of the Symp. on the First ISLSCP Field Experiment (FIFE). Published by the American Meteorological Society, Feb 4-9, 1990, 92-97.
- Bréon, F.-M., R. Frouin and C. Gautier, 1990: Cloud radiative forcing variability during FIFE. Proc. of the 7th Conf. on Atmospheric Radiation, July 23-27, 1990, San Francisco, CA. Published by the American Meteorological Society, 173-179.
- Bréon, F.-M., R. Frouin and C. Gautier, 1991: Global shortwave energy budget at the earth's surface from ERBE observations. (to be submitted).
- Darnell, W. L., S. K. Gupta and W. F. Staylor, 1983: Downward longwave radiation at the surface from satellite measurements. *J. Clim. Appl. Meteor.*, 22, 1956-1960.
- Frouin, R. and C. Gautier, 1990: Variability of photosynthetically available and total solar irradiance at the ocean surface during FIFE: a satellite description. Proc. of the Symp. on the First ISLSCP Field Experiment (FIFE). Published by the American Meteorological Society, Feb 4-9, 1990, 98-104.

- Frouin, R. and E. Middleton, 1990: A differential absorption technique to estimate total water vapor amounts. Proc. of the Symp. on the First ISLSCP Field Experiment (FIFE). Published by the American Meteorological Society, Feb 4-9, 1990, 135-139.
- Frouin, R., C. Gautier and J.-J. Morcrette, 1988: Downward longwave irradiance at the ocean surface from satellite data: Methodology and in-situ validation. *J. Geophys. Res.*, 93, (C1), 597-619.
- Frouin, R., D. W. Lingner, C. Gautier, K.S. Baker and R.C. Smith, 1989: A simple analytical formula to compute clear sky total and photosynthetically available solar irradiance at the ocean surface. *J. Geophys. Res-Oceans*, 94, 9731-9742.
- Frouin, R., F.-M. Bréon and C. Gautier, 1990: Validation of radiative transfer models during the First ISLSCP Field Experiment. Proc. of the 7th Conf. on Atmospheric Radiation, San Francisco, Jul. 23-27, 1990, Published by the American Meteorological Society, Feb 4-9, 1990, 429-435.
- Frouin, R., P.-Y. Deschamps, and P. Lecomte, 1990: Determination from space of total water vapor amounts by differential absorption near 940 nm: theory and airborne verification. *J. Appl. Meteor.*, 29, 448-460.
- Gautier, C., G. Diak and S. Masse, 1980: A Simple physical model to estimate incident solar radiation at the surface from GOES satellite data. *J. Appl. Meteor.*, 19, 1005-1012.
- Gupta, S. H., 1989: A parameterization for Longwave surface radiation from sun-synchronous satellite data. *J. Clim.*, 2, 305-320.
- Morcrette, J.J., 1984: Sur la paramétrisation du rayonnement dans les modèles de la circulation générale atmosphérique. Phd. Thesis, 630, Univ. of Lille, France.
- Podaire, A., P.-Y. Deschamps, R. Frouin, and G. Asrar, 1991: Optimum combinations of visible and near-infrared reflectances for estimating the fraction of photosynthetically available radiation absorbed by plants. Proc. 5th Int. Col. on Physical Signatures in Remote Sensing, Courchevel, France, 14-18 January 1991, ESA SP-319,405-408.
- Tanré, D., C. Deroo, P. Duhaut, M. Herman, J.-J. Morcrette, J. Perbos, and P.-Y. Deschamps, 1985: Effets atmosphériques en télédétection-logiciel de simulation du signal satellitaire dans le spectre solaire. Proc. 3rd Int. Col. on Spectral Signatures of Objects in Remote Sensing, Les Arcs, France 16-20 December 1985.
- Verhoef, W., 1984: Light scattering by leaf layers with application to canopy reflectance modeling: the SAIL model. *Rem. Sen. Environ.*, 125-141.

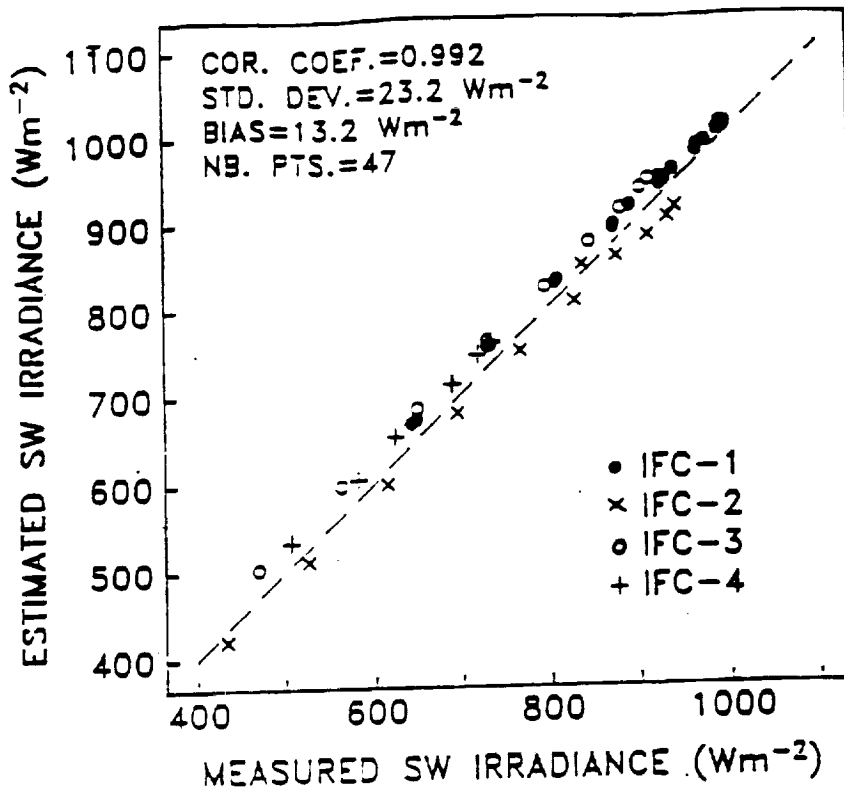


Fig. 1 Performance of the Tanré et al. (1985) model to estimate downward solar (shortwave) irradiance at the surface under clear skies. Values are half-hourly averages.

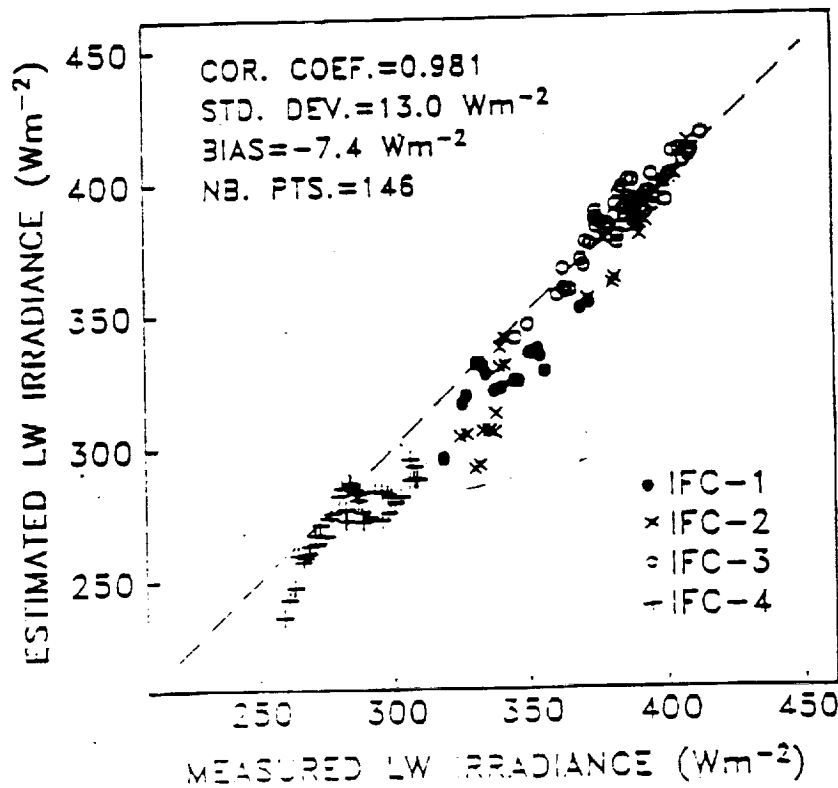


Fig. 2 Performance of the Morcrette (1984) model to estimate downward terrestrial (longwave) irradiance at the surface under clear skies. Values are half-hourly averages.

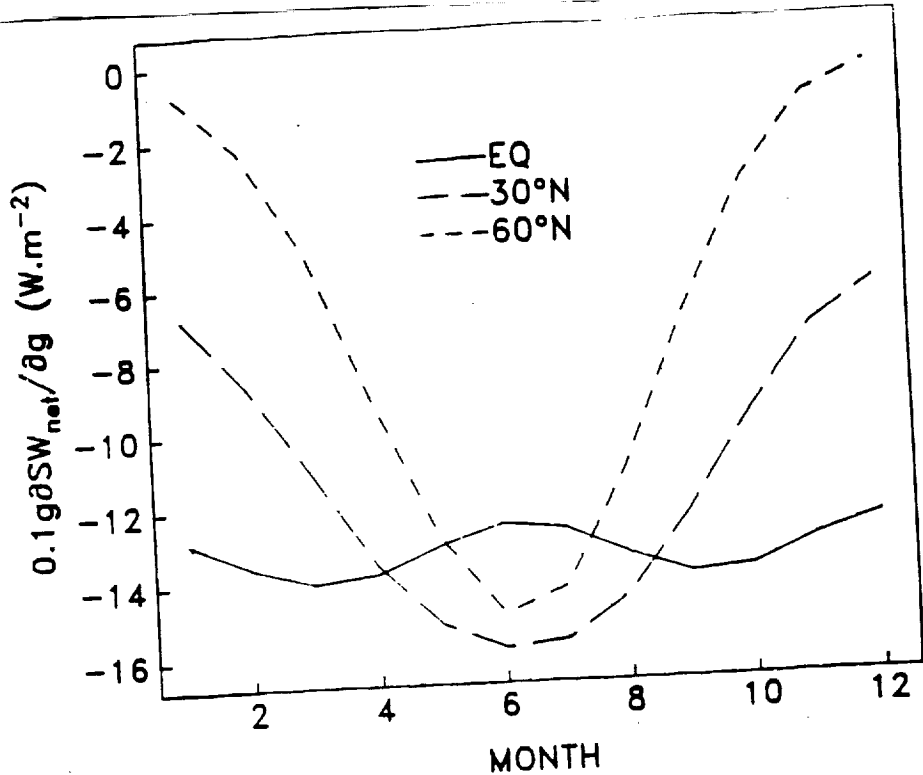


Fig. 3 Sensitivity of monthly-averaged absorbed solar irradiance at the earth's surface to a 10% increase in calibration gain, g . The sky is 50% covered by clouds of 0.4 optical thickness, the surface albedo is 0.2, and the clear atmosphere is standard.

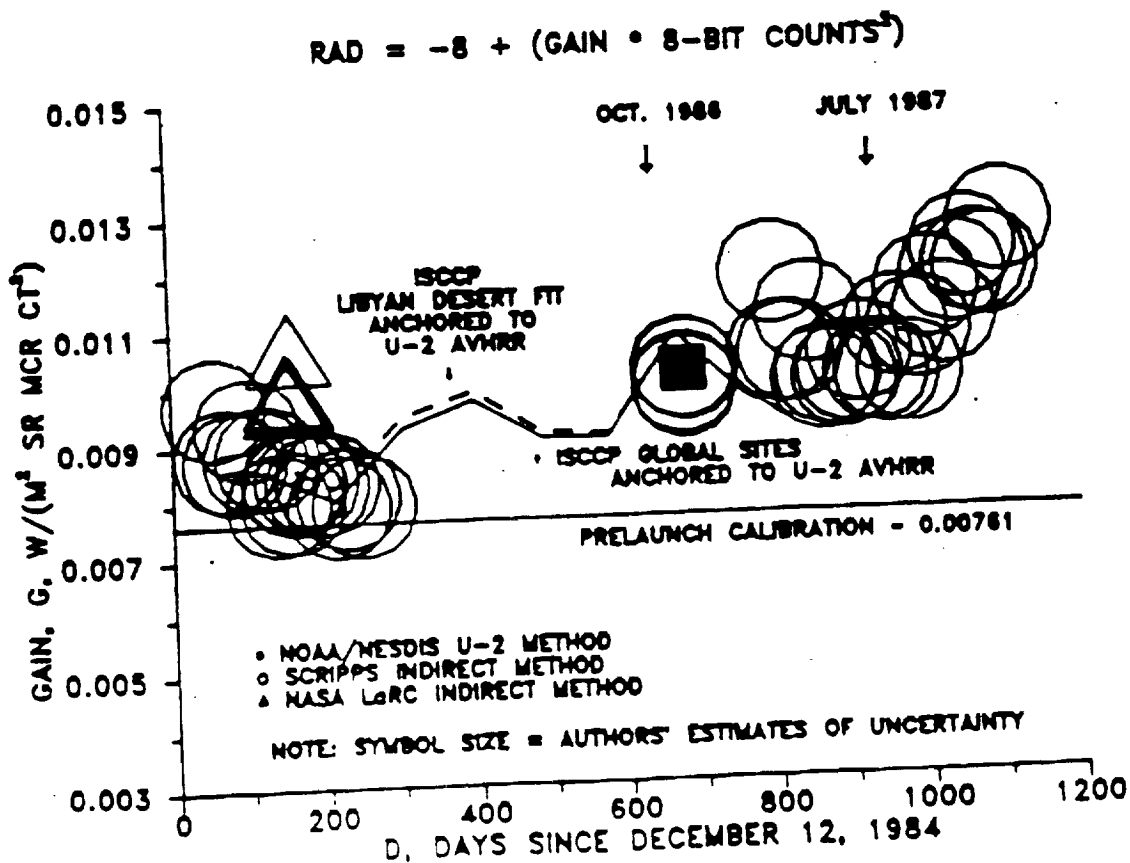


Fig. 4 Evolution of the calibration gain of GOES-6 VISSR solar channels.

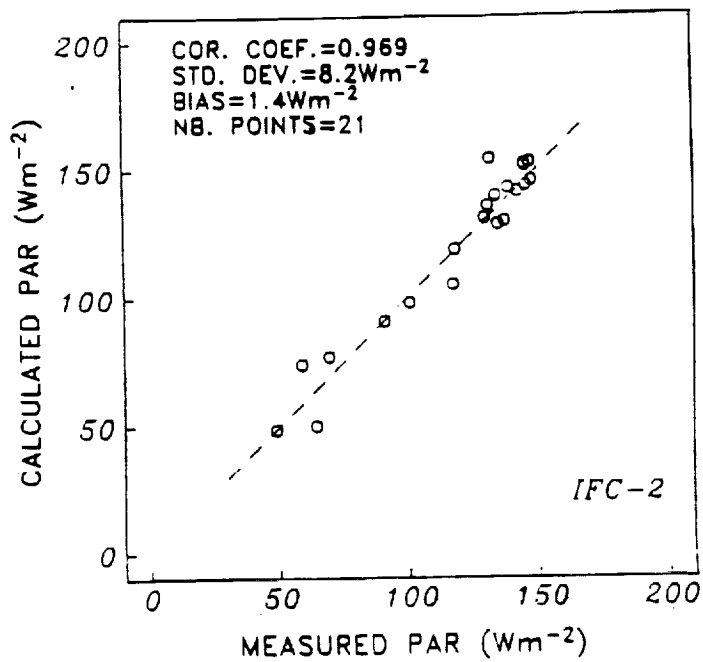
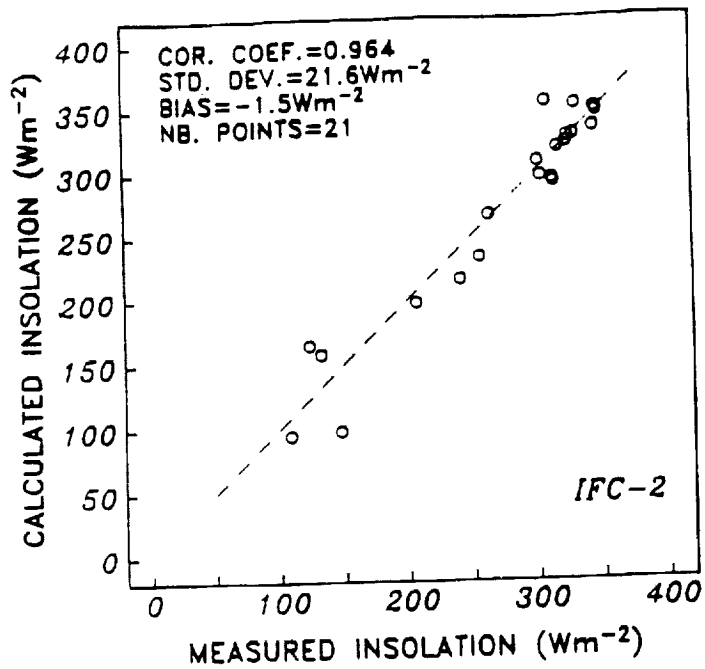


Fig. 5 Scatter plots of calculated versus measured daily insolation (top) and PAR (bottom) during FIFE's second IFC. The measured values are averages of station 5 and 26 data (insolation) and station 5 and 21 data (PAR).

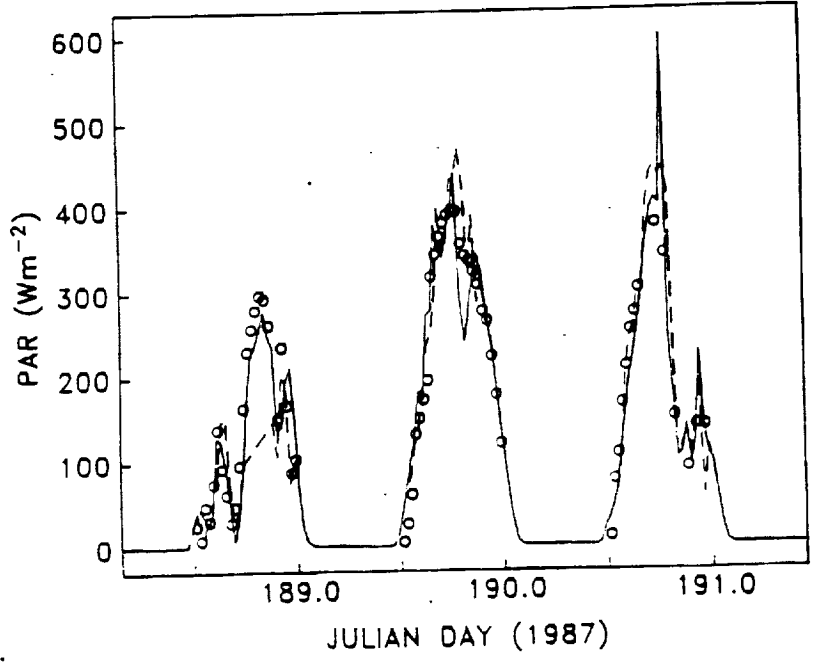
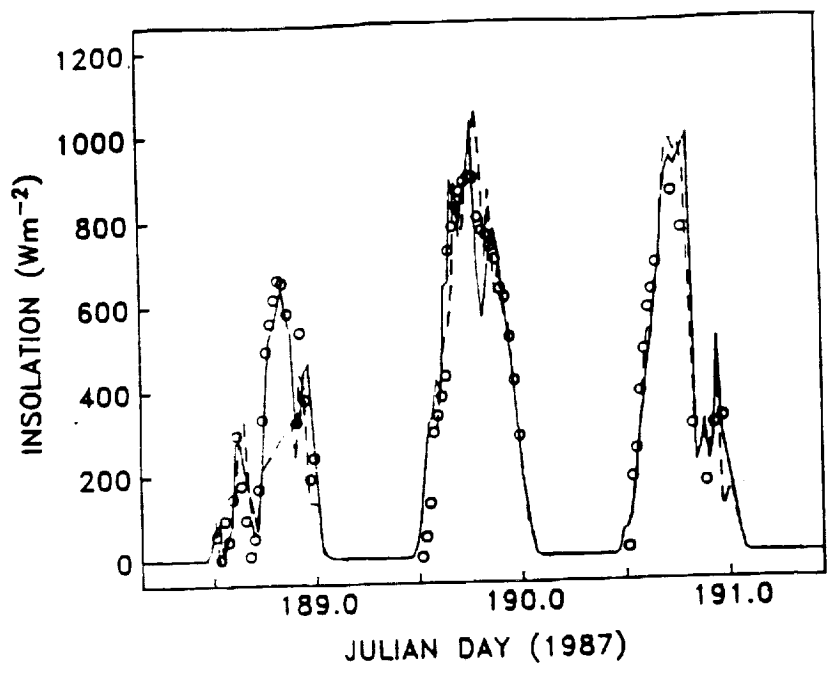


Fig. 6 Calculated versus measured insolation (top) and PAR (bottom) for selected days during FIFE's second IFC. Satellite estimates are instantaneous, whereas measured values are half-hourly averaged.

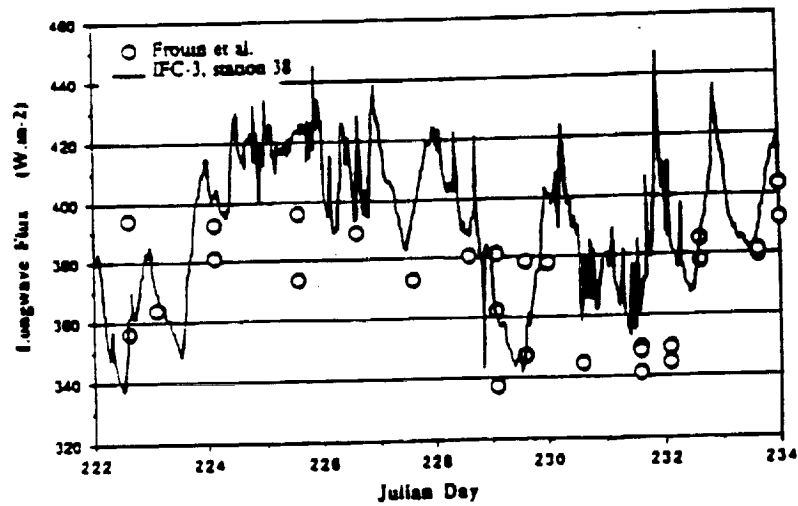
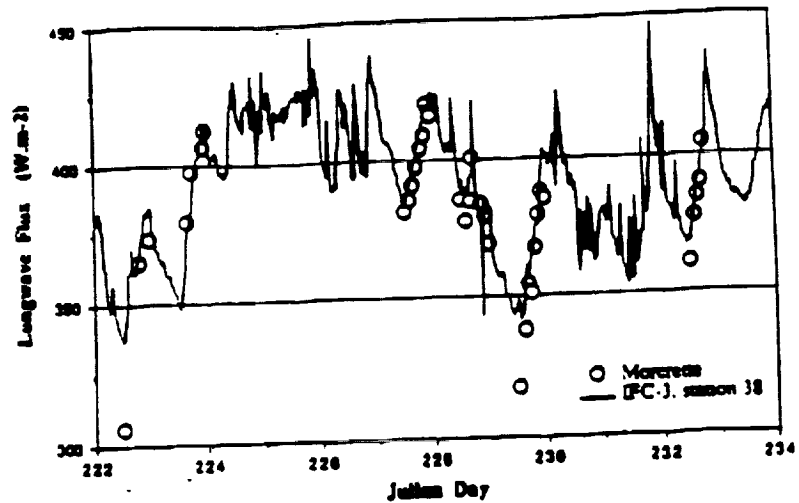
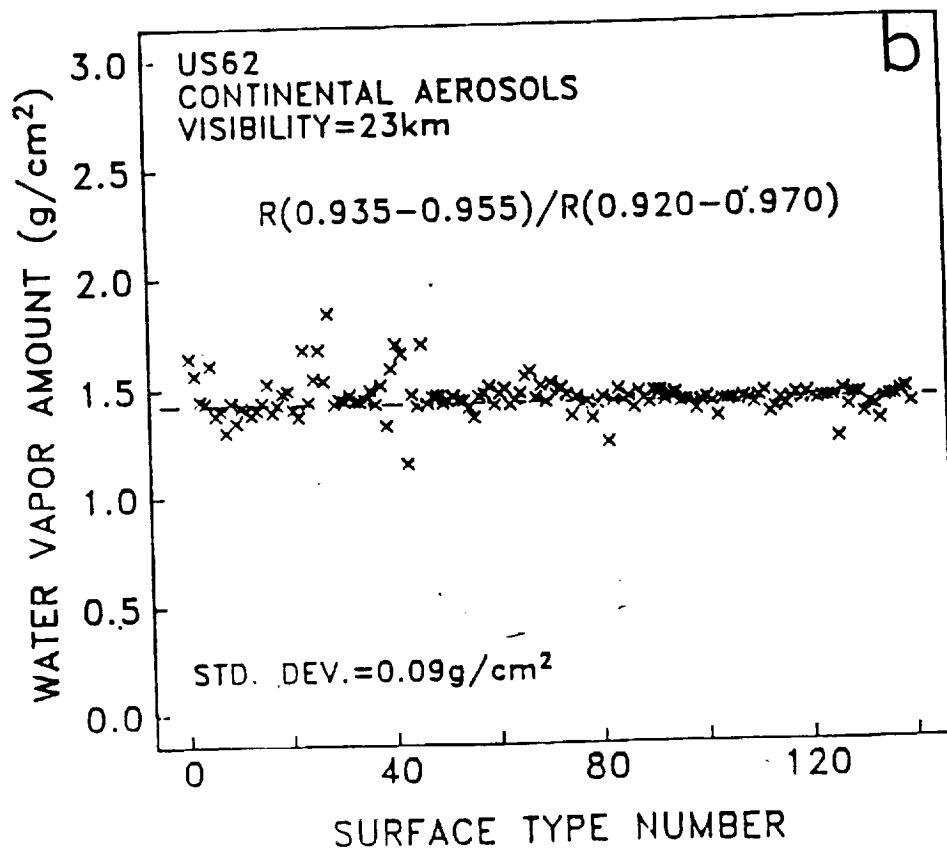
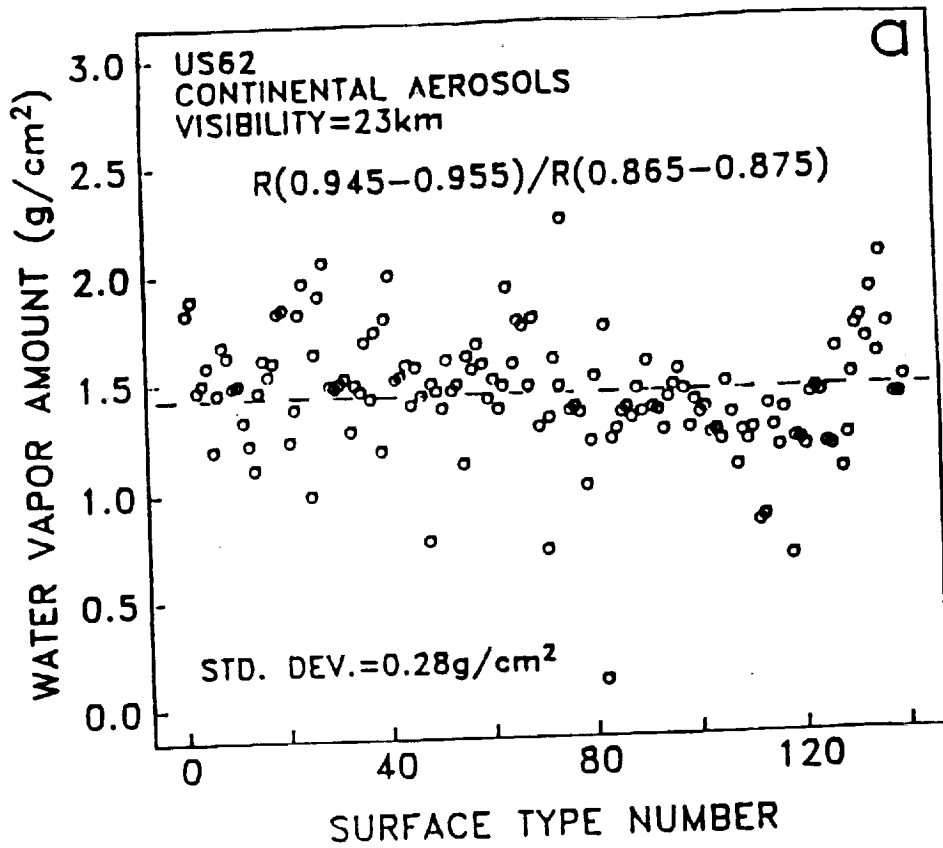


Fig. 7 Time series of measured and calculated downward longwave flux at the surface during FIFE's third IFC. Top: longwave flux calculations are made during clear sky periods (determined from sky photographs) using radiosonde data. Bottom: longwave flux calculations are made in clear and cloudy conditions according to Frouin et al.'s (1989) method C using TOVS data.



ORIGINAL PAGE IS
OF POOR QUALITY

Fig. 8 Simulations of the retrieved total water vapor amount for various surface targets when viewing the surface in channels: 0.945 - 0.955 μm and 0.865 - 0.875 μm (a), and 0.935 - 0.955 μm and 0.920 - 0.970 μm (b). The standard deviation around the actual value (dashed line) is reduced from 0.28 $g\ cm^{-2}$ to 0.09 $g\ cm^{-2}$ when using the channels centered on the same wavelength.

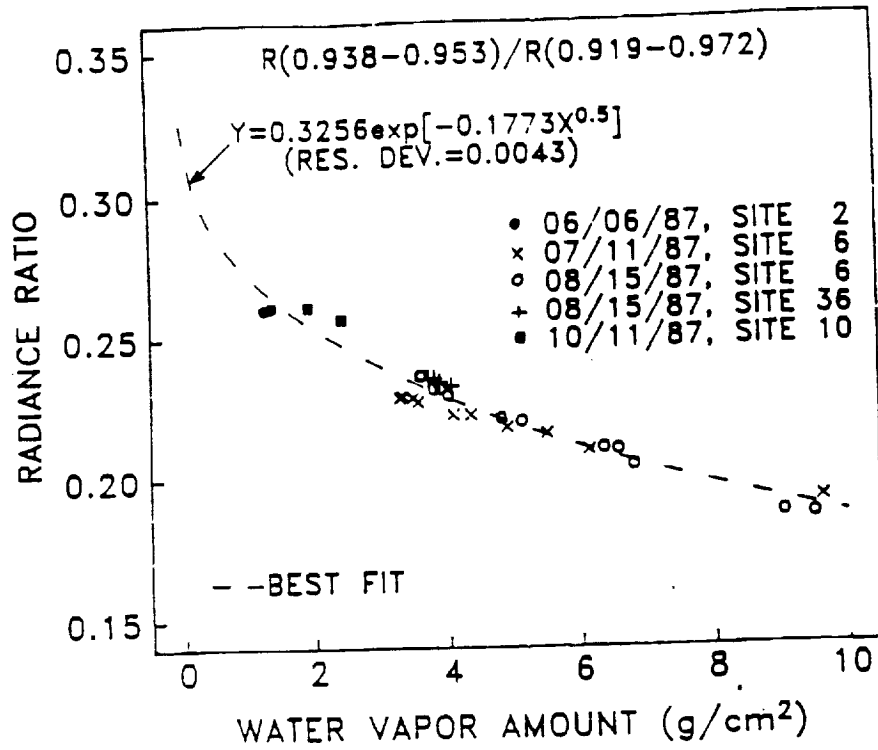
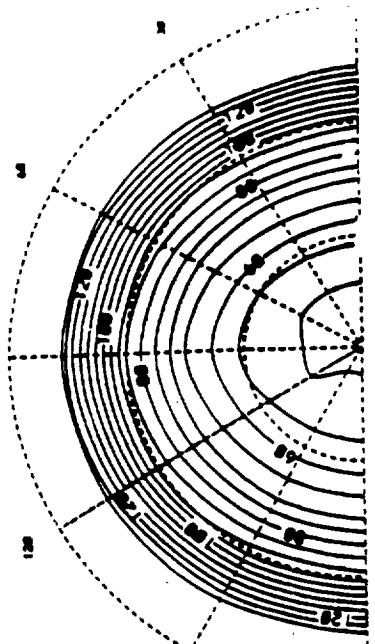
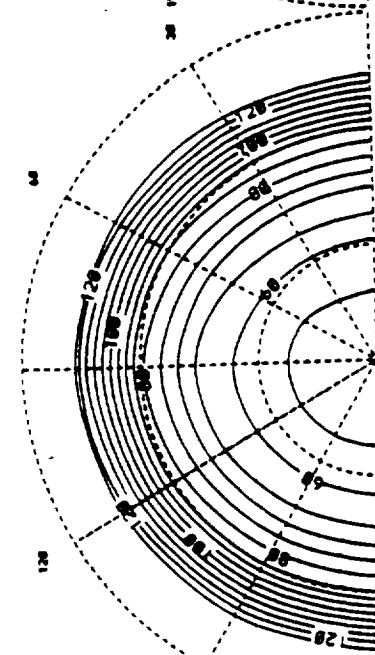


Fig. 9 Experimental and theoretical relationship between radiance ratio and water vapor amount. The channels selected are 938-953 nm (narrow) and 919-972 nm (wide).

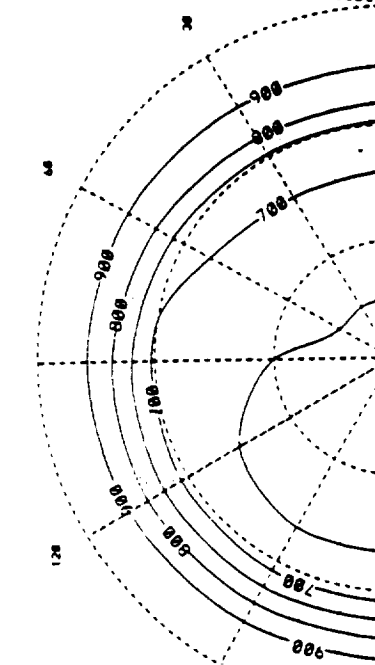
$t_{\text{etas}}=60/45N/\text{jul}/\text{erecto}/\text{NDVI}$



$t_{\text{etas}}=60/45N/\text{jul}/\text{sphero}/\text{NDVI}$



$t_{\text{etas}}=60/45N/\text{jul}/\text{plano}/\text{NDVI}$



APAR Residual Error (x1,000)

APAR Residual Error (x1,000)

APAR Residual Error (x10,000)

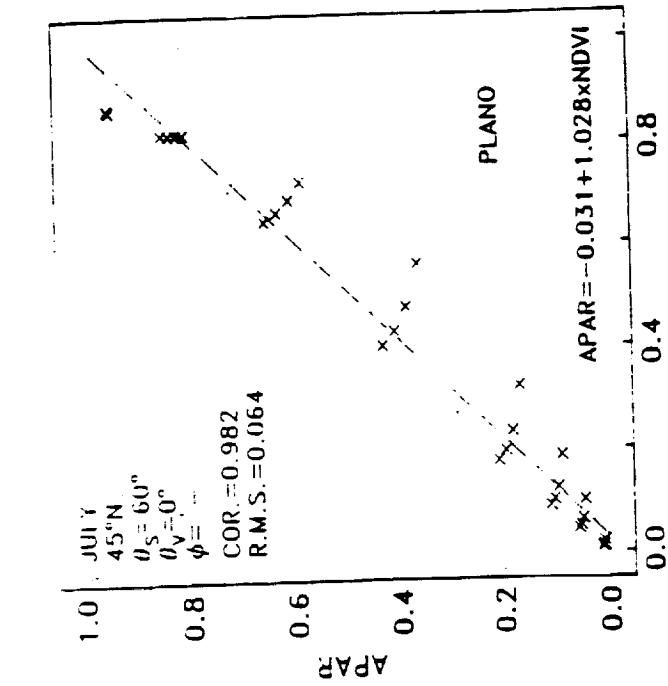
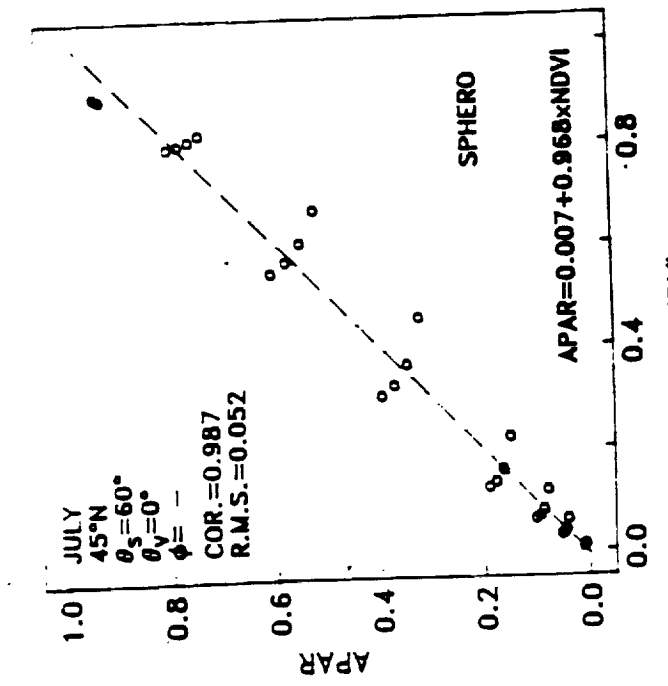
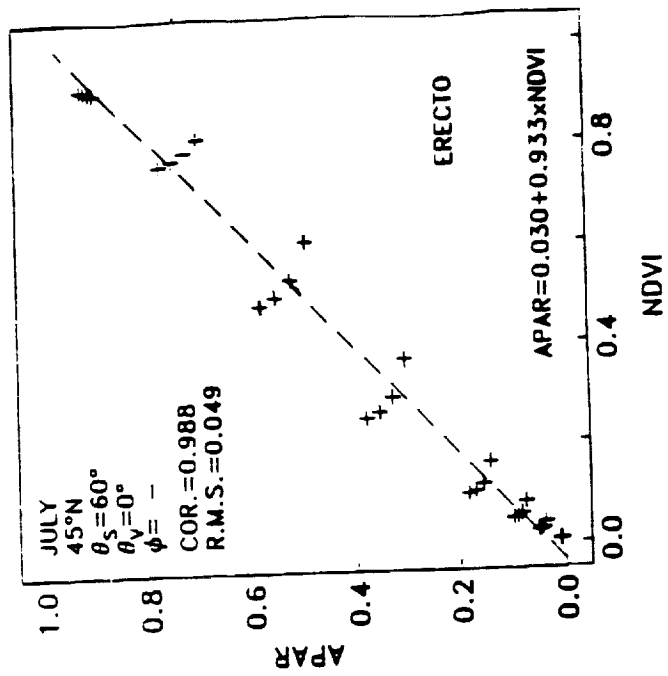
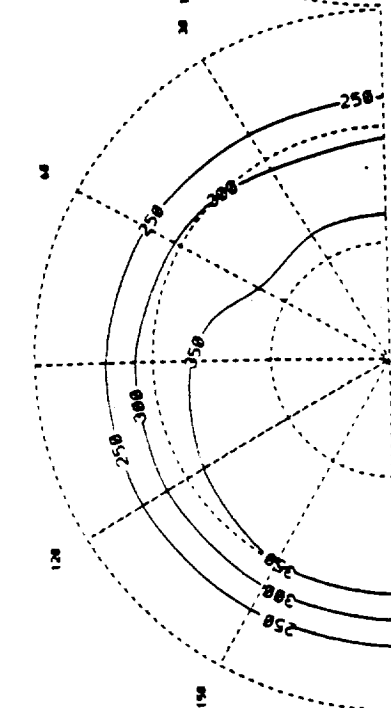


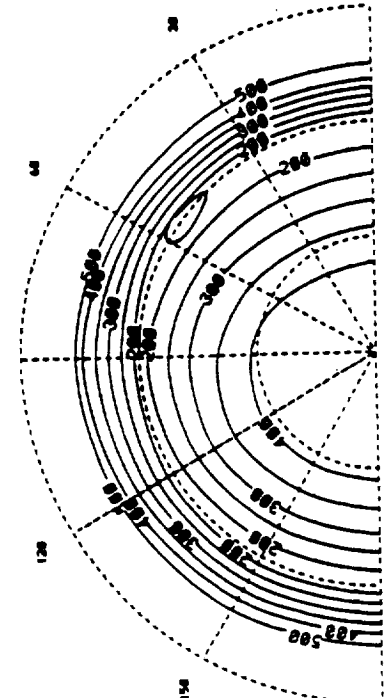
Fig. 10 Top: Daily-averaged APAR residual error as a function of viewing zenith angle, θ_v , and relative azimuth angle, ϕ , for a sun at 60° from zenith in July and at 45°N (APAR is obtained from normalized difference of reflectances, NDVI). Bottom: scatter plot of daily-averaged APAR versus instantaneous NDVI. Each set of polar diagrams and scatter plots corresponds to planophile, sphero and erecto canopy types, respectively. At moderate values of leaf area index (APAR and NDVI values around 0.5), planophile and erecto canopy types result in points aligned perpendicularly to the best fit line (dotted line), which indicates that the APAR versus NDVI relationship is not only non-linear, but also strongly depends upon the type of background.

tetas=60/45N/jul/plano/ro



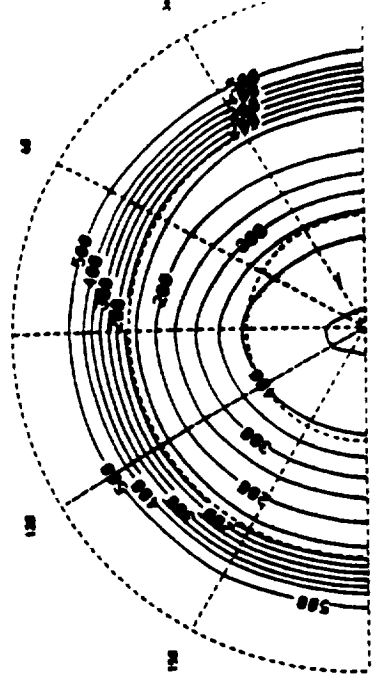
APAR Residual Error (x10,000)

tetas=60/45N/jul/sphero/ro



APAR Residual Error (x10,000)

tetas=60/45N/jul/erecto/ro



APAR Residual Error (x10,000)

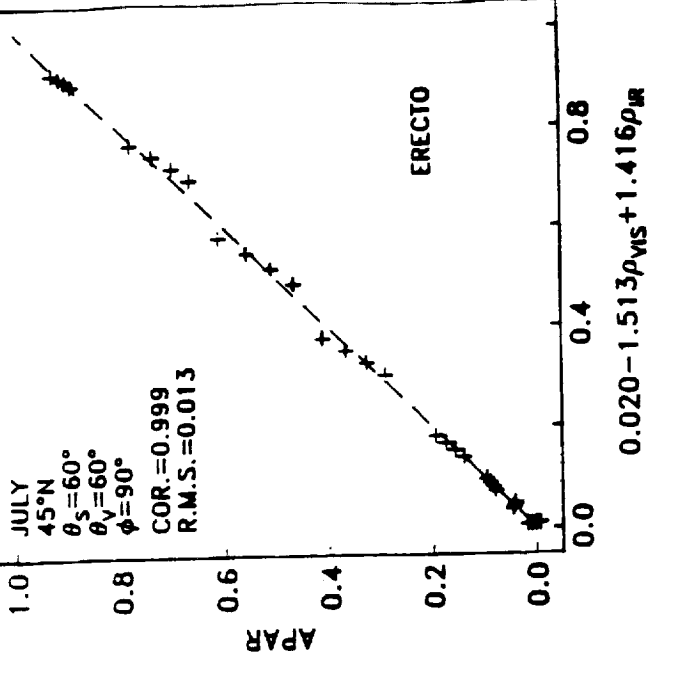
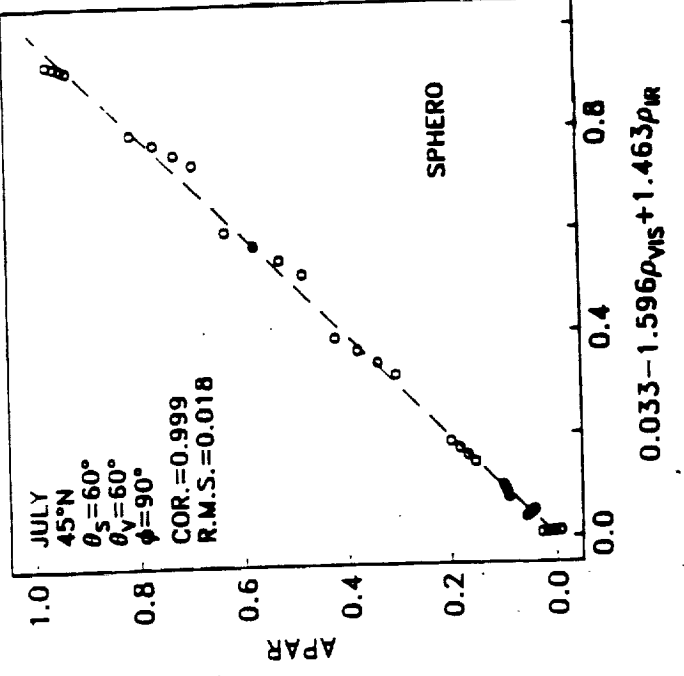
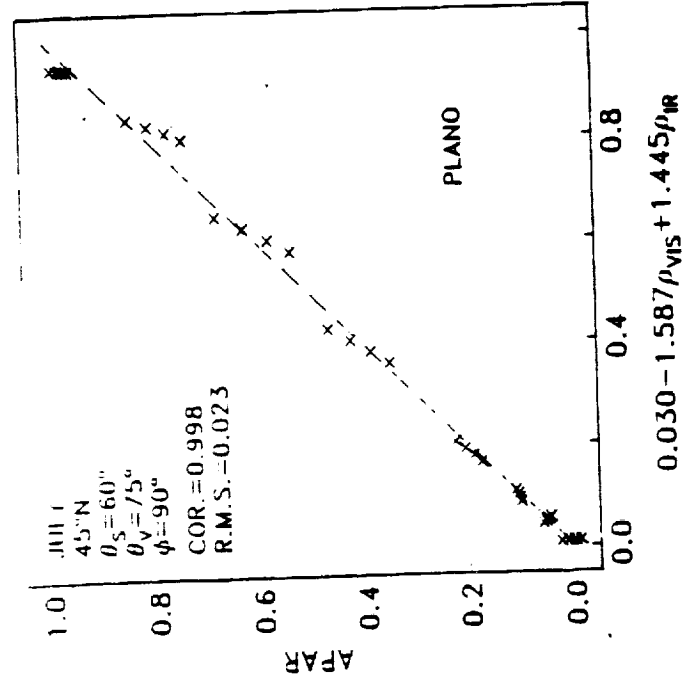


Fig 1 Same as Fig 9 but linear combinations of reflectances in the visible and near-infrared, ρ_{vis} and ρ_{ir} , respectively. Compared to Fig 9 and for the θ_v 's and ϕ 's indicated, daily-averaged APAR residual error is substantially reduced. Points corresponding to a same leaf area index, but different background reflectance, are now more aligned along the best fit line. To reduce the daily-averaged APAR residual error it is preferable to view the target at a zenith angle as high as possible in the case of a planophile canopy (the viewing geometry effect, however, remains small) and around 60° in the case of spherophile and erectophile canopies.

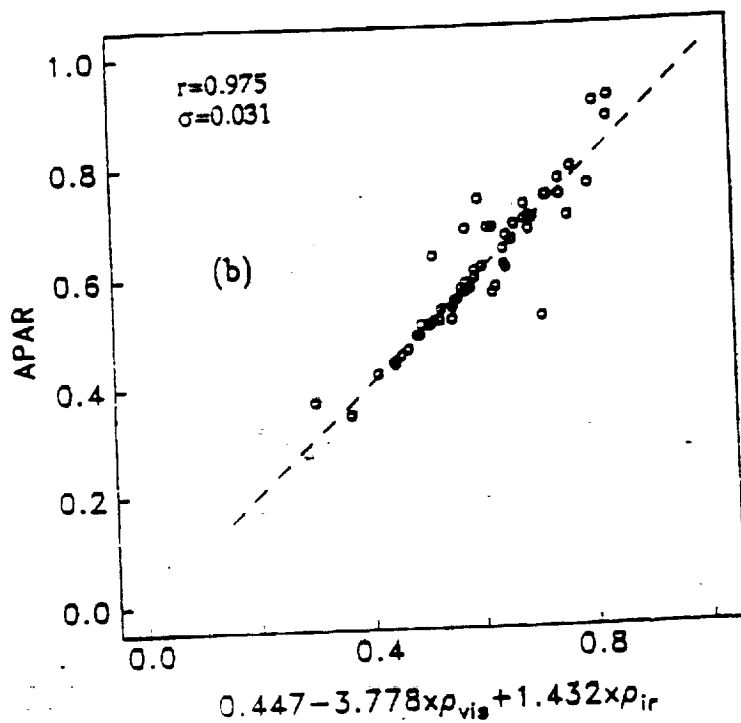
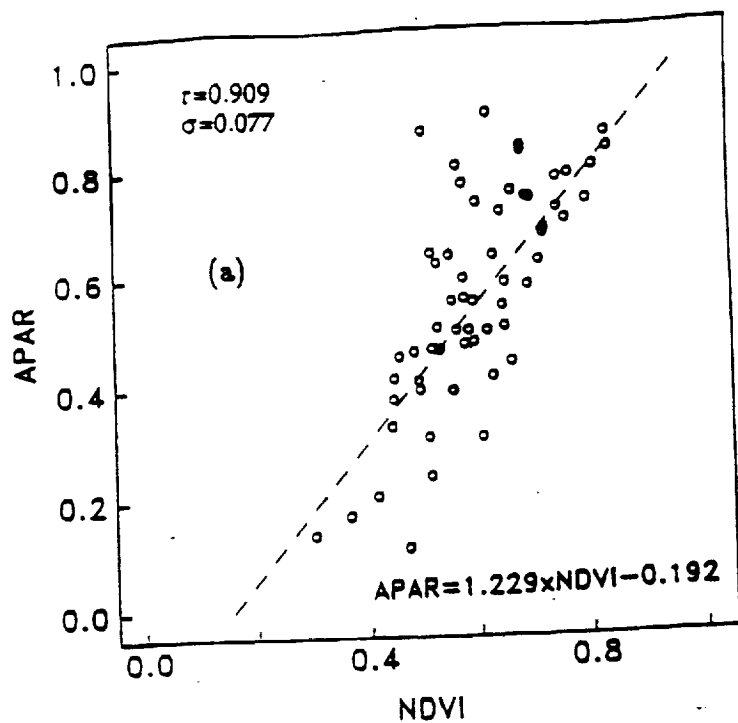


Fig. 12 (a) Estimate of APAR based on NDVI. (b) Estimate of APAR based on optimized linear channel combination (OLCC) scheme. Both are derived from nadir measurements by an Exotech radiometer during the 1989 FIFE IFC. The OLCC scheme is shown to be a potentially better predictor for APAR.

AUGUST 4 VS AUGUST 8, 1989 - SITE 16

PYRANOMETER MSMTS -- PARABOLA SITE

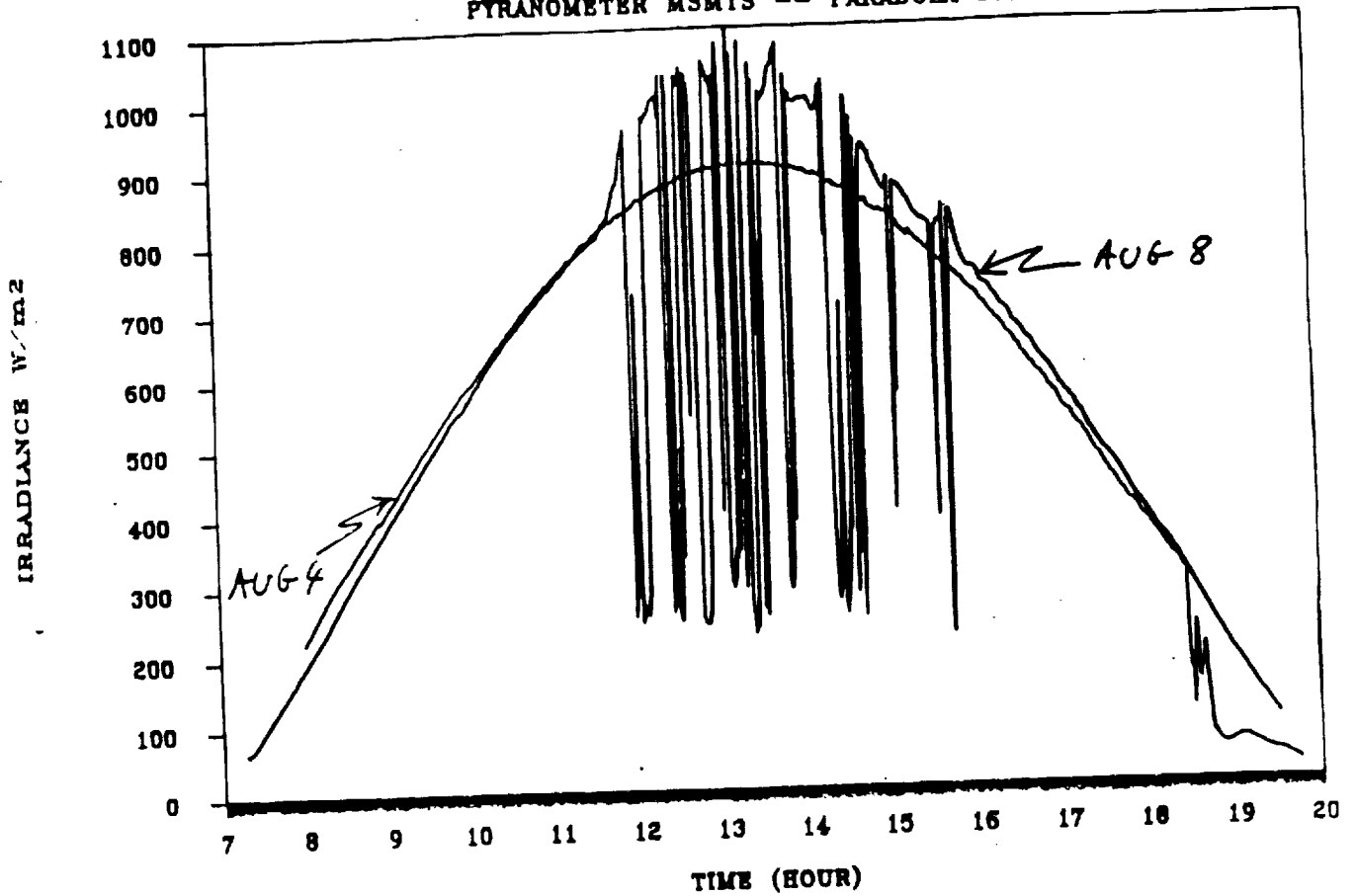
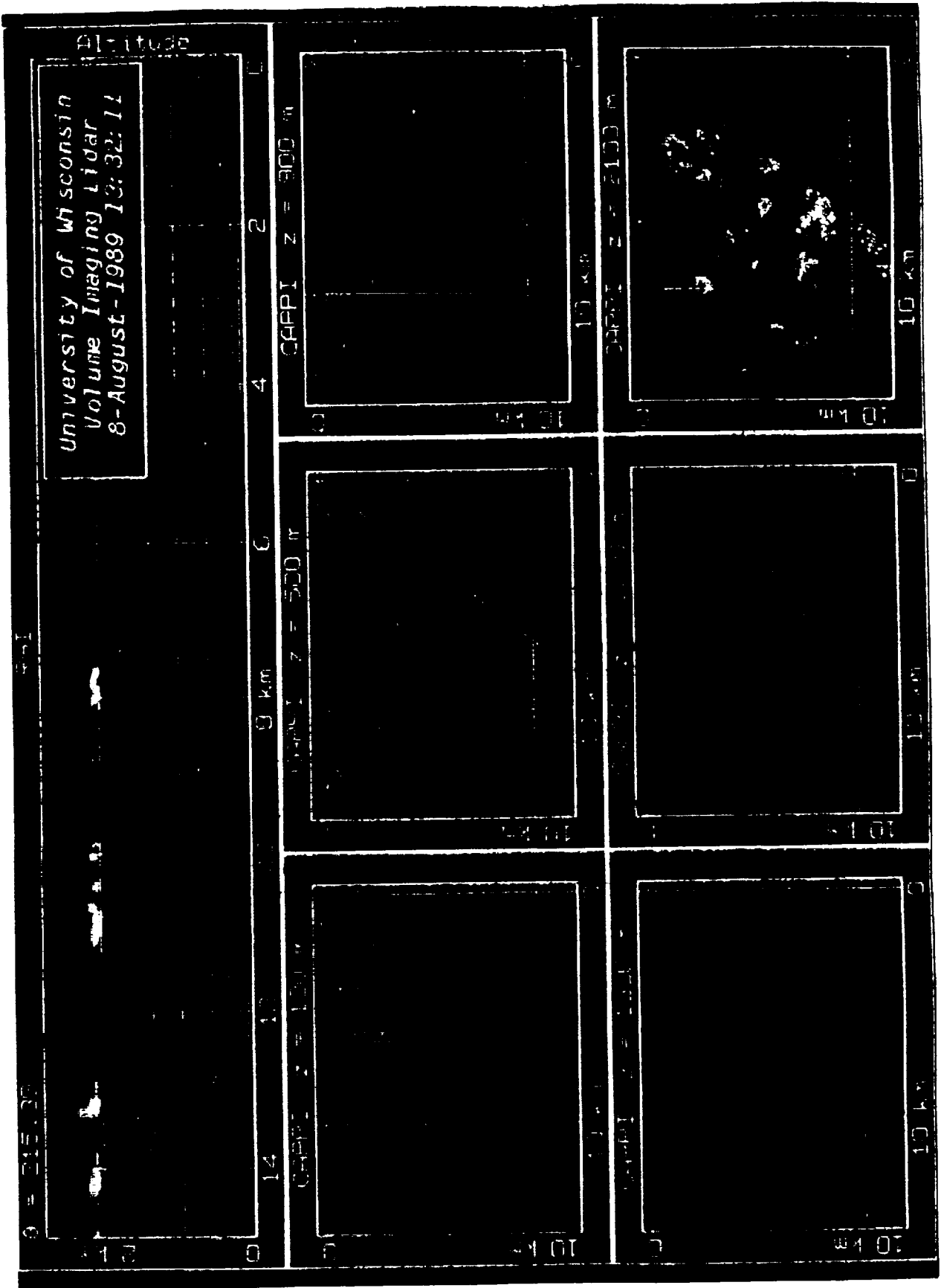


Fig. 13 Surface solar irradiance on August 4 and 8, 1989 at site 16 in the Konza prairie, Kansas (site 16). (Courtesy of Don Deering and Tom Eck.)

Fig. 14 Volume imaging lidar backscattering coefficient on August 8, 1989 at 13:32 local time. at a few kilometers from site 16 in the Konza prairie, Kansas. (Courtesy of Eloranta.)



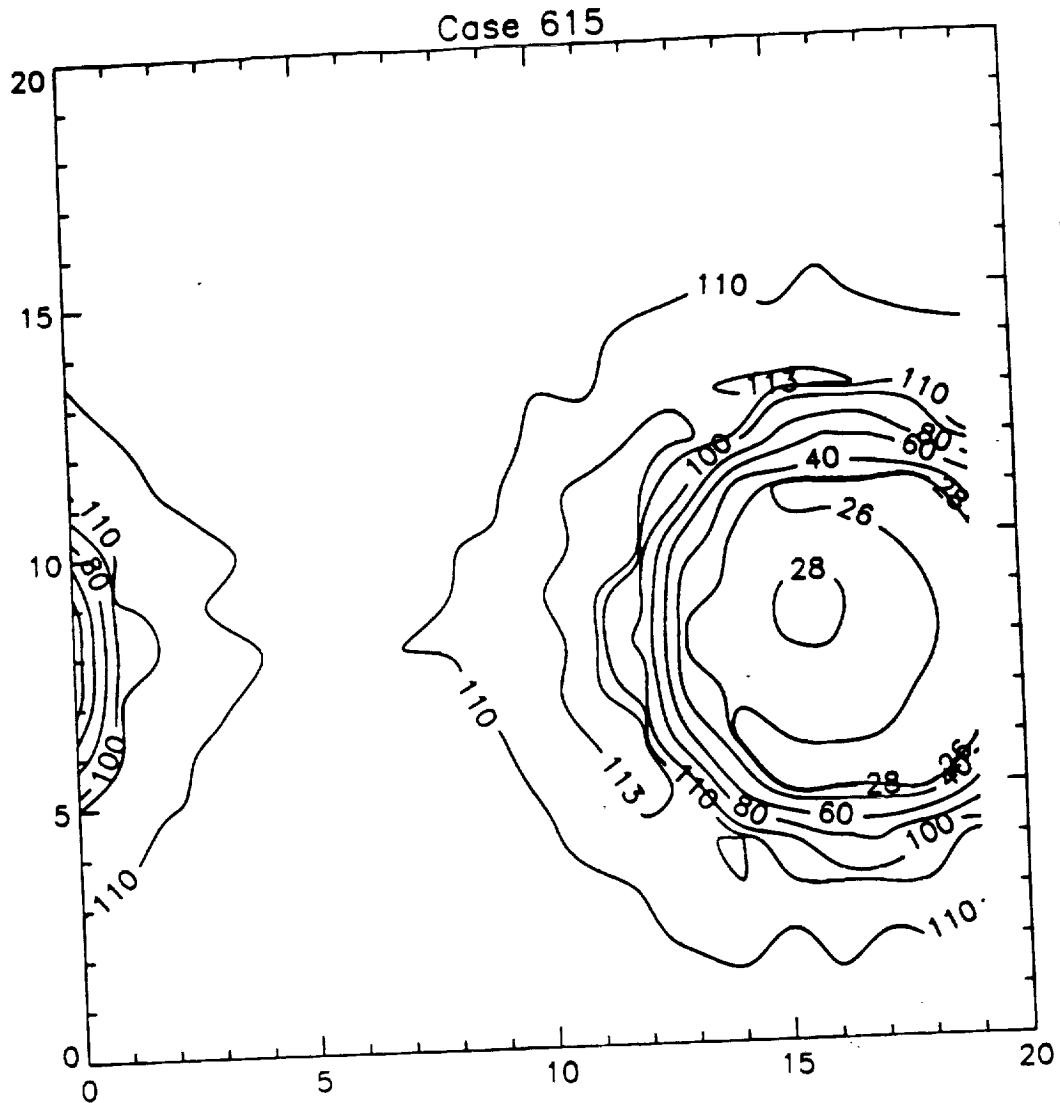


Fig. 15 Monte Carlo simulations of the spatial distribution of cloud transmittance (in %) on August 8, 1989 at site 16 in the Konza prairie, Kansas, at 13:30 local time. The clouds are cylindrical of radius 500m, separated by 2,500m, and located between 2,000 and 2,200m (geometrical thickness of 200m). The cloud optical thickness is 12.

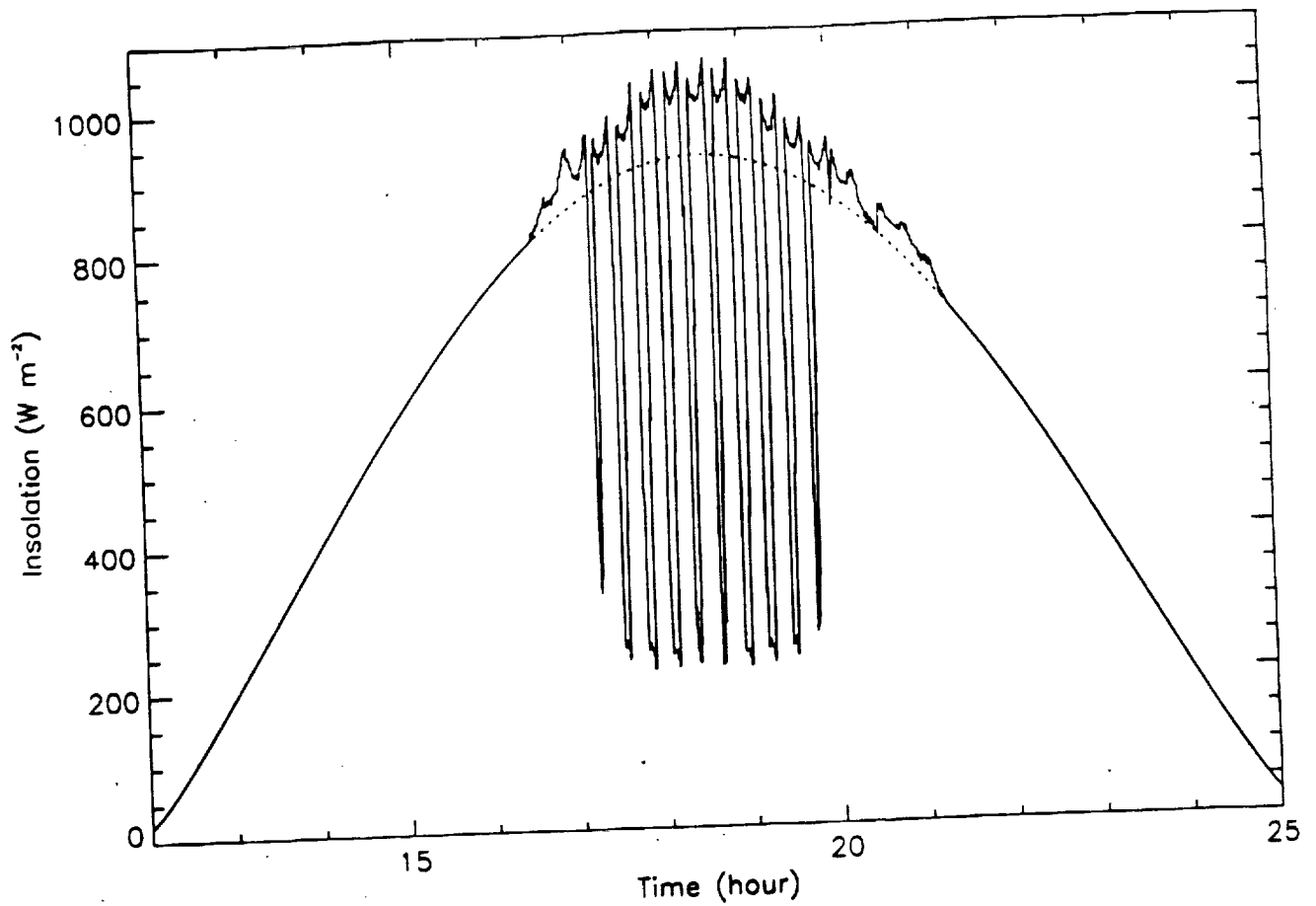
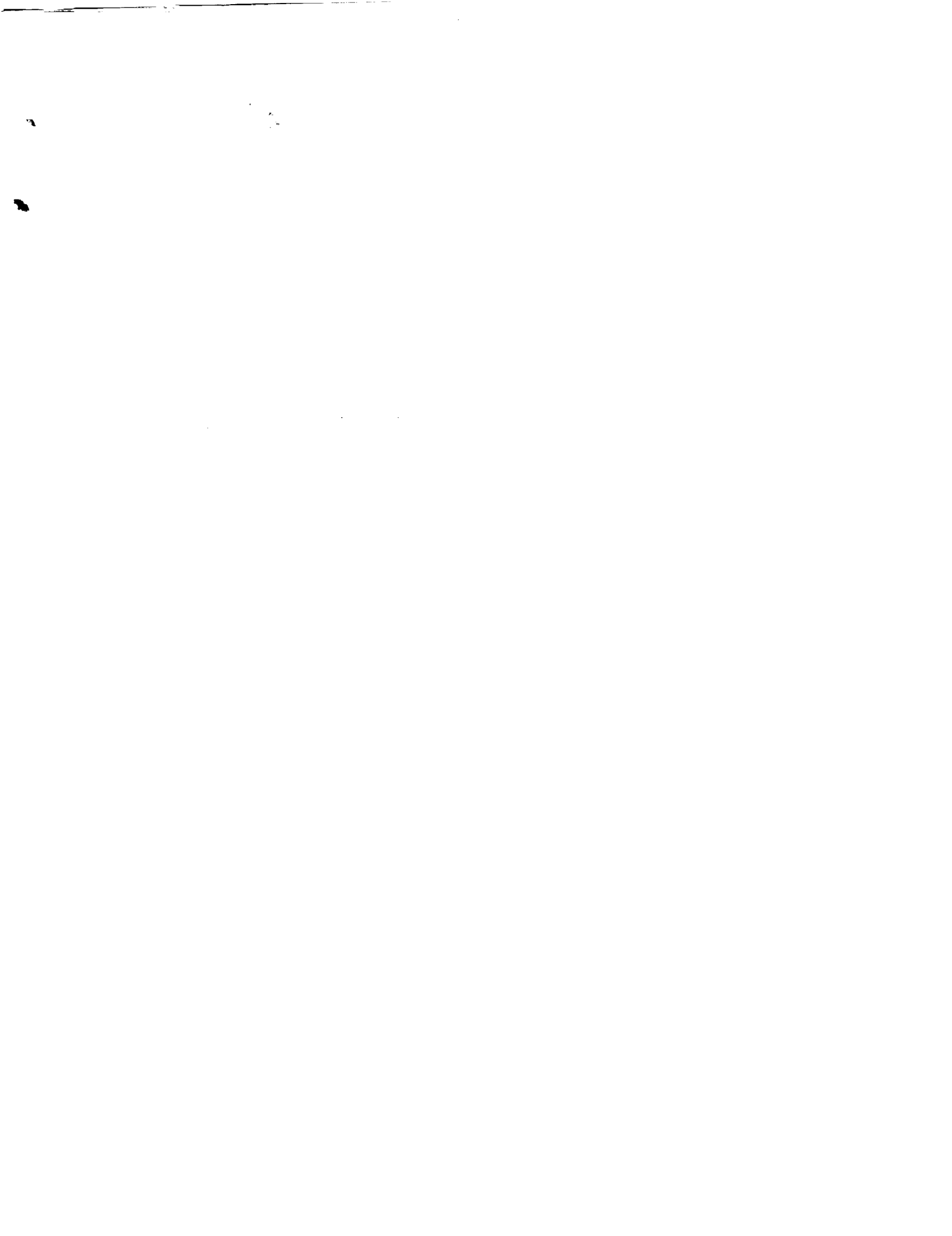


Fig. 16 Monte Carlo simulations of the downward shortwave irradiance on August 8, 1989 at site 16 in the Konza prairie, Kansas. The cloud field is advected at the observed velocity of 4 ms^{-1} . Many of the features of the pyranometer trace (Fig. 16) are reproduced quantitatively.



PREV ANN
A92-13983

Appendix 1

RADIATIVE TRANSFER MODEL VALIDATIONS
DURING THE FIRST ISLSCP FIELD EXPERIMENT

R. Frouin, F.-M. Bréon, C. Gautier

*Proc. 7th Conf. on Atmospheric Radiation, San Francisco, CA, July 23-27, 1990,
429-435, Published by the American Meteorological Society*

RADIATIVE TRANSFER MODEL VALIDATIONS DURING THE FIRST ISLSCP FIELD EXPERIMENT

Robert Frouin, Francois-Marie Bréon, and Catherine Gautier

California Space Institute
Scripps Institution of Oceanography
La Jolla, California 92093

1. INTRODUCTION

Simple (highly parameterized, analytical) radiative transfer models are important for climate studies. While retaining the essential physics of the problem, they alleviate the computational burden of more sophisticated or 'exact' schemes, which is particularly useful in general circulation models. The simplified assumptions are justified not only because of computational efficiency arguments, but also because some of the governing parameters are not determined or known with sufficient accuracy to justify a detailed description of secondary processes.

Among simplified schemes, the models of Tanré et al., (1979) and Morcrette (1984) have been used extensively to compute downward solar (shortwave) and terrestrial (longwave) irradiance at the earth's surface, respectively (e.g., Gautier et al., 1988; Frouin et al., 1988; Gautier and Frouin, 1990). Although these models have been verified against exact calculations or line-by-line models, they have not been validated against in situ measurements.

During the First ISLSCP Field Experiment (FIFE) concomitant radiosonde launches, sky photographs, aerosol turbidity and radiation measurements were made, offering the opportunity to compare model outputs to surface-measured fluxes. The comparisons are presented here, but only in clear sky conditions because the available data did not permit adequate characterization of some of the important cloud parameters (e.g., cloud vertical extension). Furthermore, the model of Tanré et al. (1979) is only valid for clear skies.

First, we briefly describe the radiative transfer models and summarize previous comparisons with exact calculations of more detailed models; then we present the FIFE data used in the comparisons, and finally we report on the comparison statistics and discuss some implications for climate studies.

2. RADIATIVE TRANSFER MODELS

2.1 The 5S model

The Simulation of the Satellite Signal in the Solar Spectrum (5S) code (Tanré et al., 1985; 1986) computes the solar radiation backscattered to space by the earth-atmosphere system. Given a Lambertian ground target and a clear atmosphere, the code estimates the target's apparent reflectance by taking into account the effects of scattering by molecules and aerosols, gaseous absorption, and spatial inhomogeneities in the surface reflectance. The input parameters, namely solar and viewing geometries, atmosphere model, surface reflectance, and spectral band, can be specified from standard or user-defined conditions. In addition to apparent reflectance, the code provides gaseous transmittance and irradiance at the surface, as well as the various components of the satellite signal. Furthermore, exact calculations at selected wavelengths allows the user to assess the code's accuracy.

Based on Tanré et al., (1979), the top-of-atmosphere signal is expressed as a function of the successive orders of radiation interactions in the coupled surface-atmosphere system. If ρ is the reflectance of the target, and ρ_e that of its environment, the apparent reflectance is written as:

$$\rho^*(\mu, \mu', \phi) = t_g(\mu, \mu') \left\{ \rho_s(\mu, \mu', \phi) + \frac{e^{-\tau/\mu} + t_d(\mu)}{1 - \rho_e S} \left[\rho_e e^{-\tau/\mu'} + \rho_e t_d(\mu) \right] \right\} \quad (1)$$

where $\theta = \arccos(\mu)$ and $\theta' = \arccos(\mu')$ are the solar and viewing zenith angles, respectively, ϕ is the relative azimuth angle between solar and viewing directions, τ is the atmospheric optical thickness, t_g is the gaseous transmittance, ρ_e is the intrinsic atmospheric transmittance, t_d is the diffuse

atmospheric transmittance, and S is the spherical albedo of the atmosphere. The first term enclosed in the curly brackets represents the contribution of photons backscattered to space without surface reflection, whereas the second term characterizes photons that have sustained one or multiple surface reflections. Absorption by atmospheric gases is considered as a single multiplicative factor dependent on the direct paths sun-to-surface and surface-to-sensor. Decoupling absorption and scattering processes is justified since, on the one hand, ozone absorption is located at altitudes where molecules are rarified, and on the other, water vapor and carbon dioxide absorption occurs above 850 nm where molecular scattering is negligible, and first and second orders of aerosol scattering (predominantly forward) reconstitute almost all of the diffuse radiation. According to Tanré et al., (1986), the error introduced by separating the two processes is smaller than one percent, except for grazing incidence or observation directions ($\mu, \mu' < 0.1$).

The atmospheric functions t_d and S are approximated by analytical formulas determined empirically from exact radiative transfer calculations performed for a wide range of model atmospheres. Table 1 shows the disparity between 5S and exact calculations of the total diffuse atmospheric transmittance, $e^{-\tau/\mu} + t_d$, for various zenith angles and a wavelength of 850 nm (near the equivalent wavelength for the entire solar spectrum). Results are presented for two atmospheres, clear and hazy. The differences are small, generally less than 1%, but reach 1.6% when θ equals 60° and the atmosphere is hazy.

Table 1. Comparison of 5S and exact calculations of the atmospheric total diffuse transmittance at 850nm.

Atmosphere	$\theta = 15^\circ$		$\theta = 60^\circ$	
	5S	Exact	5S	Exact
Clear	0.973	0.973	0.926	0.924
Hazy	0.926	0.927	0.819	0.806

The gaseous transmittance, t_g is computed from two exponential random band models, that of Goody (1964) for water vapor, and of Malkmus (1967) for oxygen, ozone, and carbon dioxide. The spectral resolution, 20 cm^{-1} , is sufficient to apply the random band models confidently. Table 2 compares the gaseous transmittance in the total solar spectrum computed with 5S and a well-known code, LOWTRAN-6 (Kneizys et al., 1983). For all the atmospheres and zenith angles considered, the agreement is better than 1.5%, with 5S giving values systematically higher. This may be due to the fact that LOWTRAN-6, unlike 5S, neglects the influence of temperature on the molecular absorption coefficient, and approximates molecular line absorption by a one parameter band model.

Table 2. Atmospheric gaseous transmittance in the spectral interval 250-4000nm computed with 5S and LOWTRAN-6.

Atmosphere	$\theta = 15^\circ$		$\theta = 60^\circ$	
	5S	LOWTRAN-6	5S	LOWTRAN-6
Tropical	0.828	0.820	0.793	0.782
Midlatitude Summer	0.838	0.830	0.803	0.794
Midlatitude Winter	0.876	0.865	0.844	0.834
Subarctic Summer	0.850	0.841	0.815	0.806
Subarctic Winter	0.893	0.880	0.862	0.850

2.2 The wide-band model of Morcrette (1984)

This model (see also Morcrette et al., 1986) is based on a highly parameterized scheme developed for GCMs. In a clear atmosphere, upward and downward longwave irradiances at altitude z are computed from the radiative transfer equation developed into:

$$F^+(z) = \pi \int_0^\infty dv \{ [B_s - B(0)] t(z, 0; r) + B(z) - \int_0^z dz' \frac{dB(z')}{dT} \frac{dT(z')}{dz} t(z, z'; r) \} \quad (2)$$

$$F^-(z) = \pi \int_0^\infty dv \{ B(Z) t(z, Z) - B(z) + \int_z^Z dz' \frac{dB(z')}{dT} \frac{dT(z')}{dz'} t(z', z; r) \} \quad (3)$$

where z is altitude, $B(z)$ is the Planck function at temperature $T(z)$, $t(z, z'; r)$ is the atmospheric transmittance between altitudes z and z' evaluated in the equivalent direction $\mu=1/r$ (r is the diffusivity factor), B_s characterizes the surface emission, Z is the top-of-atmosphere altitude, ν is frequency, and superscripts + and - denote upward and downward fluxes, respectively. In (2), the effect of a surface emissivity ϵ less than unity is taken into account by writing B_s as $\epsilon B(T_s) + (1-\epsilon) F^-(0)$ where T_s is the surface temperature.

To evaluate the integral over z on the right-hand side of (2) and (3), the atmosphere is divided in N layers of arbitrary thickness. Temperature and absorber amounts are specified at each level separating these layers. In spectral regions where atmospheric absorption is strong, the radiative energy is exchanged over short distances. Integration over the layer adjacent to the surface is therefore performed using a 2-point Gaussian quadrature. For the other layers, a simple trapezoidal rule is applied. When compared with a more accurate 32-point Gaussian quadrature for all layers, the simpler integration scheme gives a maximum 4 Wm^{-2} error in the downward flux at the surface (Morcrette and Fouquart, 1985).

To perform the integration over ν Rodgers' (1967) emissivity approach is followed. Four spectral intervals are considered ($0-500\text{ cm}^{-1} + 1250-2820\text{ cm}^{-1}$, $500-800\text{ cm}^{-1}$, $800-1250\text{ cm}^{-1}$, and $970-1110\text{ cm}^{-1}$), in which atmospheric absorption is due mainly to water vapor and carbon dioxide (first three intervals) or ozone (last interval). Absorption by minor gaseous constituents (e.g., methane, nitrous oxide) and aerosols is neglected. The contribution of each spectral interval to $F^*(z)$ and $F(z)$ is evaluated using normalized transmissivity functions. Absorption by water vapor is treated with the statistical band model of Goody (1952) whereas absorption by carbon dioxide and ozone is modeled according to Malkmus (1967). At high altitudes, these models are modified to account for the Voigt profile of the absorption lines. The strong line approximation is used for water vapor and carbon dioxide, and the weak line approximation for ozone. To account for temperature and pressure dependence on absorption, the Curtis-Godson approximation is applied and equivalent absorber amounts are defined accordingly. For more details, see Morcrette (1984) and Morcrette et al., (1986).

The wide-band model of Morcrette (1984) has been compared with a more detailed, narrow-band model (Morcrette and Fouquart, 1985) and with Scott and Chedin's (1981) line-by-line model. In the comparison, the agreement was within 2-3%. This is illustrated in Table 3 from Bréon et al., (1990), which shows the downward longwave irradiance at the surface $F(0)$ obtained with the wide-band and line-by-line models for typical atmospheres. The differences are small, generally a few Wm^{-2} . Morcrette's (1984) model, however, appears to be more sensitive than the line-by-line model to changes in atmospheric temperature and water vapor (the range of values is 231.3 Wm^{-2} instead of 225.5 Wm^{-2}).

Table 3. Downwelling longwave irradiance at the surface (in Wm^{-2}) computed using 4A and Morcrette (1984) models. (After Bréon et al., 1990.)

Atmosphere	Radiative Transfer Model	
	4A (line-by-line)	Morcrette (Wide-Band)
Tropical	390.6	395.1
Midlatitude Summer	341.8	346.2
Midlatitude Winter	213.1	214.9
Subarctic Summer	289.3	295.7
Subarctic Winter	165.1	163.8

3. DATA

The data used to verify the 5S model and the wide-band model of Morcrette (1984) comprise shortwave and longwave radiative fluxes from pyranometers and pyrgeometers, fractional cloud cover from a sky camera, vertical profiles of air temperature and water vapor mixing ratio from

radiosondes, and aerosol optical thickness and Ångström exponent from sunphotometers. The measurements were made during FIFE's four Intensive Field Campaigns (IFCs), which took place in 1987 during the various phases of the vegetation seasonal cycle, namely green-up (26 May - 6 June: IFC-1), peak greenness (25 June - 15 July: IFC-2), dry down (10 August - 21 August: IFC-3), and senescence (5 October - 15 October: IFC-4). The experimental site, located on the Konza Prairie near Manhattan, Kansas, is an approximate $15 \times 15\text{ km}$ square with various topological features including plateau, slope and creek. Fig. 1 shows the location of the site and, within the site, the measuring stations selected in the present study.

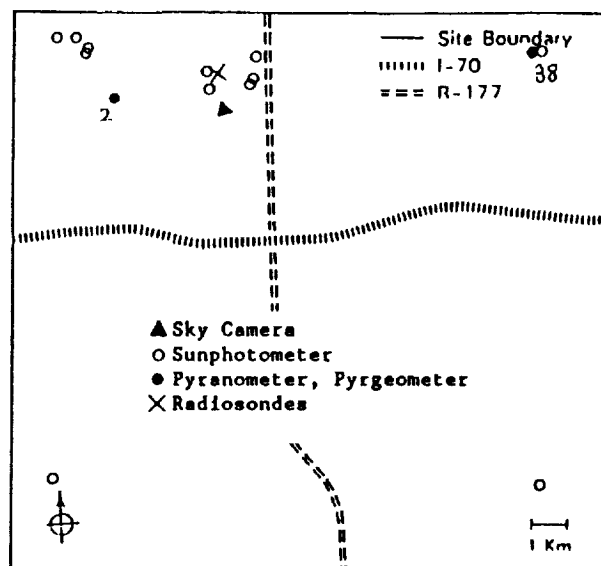


Fig. 1. Map of the FIFE site, centered at $39^{\circ} 04' \text{ N}$ and $96^{\circ} 30' \text{ W}$, showing the location of the sky camera, radiosondes, and radiation stations selected in the study.

The radiative flux measurements are those made at stations 2 and 38 (see Fig. 1). Table 4 compares, for downward shortwave and longwave irradiances the values obtained at the two stations under virtually clear skies (fractional cloud cover less than 5%). The r.m.s. differences are small at the scale considered (half-hour), representing only 2.6% and 1.7% of the average shortwave and longwave irradiances, respectively, and the biases are negligible. The agreement between the datasets further indicates that spatial variability of the clear atmosphere is small over the distance between the two stations; therefore, in the model computations one can confidently use concomitant atmospheric data at nearby (not necessarily the same) locations. For the comparisons, we averaged radiative flux measurements at the two stations.

Surface albedo was deduced by ratioing upward and downward shortwave irradiances. The albedo values at the two stations exhibited significant changes (not shown here), especially at large solar zenith angles. Nevertheless, we averaged those values for use in the 5S model further assuming that spectral surface reflectance is constant in the entire solar spectrum and equal to the broadband surface

Table 4. Comparison statistics of downwelling irradiance measured by stations 2 and 38 during FIFE. Fractional cloud cover, as estimated from the sky photographs, is less than 5%. Average and range values correspond to station 2.

Parameter	Nb. Pts.	Ave. (Wm^{-2})	Range* (Wm^{-2})	Corr. Coef.	r.m.s. Diff. (Wm^{-2})	Bias (Wm^{-2})
Shortwave Irradiance	326	476.4	294.5	0.999	12.4	2.1
Longwave Irradiance	339	355.1	44.1	0.991	6.1	0.9

* One standard deviation

albedo. This procedure is questionable, indeed, but somewhat justified because (1) the comparison is limited to the domain of validity of the 5S code, that is solar zenith angles less than 60° , and (2) the effect of surface albedo on downward shortwave irradiance is small.

To select clear sky conditions, we used fractional cloud cover data (hourly values) derived from photographs taken by an uplooking automatic camera. The camera was located within a few kilometers of stations 2 and 38 (Fig. 1). In deriving fractional cloud cover, the percentage of cloudy areas in the photographs were corrected by the viewing angle of each area relative to the vertical. Since the camera operated in the visible, no cloud data were available at night. We therefore limited the longwave irradiance comparison to daytime.

The vertical profiles of temperature and water vapor mixing ratio were obtained from radiosonde measurements of pressure, temperature, and wet bulb temperature. The radiosondes were launched nearby stations 2 and 38 (Fig. 1). More than 6 radiosondes were launched on average per day, mostly during daytime. The calculated water vapor mixing ratio sometimes showed negative values, especially during IFC-4. This was the result of improper wet bulb temperature measurements below 273K. We therefore removed all the water vapor information corresponding to wet bulb temperatures below that value. The data was completed using climatological profiles, noting that the water vapor mixing ratio cannot be larger than the saturation value.

Aerosol optical thickness and Ångström exponent are those inferred from total atmospheric optical thickness measurements at different wavelengths by several sunphotometers distributed within the FIFE site (Fig. 1). The measurements were made at frequent time intervals (typically every half-hour) when the sun was not obscured by clouds (the basis of the method). In general, the aerosol optical thicknesses were small, rarely exceeding 0.4; the largest ones occurred during IFC-2. Diurnal variability was significant (typically 50% of the average values), and so were the differences between nearby stations. The Ångström exponent exhibited much more variability, mainly due to errors in its determination from already noisy (to about 20%) optical thicknesses. Since the aerosol optical thicknesses were small and, therefore, the aerosol

influence on surface solar irradiance also small, we decided to use in the 5S model the average of all the concomitant aerosol optical thicknesses and of all the Ångström exponents.

4. RESULTS AND DISCUSSION

4.1 Performance of the 5S model

Table 5 summarizes the data, except ozone amount, used in the 5S model to compute downward shortwave irradiance at the surface. The cases selected correspond to fractional cloud cover less than 5% (sky non obscured) and sun zenith angle less than 60° . Furthermore, we only kept the data when all the parameters were measured within ± 30 minutes of the shortwave irradiance measurements at stations 2 and 38. In the calculations, ozone amount was fixed at 0.34 atm. cm since the effect of ozone variations is small (a few Wm^{-2}). The 5% limit in cloud cover is somewhat arbitrary, but justified to the extent that no significant changes in the comparison statistics were found when lowering the 5% limit to 0%.

As seen in Table 5, the optical thicknesses are small (0.23 is typical of a clear atmosphere), the maximum values occurring during IFC-2 (0.29 on Julian day 192). The Ångström exponents vary moderately around the value of 1, which is characteristic of continental aerosols (70% of dust-like component, 29% of water-soluble component, and 1% of soot component). During IFC-2, however, values as low as 0.52 were computed, indicating the possible presence of larger, perhaps less absorbing, particles on average. The values obtained on Julian day 157, 0.13 for optical depth and 1.00 for Ångström exponent, may be compared to those reported by Wrigley et al. (1990), 0.12 and 1.17, respectively. The agreement is good, giving confidence to our values.

From the Ångström exponent, we have an idea of the aerosol type. By mixing various percentages of dust-like, water soluble, and soot components, we found for each case a combination that gives the Ångström exponent obtained from the measurements and a single scattering albedo of 0.89. This value for the single scattering albedo corresponds to the determination of Wrigley et al. (1990), who reported values ranging from 0.889 to 0.891 on Julian day 284. Without other information, we used 0.89 for all cases. Our procedure is subjected to errors, indeed, all the more as the aerosol scattering phase function is another unknown (fortunately the forward peak, of interest here, is not as variable as the backward peak); but we have to keep in mind that the optical thicknesses are small, reducing to some extent the uncertainties associated with unknown single scattering albedo and phase function.

Table 5. Parameters used in the SS model. θ is the sun zenith angle, A_s is surface albedo, N is fractional cloud coverage, U_w is vertically integrated with vapor amounts, τ_{550} is aerosol optical thickness at 550nm, and α is Ångström exponent. All these parameters, except θ , were measured in situ during FIFE by pyranometers (A_s), sky camera (N), radiosondes (U_w), and sunphotometers (τ_{550} , α).

Date	θ ($^\circ$)	A_s	N (%)	U_w (gcm^{-2})	τ_{550}	α
155.688	29.34	0.18	0.0	1.93	0.13	1.11
155.708	24.57	0.18	0.0	2.04	0.14	1.07
155.729	20.33	0.17	0.0	2.12	0.13	1.00
155.750	17.48	0.17	0.0	2.21	0.13	0.99
155.771	16.76	0.17	0.0	2.30	0.13	0.99
155.792	18.42	0.17	0.0	2.30	0.12	1.03
155.813	21.93	0.17	1.7	2.29	0.12	1.07
155.833	26.31	0.17	2.9	2.27	0.12	1.07
155.854	31.52	0.17	3.2	2.14	0.11	1.05
155.875	37.07	0.17	1.9	1.97	0.11	1.00
155.896	42.81	0.18	1.9	1.81	0.11	1.01
155.917	48.65	0.18	1.5	1.82	0.11	1.02
156.792	18.30	0.17	3.6	2.10	0.13	1.30
156.813	21.81	0.17	3.2	2.08	0.13	1.29
156.833	26.20	0.17	3.0	2.07	0.12	1.24
156.854	31.42	0.17	2.7	2.06	0.11	1.12
156.875	36.97	0.17	1.9	2.04	0.10	1.09
156.896	42.71	0.18	0.5	2.03	0.11	1.19
156.917	48.55	0.18	0.0	2.02	0.11	1.35
157.833	26.09	0.17	0.0	1.89	0.13	1.00
187.688	30.09	0.18	4.8	5.05	0.20	1.03
192.583	59.35	0.22	0.0	4.04	0.25	0.56
192.604	53.48	0.21	0.8	4.17	0.26	0.55
192.625	47.62	0.20	3.0	4.37	0.27	0.62
192.646	41.80	0.19	2.4	4.57	0.27	0.62
192.667	36.08	0.18	2.3	4.64	0.27	0.58
192.688	30.57	0.18	2.0	4.59	0.27	0.56
192.708	25.68	0.18	1.1	4.55	0.27	0.61
192.729	21.21	0.17	0.3	4.67	0.29	0.53
192.750	17.97	0.17	1.5	4.79	0.29	0.52
192.771	16.70	0.17	4.5	4.91	0.29	0.62
229.771	25.16	0.17	0.0	2.82	0.10	0.94
229.792	26.02	0.17	0.0	3.01	0.10	0.96
229.813	28.45	0.17	0.0	3.23	0.09	0.99
229.833	31.91	0.17	0.4	3.41	0.09	1.01
229.854	36.37	0.17	0.9	3.47	0.09	1.03
229.875	41.39	0.17	1.5	3.53	0.08	1.05
229.896	46.78	0.18	2.8	3.60	0.08	1.07
229.917	52.41	0.18	2.9	3.68	0.08	1.09
229.938	58.18	0.19	3.2	3.77	0.08	1.12
280.771	44.54	0.17	0.8	1.66	0.07	0.74
280.792	45.66	0.17	0.8	1.72	0.06	0.81
280.813	47.79	0.17	0.8	1.77	0.06	0.88
280.833	50.64	0.17	0.4	1.78	0.06	0.95
280.854	54.34	0.17	0.0	1.80	0.06	1.02
280.875	58.63	0.17	0.0	1.81	0.05	1.10
284.833	52.14	0.17	0.0	1.33	0.08	1.37

Figure 2 shows the results of the comparison. On a half-hourly time scale, the correlation coefficient is above 0.99, the standard deviation is 23.2 Wm^{-2} (about 3% of the average value), and the bias is 13.2 Wm^{-2} (overestimation by the 5S model). Examining each IFC separately reveals that overestimation occurs for all IFCs, except IFC-2. In the case of IFC-2, the 5S model gives lower solar irradiances. As indicated above, the Ångström exponent during IFC-2 exhibits relatively smaller values which may be associated with less absorbing aerosols (single scattering albedo closer to 1). Therefore we may have overestimated aerosol absorption in the model, and, consequently, underestimated surface shortwave irradiance. In fact, because of uncertainties in the model input parameters, the 13.2 Wm^{-2} bias may not be significant.

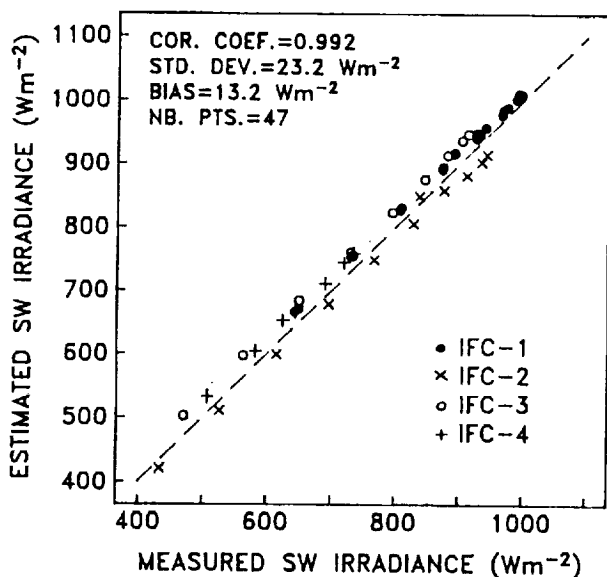


Fig. 2. Estimated versus measured downward shortwave irradiance at the surface (half hourly averages). Sky conditions are virtually clear (fractional cloud cover less than 5%).

4.2 Performance of the wide-band model of Morcrette (1984)

We ran the model of Morcrette (1984) with the temperature and water vapor mixing ratio profiles determined from the radiosonde observations. Ozone mixing-ratio profiles were climatological, and the carbon dioxide mixing-ratio was fixed at 350 ppm. As for the shortwave irradiance comparison, we limited the computations to cases for which the fractional cloud coverage was less than 5%. Furthermore, we kept only the cases for which the radiosonde launches occurred within ± 30 minutes from the longwave radiation flux measurements. The number of cases selected, 146, is much higher than that used to verify the 5S model, 47.

Figure 3 shows the result of the comparison. On a half-hourly time scale, the correlation coefficient, 0.98, is high and the standard deviation, 13.0 Wm^{-2} , is small, representing 3.7% of the average value. A

-7.4 Wm^{-2} bias is computed, indicating slight underestimation by the model. The agreement is good for values above 370 Wm^{-2} , which mostly occurred during IFC-2 and IFC-3 (warmer and more humid atmosphere). Below that value, the model tends to underestimate surface longwave irradiance, in some instances by as much as 40 Wm^{-2} . We find, as in the comparison with the line-by-line model, that Morcrette's (1984) model is more sensitive to changes in atmospheric temperature and water vapor. The difference, however, is that the best results are now obtained for relatively warm and humid atmospheres.

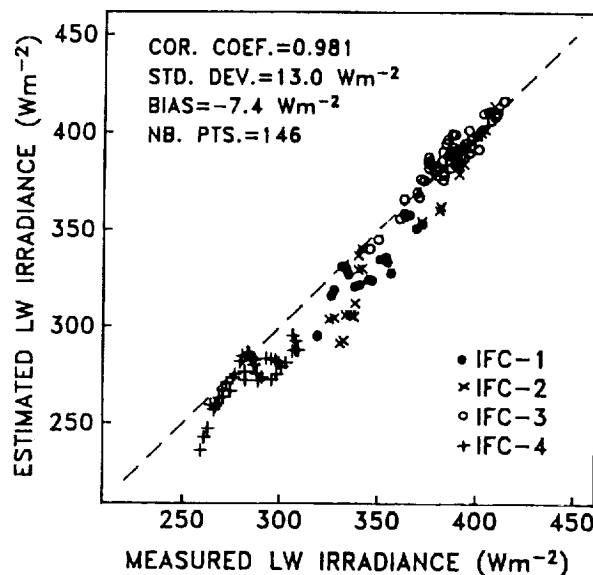


Fig. 3. Same as Fig. 2, but longwave irradiance.

5. SUMMARY AND CONCLUSIONS

Using surface and atmosphere data acquired during FIFE, we have compared the outputs of two radiative transfer models, the 5S model based on Tanré et al. (1979) and the wide-band model of Morcrette (1984), to surface radiation fluxes (downward shortwave and longwave, respectively). The comparisons were made on a half-hourly time scale in virtually clear sky conditions (fractional cloud cover less than 5%). The results show a good agreement between calculated and measured fluxes, namely correlation coefficients above 0.98 and standard deviations of 23.2 Wm^{-2} (2.7%) and 13.0 Wm^{-2} (3.7%) for shortwave and longwave irradiances, respectively. The 5S model overestimated shortwave irradiance by 13.2 Wm^{-2} on average, whereas the model of Morcrette (1984), underestimated longwave irradiance by 7.4 Wm^{-2} . If significant, these biases may compensate partially when computing the radiation budget at the surface. On longer time scales (e.g., daily or monthly), more suitable for climate studies, we expect the standard deviations to be reduced substantially. The model of

Morcrette (1984) performed better in relatively warm and humid atmospheres and appeared slightly too sensitive to atmospheric changes. From our study, unfortunately, we cannot conclude on the aspects of the radiative transfer models that need improvements. This would have required a more extensive and complete set of measurements. Using the 5S model (or a derived parameterization) with typical continental aerosols, a visibility of 23 km, and climatological water vapor amounts instead of measured atmospheric properties leads to a similar standard deviation and an even reduced bias for the shortwave irradiance at the surface. This suggests that standard and/or climatological, eventually seasonally-varying, atmospheric parameters may be sufficient to estimate clear sky shortwave irradiance at the surface accurately.

The comparisons made in this paper demonstrate the suitability of the 5S model and the model of Morcrette (1984) for surface radiation budget studies, at least in clear sky conditions. However, clear skies do not represent general atmospheric conditions, and validation studies are necessary to assess model uncertainties in the presence of clouds. The problem is much more complicated, indeed, because clouds are highly variable and their properties are difficult to measure accurately. Programs such as the Atmospheric Radiation Measurement program of the Department of Energy, however, may provide the appropriate measurements. In any case, it is anticipated that the uncertainties will be larger in cloudy conditions. Clouds, in particular, are generally not plane-parallel, but plane-parallel theory is used in Morcrette's (1984) model. Experiments may be useful here, for instance, to determine suitable corrections. When estimating the surface radiation budget from space observations, plane parallel approximations are currently used to estimate the governing cloud parameters. It may be found, because of the uncertainties in deriving secondary cloud parameters, that improving some aspect of the radiative transfer models are unnecessary.

6.0 ACKNOWLEDGMENTS

This work was supported by the National Aeronautics and Space Administration under Grant NAG55-900 and by the California Space Institute. We wish to thank D. Tanré for helpful discussions, M. Petrie and B. Bloomfield for their editing help, and J. Correa and the Staff of the FIFE information system for their technical support.

7.0 REFERENCES

- Baker, K. S., and R. Frouin, 1987: Relation between photosynthetically available radiation and total insolation at the ocean surface under clear skies. *Limnol. Oceanog.*, 32, 1370-1377.
- Bréon, F. -M., R. Frouin and C. Gautier, 1990a: Satellite estimates of downwelling longwave irradiance at the surface during FIFE: A satellite description. *Symposium on FIFE, The First ISLSCP Field Experiment, Feb. 7-9, 1990, Anaheim, CA. (preprints)*, 92-97.
- Frouin, R., C. Gautier, K.B. Katsaros and R.J. Lind, 1988: A comparison of satellite and empirical formula techniques for estimating insolation over the oceans. *J. Appl. Meteor.*, 27, (9), 1016-1023.
- Frouin, R., C. Gautier and J.-J. Morcrette, 1988: Downward longwave irradiance at the ocean surface from satellite data: Methodology and in-situ validation. *J. Geophys. Res.*, 93, (C1), 597-619.
- Frouin, R., D. W. Lingner, C. Gautier, K.S. Baker and R.C. Smith, 1989: A simple analytical formula to compute clear sky total and photosynthetically available solar irradiance at the ocean surface. *J. Geophys. Res.-Oceans*, 94, 9731-9742.
- Gautier, C., R. Frouin and J.-Y.R. Simonot, 1988: An attempt to remotely sense from space the surface heat budget over the Indian ocean during the 1979 monsoon. *Geophys. Res. Lett.*, 15, (10), 1121-1124.
- Gautier, C., and R. Frouin, 1990: Net surface solar irradiance variability in the central and eastern equatorial Pacific during 1982-1985. *J. Climate (submitted)*.
- Goody, R. M., 1964: Atmospheric radiation. *Oxford Univ. Press, New York, NY*, 436 pp.
- Kneizys, F.X., E. P. Shettle, W.O. Gallery, J.H. Chetwynd, Jr., L.W. Ahreu, J.E.A. Selby, S.A. Clough and R.W. Fenn, 1983: Atmospheric transmittance/radiance: Computer code LOWTRAN-6. *Env. Res. Paper No. 846 Air Force Geophysics Laboratory, Hanscom AFB, MA*.
- Malkmus, W., 1967: Random Lorentz band model with exponential-tailed S-1 line intensity. *J. Opt. Soc. Am.*, 57, 323-329.
- Morcrette, J.J., 1984: Sur la paramétrisation du rayonnement dans les modèles de la circulation générale atmosphérique. *Thèse de Doctorat d'Etat No. 630. Univ. de Lille France*.
- Morcrette, J.J., and Y. Fouquart, 1985: On systematic errors in parameterized calculations of the longwave radiation transfer. *Q. J. R. Meteorol. Soc.*, 111, 691-708.
- Morcrette, J.J., L. Smith and Y. Fouquart, 1986: Pressure and temperature dependence of the absorption in longwave radiation parameterizations. *Contrib. Atmos. Phys.*, 59, 455-469.
- Scott, N. A., and A. Chedin, 1981: A fast line-by-line method for atmospheric absorption computations: The automatized atmospheric absorption atlas. *J. Climate and Appl. Meteor.*, 20, (7), 802-812.
- Tanré, D., M. Herman, P.Y. Deschamps and A. de Lencastre, 1979: Atmospheric modeling for space measurements of ground reflectances, including bidirectional properties. *Appl. Opt.*, 18, (21), 3587-3594.
- Tanré, D., C. Deroo, P. Duhaut, M. Herman, J.J. Morcrette, J. Perbos and P.Y. Deschamps, 1985: Effets atmosphériques en télédétection-logiciel de simulation du signal satellitaire dans le spectre solaire. *Proc. 3rd Int'l Colloquium on Spectral Signatures of Objects in Remote Sensing, Les Arcs, France, Dec 16-20*.
- Tanré, D., C. Deroo, P. Duhaut, M. Herman, J.J. Morcrette, J. Perbos and P.Y. Deschamps, 1986: Simulation of the Satellite Signal in the Solar Spectrum (5S). *Internal Report, Laboratoire d'Optique Atmosphérique, Université de Lille, France*, 264pp.
- Wrigley, R.C., M.A. spanner, R.E. Slye, R.F. Pueschel and J.M. Livingston, 1990: Optical depth measurements and atmospheric correction of remotely sensed data for FIFE. *Symposium on FIFE, the First ISLSCP Field Experiment, Feb. 7-9, 1990, Anaheim, CA. (preprints)*, 127-134.

Morcrette (1984) performed better in relatively warm and humid atmospheres and appeared slightly too sensitive to atmospheric changes. From our study, unfortunately, we cannot conclude on the aspects of the radiative transfer models that need improvements. This would have required a more extensive and complete set of measurements. Using the 5S model (or a derived parameterization) with typical continental aerosols, a visibility of 23 km, and climatological water vapor amounts instead of measured atmospheric properties leads to a similar standard deviation and an even reduced bias for the shortwave irradiance at the surface. This suggests that standard and/or climatological, eventually seasonally-varying, atmospheric parameters may be sufficient to estimate clear sky shortwave irradiance at the surface accurately.

The comparisons made in this paper demonstrate the suitability of the 5S model and the model of Morcrette (1984) for surface radiation budget studies, at least in clear sky conditions. However, clear skies do not represent general atmospheric conditions, and validation studies are necessary to assess model uncertainties in the presence of clouds. The problem is much more complicated, indeed, because clouds are highly variable and their properties are difficult to measure accurately. Programs such as the Atmospheric Radiation Measurement program of the Department of Energy, however, may provide the appropriate measurements. In any case, it is anticipated that the uncertainties will be larger in cloudy conditions. Clouds, in particular, are generally not plane-parallel, but plane-parallel theory is used in Morcrette's (1984) model. Experiments may be useful here, for instance, to determine suitable corrections. When estimating the surface radiation budget from space observations, plane parallel approximations are currently used to estimate the governing cloud parameters. It may be found, because of the uncertainties in deriving secondary cloud parameters, that improving some aspect of the radiative transfer models are unnecessary.

6.0 ACKNOWLEDGMENTS

This work was supported by the National Aeronautics and Space Administration under Grant NAGS5-900 and by the California Space Institute. We wish to thank D. Tanré for helpful discussions, M. Petrie and B. Bloomfield for their editing help, and J. Correa and the Staff of the FIFE information system for their technical support.

7.0 REFERENCES

- Baker, K. S., and R. Frouin, 1987: Relation between photosynthetically available radiation and total insolation at the ocean surface under clear skies. *Limnol. Oceanog.*, 32, 1370-1377.
- Béon, F.-M., R. Frouin and C. Gautier, 1990a: Satellite estimates of downwelling longwave irradiance at the surface during FIFE: A satellite description. *Symposium on FIFE, The First ISLSCP Field Experiment, Feb. 7-9, 1990, Anaheim, CA. (preprints)*, 92-97.
- Frouin, R., C. Gautier, K.B. Katsaros and R.J. Lind, 1988: A comparison of satellite and empirical formula techniques for estimating insolation over the oceans. *J. Appl. Meteor.*, 27, (9), 1016-1023.
- Frouin, R., C. Gautier and J.-J. Morcrette, 1988: Downward longwave irradiance at the ocean surface from satellite data: Methodology and in-situ validation. *J. Geophys. Res.*, 93, (C1), 597-619.
- Frouin, R., D. W. Lingner, C. Gautier, K.S. Baker and R.C. Smith, 1989: A simple analytical formula to compute clear sky total and photosynthetically available solar irradiance at the ocean surface. *J. Geophys. Res.-Oceans*, 94, 9731-9742.
- Gautier, C., R. Frouin and J.-Y.R. Simonot, 1988: An attempt to remotely sense from space the surface heat budget over the Indian ocean during the 1979 monsoon. *Geophys. Res. Lett.*, 15, (10), 1121-1124.
- Gautier, C., and R. Frouin, 1990: Net surface solar irradiance variability in the central and eastern equatorial Pacific during 1982-1985. *J. Climate (submitted)*.
- Goody, R. M., 1964: Atmospheric radiation. *Oxford Univ. Press, New York, NY*, 436 pp.
- Kneizys, F.X., E. P. Shettle, W.O. Gallery, J.H. Chetwynd, Jr., L.W. Ahreu, J.E.A. Selby, S.A. Clough and R.W. Fenn, 1983: Atmospheric transmittance/radiance: Computer code LOWTRAN-6. *Env. Res. Paper No. 846 Air Force Geophysics Laboratory, Hanscom AFB, MA*.
- Malkmus, W., 1967: Random Lorentz band model with exponential-tailed S-1 line intensity. *J. Opt. Soc. Am.*, 57, 323-329.
- Morcrette, J.J., 1984: Sur la paramétrisation du rayonnement dans les modèles de la circulation générale atmosphérique. *Thèse de Doctorat d'Etat No. 630. Univ. de Lille France*.
- Morcrette, J.J., and Y. Fouquart, 1985: On systematic errors in parameterized calculations of the longwave radiation transfer. *Q. J. R. Meteorol. Soc.*, 111, 691-708.
- Morcrette, J.J., L. Smith and Y. Fouquart, 1986: Pressure and temperature dependence of the absorption in longwave radiation parameterizations. *Contrib. Atmos. Phys.*, 59, 455-469.
- Scott, N. A., and A. Chedin, 1981: A fast line-by-line method for atmospheric absorption computations: The automatized atmospheric absorption atlas. *J. Climate and Appl. Meteor.*, 20, (7), 802-812.
- Tanré, D., M. Herman, P.Y. Deschamps and A. de Lefte, 1979: Atmospheric modeling for space measurements of ground reflectances, including bidirectional properties. *Appl. Op.*, 18, (21), 3587-3594.
- Tanré, D., C. Deroo, P. Duhaut, M. Herman, J.J. Morcrette, J. Perbos and P.Y. Deschamps, 1985: Effets atmosphériques en télédétection-logiciel de simulation du signal satellitaire dans le spectre solaire. *Proc. 3rd Int'l Colloquium on Spectral Signatures of Objects in Remote Sensing, Les Arcs, France, Dec 16-20*.
- Tanré, D., C. Deroo, P. Duhaut, M. Herman, J.J. Morcrette, J. Perbos and P.Y. Deschamps, 1986: Simulation of the Satellite Signal in the Solar Spectrum (5S). *Internal Report, Laboratoire d'Optique Atmosphérique, Université de Lille, France*, 264pp.
- Wrigley, R.C., M.A. spanner, R.E. Slye, R.F. Pueschel and J.M. Livingston, 1990: Optical depth measurements and atmospheric correction of remotely sensed data for FIFE. *Symposium on FIFE, the First ISLSCP Field Experiment, Feb. 7-9, 1990, Anaheim, CA. (preprints)*, 127-134.



PREV. ANN
N 89 - 10335

Appendix 2

SENSITIVITY OF SATELLITE-DERIVED NET SHORTWAVE IRRADIANCE
AT THE EARTH'S SURFACE TO RADIOMETRIC CALIBRATION

C. Gautier, R. Frouin

*Proc. 4th Int. Col. on Spectral Signatures of Objects in Remote Sensing,
Courchevel, France, January 18-22, 1988, ESA SP-287, 179-185*

SENSITIVITY OF SATELLITE-DERIVED NET SHORTWAVE IRRADIANCE AT THE EARTH'S SURFACE TO RADIOMETRIC CALIBRATION

C Gautier & R Frouin

89N10335

California Space Institute
Scripps Institution of Oceanography
La Jolla, California 92093-0221

ABSTRACT

We examine the effect of radiometric calibration uncertainties on satellite-derived net shortwave irradiance at the earth's surface. Using Ref. 5's satellite technique, we express the net shortwave irradiance sensitivity to calibration as a function of two basic components that depend on surface and cloud albedo sensitivities, respectively. The analysis of these sensitivities for a wide range of atmospheric and surface conditions, as well as radiation geometries, shows that a 10% uncertainty in the calibration induces up to 70 Wm^{-2} errors in instantaneous net shortwave irradiance (negative when the calibration uncertainty is positive). The maximum relative errors are obtained in overcast conditions when cloud albedos are high. On a monthly time scale, the induced error becomes typically 13 Wm^{-2} in the tropics and 16 Wm^{-2} in higher latitude regions during summer. The error almost vanishes at high latitudes during winter. A 10% positive uncertainty in the calibration gives a net shortwave irradiance error similar to that induced by the 3-hour sampling of the ISCCP Project.

Keywords: Net shortwave irradiance, radiometric calibration, satellite, surface albedo, cloud albedo, sensitivity, climate.

1. INTRODUCTION

Although the earth's climate is expected to undergo changes in response to radiative forcing induced by increased trace gases, it is not clear how these changes will take place or how they will affect atmospheric and oceanic circulation, precipitation patterns, and cloud cover distribution. Monitoring radiative fluxes at the earth's surface and the top of the atmosphere over climatic time scales can give us some clues as to the nature of these changes.

Long-term monitoring of radiative fluxes necessitates assimilation of observations, data analysis, and radiation transfer models for determining fluxes and their eventual changes. Since it is anticipated that radiative flux changes will be marginally above the noise level, at least over the next decade, it is crucial that the observations have long-term consistency so that small changes be detected early. This can only be achieved if careful calibration of observing instruments is performed.

Successful attempts to estimate radiative fluxes at the earth's surface (e.g., Refs. 5, 4, and 9) have involved high space- and time-resolution spectral (visible and infrared) radiances from imaging satellite radiometers. While instruments measuring in the thermal infrared are generally checked in flight with blackbodies of known temperature, instruments measuring in the visible lack on-board calibration. These instruments, nonetheless, can be calibrated by other means and have been used in validated methods to estimate net shortwave irradiance at the earth's surface.

It is therefore important to assess the effects of potential calibration errors on net shortwave irradiance estimates. This is accomplished in the present paper using Ref. 5's model. After briefly reviewing net shortwave irradiance accuracy requirements for climate studies, we examine how the various satellite-derived model parameters, and, therefore, the net shortwave irradiance, are sensitive to calibration. We then discuss the results in view of other potential sources of uncertainty, in particular temporal sampling. We conclude with a few recommendations for climate monitoring.

2. REQUIREMENTS

The accuracy to which satellite-derived net shortwave irradiance at the earth's surface needs to be determined depends upon the application of interest and its time scale. For instance, when attempting to describe surface net heat flux variations associated with the El-Niño/Southern Oscillation (ENSO) phenomenon over the Pacific Ocean, which are on the order of 200 Wm^{-2} , an accuracy of about 10 Wm^{-2} over monthly time scales and spatial scales of 2° of latitude by 10° of longitude is required (TOGA Scientific Plan). In other oceanic regions where climatic changes are smaller over similar time scales, a better accuracy is required.

Over land, shortwave irradiance flux is important for validating General Circulation Models (GCM), providing GCM boundary conditions, and studying surface-atmosphere interactions. The requirements for these studies are more stringent than for those over the ocean because there is a need to know the spectral composition and angular distribution dependence of the shortwave irradiance in addition to the total amount. If the requirement is limited to the amount, the accuracy is also 10 Wm^{-2} , but over smaller time (1-10 days) and space (50-100 km) scales.

3. NET SHORTWAVE IRRADIANCE SENSITIVITY TO CALIBRATION

3.1. Derivation of Calibration Effects

Our investigation of the sensitivity of satellite-derived net shortwave irradiance at the surface to calibration is based on computations performed with the model of Ref. 5, later refined by Ref. 2. The net shortwave irradiance at the earth's surface, SW_{net} , is expressed as

$$SW_{net} = (1 - A_s) \left[(1 - N) SW_{clear} + NSW_{cloud} \right] \quad (1)$$

where A_s is the surface albedo, N is the cloud cover, and SW_{clear} and SW_{cloud} denote the downward shortwave irradiance in clear and cloudy conditions, respectively. To estimate A_s , SW_{clear} , and SW_{cloud} , the following equations are used:

$$A_s = \frac{\pi L_{sat} - S_0 \alpha t_{os}(\theta_0, \theta)}{S_0(1 - \alpha)(1 - \alpha') t_{os}(\theta_0, \theta)} \quad (2)$$

$$SW_{clear} = S_0(1 - \alpha)(1 + A_s \alpha') t_{os}(\theta_0) t_w(\theta_0) \quad (3)$$

$$SW_{cloud} = S_0(1 - \alpha)(1 - A_c - a_c) t_{os}(\theta_0) t_w(\theta_0)_a t_w(\theta_0)_b \quad (4)$$

where S_0 is the solar constant (instantaneous), L_{sat} is the GOES Visible Infrared Spin Scan Radiometer (VISSR) radiance in the visible, α and α' are the scattering coefficients for direct and diffuse radiation, respectively, θ_0 is the solar zenith angle, θ is the viewing zenith angle, A_c is the cloud albedo, a_c is the cloud absorption, t_{os} is the ozone transmittance, t_w is the water vapor transmittance, and subscripts "a" and "b" refer to the water vapor absorption above and below clouds. In Eq. (4), A_c is obtained by solving the following quadratic equation:

$$\frac{\pi L_{sat}}{S_0 t_{os}(\theta_0, \theta)} = \alpha + (1 - \alpha)(1 - \alpha') A_c + \alpha'(1 - \alpha)(1 - \alpha') A_c^2 + (1 - \alpha)(1 - \alpha')(1 - A_c - a_c)^2 A_s \quad (5)$$

and a_c is fixed at 20% of A_c . To estimate N , a threshold technique is employed (for details, see Ref. 5) or, alternatively, Ref. 1's spatial coherence technique.

In order to examine how the SW_{net} estimates are sensitive to the calibration of the GOES VISSR solar channel, the only wavelength channel used in Ref. 5's technique, we may linearize Eq. (1) about a reference state:

$$SW_{net} = \overline{SW}_{net} + \frac{\partial SW_{net}}{\partial g} (SW_{net} - \overline{SW}_{net}) \quad (6)$$

where g is the calibration gain that allows conversion of satellite digital counts into shortwave radiances and the overbar denotes the reference state. To simplify Eq. (6), we have assumed that the calibration is entirely defined by the gain g . For a particular reference state, $\partial SW_{net}/\partial g$ thus represents the sensitivity to calibration of the net shortwave irradiance. Our objective is to estimate $\partial SW_{net}/\partial g$ for a wide range of reference states (atmospheric and surface conditions) and assess the effect of time averaging on $\partial SW_{net}/\partial g$.

Applying the operator $\partial/\partial g$ to both sides of Eq. (1) and using Eq. (2) yields the following expression for $\partial SW_{net}/\partial g$:

$$\begin{aligned} \frac{\partial SW_{net}}{\partial g} = & -\frac{\partial A_s}{\partial g} \left[(1 - N) \frac{(1 - \alpha' + 2\alpha' A_s)}{(1 + \alpha' A_s)} \overline{SW}_{clear} \right. \\ & \left. + N \overline{SW}_{cloud} \right] + \frac{\partial N}{\partial g} (1 - \overline{A}_s) (\overline{SW}_{cloud} - \overline{SW}_{clear}) \\ & - \frac{\partial A_c}{\partial g} \frac{\overline{N}(1 - \overline{A}_s) \overline{SW}_{cloud}}{(1 - \overline{A}_c - \overline{a}_c)} \quad (7) \end{aligned}$$

This expression is convenient since $\partial SW_{net}/\partial g$ appears as a linear combination of $\partial A_s/\partial g$, $\partial N/\partial g$, and $\partial A_c/\partial g$, the sensitivities to the various satellite-derived parameters involved in the SW_{net} computation.

Let us now examine $\partial A_s/\partial g$, $\partial N/\partial g$, and $\partial A_c/\partial g$ separately. First, $\partial A_s/\partial g$ is difficult to estimate when N is obtained with the threshold technique because clouds are inhomogeneous spatially. In this case, depending on the spatial distribution of vertically integrated liquid water and, hence, A_c within the study area of fractional coverage \overline{N} , $\partial N/\partial g$ can take a wide range of values; tracking down the most probable values would require an involved statistical analysis of a large variety of cloud fields. This is certainly beyond the scope of our study. Furthermore, even if we try to simplify the problem by taking A_c as a constant, $\partial N/\partial g$ then becomes a Dirac function of $\overline{L}_{sat} - \overline{L}_{sat}^*$, \overline{L}_{sat}^* being the threshold, which is obviously not realistic. When the spatial coherence technique is used, however, $\partial N/\partial g$ can be readily obtained. We then have:

$$N = \frac{\overline{L}_{sat} - \overline{L}_{sat}^*}{\overline{L}_{sat}^* - \overline{L}_{sat}} \quad (8)$$

where superscripts "s" and "c" refer to the satellite radiance in the clear and cloudy regions of the study area, respectively. Since

$$\overline{L}_{sat} = g f(\overline{CN}_{sat}) \quad (9)$$

where \overline{CN}_{sat} is the satellite digital count in the reference state and f is a function of the digital count only, the ratio on the right hand side of Eq. (8) does not depend on g . This leads to

$$\frac{\partial N}{\partial g} = 0 \quad (10)$$

At first sight, Eq. (10) suggests that Ref. 1's method should be employed to minimize the influence of calibration errors on SW_{net} estimates. This cannot yet be confirmed because $\partial N/\partial g \neq 0$ might reduce the absolute value of $\partial SW_{net}/\partial g$ as a result of compensations between terms (see Eq. [7]). Still, in view of the aforementioned difficulty of estimating $\partial N/\partial g$ when the threshold technique is used and since $\partial N/\partial g = 0$ when the spatial coherence technique is used, which can always be done, we shall ignore hereafter $\partial N/\partial g$ in Eq. (7).

Differentiating Eqs. (2) and (5) yields the following expressions for $\partial A_s/\partial g$ and $\partial A_c/\partial g$:

$$\frac{\partial A_s}{\partial g} = \frac{\overline{\alpha} + (1 - \overline{\alpha})(1 - \overline{\alpha}') \overline{A}_s}{g(1 - \overline{\alpha})(1 - \overline{\alpha}')} \quad (11)$$

$$\begin{aligned} \frac{\partial A_c}{\partial g} = & \left[\alpha(1.2A_c)(1 - 1.2A_c) + (1 - \alpha)(1 - \alpha') A_c + \right. \\ & \left. \alpha'(1 - \alpha)(1 - \alpha') A_c^2 \right] / \\ & (1 - \alpha)(1 - \alpha') [1 - 2.4A_s + (2\alpha' + 2.88A_s) A_c] \quad (12) \end{aligned}$$

where we have used Eq. 5 and the corresponding equation for clear sky conditions. We see that $\partial A_s/\partial g$ is a linear function of A_s , while $\partial A_c/\partial g$ is a more complex function of A_c as well as A_s . Both sensitivities are influenced by atmospheric scattering, but not by ozone absorption. We also note that $\partial A_s/\partial g \neq 0$ when $A_s = 0$, but $\partial A_c/\partial g = 0$ when $A_c = 0$.

3.2. Results and Discussion

In all the results presented and discussed below we assume, for ease of interpretation, that the calibration uncertainty is 10% of the gain. This corresponds to the uncertainty achieved with present post-launch calibration techniques, be they vicarious using ground targets (Ref. 3) or direct using suitably equipped aircraft (Ref. 8).

First, we examine the sensitivity to calibration of the surface albedo (Fig. 1) and cloud albedo (Fig. 2), as expressed in Eqs. (11) and (12). Figure 1 indicates that $\partial A_s/\partial g$ depends only slightly on θ_0 and that a 10% uncertainty in the calibration yields about the same uncertainty on A_s . The same type of dependence on θ_0 and A_c instead of A_s is obtained for $\partial A_c/\partial g$ (Fig. 2). When A_s becomes large (> 0.3), however, $\partial A_c/\partial g$ increases rapidly at small A_c values. Thus, over land, where A_s can be large, we expect up to 100% SW_{net} uncertainties for clouds of small A_c (i.e., low liquid water content). This effect is quite important, even though SW_{net} is considerably reduced when A_s becomes large.

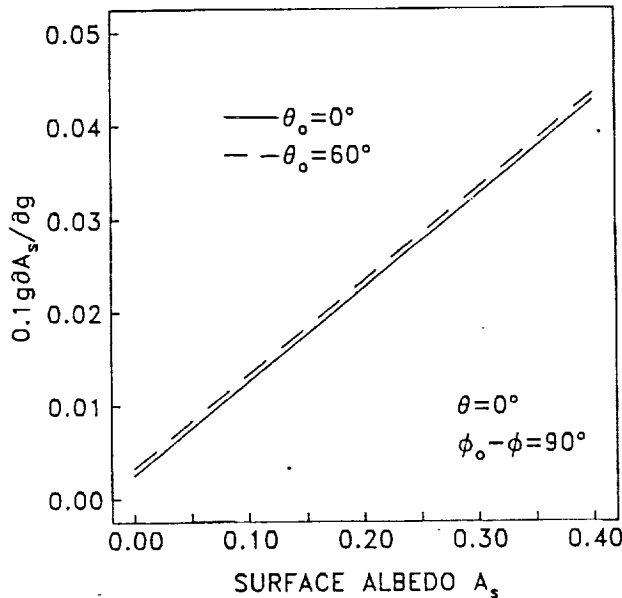


Fig. 1: Sensitivity of surface albedo to calibration gain for solar zenith angles of 0 and 60°.

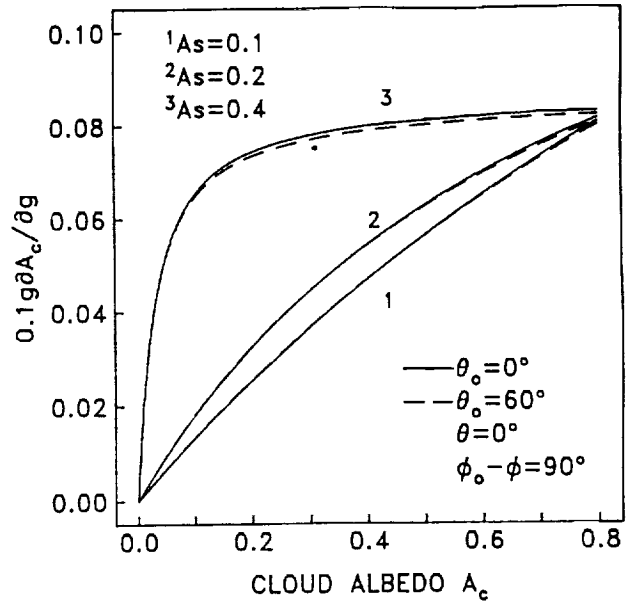


Fig. 2: Sensitivity of cloud albedo to calibration gain for various surface albedos and solar zenith angles of 0 and 60°.

Next we look at the SW_{net} sensitivity to a 10% uncertainty in the calibration (Fig. 3). The results are presented as a function of the most important parameters involved, namely A_s (Fig. 3a), N (Fig. 3b), A_c (Fig. 3c), and θ_0 (Fig. 3d). As indicated in the previous section, the SW_{net} sensitivity is made up of two terms (since we neglect $\partial N/\partial g$) that depend on $\partial A_s/\partial g$ and $\partial A_c/\partial g$, respectively. Their contribution is also shown in Fig. 3. For the atmospheric and surface conditions selected, we find similar sensitivity ranges for all parameters, with a 75 Wm^{-2} maximum when $N = 1$. For instance, the SW_{net} sensitivity decreases with θ_0 , from about -50 Wm^{-2} for $\theta_0 = 0^\circ$ to -5 Wm^{-2} for $\theta_0 = 80^\circ$.

Lastly, we analyze the sensitivity of monthly-averaged SW_{net} to calibration during the year for various latitudes. The results are presented in Fig. 4. As could be expected from Fig. 3d, the sensitivity is larger in the tropics most of the year (except in the summer). The monthly SW_{net} sensitivity is only about -13 Wm^{-2} in the tropical region compared to an instantaneous SW_{net} sensitivity on the order of -70 Wm^{-2} . These results are to be compared with the accuracy obtained in estimating SW_{net} over the ocean in the tropics (e.g., Refs. 6 and 7) which is about 18 Wm^{-2} on a daily basis, when assessed by comparing satellite predictions with surface measurements.

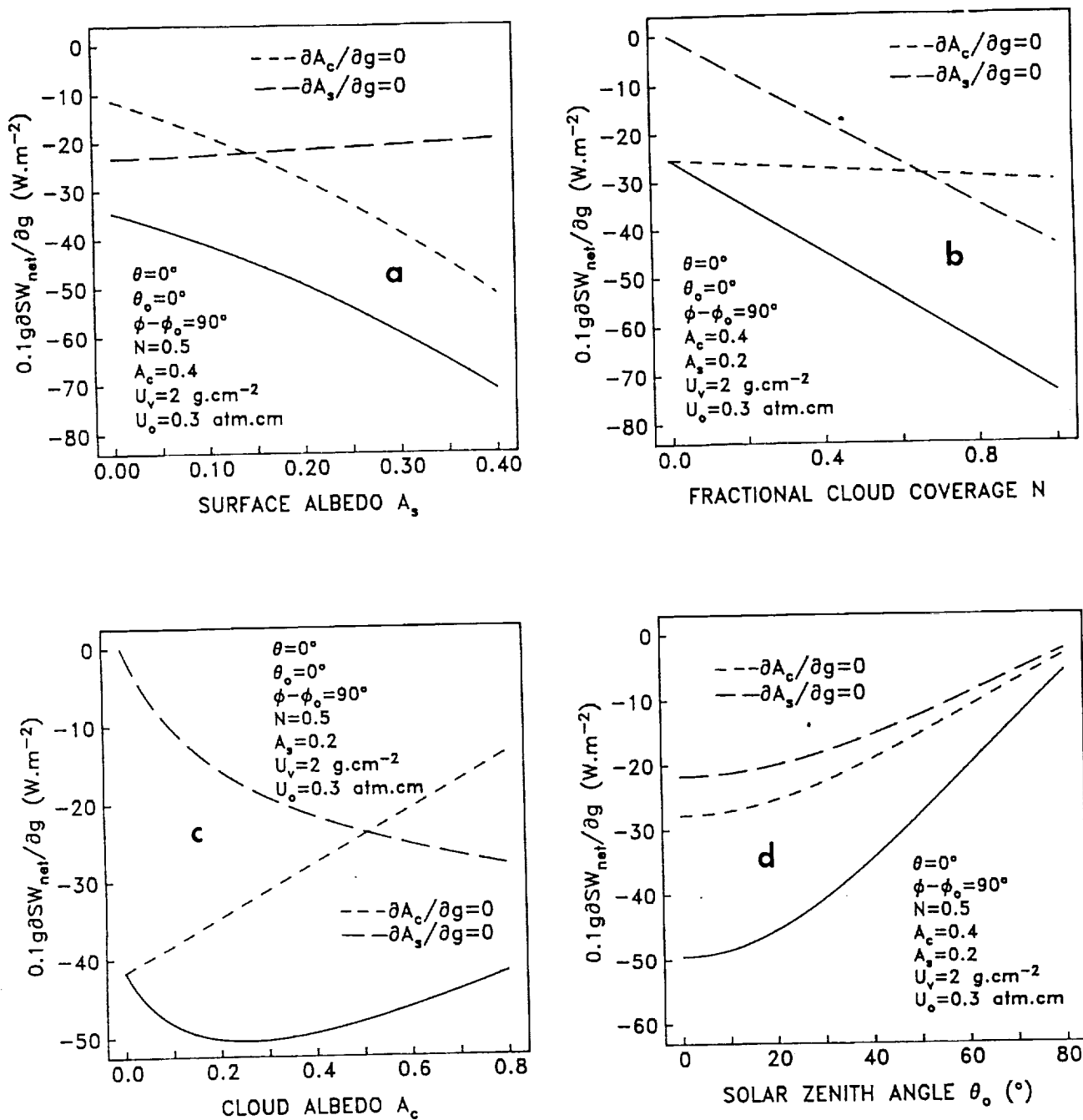


Fig. 3: Sensitivity of net shortwave irradiance at the earth's surface to calibration gain as a function of the various satellite-derived model parameters: surface albedo (a), fractional cloud coverage (b), cloud albedo (c), and solar zenith angle (d).

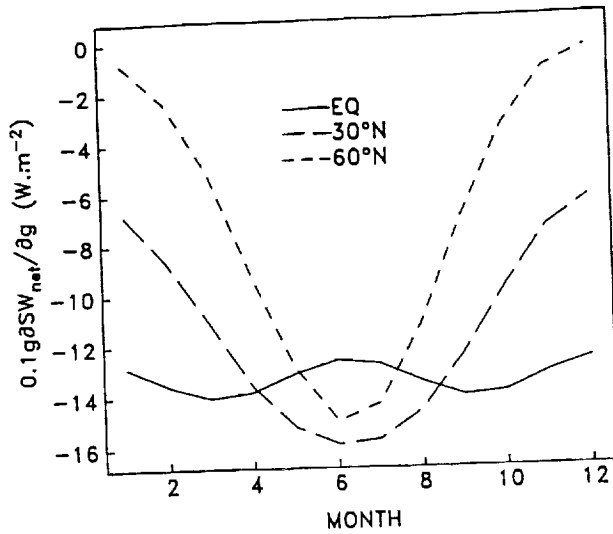


Fig. 4: Sensitivity of monthly-averaged net shortwave irradiance at the earth's surface to calibration gain during the course of the year for various latitudes. The surface and atmospheric conditions are those of Fig. 3.

4. OTHER SOURCES OF UNCERTAINTY

Uncertainties in determining large-scale net shortwave irradiance at the surface have other sources than calibration. For example, they may originate from applying an imperfect model to the satellite radiances and from inadequate cloud sampling. Most of these uncertainties have a random component such that when averages are computed, the uncertainties are reduced. Calibration uncertainty, however, generally introduces a bias (calibration fluctuations have long time periods) that does not diminish through averaging procedures. While it is not our intention in the present paper to make an exhaustive study of the uncertainties that might affect SW_{net} computations, it is interesting to compare the uncertainty due to calibration to that resulting from temporal sampling, for instance. In order to provide orders of magnitude, we write SW_{net} as a function of a cloud parameter, CL , which represents the integrated effects of clouds on the shortwave irradiance:

$$SW_{net} = (1 - A_s)SW_{clear}(1 - CL) \quad (13)$$

If Δh denotes the sampling interval, the sensitivity of SW_{net} to Δh can be expressed as:

$$\frac{\partial SW_{net}}{\partial \Delta h} = \frac{\partial SW_{clear}}{\partial \Delta h} (1 - A_s)(1 - CL) - \frac{\partial CL}{\partial \Delta h} SW_{clear}(1 - A_s) \quad (14)$$

where we neglected $\partial A_s / \partial (\Delta h)$. To compute $\partial SW_{net} / \partial \Delta h$, we have to assume a variation of CL with time. In the tropics, for instance, a typical diurnal cycle exists that can be parameterized as

$$CL(h) = 0.5 - 0.2 \cos\left(2\pi \frac{h - h_0}{24}\right) \quad (15)$$

where h_0 is local noon.

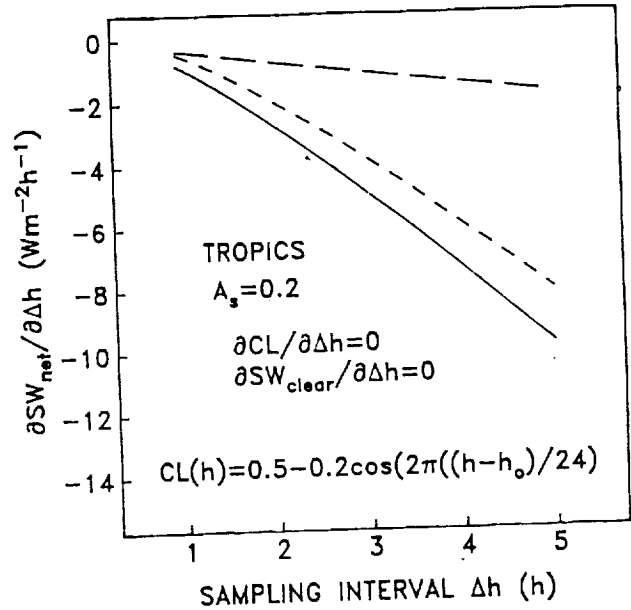


Fig. 5: Sensitivity of monthly-averaged net shortwave irradiance at the earth's surface to sampling interval. A typical diurnal variation is assumed for the cloud parameter.

When Eq. 15 is used and SW_{net} averaged over one month, we obtain the results presented in Fig. 5. We see that $\partial SW_{net} / \partial \Delta h$ reaches -12 Wm^{-2} when $\Delta h = 5$ and that the largest contribution comes from sampling SW_{clear} . If we change Δh from 1 to 3 hours, for example, SW_{net} will change by:

$$\begin{aligned} \Delta SW_{net} &= SW_{net}(\Delta h = 3) - SW_{net}(\Delta h = 1) \\ &\approx 3 \left(\frac{\partial SW_{net}}{\partial \Delta h} \right)_{\Delta h=3} - \left(\frac{\partial SW_{net}}{\partial \Delta h} \right)_{\Delta h=1} \\ &\approx -15 \text{ Wm}^{-2} \end{aligned} \quad (16)$$

This bias is similar in magnitude to that introduced by a calibration uncertainty of 10%. It is interesting to note that, for the conditions considered, the sampling adopted in the International Satellite Cloud Climatology Program (ISCCP, i.e., 3 hours) introduces a bias of -15 Wm^{-2} .

5. SUMMARY AND RECOMMENDATIONS

We have performed a study of the sensitivity of the net shortwave irradiance at the earth's surface to calibration. This study has showed that a uncertainty in the calibration leads to uncertainties up to -70 Wm^{-2} for instantaneous values of net shortwave irradiance in overcast conditions and up to about -15 Wm^{-2} for monthly averaged values. In the tropical regions, the monthly averaged uncertainty is -13 Wm^{-2} . This uncertainty appears as a bias with a sign opposite to that of the calibration bias, i.e., a positive bias in calibration induces a negative bias on net shortwave irradiance. We have compared the uncertainty due to calibration to that introduced by temporal sampling. We have found that the ISCCP sampling (3-hour) introduces a bias of typically -15 Wm^{-2} in the tropics. This indicates that, if the calibration bias is negative, the biases introduced by the calibration could compensate that introduced by temporal sampling. The amount of compensation could

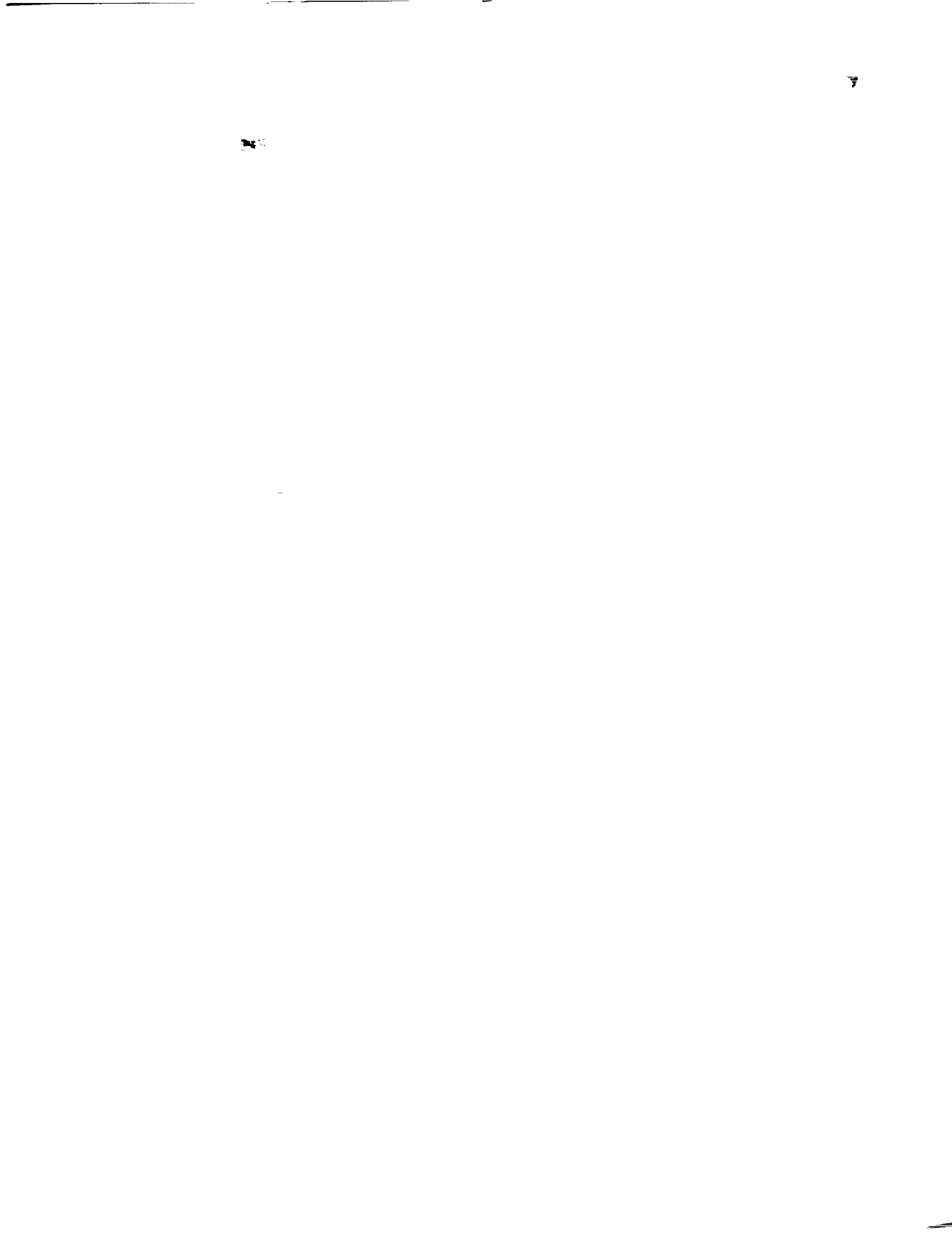
be partly assessed by comparing monthly-averaged estimations of net shortwave irradiance from satellite observations to those obtained from pyranometer measurements.

Considering the results just summarized, it is very important to improve the calibration of spectral radiances used to compute net shortwave irradiance at the earth's surface, such as those from imaging radiometers. This calibration can be performed on-board future instruments, but for present instruments it must be done using a combination of complementary techniques. Calibration of the visible radiances is important for ISCCP data sets since they are, at present, only normalized to one particular visible sensor, which is itself poorly calibrated. We recommend that a calibration strategy be established with the objectives of providing both long-term calibration changes and the best possible absolute instantaneous calibration. Such a strategy could involve a continuous monitoring of calibration targets and a complete calibration experiment that provides the necessary measurements to apply all possible calibration methods.

Acknowledgments. This work has been supported by NOAA grant NA86AA-D-AC051 and NASA contract 14195C. We wish to thank Bob Markworth for typesetting this paper and Brian Bloomfield for editing it.

REFERENCES

1. Coakley, J.A., and F.P. Bretherton, 1982: "Cloud Cover from High-Resolution Scanner Data: Detecting and Allowing for Partially Filled Fields of View." *J. Geophys. Res.*, **87**(C7), 4917-4932.
2. Diak, G. and C. Gautier, 1983: "Improvements to a Simple Physical Model for Estimating Insolation from GOES Data." *J. Climate and Appl. Meteor.*, **22**(3), 505-508.
3. Frouin, R., and C. Gautier, 1987: "Calibration of NOAA-7 AVHRR, GOES-5, and GOES-6 VISSR/VAS Solar Channels." *Remote Sens. of Environ.*, **22**, 73-101.
4. Frouin, R., C. Gautier, K.B. Katsaros, and R.J. Lind, 1988: "A Comparison of Satellite and Empirical Formula Techniques for Estimating Insolation over the Oceans." *J. Geophys. Res.* (in press).
5. Gautier, C., G. Diak and S. Masse, 1980: "A Simple Physical Model to Estimate Incident Solar Radiation at the Surface from GOES Satellite Data." *J. Appl. Meteor.*, **19**(8), 1005-1012.
6. Gautier, C., 1984: "Surface Radiation Budget." In *Large-Scale Oceanography Experiments and Satellites*, C. Gautier and M. Fieux, eds., Reidel Publishing, Dordrecht.
7. Gautier, C., 1988: "Surface Solar Irradiance in the Central Pacific at 10S, 140W during Tropic Heat: In-Situ and Satellite Measurements." To appear in *J. Climate and Appl. Meteor.*
8. Smith, G.R., R.H. Levin and R.S. Koyanagi, 1988: "Calibration of the Solar Channel of the GOES-6 VISSR Using High Altitude Aircraft Measurements." Submitted to *J. Atmos. and Oceanic Tech.*
9. Suttles, J.T., and G. Ohring (eds.), 1986: "Report of the Workshop on Surface Radiation Budget for Climate Applications," WCP-115, 144 pp.



PREV. ANN-
92A 13321

Appendix 3

VARIABILITY OF PHOTOSYNTHETICALLY AVAILABLE AND TOTAL
SOLAR IRRADIANCE AT THE SURFACE DURING FIFE:
A SATELLITE DESCRIPTION

R. Frouin, C. Gautier

Proc. Symp. on the First ISLSCP Field Experiment, Anaheim, CA, February 7-9, 1990, 98-104, Published by the American Meteorological Society

VARIABILITY OF PHOTOSYNTHETICALLY AVAILABLE AND TOTAL SOLAR IRRADIANCE AT THE SURFACE DURING FIFE: A SATELLITE DESCRIPTION

Robert Frouin and Catherine Gautier

California Space Institute A-021
Scripps Institution of Oceanography
La Jolla, California 92093

1. INTRODUCTION

Sunlight drives the energy, water, and biochemical cycles of the earth surface/atmosphere system. The flux of solar energy through the various spheres of the system, namely the stratosphere, troposphere, and hydrolithosphere, is understood generally, but specific rates and underlying processes are not well-known. This prevents our accurate prediction of the system's response to natural and anthropogenic changes, including changes inherent to the system's internal dynamics.

Over land surfaces, this study's domain of interest, insolation largely determines the surface temperature and the rate of evapotranspiration, with important consequences on air-surface interactions and the global hydrologic cycle. Precipitation, for instance, is sensitive to changes in evapotranspiration, at least on a regional scale. On the other hand, solar radiation at the wavelengths between 0.35 and $0.7 \mu\text{m}$ is used by plants in the process so fundamental for life: oxygenic photosynthesis. Photosynthetically active radiation (PAR) governs primary production, the rate of carbon fixed by terrestrial vegetation, and knowing the geographical location of the fixed carbon, as well as its rates and forms of release, is important in studying the increase in atmospheric CO_2 and trace gas concentrations.

Various methods, based on visible and near-infrared observations from meteorological satellites, have been proposed to estimate insolation at the earth's surface (e.g., Tarpley, 1979; Gautier et al., 1980; Möser and Rashke, 1984; Pinker and Ewing, 1985; and Dedieu et al., 1987). These methods offer the opportunity to map insolation accurately (within 10% on a daily time scale) over large areas and, eventually, the entire globe (global scale satellite datasets are now becoming available). The perspective of a global, long-term climatology of surface insolation, which can only be established using satellites, should help in the investigation of the climate system's sensitivity to surface processes by providing validation capabilities and boundary conditions.

While numerous studies have been devoted to estimating insolation from satellite data, no satellite-based method has been proposed for PAR. This is because, for many applications involving small space and time scales, PAR can be measured directly. Furthermore, it has often proved satisfactory to take PAR as a more or less constant fraction of insolation. The relationship between PAR and insolation, however, depends on atmospheric conditions and radiation geometry (e.g., Baker and Frouin, 1987). Clouds, in particular, which do not absorb at PAR wavelengths but do absorb substantially in the near-infrared, increase the ratio of PAR and insolation. Therefore, deducing PAR from a satellite estimate of insolation (also subject to uncertainty) is not optimum. Moreover, since meteorological satellites

(except METEOSAT) carry instruments that measure in spectral channels resembling more the PAR wavelength range than the entire solar spectrum, it appears appropriate to use these data to estimate PAR directly.

In the present study, we apply the satellite method of Gautier et al. (1980) to GOES-6 Visible and Infrared Spin Scan Radiometer (VISSR) data acquired during the First ISLSCP Field Experiment (FIFE). The objective is to assess whether the method can provide quantitative information on the temporal variability of PAR and insolation during the experiment. First, we describe the salient features of the Gautier et al. (1980) method and indicate how the method is modified to yield PAR. The problem, in this case, is simplified since the VISSR solar channel is mostly sensitive to photosynthesis wavelengths, and cloud absorption vanishes in the radiative transfer model. Subsequently, we discuss the calibration of the VISSR solar channels, and then we compare the satellite estimates to the in situ measurements. The suitability of deriving PAR from insolation is evaluated, with implications for global studies of photosynthetic activity, since large-scale satellite climatologies of insolation are now becoming available. Finally, the importance of clouds in modulating insolation and PAR is analyzed, and we conclude with a perspective on future work.

2. METHOD

The method used to compute surface insolation, originally developed by Gautier et al. (1980), is based on simple, physical modeling of the most important radiative processes occurring within the atmosphere, namely scattering and absorption by molecules, clouds, and aerosols. Since variability of surface insolation results primarily from changes in solar zenith angle and cloudiness, the method focuses on determining the effect of clouds on surface insolation (solar zenith angle can be computed accurately from simple formulas). The method accomplishes this by computing cloud albedo, the governing cloud parameter, from GOES VISSR measurements in the visible. The repeat coverage of the GOES VISSR data (one observation every 30 minutes) allows one to adequately sample the diurnal cloud variability, a strength of the method.

In the computational procedure, we first determine from a time series of satellite images (typically 15 days) the minimum brightness count at each observation time during the day. This minimum count defines a threshold (taken a few counts higher) that is used to classify each GOES VISSR pixel as clear or cloudy. The procedure, indeed,

does not allow one to determine whether the pixel is partially contaminated by clouds or not. We utilize full resolution data, however, which minimizes the error introduced by not modeling the resulting effect on insolation. Once the pixel's nature (clear or cloudy) has been determined, we apply clear and cloudy sky radiative transfer models accordingly.

In clear sky conditions, surface insolation is expressed as:

$$I_o = S_o \left(\frac{r}{r_o}\right)^{-2} \cos \theta \exp(-C_1 / \cos \theta) / (1 - C_2 A_s) \times \exp\left[-a_o \left(\frac{u_o}{\cos \theta}\right)^{b_o}\right] \exp\left[-a_w \left(\frac{u_w}{\cos \theta}\right)^{b_w}\right] \quad (1)$$

where S_o is the solar constant, r/r_o is the ratio of actual to mean earth-sun distance, θ is solar zenith angle, u_o and u_w are ozone and water vapor amounts, respectively, A_s is surface albedo, and a_o , b_o , a_w , b_w , C_1 , and C_2 are coefficients (C_1 and C_2 depend on the type and concentration of aerosols). The term $1 - C_2 A_s$ accounts for photons that have sustained multiple surface reflections. Equation (1) differs from that of the original model, but not in essence. Ozone and water vapor amounts are specified from climatology and A_s is obtained by solving the following equation.

$$A_{sat}(CN_{min}) = \alpha + (1 - \alpha)(1 - \alpha_1)(1 - a_o)A_s \quad (2)$$

where A_{sat} is the albedo measured at the satellite (the surface is assumed to reflect solar radiation isotropically), CN_{min} is the minimum brightness count, α and α_1 are direct and diffuse reflection coefficients, respectively, and a_o characterizes ozone absorption. Equation (2) simply states that A_{sat} is the sum of an atmospheric component (photons reflected back to space without surface reflection), and the signal reflected by the surface and diffusely transmitted to space.

In cloudy sky conditions, the clear sky formulation is modified to account for reflection and absorption by clouds which are assumed to occur in one layer. Cloudy sky insolation is therefore given by:

$$I_c = I_o(1 - A_c - a_c) \quad (3)$$

where A_c is cloud albedo and a_c is cloud absorption (taken as a constant fraction of A_c). In Eq. (3) we neglect the effect of multiple reflections between the cloud and the surface. This effect, of order $I_c A_c A_s$, is generally small (a few Wm^{-2}). Cloud albedo is obtained by solving the following quadratic equation:

$$A_{sat} = \alpha + (1 - \alpha)(1 - \alpha_1)(1 - a_o)A_c + (1 - A_c - a_c)^2(1 - \alpha_1)(1 - a_o)A_s \quad (4)$$

where A_{sat} is the top-of-atmosphere albedo, assuming that clouds reflect solar radiation isotropically. This equation, in fact, gives A_c in the GOES VISSR solar channel (mostly wavelengths in the visible). We assume, however, that A_c takes the same value in the total solar spectrum, which is reasonably well justified (see, for instance, Welch et al., 1980).

The above formalism, developed for insolation, only requires slight modifications to become applicable to PAR. In this case, we eliminate a_c in the cloudy sky equations (clouds do not absorb in the visible), replace S_o by the extraterrestrial solar irradiance in the PAR spectral interval, and modify the coefficients of the clear model so that they represent the PAR wavelengths. For these coefficients we take the values given by Frouin et al. (1989). Since a_c does not need to be parameterized as in the insolation case, and since the VISSR solar channel mostly captures radiation in the visible (no narrow-band to broad-band transformation is necessary), we expect the model to perform better in the PAR case.

3. INSOLATION AND PAR COMPUTATIONS

We focus, in this preliminary report, on FIFE's second intensive field campaign (IFC), which took place at the end of June and the beginning of July 1987 (peak greenness of vegetation) on the Konza Prairie near Manhattan, Kansas. Figure 1 locates the experimental site and, within the site, the radiative flux stations selected for validation purposes.

To compute insolation and PAR over the FIFE area, GOES-6 VISSR visible and near-infrared (solar channel) data were acquired at full resolution (0.9 km at nadir) every half-hour during daytime. The data, 8-bit coded, navigated, but uncalibrated numerical counts, were made available by the Space Science and Engineering Center of the University of Wisconsin, Madison. In a preprocessing stage, we calibrated and checked the data for navigational errors and quality.

Calibration was achieved by regularly applying (twice a month) the indirect calibration method described in Frouin and Gautier (1987). This method, which uses space and the White Sands Monument area in New Mexico as calibration targets, computes the radiance measured at satellite altitude using a fairly accurate radiative transfer model, the model of Tanré et al. (1986). The relevant atmospheric characteristics are estimated from either climatological data (ozone amount, aerosol size-frequency distribution, and refractive index) or observations at nearby meteorological stations (water vapor amount and aerosol loading). The method's theoretical accuracy is 8%, but it might even be better, as comparisons with a more direct method involving high-flying aircraft have suggested (Whitlock et al., 1987). Figure 2 shows the calibration gain (relates count-squared to reflectance) obtained during 1987. In the figure, each point corresponds to a daily average performed with three White Sands observations near local noon and one observation of space. The vertical bars represent one standard deviation (around the daily average) of individual calibrations. Somewhat erratic fluctuations are observed from one gain estimate to the next, in some instances reaching 10%. Changes of such amplitude, however, are at the limit of the uncertainty level. In addition to the relatively high-frequency fluctuations, the gain exhibits a low-frequency variation, with minimum values in April, May, June, and July. Prior to 1987, similar yearly variations have been detected by other indirect calibration methods (see Whitlock et al. 1987), which

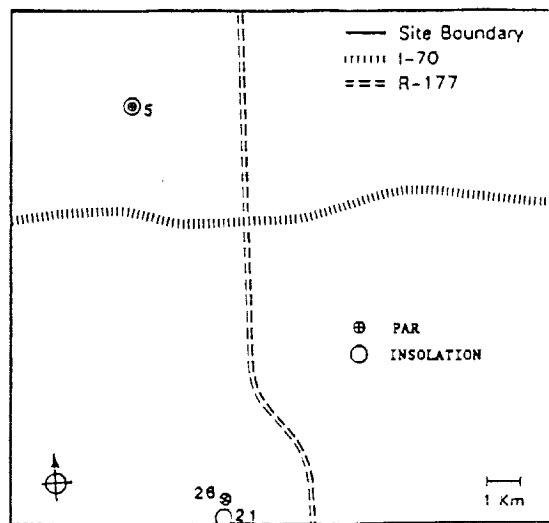


Fig. 1: Map of the FIFE site, centered at $39^{\circ} 04' N$ and $96^{\circ} 30' W$, showing the location of the insolation and PAR stations selected in the study.

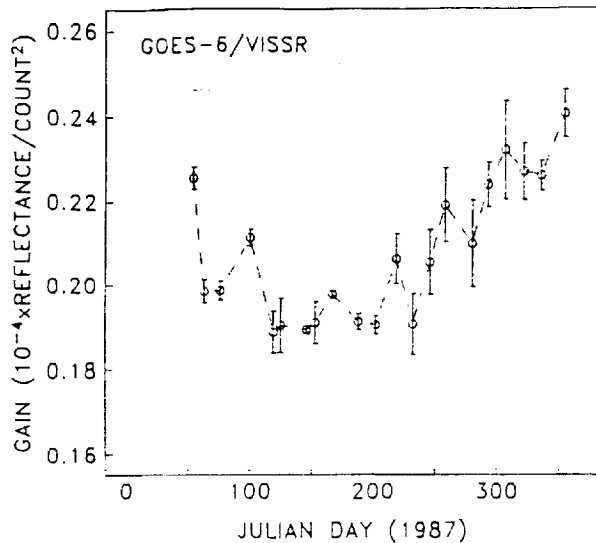


Fig. 2: Calibration gain of the GOES-6 VISSR solar channel during FIFE. The prelaunch value is 0.154×10^{-4} reflectance/count².

suggest that the observed feature is actual and not the result of a bias in the method. From July to December 1987, the gain increased by approximately 36%. Compared to the prelaunch gain, the gain at the end of 1987 reads higher by 64%.

Navigation was checked by comparing the computed earth coordinates of reference points on the surface, in particular small lakes (that appear very black on the visible images), to the actual coordinates. The agreement was generally good, within a few kilometers. In extracting the FIFE area from the satellite images, we therefore shifted the pixel lines and samples accordingly. Note, however, that navigational errors of a few kilometers, although they change the actual radiation geometry, do not affect the insolation and PAR results significantly (errors in the parameterization of atmospheric process largely dominate).

After the preprocessing stage, we produced instantaneous and daily estimates of insolation and PAR by applying the procedure described in section 2. In the calculations, we used the continental aerosol model of the International Radiation Commission (WCP, 1983) and fixed the atmospheric visibility (characterizes aerosol turbidity) at 23 km. Climatological values of 3.0 g cm^{-2} and 0.31 atm-cm were taken as representative of the water vapor and ozone amounts during the IFC, respectively. Since the surface albedo of vegetated surfaces differs substantially in the visible and total solar spectrum (vegetation reflects more in the near-infrared), we increased the VISSR-derived surface albedo by a typical factor of 1.64 in the insolation calculation (Eq. 1). The daily averages were obtained by simple trapezoidal integration, which is sufficient since the satellite observations are well-sampled in time (approximately 24 observations at 30 minute intervals during daytime). Such a simple scheme, however, biases low the daily integrals when the sampling frequency is not as high (case of missing data), especially in clear or mostly clear sky conditions.

4. COMPARISON WITH IN SITU MEASUREMENTS

For selected days during the IFC Fig. 3 shows the diurnal variation of measured insolation at stations 5 and 26 and the corresponding satellite estimates at particular times during the day. In the figure, the surface values are half-hourly averages and the satellite estimates are spatial averages over the FIFE area. Julian days 176, 177, and 178 are mostly clear, whereas the others are mostly cloudy. (Note that the Julian days are depicted with respect to GMT and not local time). We notice slight differences between the values measured by the two stations, but not a systematic bias. The discrepancy is more pronounced in cloudy conditions (e.g., day 188), which plausibly results from spatial cloud variability (stations 5 and 26 are 15 km apart). In general the satellite estimates are in agreement with the measured values; they describe well the actual diurnal cycle. Even rapid insolation changes, for instance at the end of day 177, are detected. During day 189, the satellite estimates did not see the early afternoon variations, but the two stations measured a significantly different incoming solar flux.

The same type of results are obtained for PAR (Fig. 4). Satellite estimates are in good agreement with surface values, and reproduce well the diurnal cycle. The surface PAR data, however, are noisier than the surface insolation data. Station 5, for instance, which measured

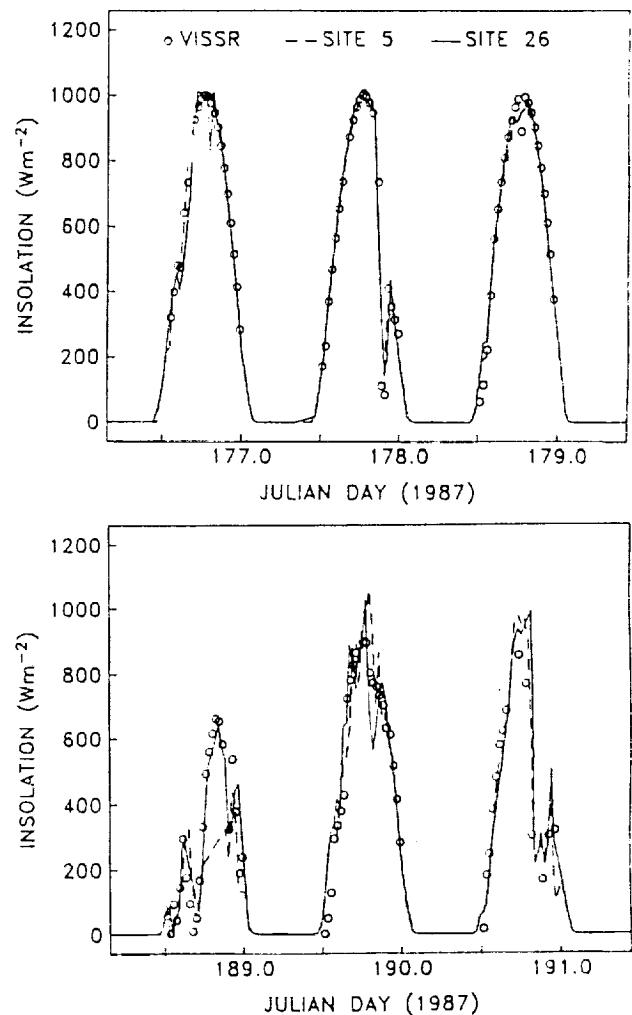


Fig. 3: Calculated and measured insolation for selected days during FIFE's second IFC. Satellite estimates are instantaneous, whereas measured values are half-hourly averaged.

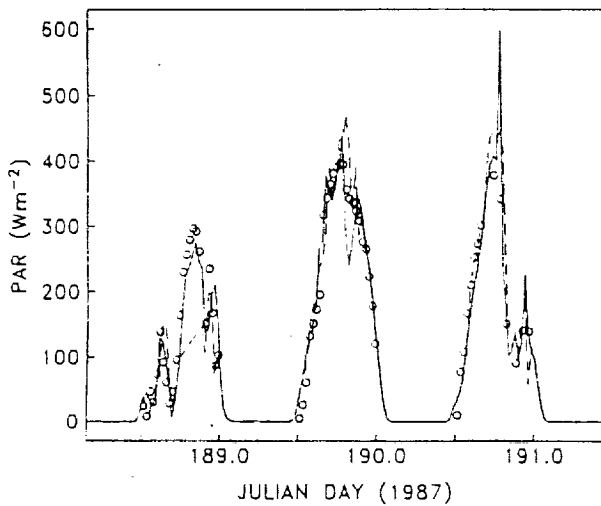
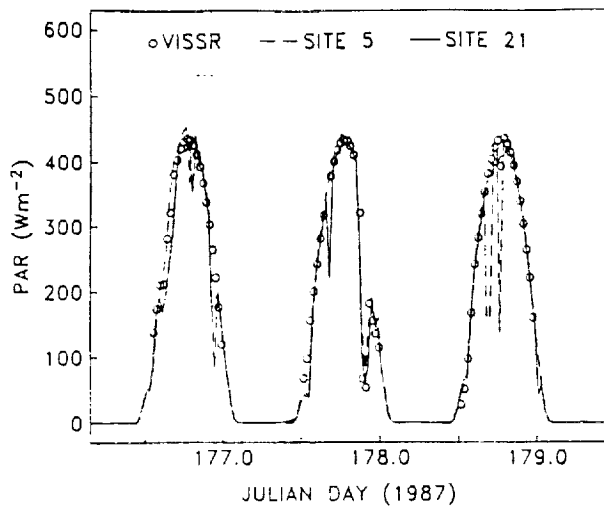


Fig. 4: Same as Fig. 3 but for PAR.

both PAR and insolation, reports anomalously low PAR values on day 178. Examining Figs. 3 and 4, we note the similar diurnal variation of PAR and insolation, which indicates, as we know, that the two quantities are highly correlated.

Figures 5 and 6 show, respectively, the temporal variation of daily insolation and PAR during the entire IFC (21 days total). The agreement is generally within 15-20 Wm^{-2} for insolation and 5-10 Wm^{-2} for PAR. Day 182, however, stands out. The method, in that case, did not detect much cloudiness. In fact, the clouds during day 182 exhibited brightness count values slightly less than the clear/cloudy threshold and, therefore, were not seen. This is, indeed, the disadvantage of using a threshold to separate clear and cloudy pixels; notwithstanding, with exception of that day, the clouds were distinguished properly. If we now examine the scatter plots of estimated versus measured daily insolation and PAR (Figs. 7 and 8), we do not notice a bias in the satellite estimates (the lowest values on the plots), the PAR estimates are closer to the line of slope 1 than the insolation estimates, which indicates a better performance of the satellite method in the case of PAR. This is somewhat expected, as mentioned in the introduction, since the modeling of the cloud processes is simplified for PAR. The atmospheric conditions, however, were rather clear during FIFE's second IFC, and more comparisons in the presence of clouds are necessary to quantify the improvement.

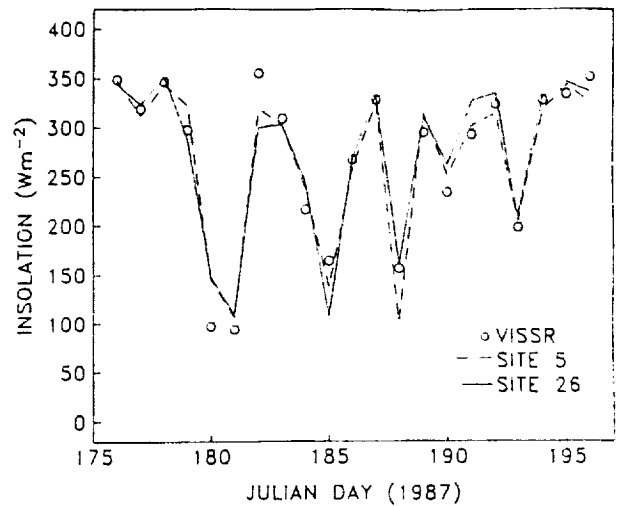


Fig. 5: Calculated and measured daily insolation during FIFE's second IFC.

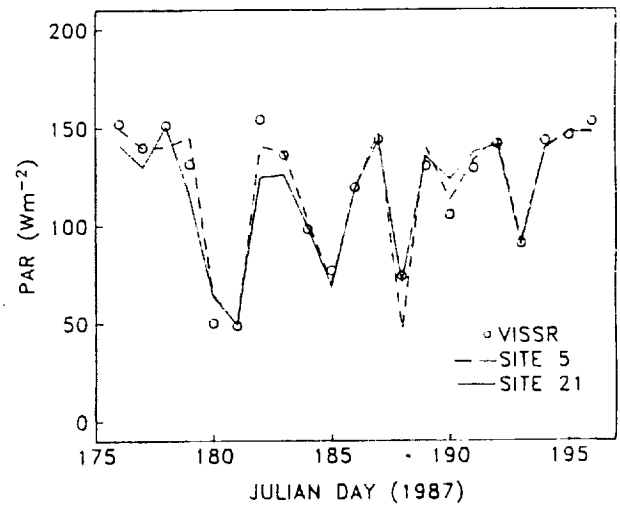


Fig. 6: Same as Fig. 5 but for PAR.

Table 1 summarizes the statistics of half-hourly and daily comparisons for both insolation and PAR. The statistics are drastically improved when passing from a half-hourly to a daily time scale. Even though the correlation coefficient is similar, yet above 0.95, the standard error of estimate decreases from 86.7 to 21.6 Wm^{-2} in the case of insolation and from 41.9 to 8.2 Wm^{-2} in the case of PAR. The bias always remains small, not exceeding a few Wm^{-2} on a half-hourly time scale, and reducing to about 1 Wm^{-2} on a daily time scale. For PAR, however, the overall statistics are better. The standard error of estimate for daily comparisons, in particular, represents only 6.5% of the average measured value in the case of PAR, but reaches almost 9% in the case of insolation. Note finally, that the results obtained for insolation are similar, in terms of comparison statistics, to those reported by Gautier et al. (1980), Diak and Gautier (1983), and Raphaël and Hay (1984), who applied the satellite method over varied terrestrial sites.

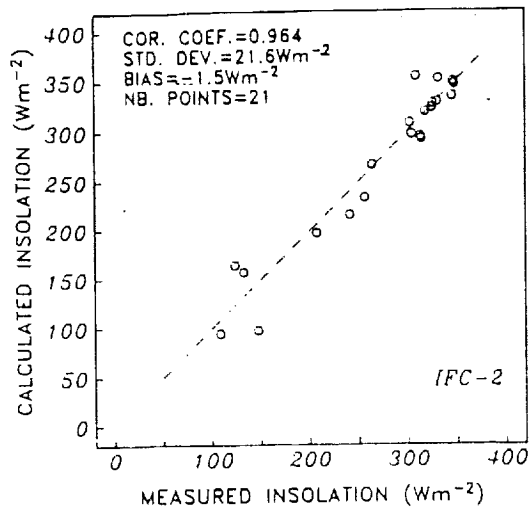


Fig. 7: Scatter plot of calculated versus measured daily insolation during FIFE's second IFC. The measured values are averages of station 5 and 26 data.

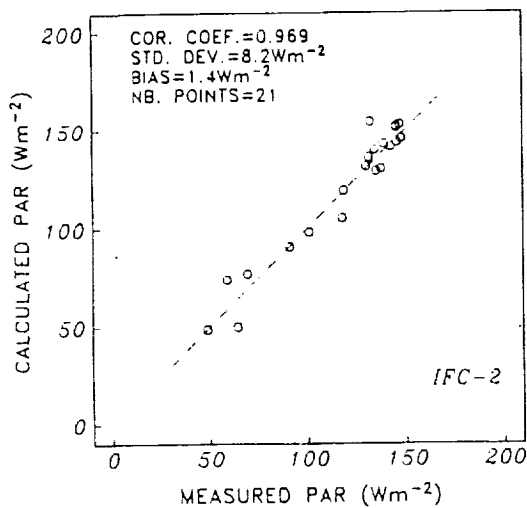


Fig. 8: Same as Fig. 7 but for PAR. The measured values are averages of station 5 and 21 data.

Table 1. Comparison statistics of calculated and measured insolation and PAR.

Parameter	Insolation		PAR	
	Half-Hourly	Daily	Half-Hourly	Daily
Correlation Coefficient	.961	.964	.950	.968
Standard Error (Wm^{-2})	86.7	21.6	41.9	8.2
Bias (Wm^{-2})	-5.3	-1.5	4.0	1.4
Number of Points	469	21	471	21

5. DISCUSSION

We have shown in the previous section that the method of Gautier et al. (1980) for insolation and its modified version for PAR provide reasonably accurate insolation estimates, especially on a daily time scale. On a half-hourly time scale, the assessment of accuracy is inherently more difficult to make since the satellite estimates are quasi-instantaneous whereas the in situ measurements are time averages. Furthermore, it is not clear whether a spatial average over 15×15 km at a given time is represented adequately by a half-hour average at a specific location. The discrepancies, however, are substantially reduced on daily integrals. The accuracy of the daily insolation estimates is sufficient, or at least useful, for large-scale surface-atmosphere interaction studies ($10 Wm^{-2}$ is typically required for climate studies) and that of PAR adequate for global primary production computations. In the latter case, the major uncertainty comes from estimating the fraction of PAR that is intercepted and absorbed by the vegetation canopy.

Insolation and not PAR, however, is being produced from global satellite datasets, such as those compiled within the framework of the International Satellite Cloud Climatology Project (ISCCP; Schiffer and Rossow, 1983). Since PAR and insolation are highly correlated (see, for instance, Figs. 3 and 4), it is interesting to compare the accuracy with which one can deduce PAR from a satellite estimate of insolation to that obtained when PAR is directly estimated from the satellite data (the method described in section 2). Figure 9 shows the ratio of daily PAR and insolation at station 5. We did not use the data of stations 21 (PAR) and 26 (insolation) because, even though these stations were close, they were not at the same location, and, therefore, spatial cloud variability may introduce errors in the ratio (in fact an anomalous value was obtained for day 185). We notice that the ratio is fairly constant around the average value of 0.448. We do not detect at this time scale, however, a tendency for the ratio to increase when average cloudiness increases, as theory predicts in cloudy conditions.

Using the average value of 0.448 for the ratio of daily PAR and insolation with the satellite estimates of daily insolation presented in section 4, we deduced PAR values that we compared to in situ measurements. The comparison statistics revealed the same correlation coefficient as in Table 1 (0.969) and a slightly larger standard error of estimate (10.0 instead of $8.2 Wm^{-2}$) and bias (2.4 instead of

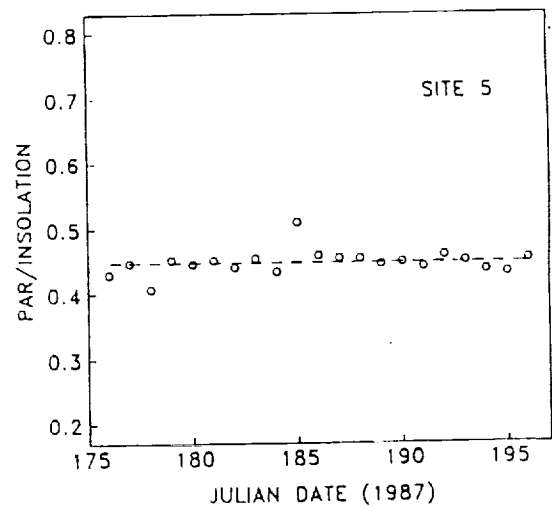


Fig. 9: Ratio of daily PAR and insolation during FIFE's second IFC.

1.4 Wm^{-2}). Although based on 21 points, these figures show convincingly that satellite estimates of insolation yield useful PAR estimates on a daily time scale. Keep in mind, however, that the ratio of PAR to insolation may change significantly depending on the type of atmosphere. In a moist and humid clear environment, it may reach values above 0.50. Large variations in the ratio, however, are not likely to occur at a specific site during a few week period (see Fig. 9). Yet in calculating PAR from insolation, we determined in situ the ratio of PAR and insolation, which minimizes the uncertainty in this ratio. On the other hand, adapting the insolation model to PAR (and this may apply to other satellite methods) is rather simple and eliminates not only the uncertainty in the PAR/insolation ratio, but also the uncertainty in cloud absorption and narrow-band to broad-band conversion, which affects insolation estimates.

Finally, since cloud radiation interactions are important to weather and climatic prediction, it is worthwhile examining the role of clouds in modulating insolation. Following Charlock and Ramanathan (1985), we define the cloud forcing on insolation (PAR) as the difference between insolation in clear and actual sky conditions. Figure 10 shows the daily cloud forcing during the IFC for both insolation and PAR. In the calculation we used the satellite estimates and computed clear sky irradiances from the clear sky models. The cloud forcing reaches about 75% of the clear sky insolation on days 180 and 181. Minimum (or maximum) values occur every 2 to 4 days, which correspond roughly to the time scale of mid-latitude atmospheric perturbances. Compared to the effect of changes in water vapor amount and aerosol type and amount (Fig. 11), the cloud forcing largely dominates (by typically one order of magnitude). This indicates, in other respects, that while developing satellite techniques to estimate insolation (or PAR), one should concentrate on the role of clouds (and, therefore, determine accurately the governing cloud parameters) rather than on the influence of the clear atmosphere.

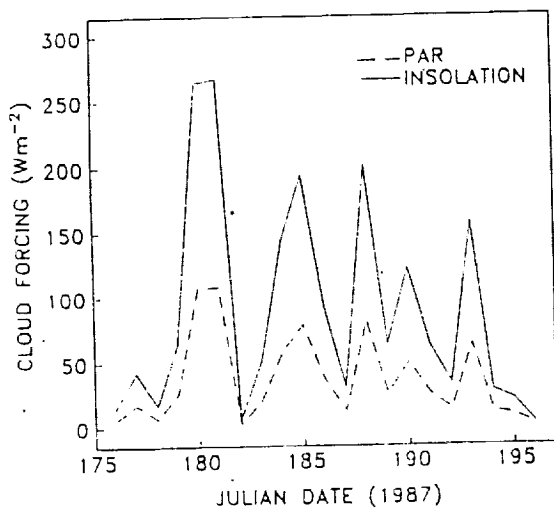


Fig. 10: Cloud forcing on daily insolation and PAR during FIFE's second IFC as deduced from the satellite estimates.

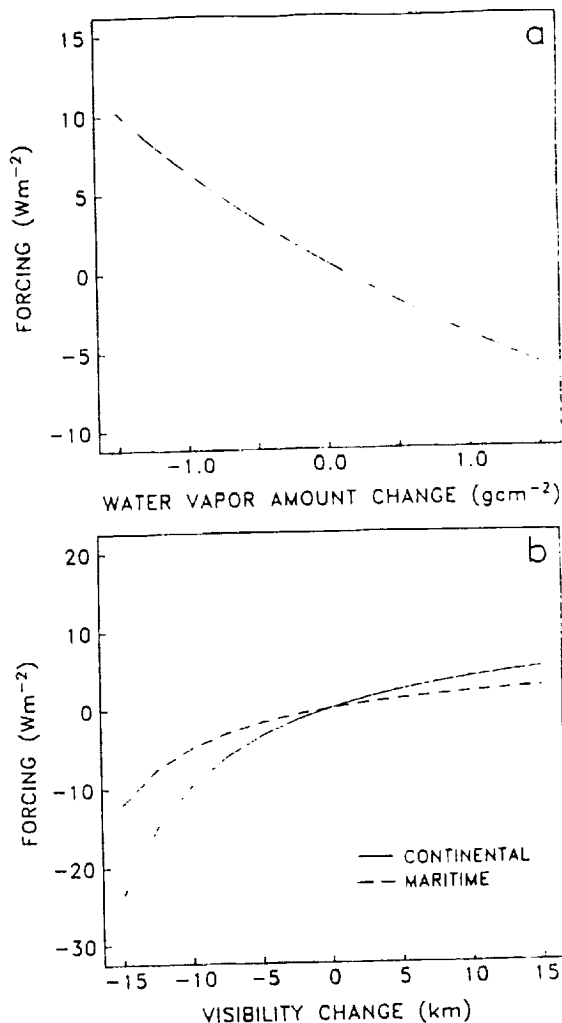


Fig. 11: Forcing on daily insolation due to changes in water vapor amount (a), and aerosol type and loading (b).

6. SUMMARY AND CONCLUSIONS

In the first part of the study, we have indicated how the satellite technique of Gautier et al. (1980) can be modified to yield PAR as well as insolation estimates. In the case of PAR, cloud absorption vanishes in the model equations and clear sky PAR is computed using the coefficients given by Frouin et al. (1989). The technique was then applied to GOES-6 VISSR data acquired during FIFE's second IFC. The computational procedure included checks of the satellite navigation and of the data quality, as well as calibration of the VISSR visible channel. The calibration, achieved using space and White Sands, New Mexico as calibration targets, revealed an important sensor degradation, reaching 64% in December 1987. Compared to in situ measurements, the satellite estimates of insolation and PAR exhibited small biases, correlation coefficients above 0.95, and standard errors of estimate of 21.6 Wm^{-2} (9%) and 8.2 Wm^{-2} (6.5%), respectively. These errors are acceptable for climate studies. The overall statistics were found to be better for PAR, which is expected since, in that case, cloud absorption does not need to be parameterized and no narrow-band to broad-band conversion is necessary. The satellite estimates also described well the diurnal variability of PAR and insolation. Using the ratio of PAR and insolation determined in situ with the satellite estimates of insolation,

we obtained daily PAR values with a slightly better r.m.s. accuracy than when PAR was directly estimated from the satellite data. This indicates that the large-scale satellite climatologies of insolation now being produced within the framework of ISCCP can be converted simply into useful climatologies of PAR for global studies of photosynthetic activity, although a more direct use of the satellite data would certainly be optimum. Examining the cloud forcing on insolation and PAR, we found that over the time period considered, clouds strongly modulate insolation with a 2-4 day time scale, variations in the characteristic of the atmosphere yielding irradiance changes of typically one order of magnitude less. This is not surprising, indeed, but the situation might be different when considering insolation variability over longer time periods (e.g., one year).

The above results, however, only concern a 3 week period. Three other IFCs were conducted during FIFE in 1987, and they correspond to different seasons and states of the vegetation (surface albedo). In addition, only data from a few surface stations were analyzed in the present study, and many more stations provided radiation data. Our next step, therefore, is to extend the conclusions drawn in this study to the other IFCs, in particular regarding accuracy of insolation and PAR methods, and contrast the surface flux variability (including spatial variability within the FIFE site) during each IFC. More work will also be devoted to the surface albedo, a parameter that needs to be specified as a boundary condition in general circulation models. We did not elaborate on this parameter in the present study because of its small influence on insolation, but this is not the case, indeed, when the net radiation budget is considered.

7. ACKNOWLEDGMENTS

This work was supported by the National Aeronautics and Space Administration under grant NAG5-900 and by the California Space Institute under grant CS87-89. We wish to thank K. Shapiro and B. Bloomfield for their editorial assistance and J. Correa and the FIFE information system for their technical support.

7. REFERENCES

- Baker, K.S. and R. Frouin, 1987: Relation between photosynthetically available radiation and total insolation at the ocean surface under clear skies. *Limnol. Oceanogr.*, **32**, 1370-1377.
- Charlock, T.P. and V. Ramanathan, 1985: The albedo field and cloud radiative forcing produced by a general circulation model with internally generated cloud optics. *J. Atmos. Sci.*, **42**, 1408-1429.
- Dedieu, G., P.Y. Deschamps and Y.H. Kerr, 1987: Satellite estimation of solar irradiance at the surface of the earth and of surface albedo using a physical model applied to Meteosat data. *J. Clim. and Appl. Meteor.*, **26**(1), 79-87.
- Diak, G. and C. Gautier, 1983: Improvements to a simple model for estimating insolation from GOES Data. *J. Clim. Appl. Meteor.*, **22**, 3, 505-508.
- Frouin, R., and C. Gautier, 1987: Calibration of NOAA-7 AVHRR, GOES-5 and GOES-6 VISSR/VAS solar channels. *Rem. Sens. Environ.*, **22**, 73-101.
- Frouin, R., C. Gautier, K. Katsaros, and R. Lind, 1988: A comparison of satellite and empirical formula techniques for estimating insolation over the oceans. *J. Appl. Meteor.*, **27**, 9, 1016-1023.
- Frouin, R., D.W. Lingner, C. Gautier, K.S. Baker, and R.C. Smith, 1989: A simple analytical formula to compute clear sky total and photosynthetically available solar irradiance at the ocean surface. *J. Geophys. Res.-Oceans*, **94**, 9731-9742.
- Gautier, C., G. Diak and S. Masse, 1980: A Simple physical model to estimate incident solar radiation at the surface from GOES satellite data. *J. Appl. Meteor.*, **19**, 1005-1012.
- Moser, W., and E. Raschke, 1984: Incident solar radiation over Europe estimated from Meteosat data. *J. Clim. and Appl. Meteor.*, **23**(1), 166-170.
- Pinker, R.T., and J.A. Ewing, 1985: Modeling surface solar radiation: Model formulation and validation. *J. Clim. and Appl. Meteor.*, **24**(5), 389-401.
- Raphael, C., and J.E., 1984: Hay An assessment of models which use satellite data to estimate solar irradiance at the earth's surface. *J. Clim. and Appl. Meteor.*, **23**, 832-844.
- Schiffer, R.A., and W.B. Rossow, 1983: The international satellite cloud climatology project (ISCCP): The first project of the world climate research programme. *Bull. Amer. Meteor. Soc.*, **64**, 779-784.
- Tanré, D., C. Deroo, P. Duhaut, M. Herman, J.J. Morcrette, J. Perbos and P.Y. Deschamps, 1985: Effets atmosphériques en télédétection-logiciel de simulation du signal satellitaire dans le spectre solaire. *Proc. 3rd Int'l Colloquium on Spectral Signatures of Objects in Remote Sensing*, Les Arcs, France, Dec 16-20.
- Tarpley, J.D., 1979: Estimating incident solar radiation at the surface from geostationary satellite data. *J. Appl. Meteor.*, **18**, 1172-1181.
- Welch, R.M., S.K. Cox and J.M. Davis, 1980: Solar radiation and clouds. E.W. Bierly, ed., *Amer. Meteor. Soc.*, Boston, MA, 96 pp.
- World Climate Program, Report of the WMO radiation commission of the IAMAP meeting of experts on aerosols and their climatic effects, *Rep. WCP-55*, Geneva, 1983.
- Whitlock C.H., W.F. Staylor, G. Smith, R. Levin, R. Frouin, C. Gautier, P.M. Teillet, P.N. Slater, J.Y. Kaufman, B.N. Holben, and S.R. LeCroy, 1988: AVHRR and VISSR satellite instrument calibration results from both cirrus and marine stratocumulus IFO periods. Presented at the FIRE Science Team meeting,vail, CO, July 11-15, 1988.





N94-10954

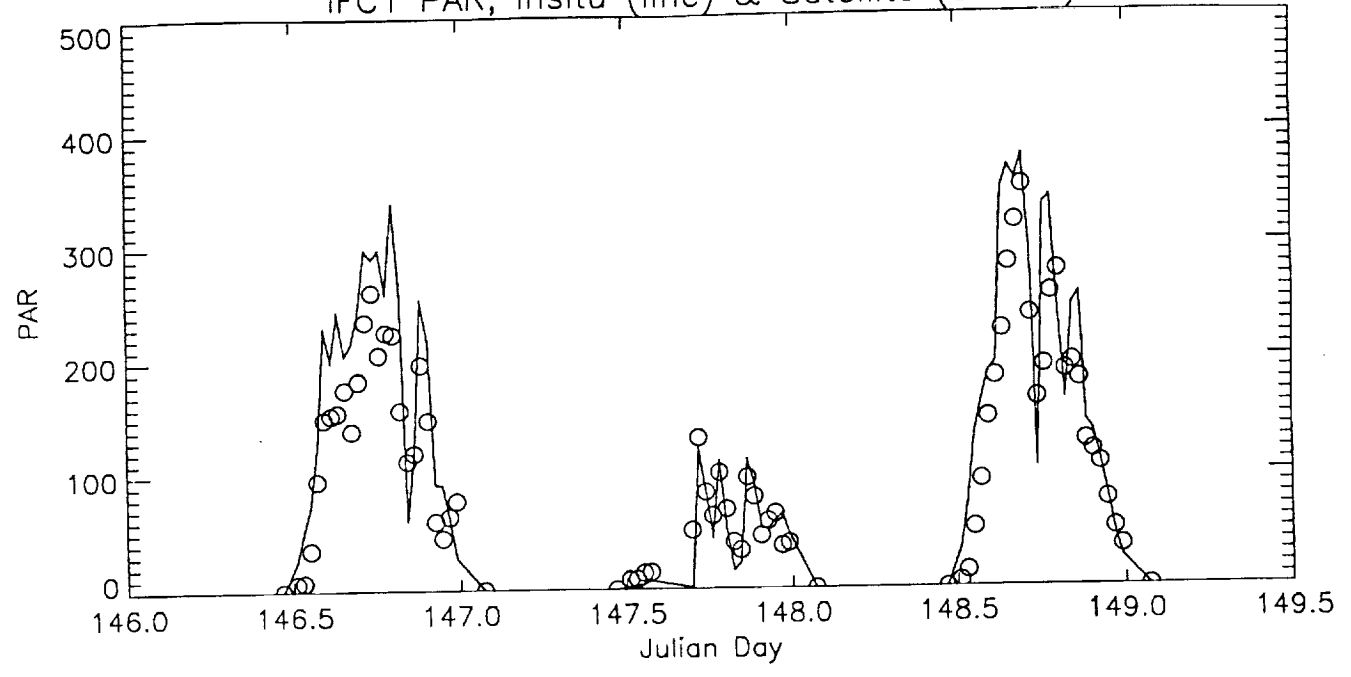
51-43
167948
P-31

Appendix 4

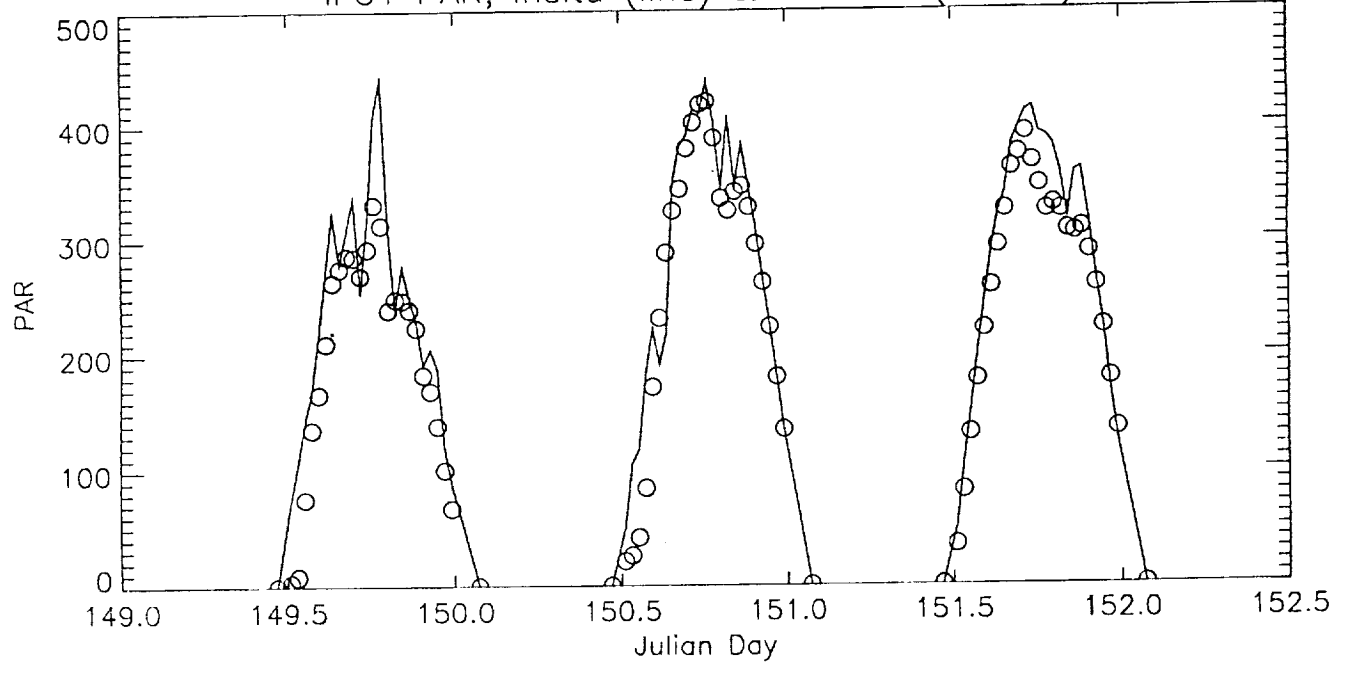
SATELLITE-DERIVED PHOTOSYNTHETICALLY AVAILABLE
AND TOTAL SOLAR IRRADIANCE AT THE SURFACE
DURING FIFE'S INTENSIVE FIELD CAMPAIGNS

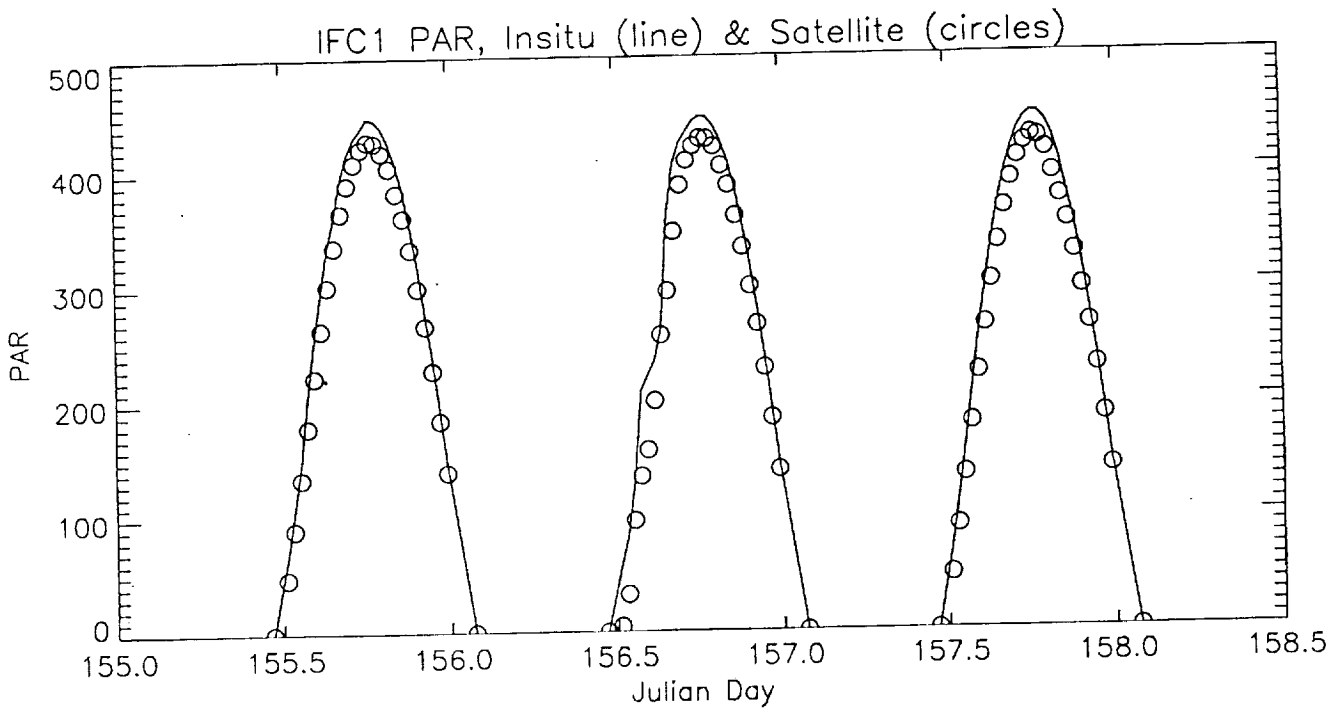
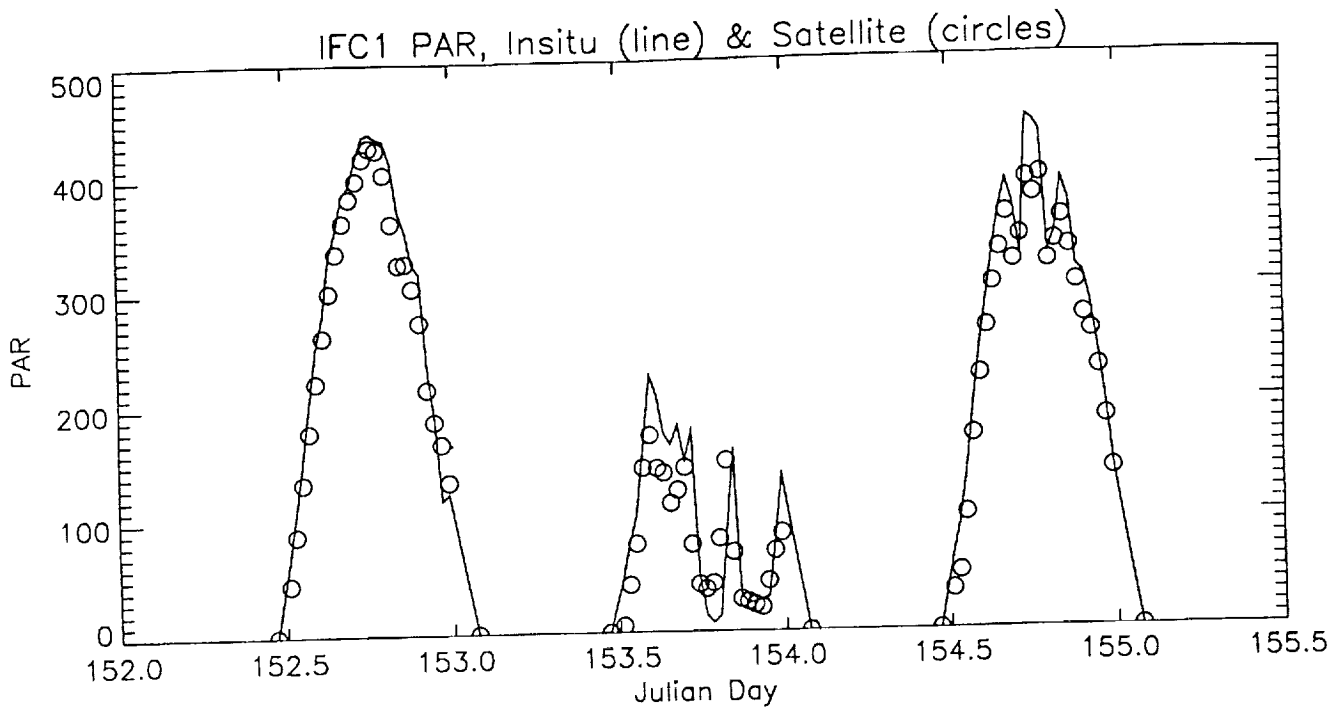
R. Frouin, J. McPherson
(Unpublished)

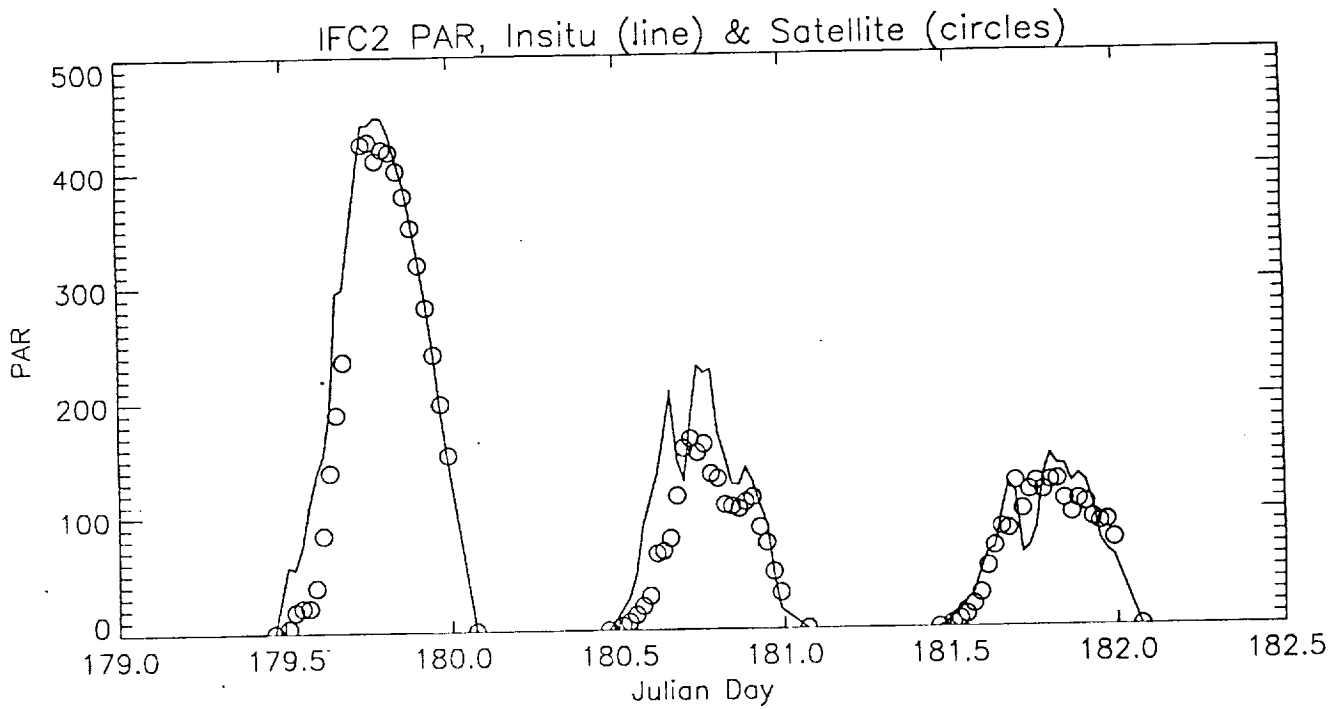
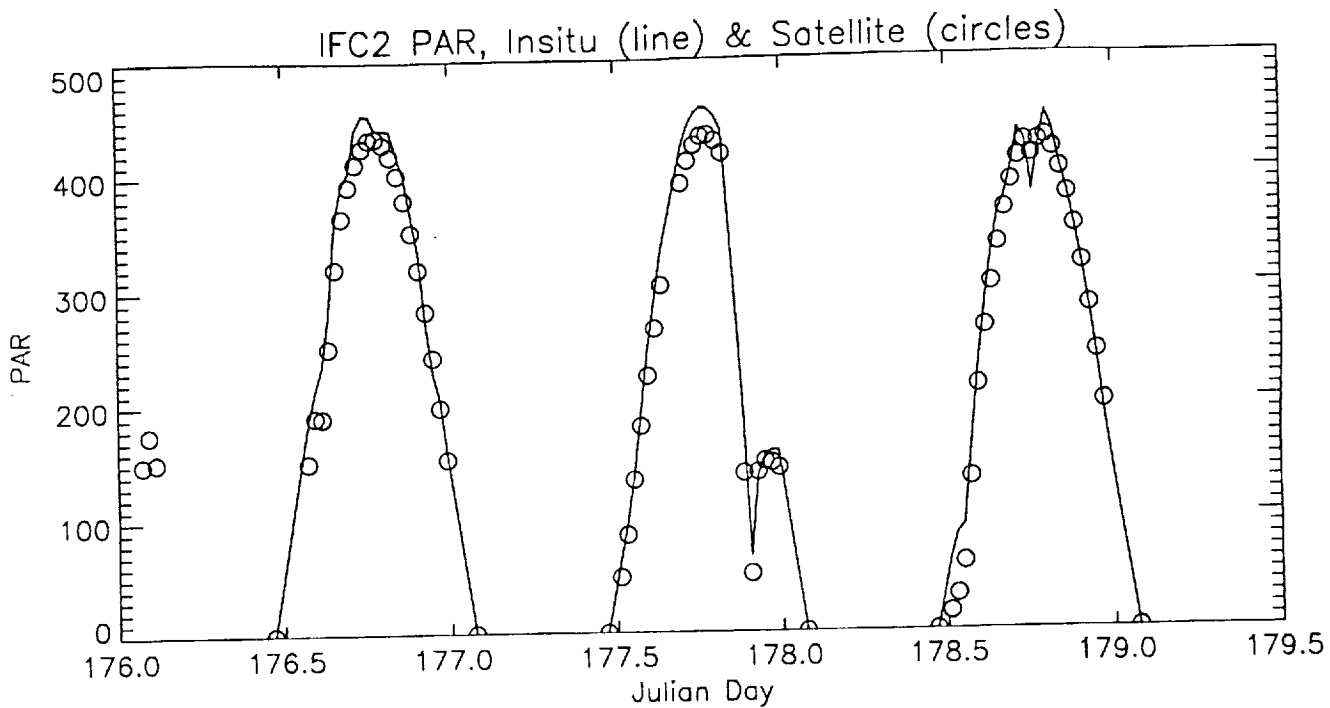
IFC1 PAR, Insitu (line) & Satellite (circles)

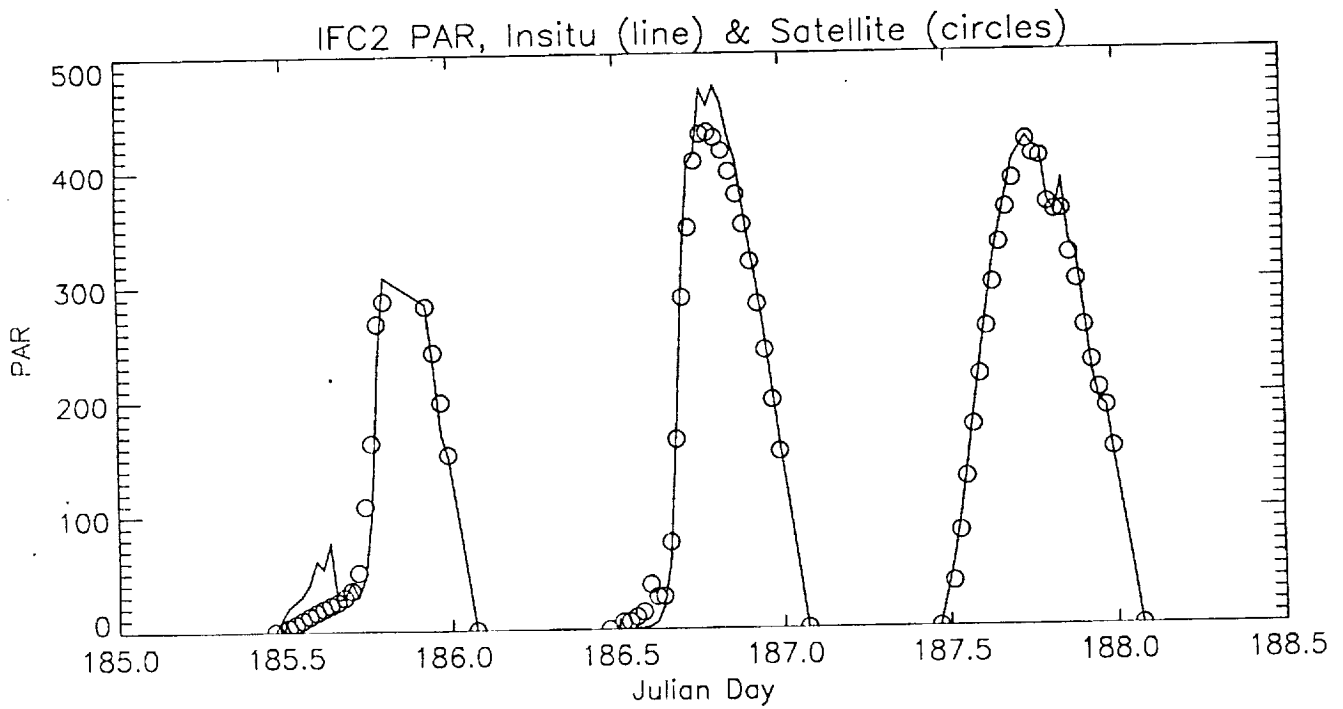
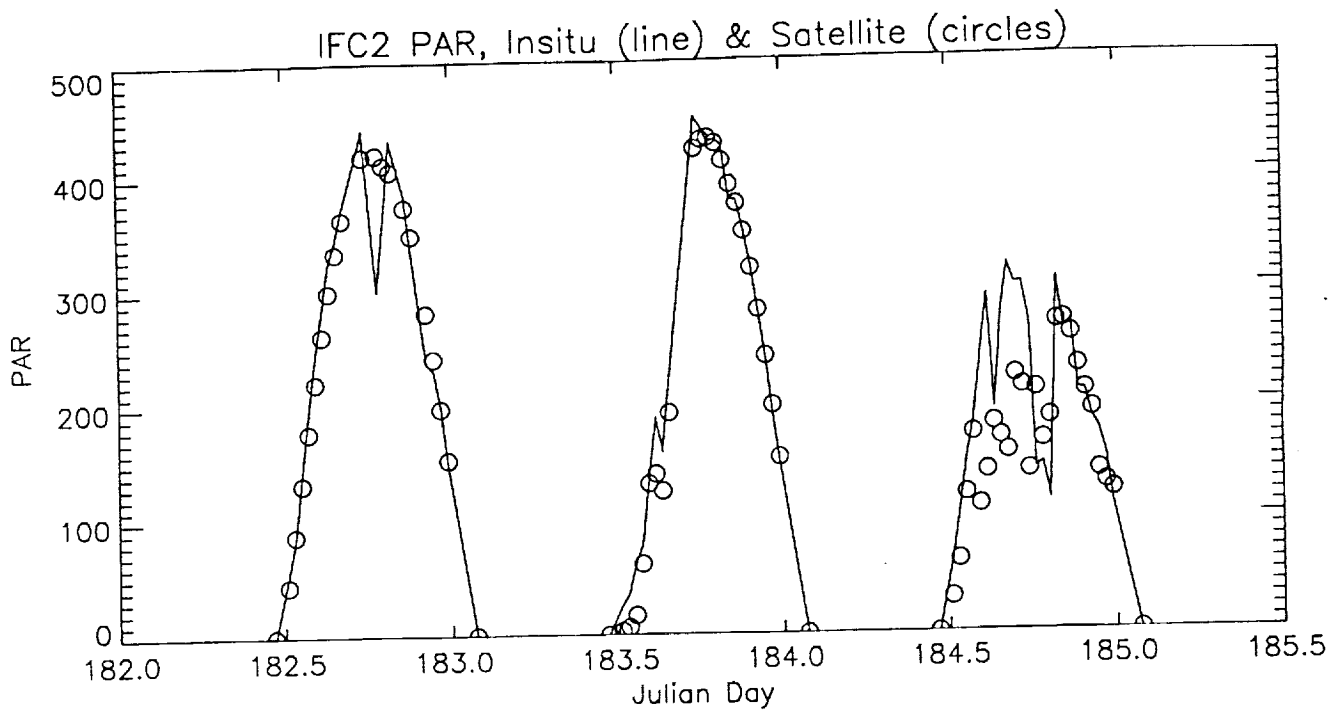


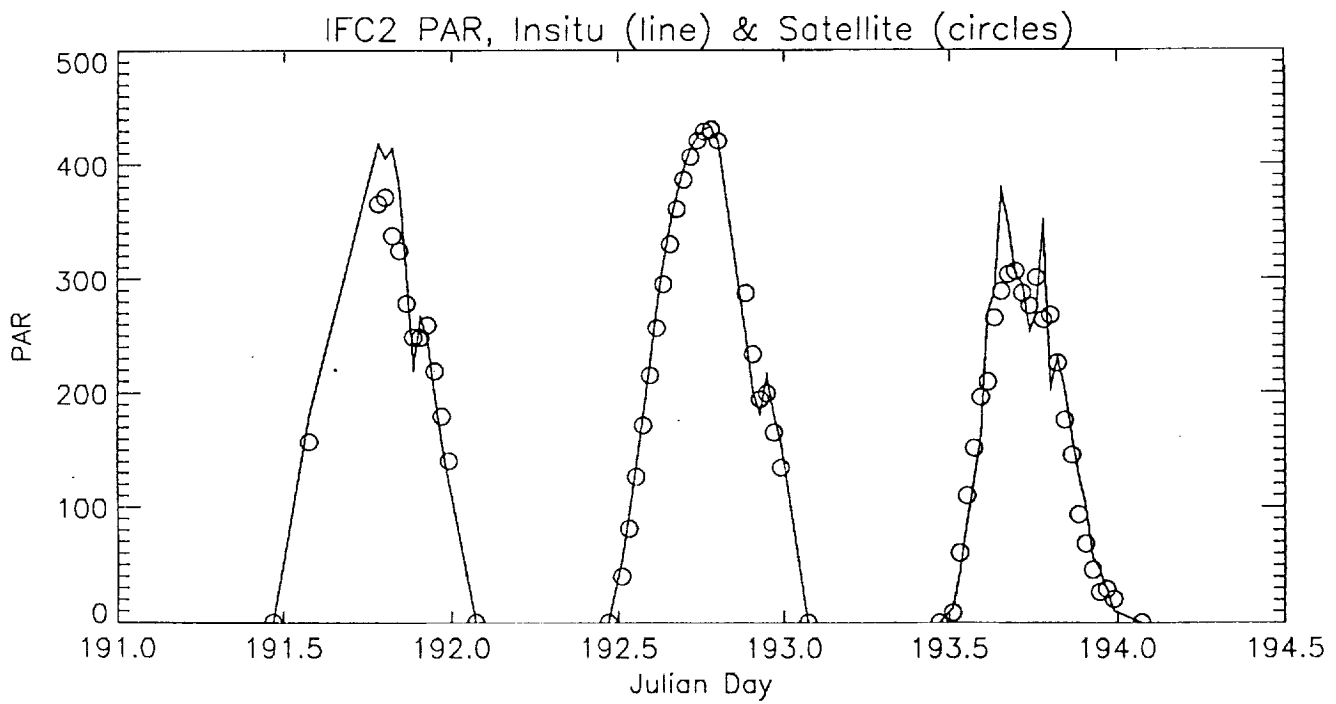
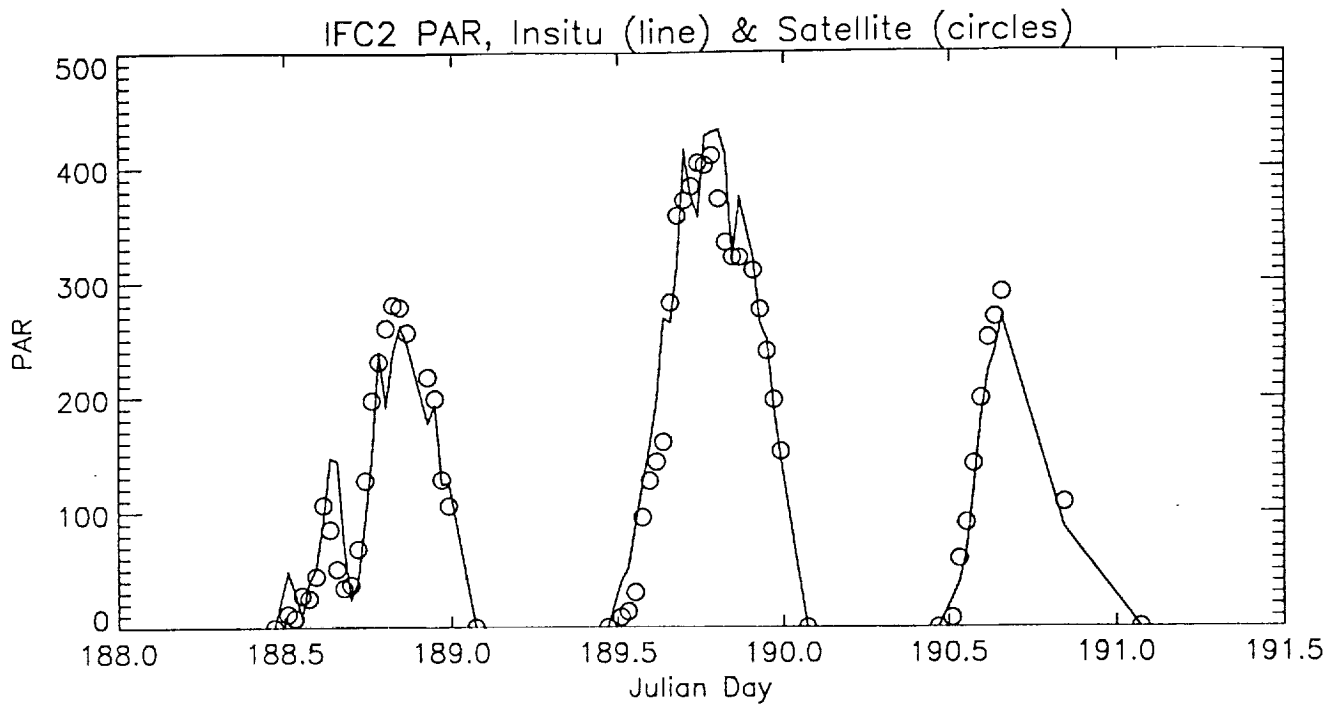
IFC1 PAR, Insitu (line) & Satellite (circles)

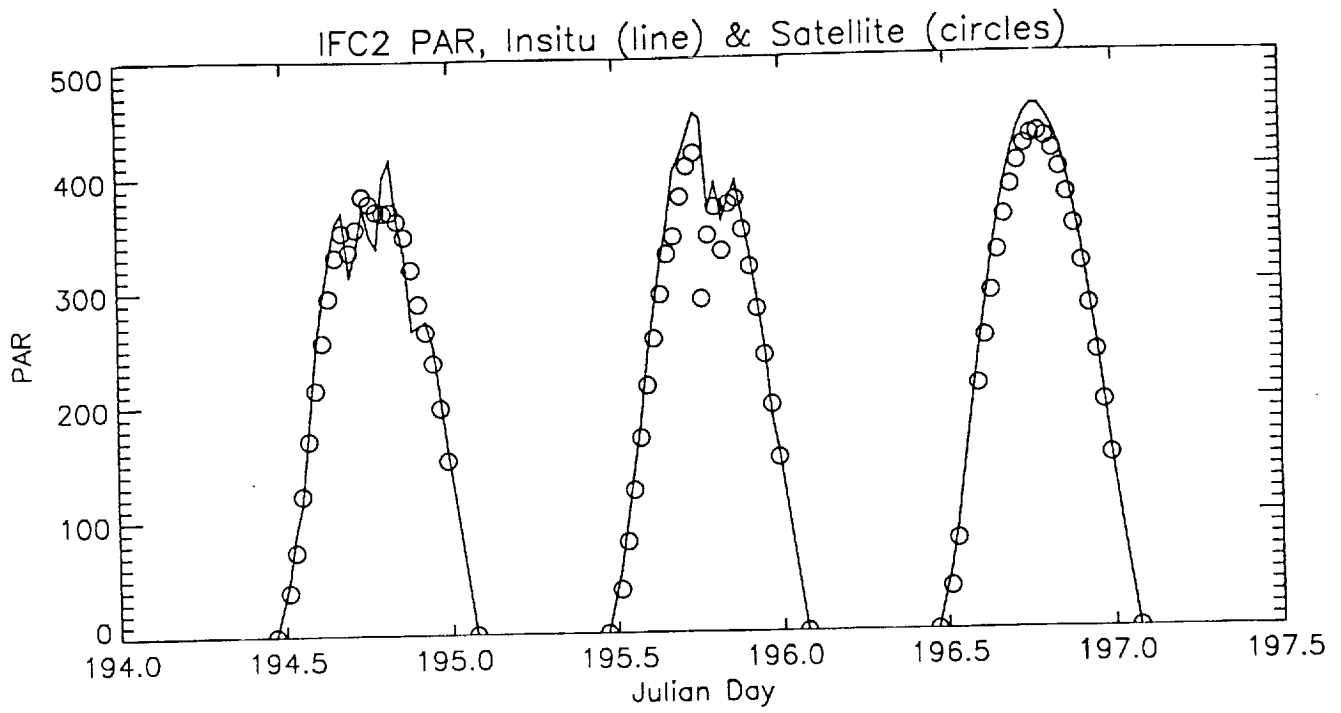


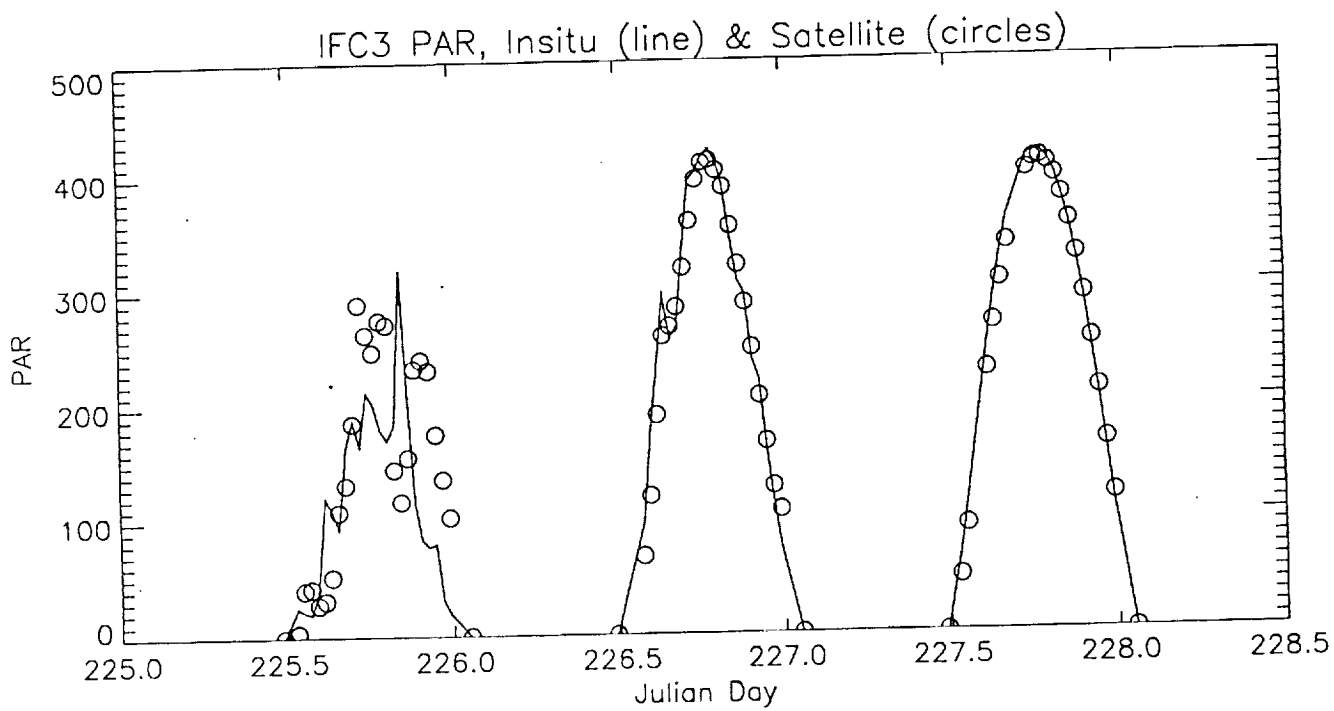
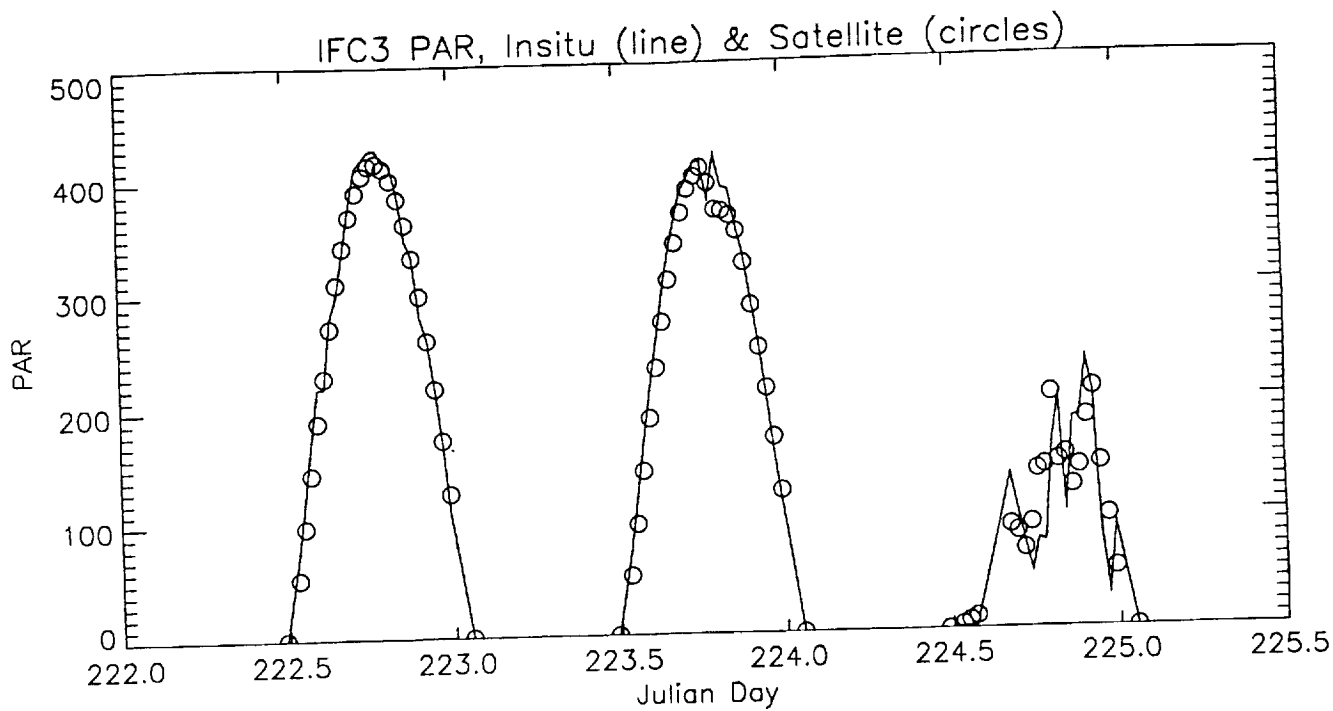


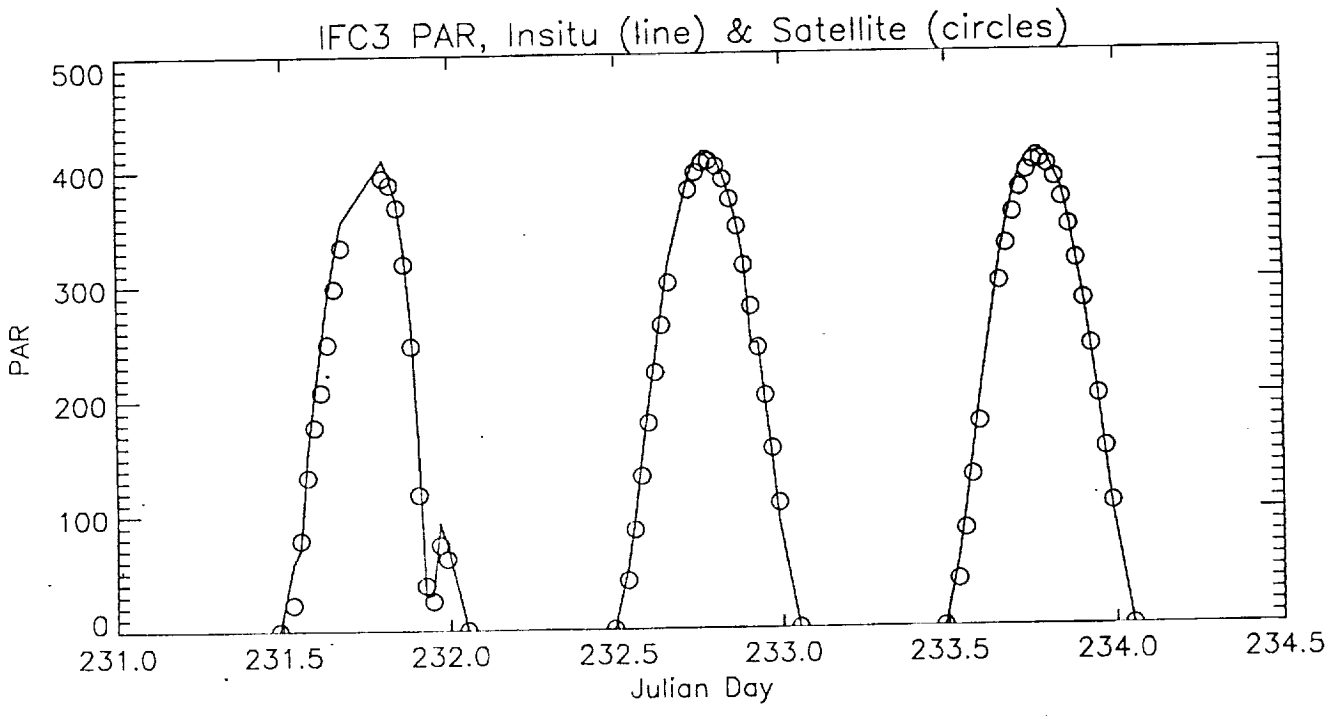
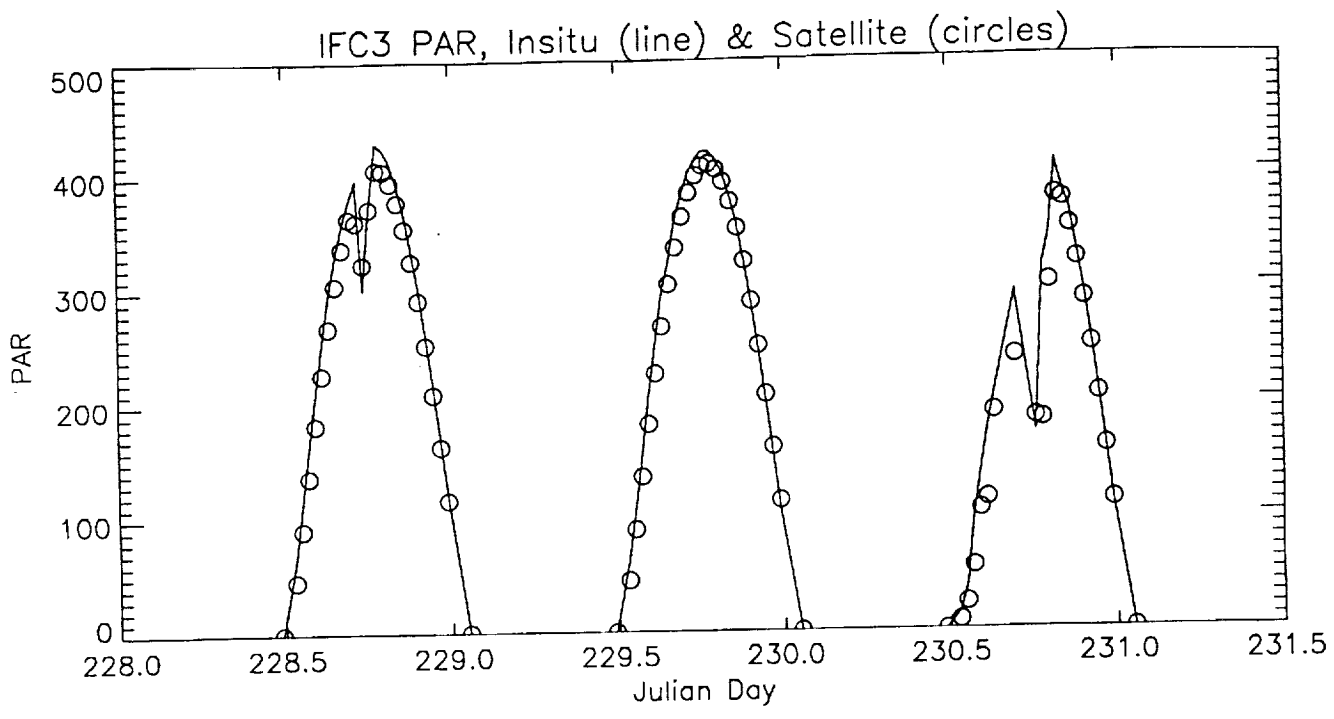


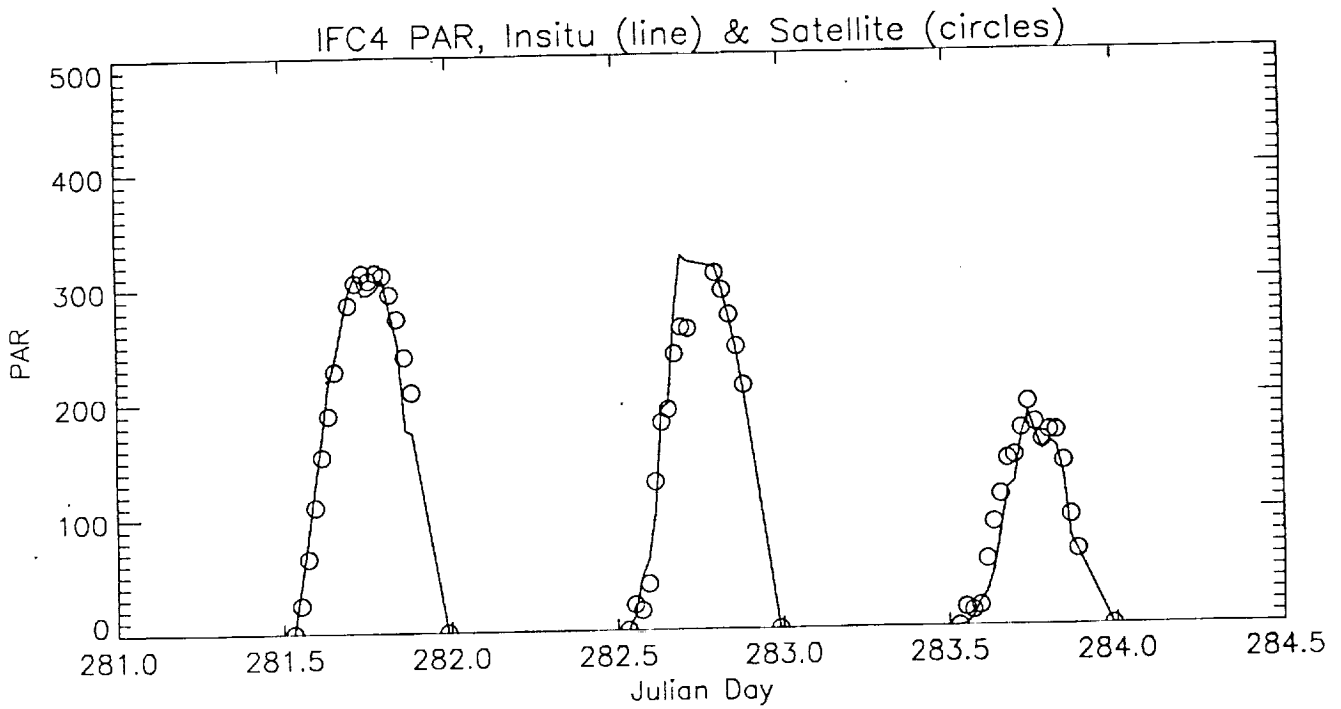
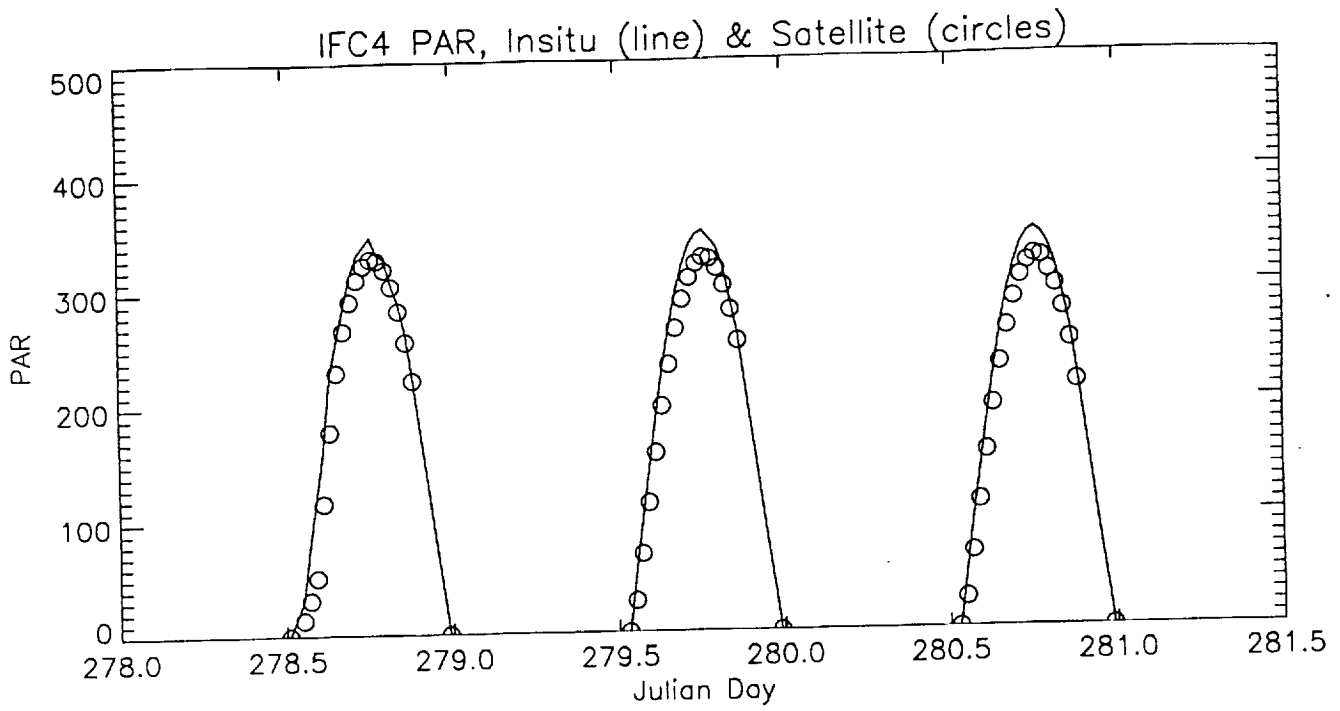


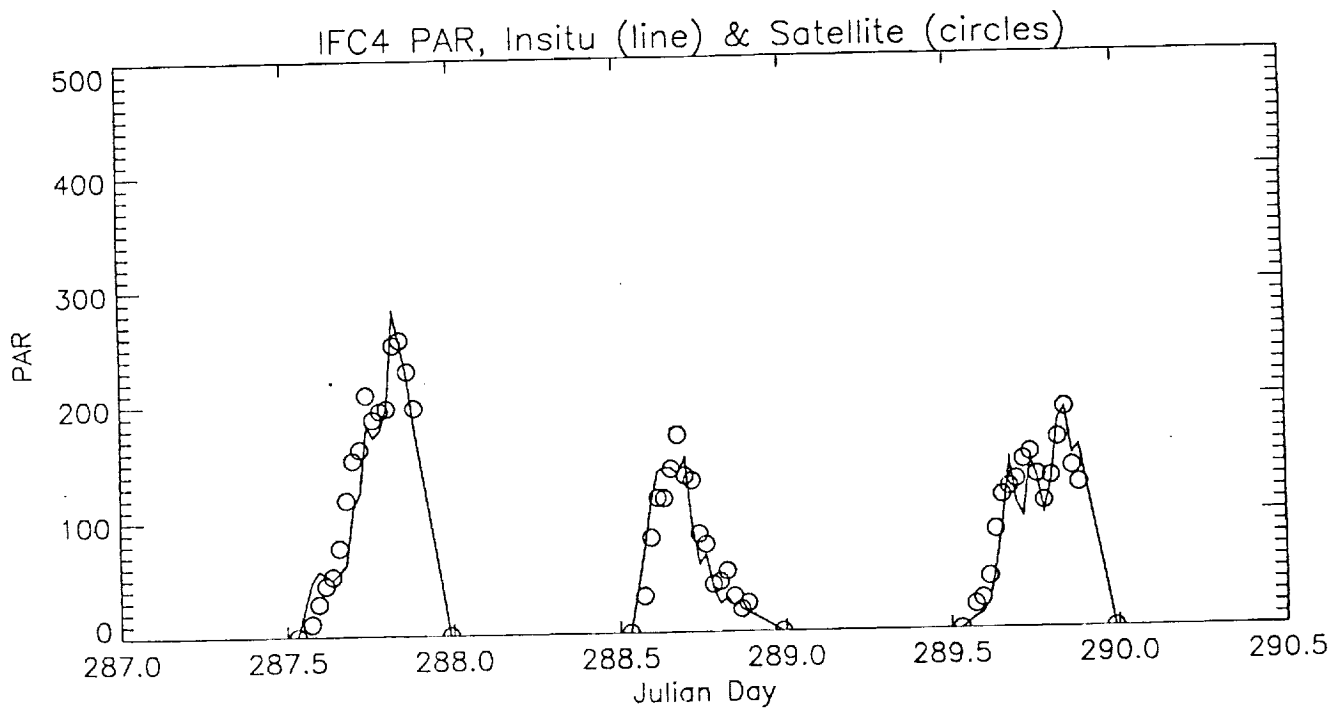
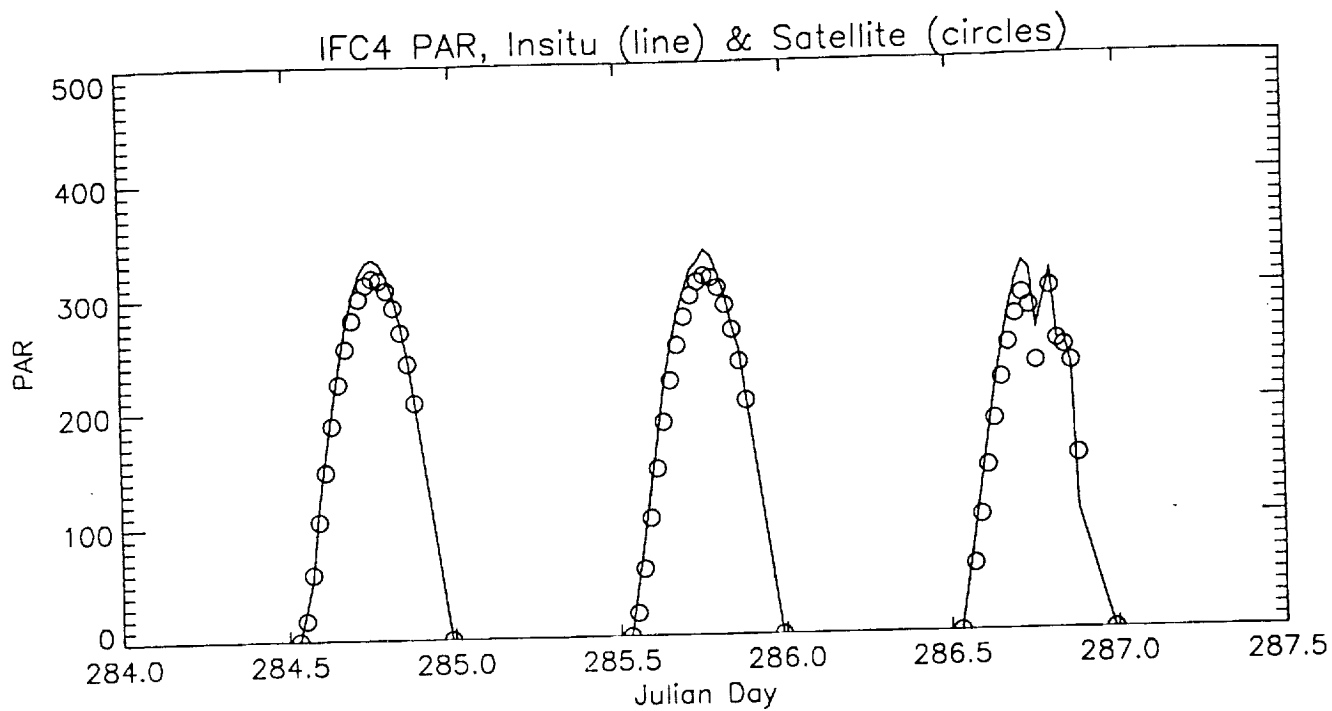


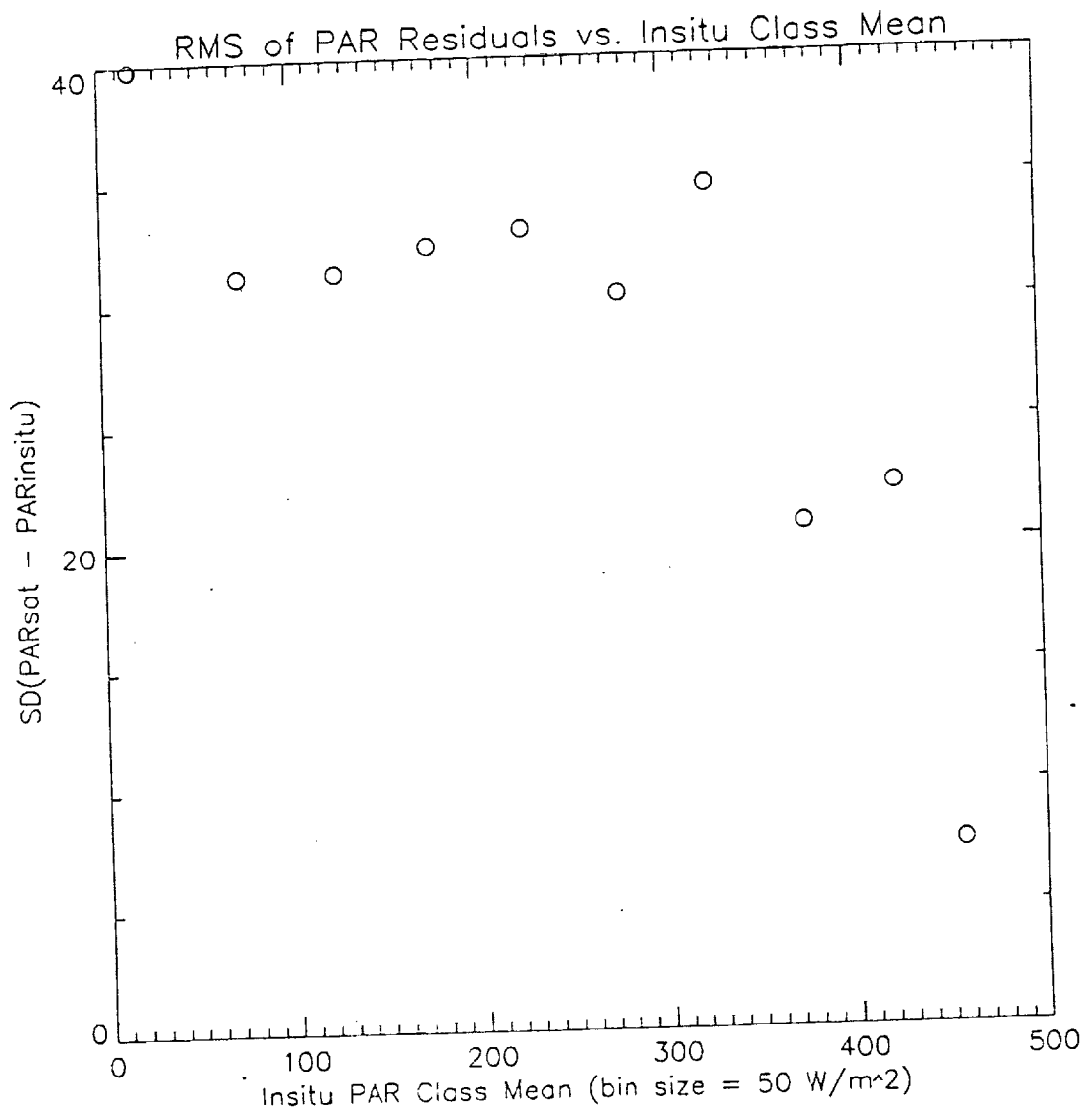


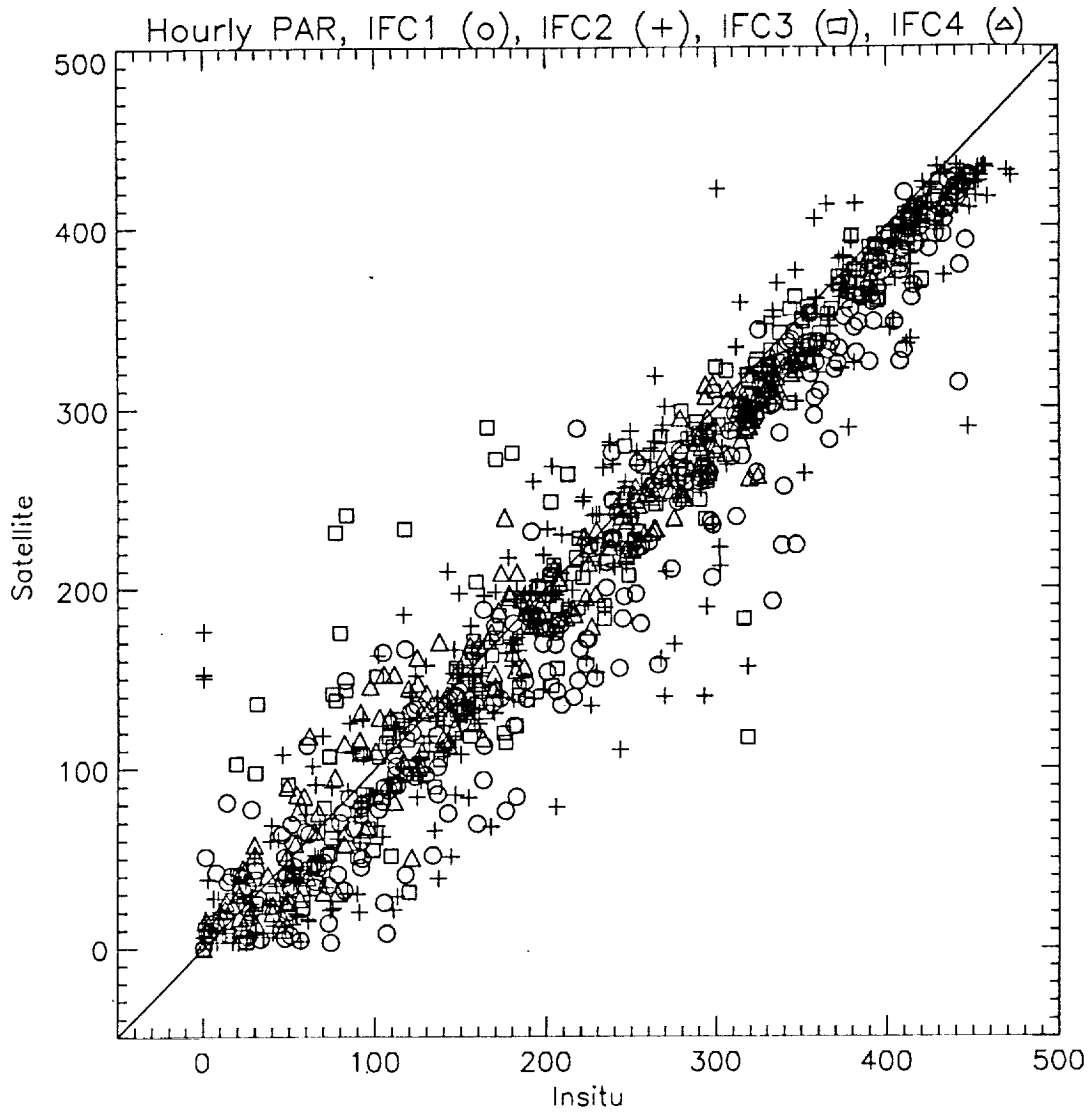




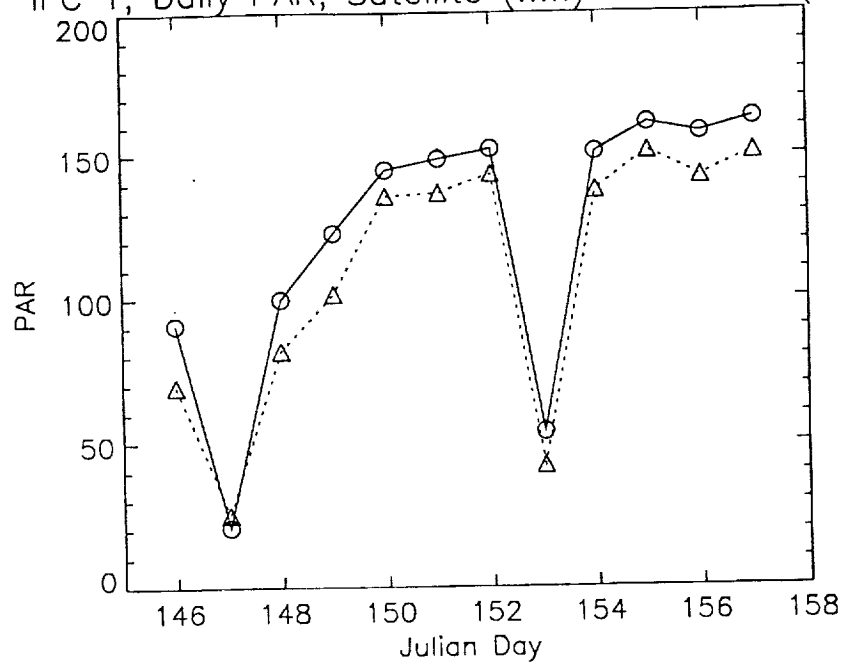




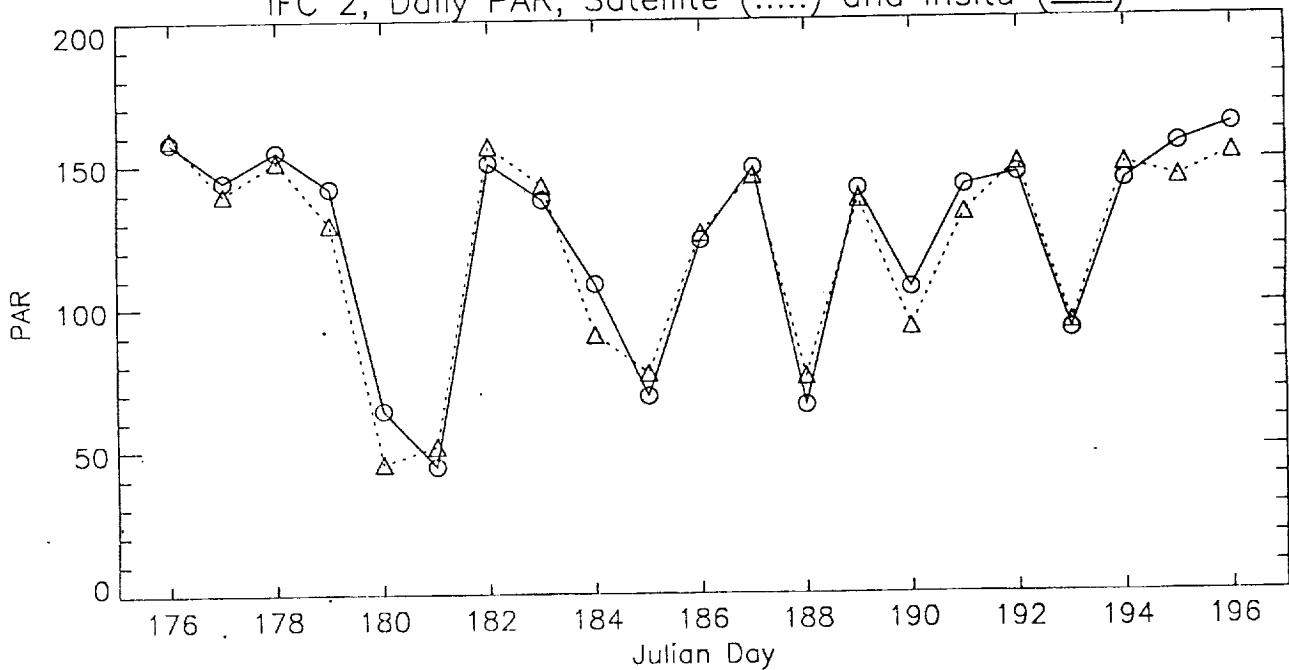




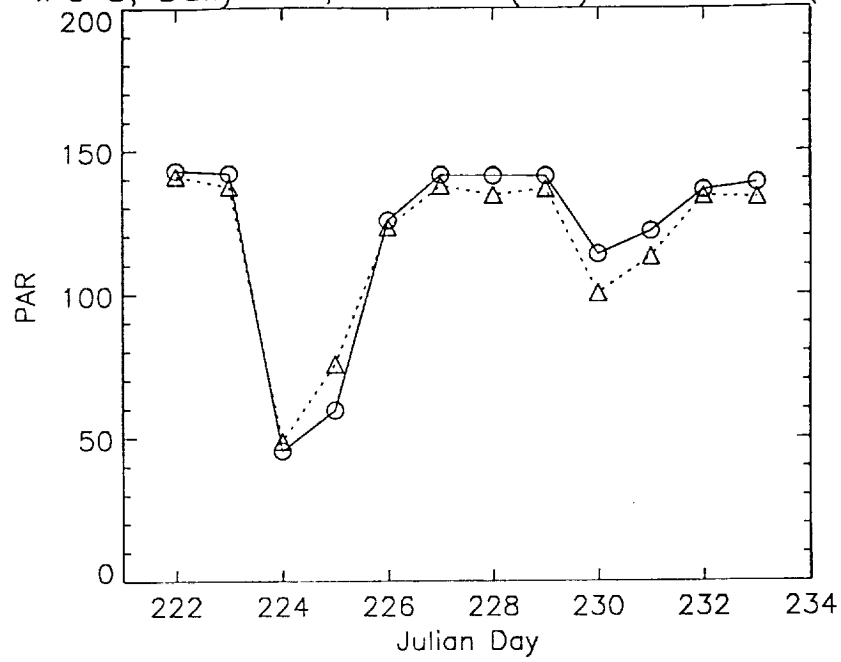
IFC 1, Daily PAR, Satellite (.....) and Insitu (—)



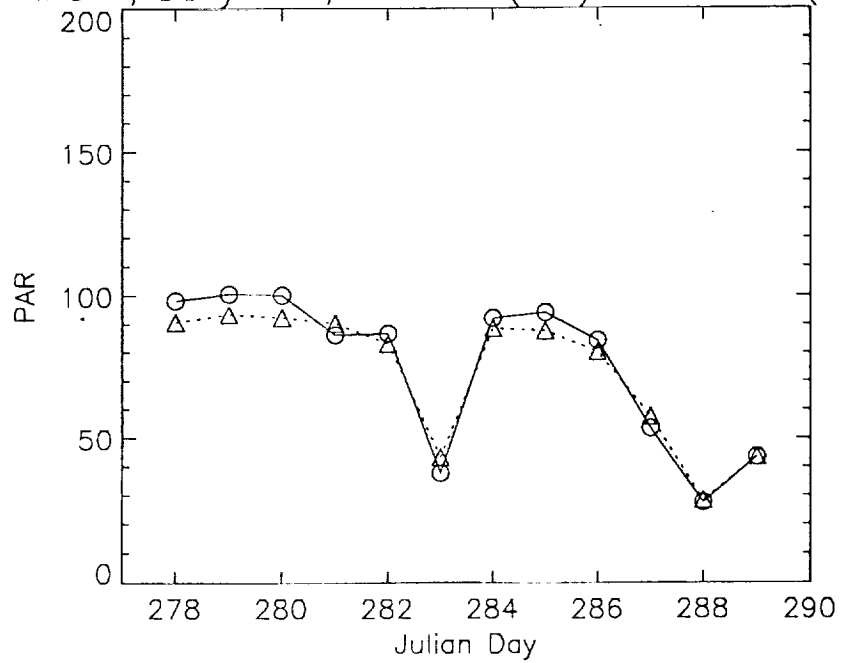
IFC 2, Daily PAR, Satellite (.....) and Insitu (—)

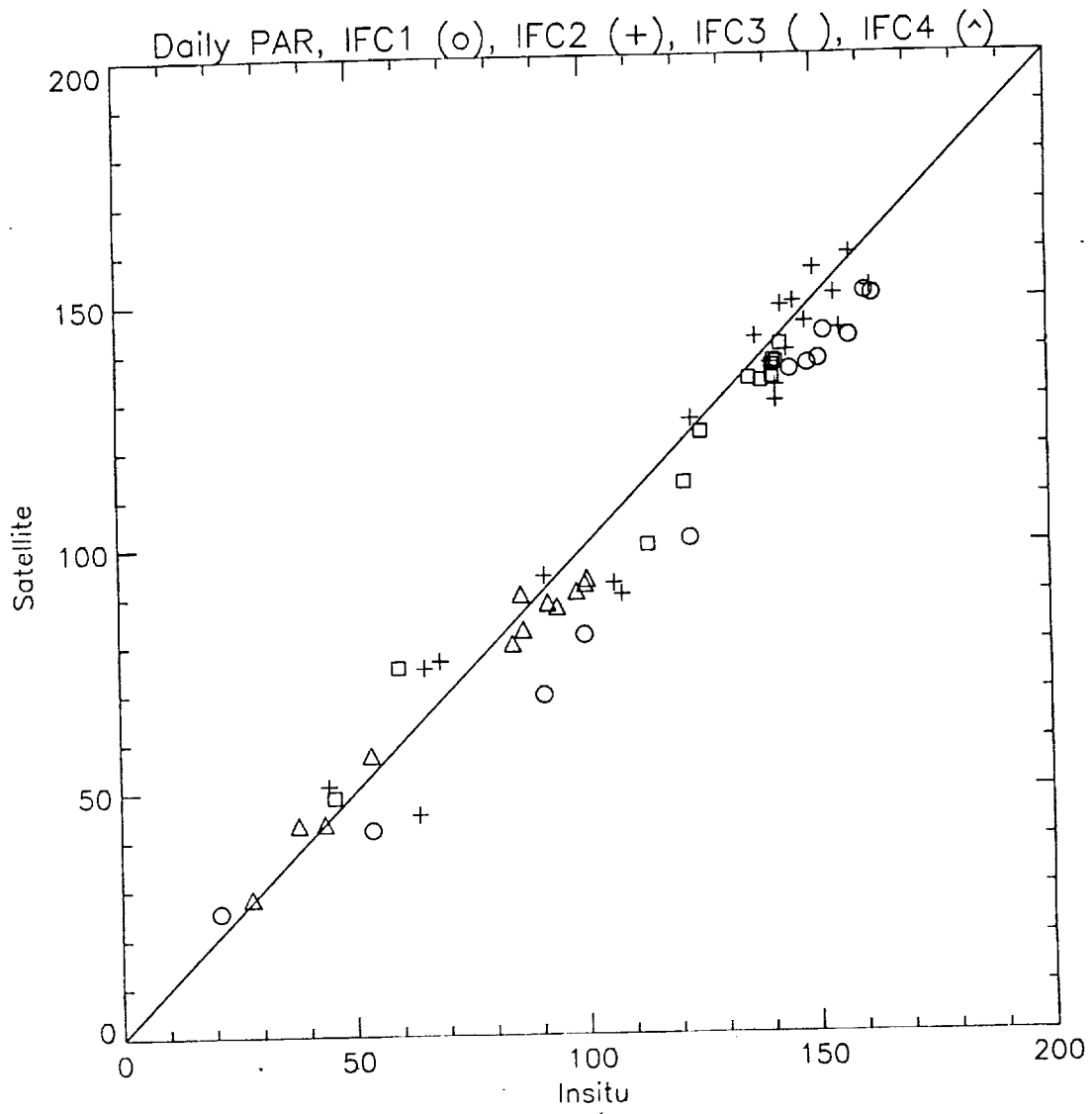


IFC 3, Daily PAR, Satellite (.....) and Insitu (—)

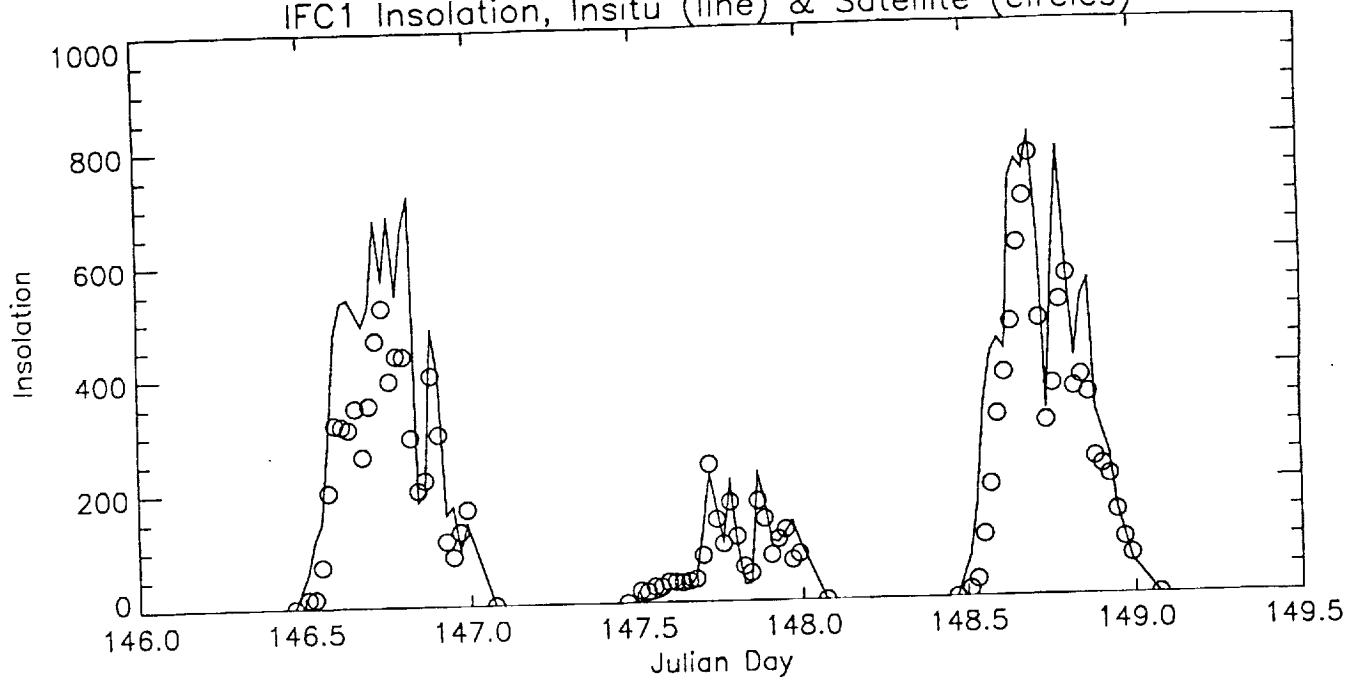


IFC 4, Daily PAR, Satellite (.....) and Insitu (—)

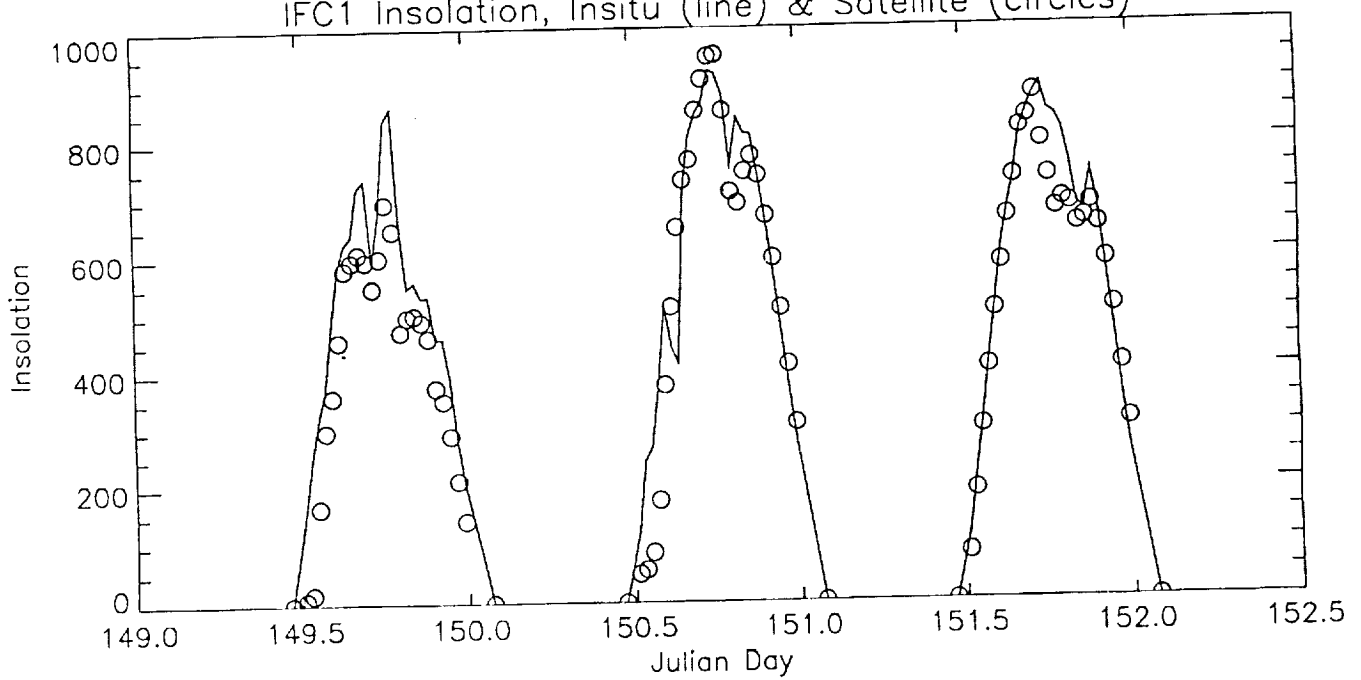


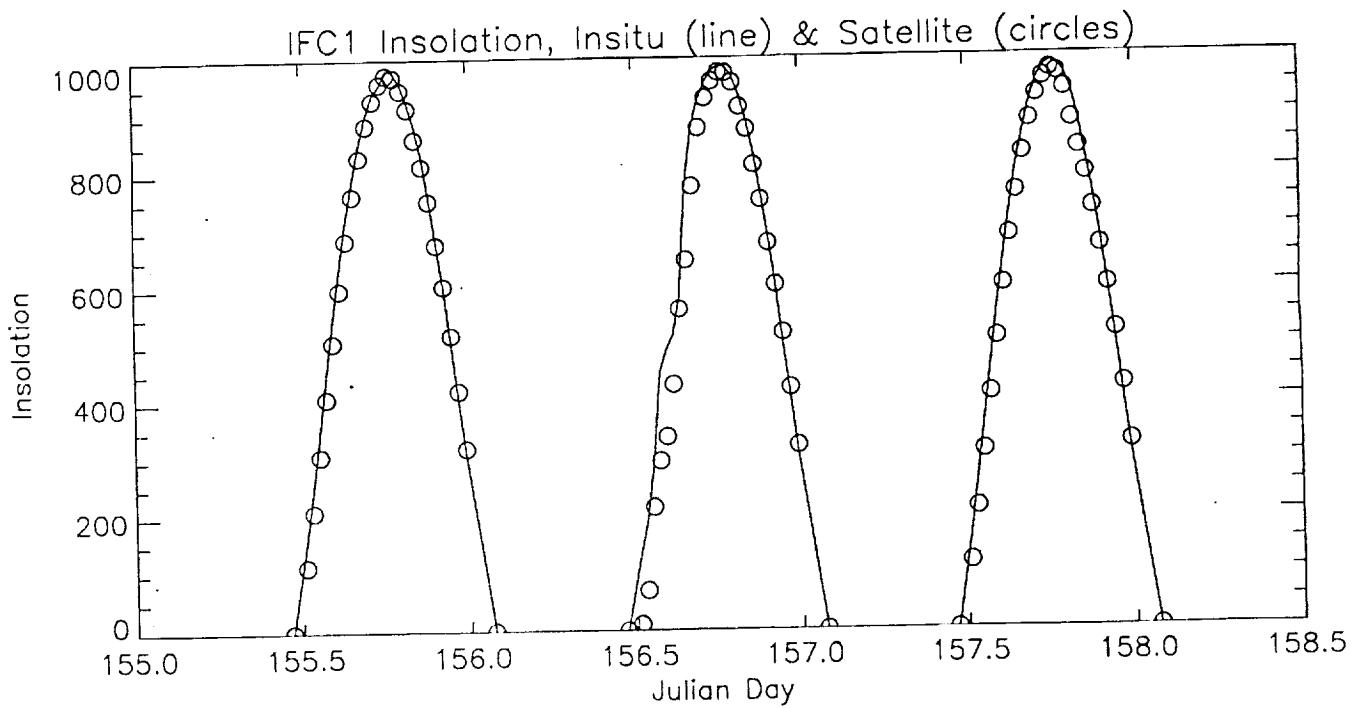
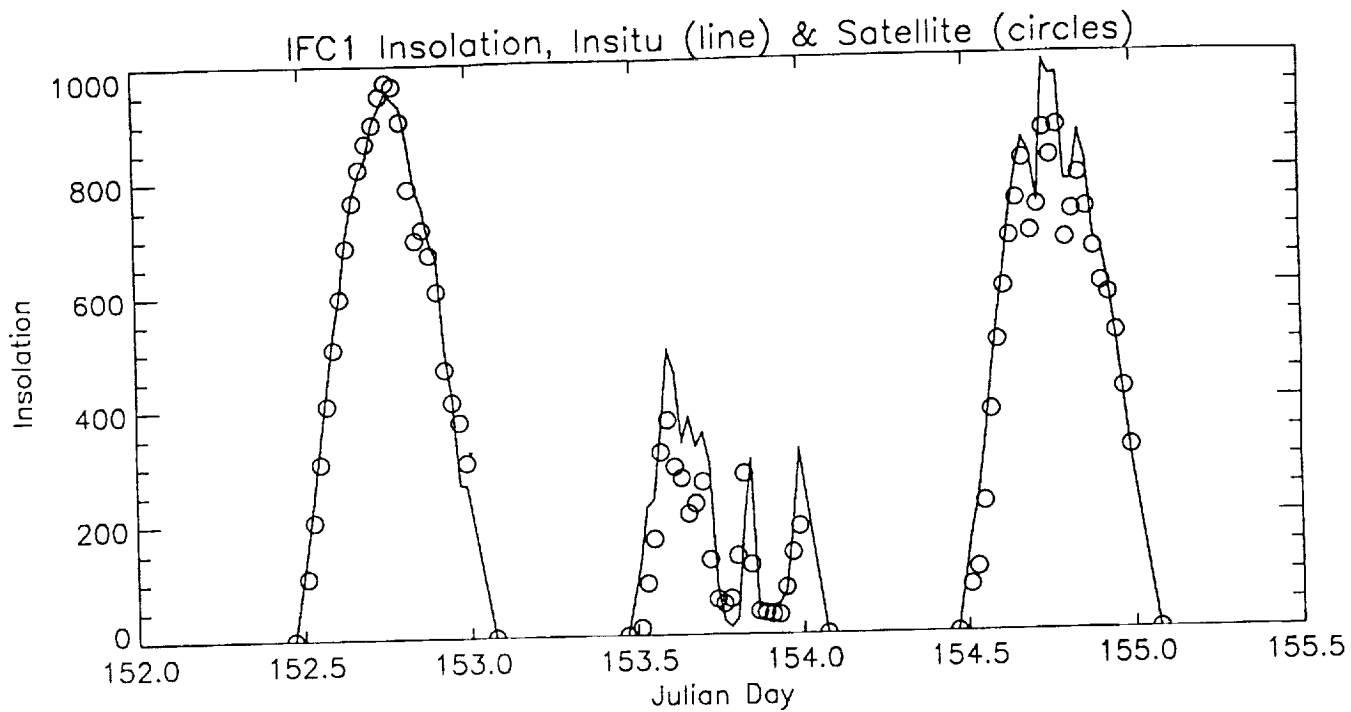


IFC1 Insolation, Insitu (line) & Satellite (circles)

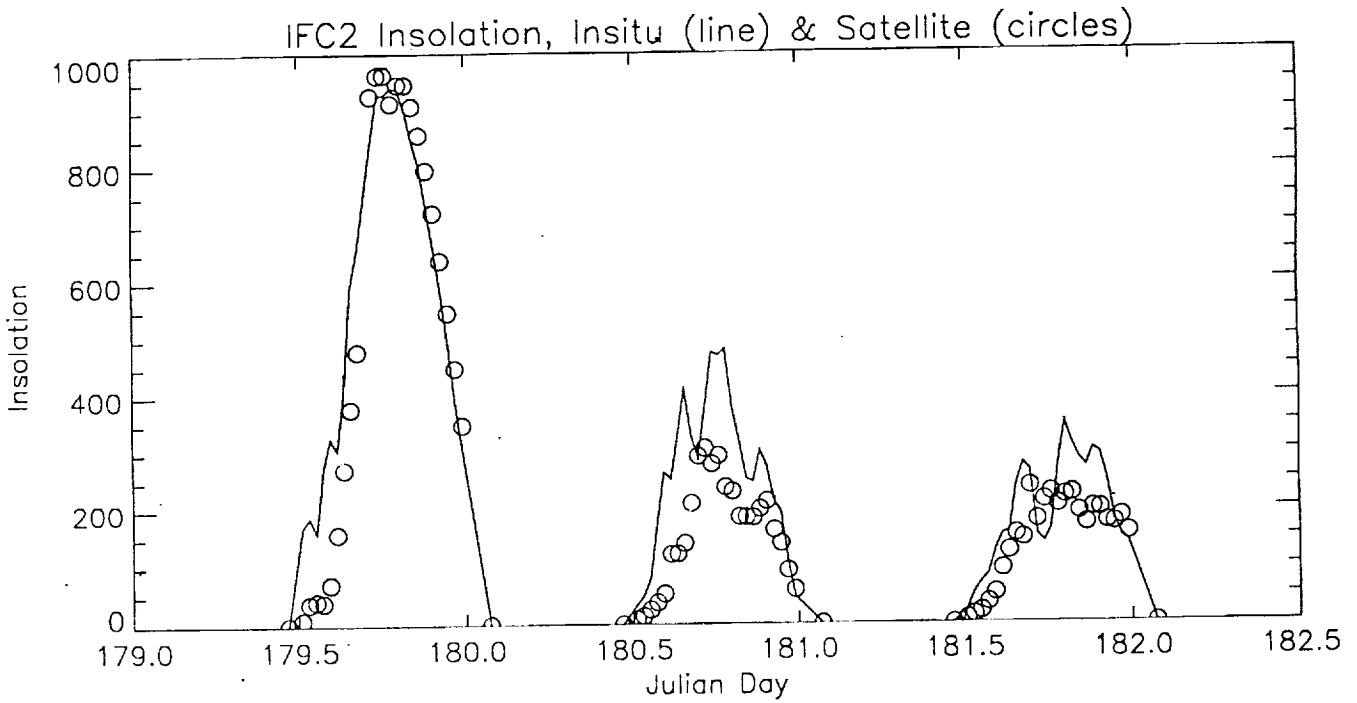
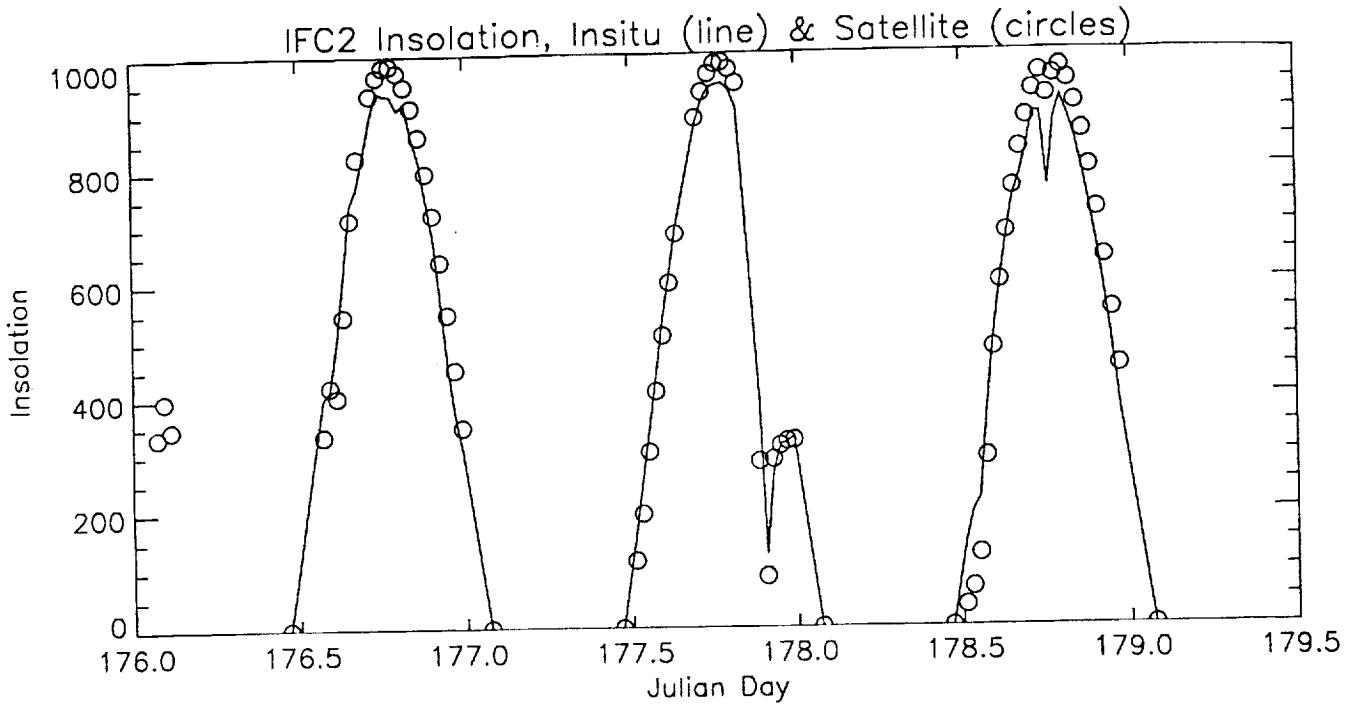


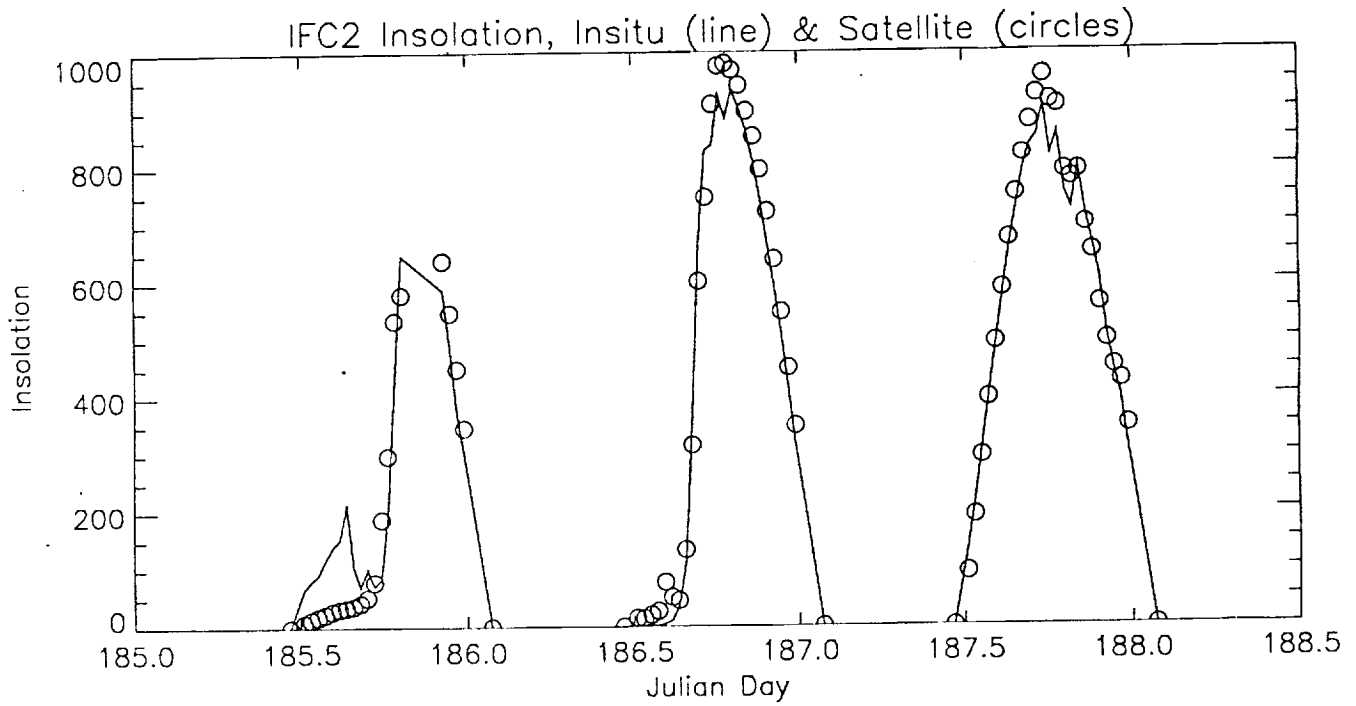
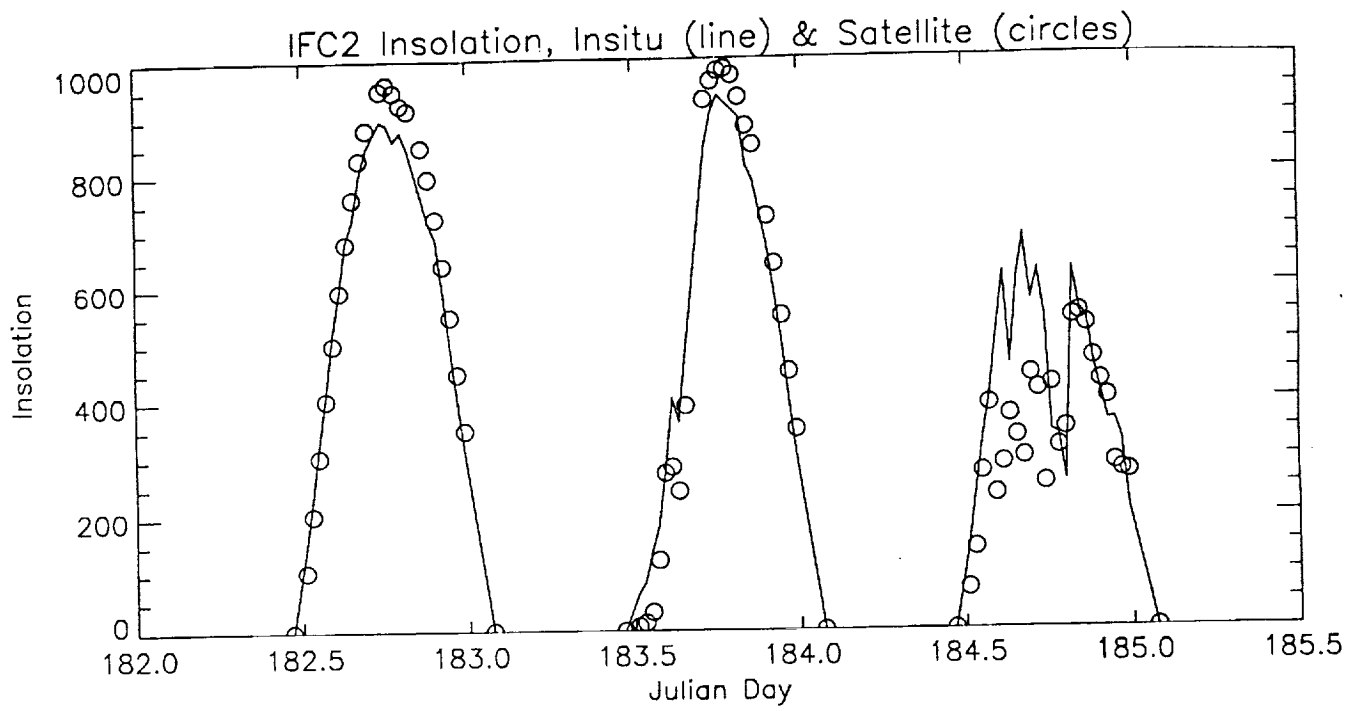
IFC1 Insolation, Insitu (line) & Satellite (circles)

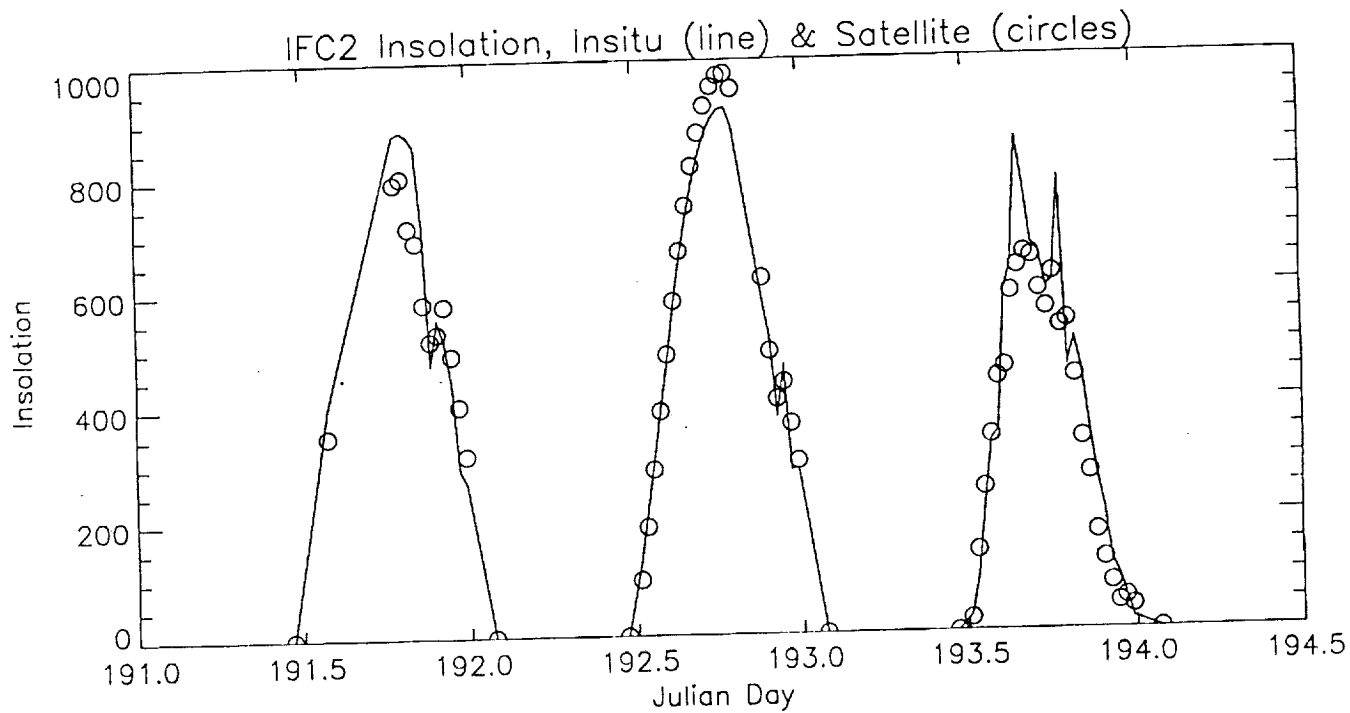
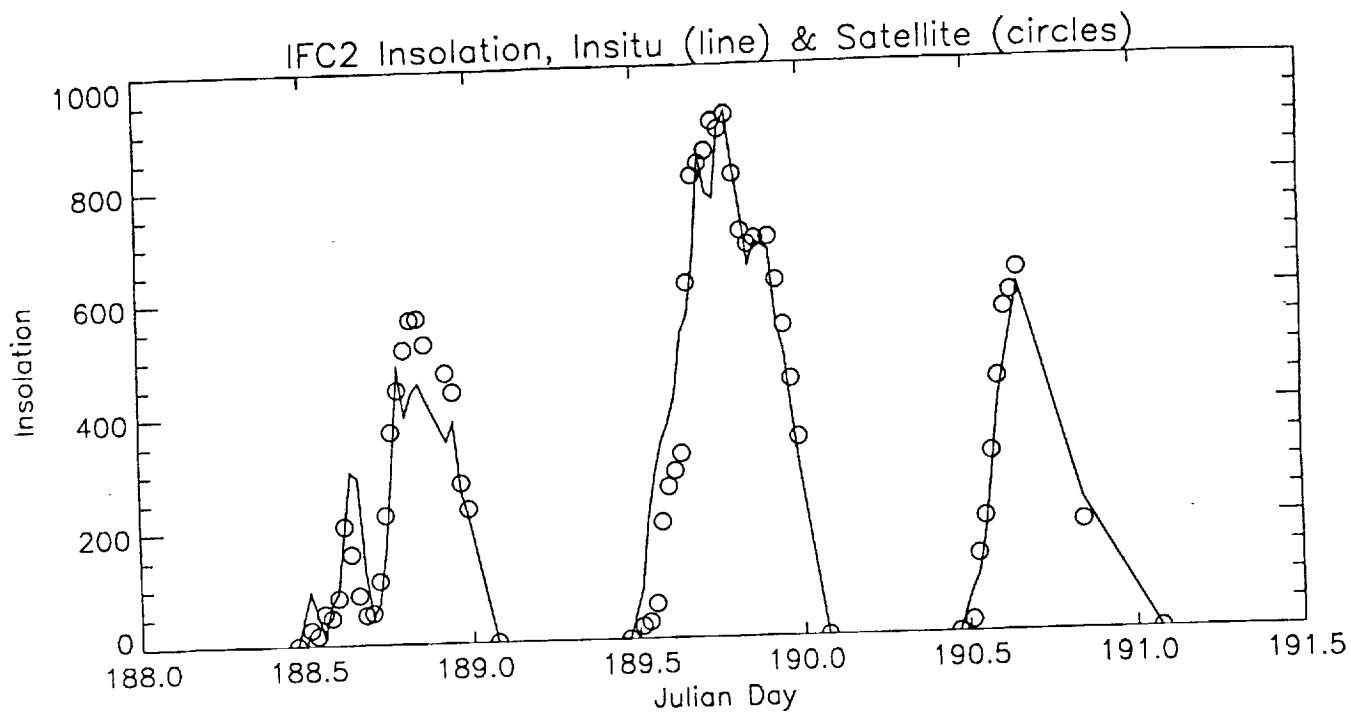




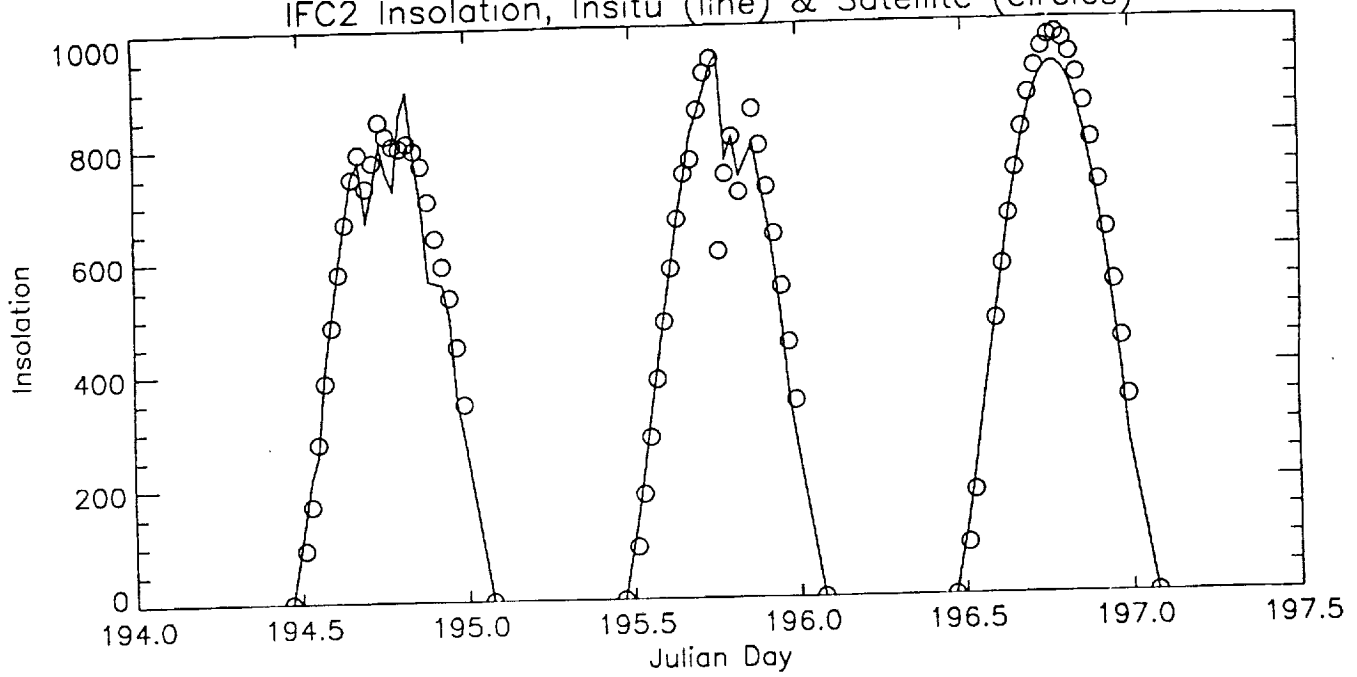
NEW

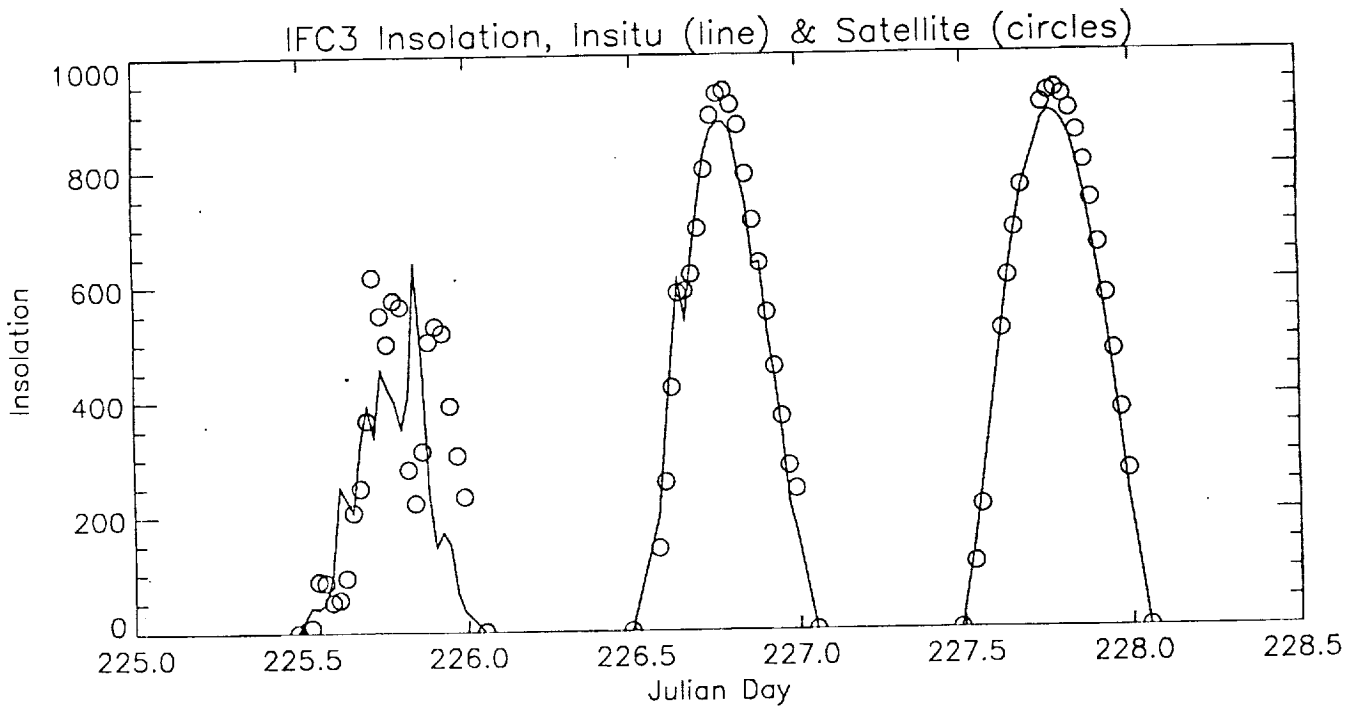
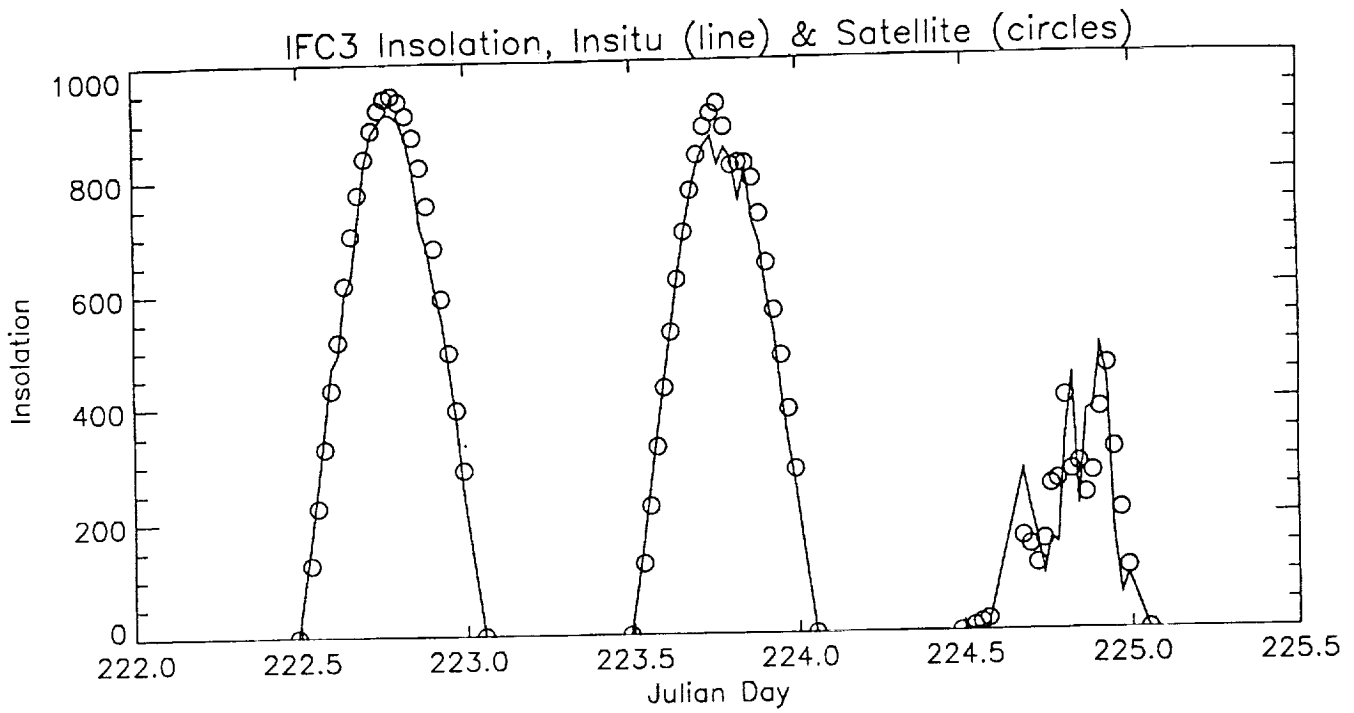




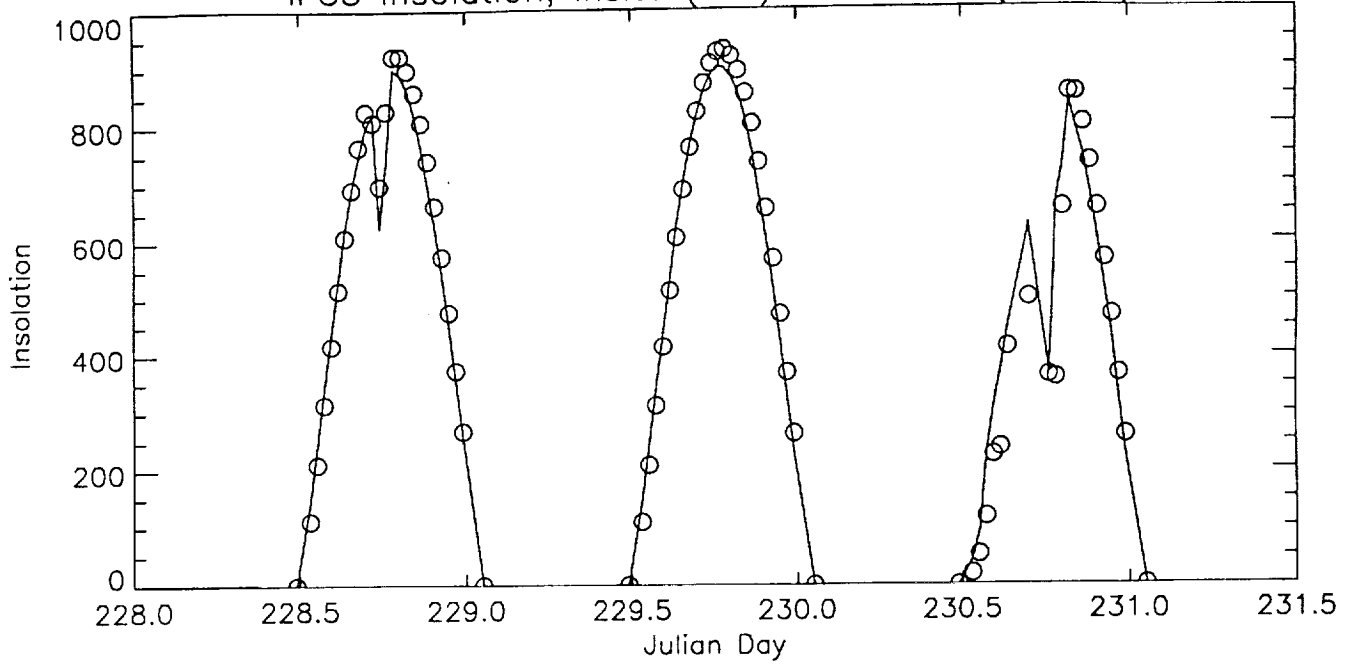


IFC2 Insolation, Insitu (line) & Satellite (circles)

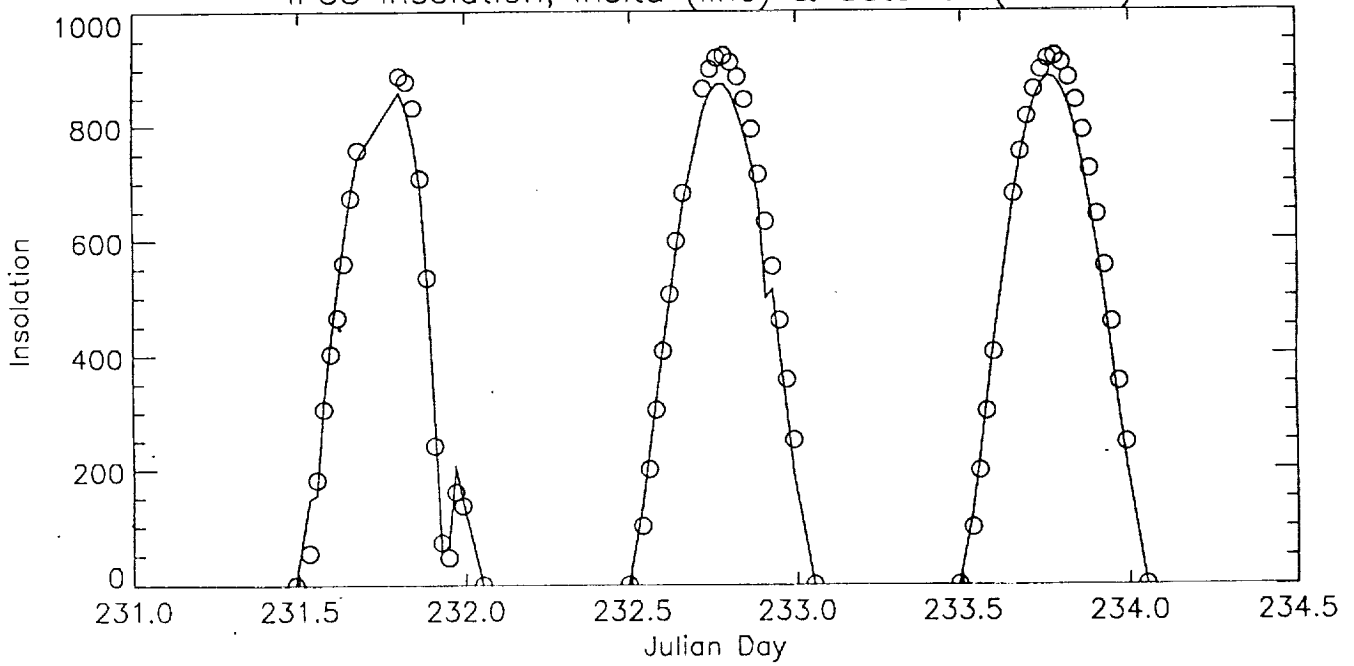


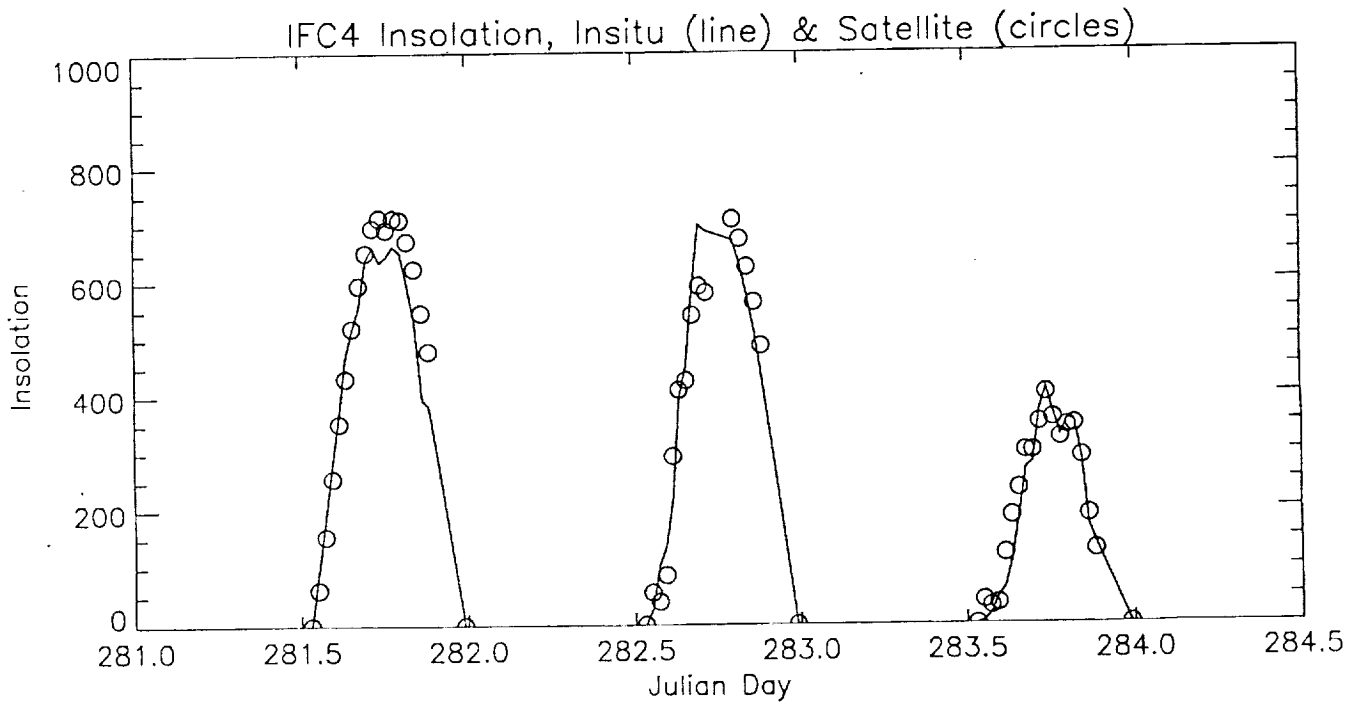
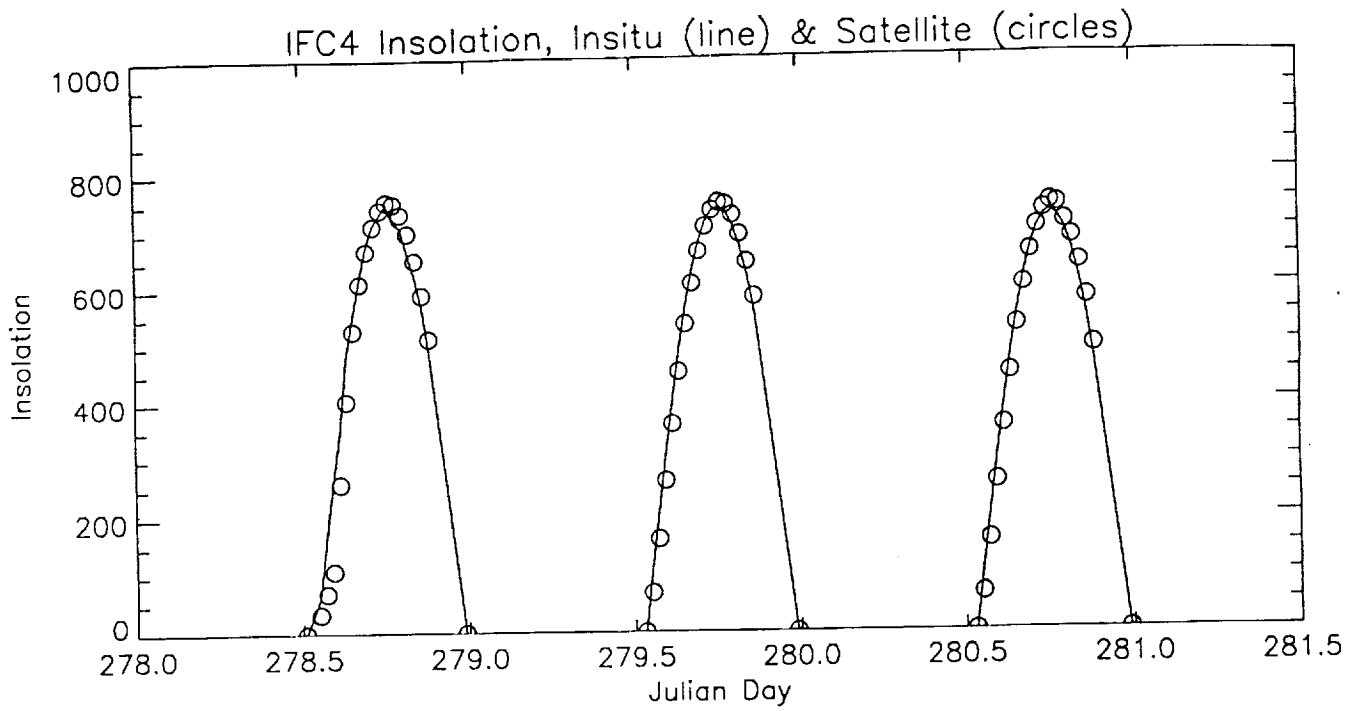


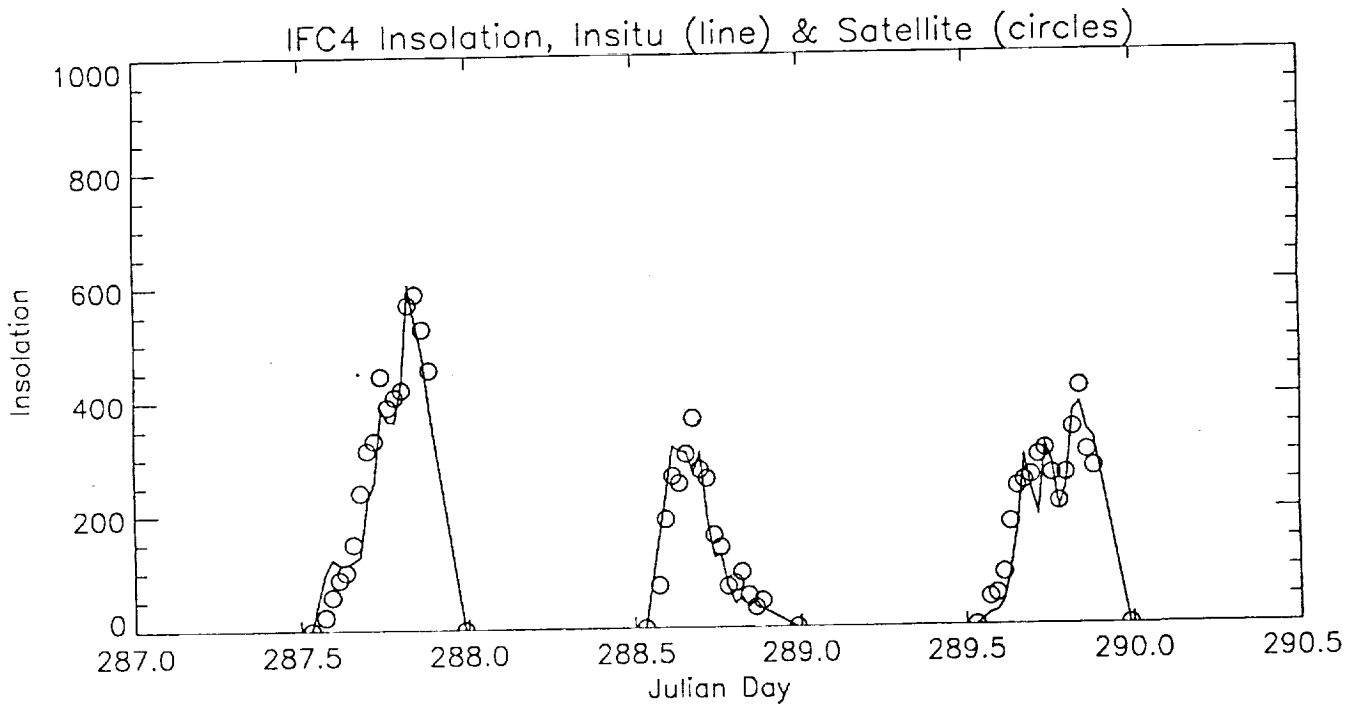
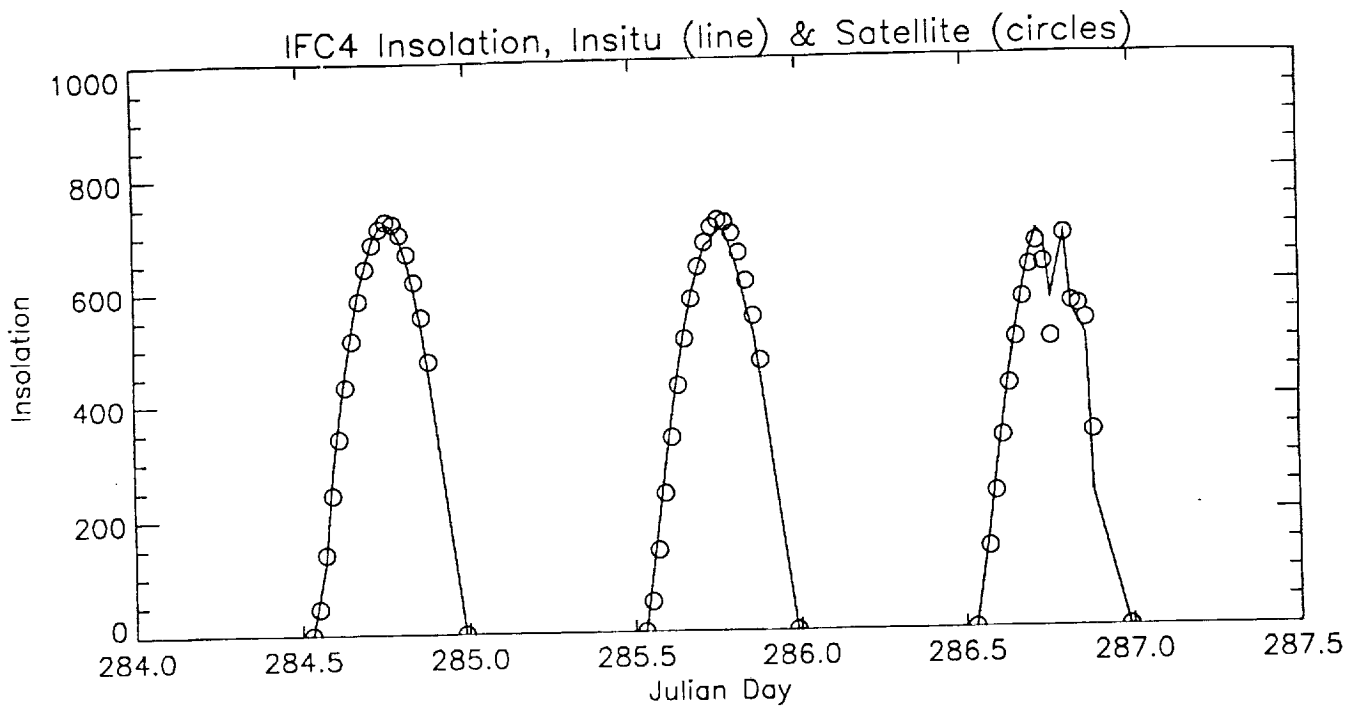
IFC3 Insolation, Insitu (line) & Satellite (circles)

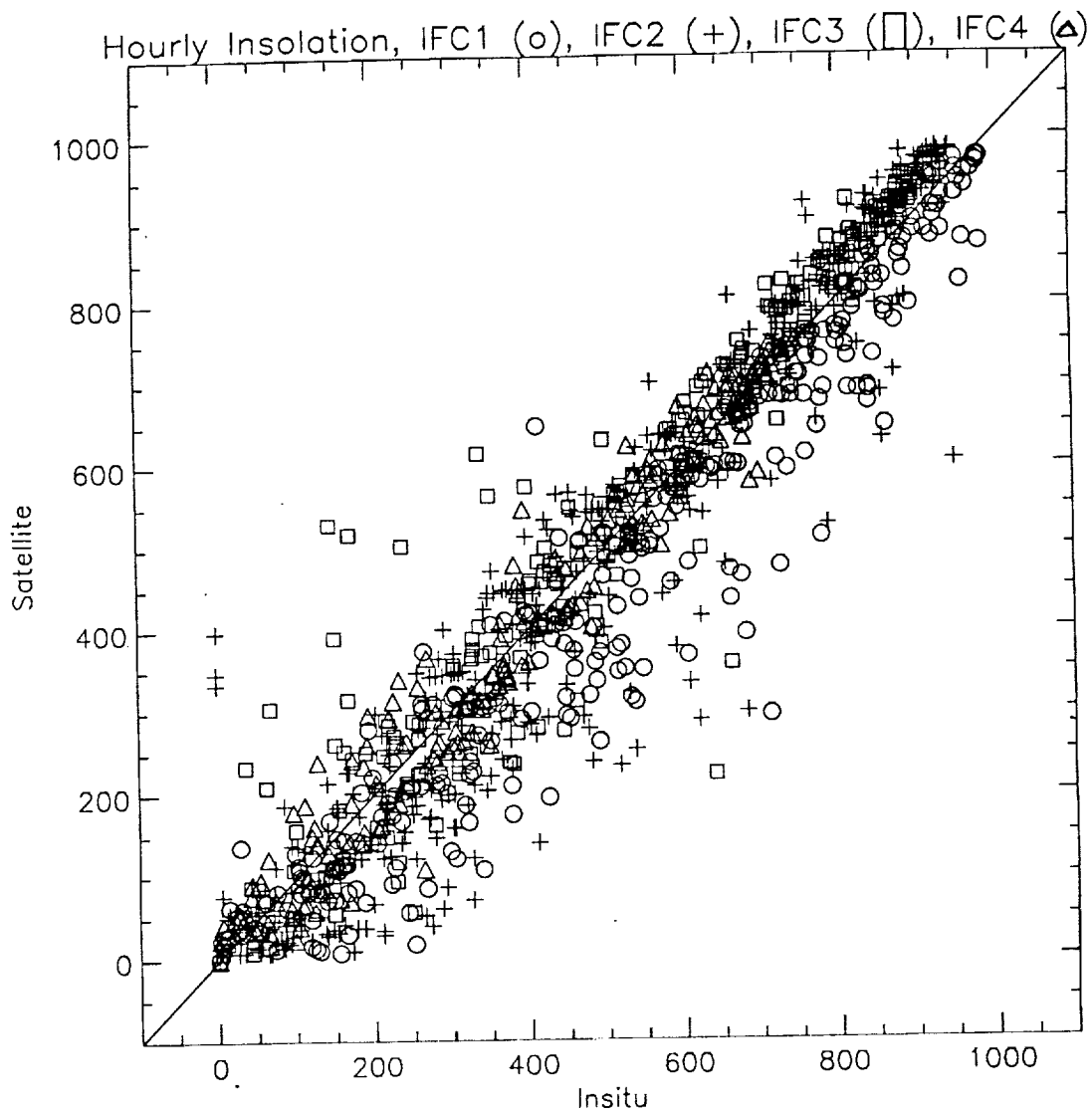


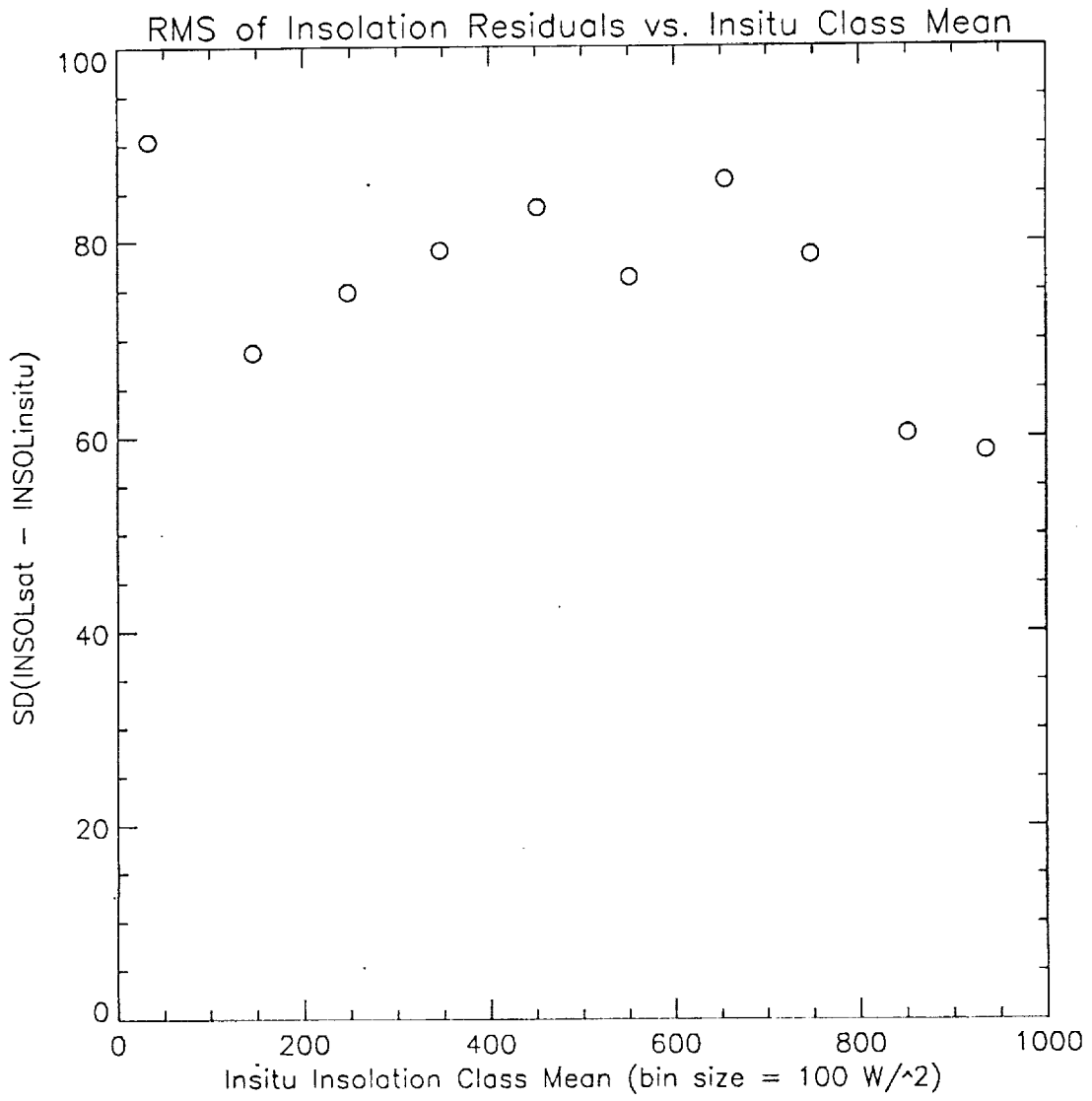
IFC3 Insolation, Insitu (line) & Satellite (circles)



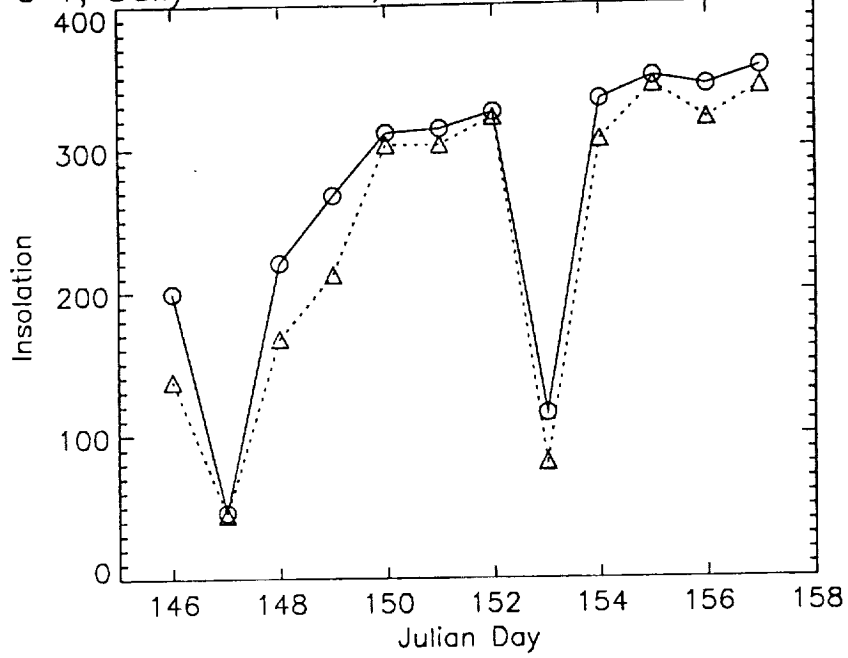




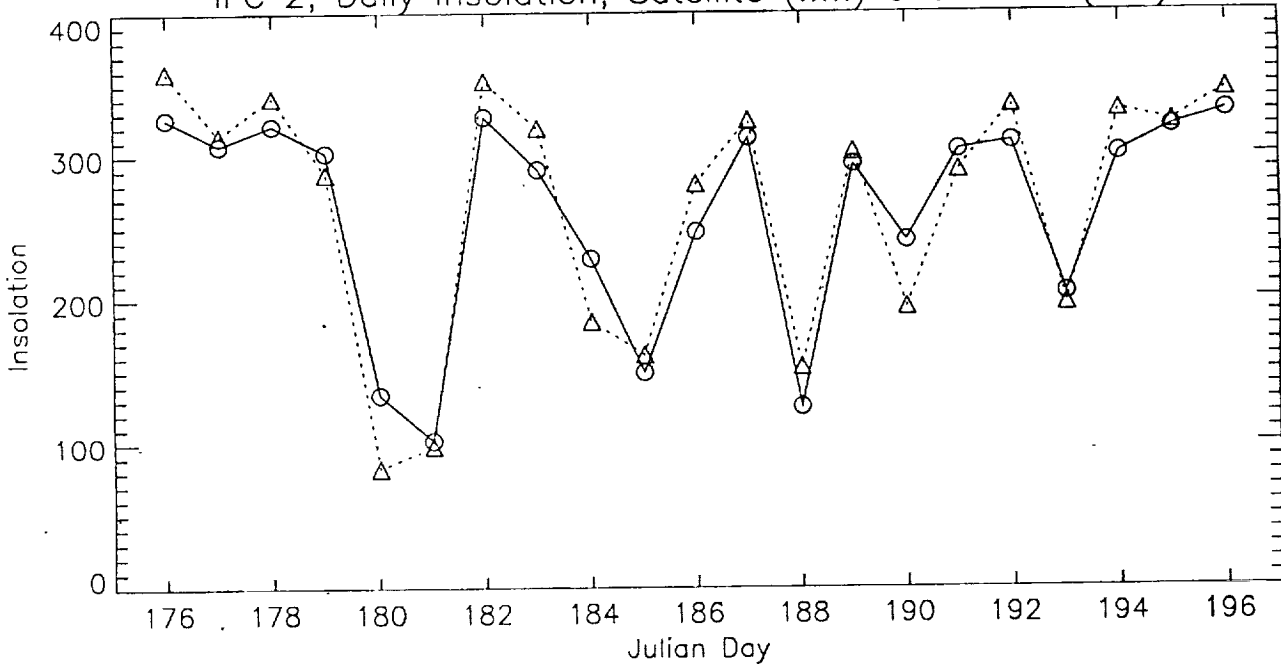




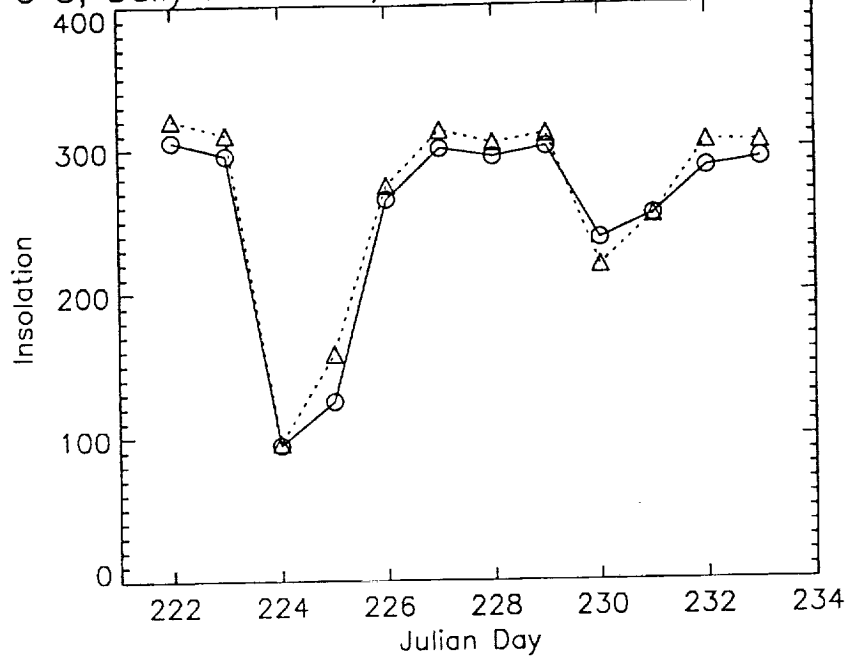
IFC 1, Daily Insolation, Satellite (.....) and Insitu (—)



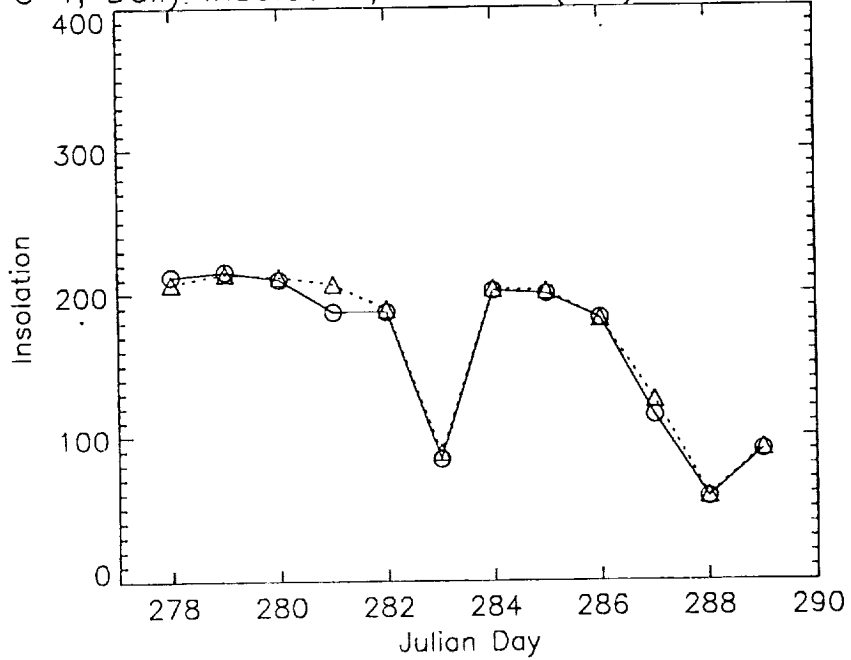
IFC 2, Daily Insolation, Satellite (.....) and Insitu (—)

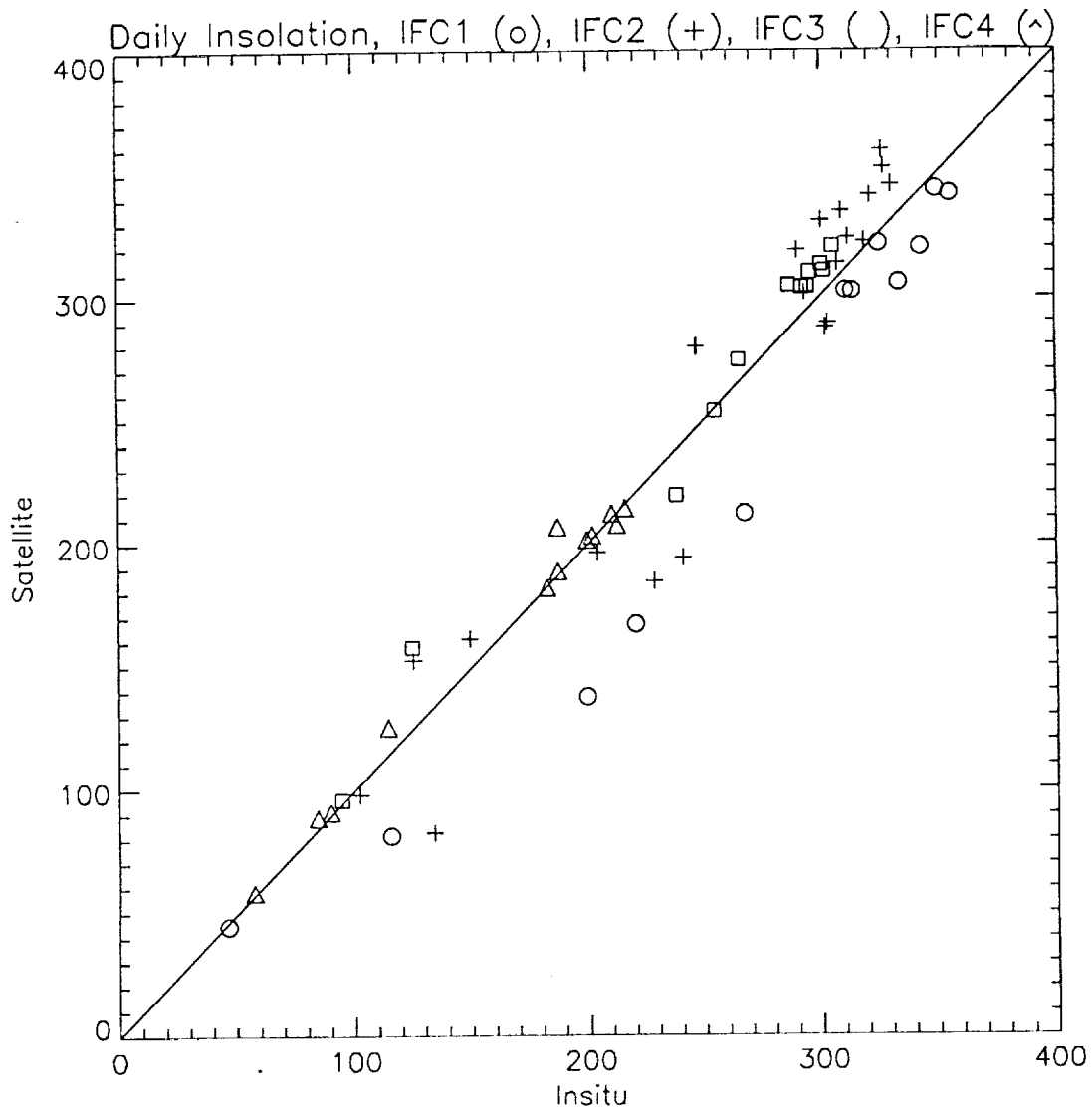


IFC 3, Daily Insolation, Satellite (.....) and Insitu (—)



IFC 4, Daily Insolation, Satellite (.....) and Insitu (—)







N94-10955

52-43
167949
P-28

Appendix 5

ESTIMATING PHOTOSYNTHETICALLY AVAILABLE RADIATION (PAR)
AT THE EARTH'S SURFACE FROM SATELLITE OBSERVATIONS

R. Frouin

Rem. Sens. Environ., submitted, 1993

Estimating Photosynthetically Available Radiation (PAR) at the Earth's Surface from Satellite Observations

Robert Frouin

Scripps Institution of Oceanography

La Jolla, California 92093-0221

Abstract

Current satellite algorithms to estimate photosynthetically available radiation (PAR) at the earth's surface are reviewed. PAR is deduced either from an insolation estimate or obtained directly from top-of-atmosphere solar radiances. The characteristics of both approaches are contrasted and typical results are presented. The inaccuracies reported, about 10% and 6% on daily and monthly time scales, respectively, are useful to model oceanic and terrestrial primary productivity. At those time scales variability due to clouds in the ratio of PAR and insolation is reduced, making it possible to deduce PAR directly from insolation climatologies (satellite or other) that are currently available or being produced. Improvements, however, are needed in conditions of broken cloudiness and over ice/snow. If not addressed properly, calibration/validation issues may prevent quantitative use of the PAR estimates in studies of climatic change. The prospects are good for an accurate, long-term climatology of PAR over the globe.

Introduction

Solar radiation reaching the earth's surface in the wavelength range 0.35-0.7 μm is used by aquatic and terrestrial plants in photosynthesis. Called photosynthetically available radiation (PAR), it governs primary production, the rate of carbon fixed by the plants. Knowing the geographical location and temporal variability of the fixed carbon and its forms of release is important in

assessing the climatic impact of anthropogenic changes such as the destruction of major vegetation systems or the increase in atmospheric carbon dioxide. PAR is defined by

$$\text{PAR}(\text{Wm}^{-2}) = \int_{0.35}^{0.7} I(\lambda) d\lambda \quad (1)$$

where $I(\lambda)$ is the downward spectral irradiance at wavelength λ . Since photosystem processes are quantum reactions, it is useful to consider the equation

$$\text{PAR}(\text{quanta m}^{-2}\text{s}^{-1}) = \frac{1}{hc} \int_{0.35}^{0.7} \lambda I(\lambda) d\lambda \quad (2)$$

where h is Planck's constant and c is the velocity of light in vacuum. Eqs. (1) and (2) indicate that PAR depends on the spectral interval considered which, for operational constraints, may sometimes differ from 0.35-0.7 μm .

Fig. 1 shows how primary production varies as a function of PAR over land (Fig. 1a) and ocean (Fig. 1b). The land case corresponds to typical, live, horizontal leaves (Sellers, 1985, Fig. 13a) and the ocean case to a 20°C, homogeneous water body (calculations were performed with the model of Morel, 1988). Over land, primary production increases rather linearly with PAR, the slope of variation depending on leaf area index (higher slope as leaf area index increases). The relationship, however, is affected little by leaf area index for leaf area indices above 4. Over the ocean, by contrast, the effect of PAR is highly non-linear in the range of PAR values generally encountered. As PAR increases, primary production becomes quickly insensitive to PAR. Saturation occurs at PAR values as low as 200 Wm^{-2} when phytoplankton concentration is as high as 1mgm^{-3} . Unlike over land, where primary production becomes independent of leaf area index at high values of the index, primary production over the ocean increases substantially even when phytoplankton concentration is high.

Fig. 1 provides some insight about the accuracy requirements for PAR. Owing to non-linearities in the relationship between primary production and PAR, the error permitted on PAR to achieve a reasonable 10% accuracy on primary production will depend on PAR as well as the biomass level. In the PAR region for which primary production can be considered directly proportional to PAR (i.e., 0-100 Wm^{-2} over land and 0-50 Wm^{-2} over the ocean), the 10% accuracy on primary production translates equally into a 10% accuracy on PAR, but 20% and 35% accuracies will be sufficient over land and ocean respectively, when PAR is above 300 Wm^{-2} . Thus, a better relative accuracy on PAR is required at low PAR values, which occur either at low solar zenith angles or in the presence of clouds; under those conditions, unfortunately, satellite algorithms are less accurate. In view of available primary production models, however, the accuracy requirements on PAR may be relaxed. The models generally incorporate the fact that the growth rate of many plants is proportional to the rate of radiant solar energy absorption by chlorophyll pigments, but this rate (absorbed PAR) and the efficiency factors (functions of plant type, environmental conditions) are difficult to estimate with accuracies comparable to those mentioned above for PAR. In other words, useful estimates of primary production may still be obtained with larger errors on PAR.

If we are to understand truly the interactions between the biosphere and the atmosphere and their effects on climate, we need to know the geographic distribution and temporal variability of primary production and, thus, PAR over the globe. Until recently, our information was based on surface pyranometer networks (essentially over land) and a few PAR sensors deployed during research experiments. The networks are clearly insufficient for global change studies; the oceans and polar regions, in particular, are virtually not sampled, and long-term time series (from well-maintained, regularly-calibrated sensors) are only existent at a few locations. Furthermore, pyranometers measure insolation, or the solar radiation incident in the spectral range 0.4-4 μm , and the relationship between PAR and insolation depends on atmospheric conditions and radiation geometry (e.g., Baker and Frouin, 1987; Pinker and Laszlo, 1992). Clouds, which do not absorb at PAR wavelengths but do absorb substantially in the near-infrared, increase the ratio of PAR and insolation. Data from the pyranometer networks can be complemented by estimates based on empirical formulas and cloud observations made routinely at meteorological stations (e.g., cloud cover, cloud

type). The formulas, unfortunately, have been established locally and are therefore difficult to apply confidently over large areas. Moreover, the dataset is uneven and too often of questionable quality. Because of these limitations, we do not yet have a clear picture of PAR's modes of variability over the globe. However the situation is being changed with existing earth-observing satellites, which provide regular coverage of the earth and observations of the basic cloud properties governing PAR variability.

Satellite Algorithms

While numerous studies have been devoted to estimating insolation from satellite data (e.g., Tarpley, 1979; Gautier et al., 1980; Möser and Rashke, 1984; Pinker and Ewing, 1985; Dedieu et al., 1987; Darnell et al., 1988), only a few satellite-based methods have been proposed for PAR, including the methods of Frouin and Gautier (1990), Eck and Dye (1991), and Pinker and Laszlo (1992). Part of the reason is that for many applications involving small space and time scales PAR can be measured directly. Furthermore, it has often proven satisfactory to take PAR as a more or less constant fraction of insolation. Deducing PAR from insolation, in fact, is the basis of Pinker and Laszlo's (1992) method, which can be qualified as indirect (requires an insolation estimate). Noting that meteorological satellites (except METEOSAT) carry instruments that measure in spectral channels resembling more the PAR wavelength range than the entire solar spectrum, Frouin and Gautier (1990) use the satellite radiances directly. Uncertainties in insolation are not propagated in that case, and the modeling of cloud effects is simplified (no narrow-band to broad-band transformation is necessary, and cloud absorption vanishes in the equations). This method, also used by Eck and Dye (1991), can be qualified as direct (does not require an insolation estimate). In what follows, we contrast the salient features of the indirect and direct methods, and we present typical results.

a Indirect approach

In Pinker and Laszlo's (1992) method, insolation (estimated using the model of Pinker and Ewing, 1985) is converted into PAR using a relationship established theoretically. This relationship depends on atmospheric conditions, which need to be specified. Under clear skies, the ratio of PAR to insolation varies little

around 0.48, except at high solar zenith angles or extreme (low as well as high) water vapor amounts (Fig. 2), and the effect of aerosol turbidity is only significant when horizontal visibility is less than 10km. This suggests that the ratio of PAR to insolation can be considered constant to a good degree of approximation under clear skies. The situation is quite different under cloudy skies. Cloud optical thickness substantially changes the ratio of PAR and insolation, which can vary by more than 50% at low solar zenith angles (Fig. 3). This variability in the PAR-to-insolation ratio is corroborated by in-situ measurements (Fig. 4). Pinker and Laszlo's (1992) procedure is to therefore apply a variable conversion factor to insolation estimates. This factor depends on cloud optical thickness and fractional amount, parameters derived from the satellite measurements. Applying this method to hourly ISCCP C1 data at 250 km resolution, Pinker and Laszlo (1992) have produced the first global map of monthly PAR, effectively demonstrating that global satellite datasets produced within the frame of ISCCP will soon result in a global, long-term climatology of PAR. Owing to non-linearity, conversion factors are applied before averaging instantaneous insolation estimates over daily and longer time scales. It may be possible to apply conversion factors to daily or monthly insolation estimates without significant loss of accuracy. Fig. 5, established from surface data collected during the First ISLSCP Field Experiment (FIFE), shows that the PAR fraction of daily insolation remains fairly constant regardless of cloud conditions. The same finding was reported by Howell et al. (1983) and Rao (1984) on a monthly time scale. At those time scales the PAR fraction variability due to clouds is reduced because it strongly depends on sun zenith angle (Fig. 4). It may, therefore, prove useful to deduce PAR directly from the various insolation climatologies (satellite or other) currently available or being produced at daily or longer time scales (e.g., Bishop and Rossow, 1991). Fig. 6 shows a typical example obtained with METEOSAT data.

b Direct approach

Frouin and Gautier's (1990) method is based on the formalism developed by Gautier et al. (1980) for insolation, that only requires slight modifications (in fact, simplifications) to be applicable to PAR. Cloud absorption vanishes in the cloudy sky model equations (clouds do not absorb at PAR wavelengths), and the clear sky model coefficients represent the PAR spectral interval instead of the total

solar spectrum. Cloud albedo, the governing cloud parameter, is computed as in Gautier et al. (1980) from geostationary satellite observations in the visible and near-infrared. Since the solar channels of geostationary satellite instruments (except the METEOSAT radiometer) mostly capture radiation in the visible no narrow-band to broad-band conversion of cloud albedo is necessary. Because of these simplifications in the radiative transfer modeling, we expect, at least in principle, more accurate results for PAR than for insolation. Furthermore, by estimating PAR directly from the satellite radiances, uncertainties due to errors on insolation estimates and on the ratio of PAR and insolation, which are inherent to Pinker and Laszlo's (1992) method, are avoided. Fig. 7 shows, for selected days during the First ISLSCP Field Experiment (FIFE), the diurnal variation of measured PAR at the study site (Konza prairie, Kansas) and the corresponding satellite estimates at particular times during the day. In the figure, the in-situ values are half-hourly averages and the satellite estimates are spatial averages over the FIFE area (15x15km). Julian days 222, 223, 226, and 227 are mostly clear, whereas days 224 and 225 are cloudy. In general, the satellite estimates compare well with the measured values; they describe the diurnal cycle properly. The larger discrepancy observed during days 225 and 226 may be linked to spatial cloud variability, which is not accounted for in the modeling (see in the next section the discussion about effects of cloud heterogeneity). For daily averages, Fig. 8 shows the temporal variation of PAR at the site during intensive field campaigns 2 and 3. Satellite estimates correspond to measurements to within 10-15 Wm^{-2} (about 10%), and more than 85% of the observed variance is explained. These comparisons, although performed for a single geographical location, are strongly indicative of the method's ability to quantify PAR variability on daily or longer time scales.

Instead of using radiances in the visible and near-infrared, Eck and Dye (1991) use radiances (or, equivalently, reflectances) in the ultraviolet and test their method with Total Ozone Mapping Spectrometer (TOMS) data. Noting that cloud reflectivity is constant across ultraviolet and PAR wavelengths and that clouds do not absorb radiation at ultraviolet and PAR wavelengths, they parameterize the effect of clouds on PAR as a simple, linear function of TOMS ultraviolet reflectance. Cloud-screening is achieved by applying a threshold technique, and the authors argue that using data in the ultraviolet makes it easier to discriminate clouds from high-albedo background surfaces, except for ice and

snow. The cloud-screening, however, may not be efficient because the TOMS data are in the form of monthly, 500x500km averages, and there is no way of assessing from the TOMS data alone whether the 500x500 km areas are partially contaminated by clouds or not. Furthermore, the radiative transfer modeling is rather crude (e.g., no correction is performed for molecular scattering above the clouds). Nevertheless, the effects do not appear significant on a monthly time scale (individual errors somewhat cancel out), as comparisons with surface measurements, which reveal less than 6% relative differences, demonstrate (Fig. 9).

Issues

The satellite algorithms so far proposed to monitor the variability of PAR over the globe utilize data from instruments (e.g., Advanced Very High Resolution Radiometer, Visible and Infrared Spin-Scan Radiometer) that are generally not calibrated after launch. These instruments have been shown to exhibit significant, even large changes in sensitivity. The resulting errors on PAR can be important, as Fig. 10 illustrates. For a cloud containing 100gm^{-2} of liquid water at 40°N , for instance, a 10% loss of sensitivity translates into errors of up to 50Wm^{-2} on monthly averages. Degradation of that amplitude is quite common, as many studies have demonstrated (e.g., Frouin and Gautier, 1987; Staylor, 1990; Whitlock et al., 1990; Brest and Rossow, 1992). Therefore, unless a check-of-calibration is maintained on a regular schedule during the lifetime of the satellites, and instruments from various satellites cross-calibrated properly, it will be difficult to extract a meaningful signal for climate studies from observed changes.

Another issue deals with cloud spatial heterogeneity. The satellite estimates are generally less accurate in conditions of partial (broken) cloudiness (see for instance the results for days 224 and 225 in Fig. 6). This is not surprising as clouds are considered plane-parallel in the modeling, and top-of-atmosphere radiance is often assumed to be isotropic. Drastic assumptions of that sort are necessary, however, to close the system of equations and reduce the problem to one of estimating PAR from a single top-of-atmosphere radiance measurement. The drawback is that large errors on the PAR estimates may be introduced for some

situations. Broken clouds, in particular, can significantly affect the spatial distribution of PAR, as the Monte Carlo simulations of Fig. 11 illustrate. For the cloud field considered, namely a regular network of cylinder clouds characterized by a radius of 0.5 km, a geometrical thickness of 0.2 km, an optical thickness of 12, and a distance between clouds of 2.5 km (typical conditions observed during the FIFE experiment on August 9, 1989), the cloud transmittance (flux transmittance) exhibits strong spatial variance, depending on whether the sun disk is obscured by the clouds or not, and reaches over 110% in areas directly illuminated by the sun. In other words, more sunlight that would be observed in clear sky conditions reaches the surface in those areas. This effect, observed by many investigators on pyranometer traces, cannot be reproduced by assuming plane-parallel clouds. Furthermore, depending on the cloud field, it may not cancel out on daily or monthly averages.

To assess the accuracy of the PAR estimates, one needs to compare them to other data, particularly surface measurements. The networks of well-calibrated PAR sensors, unfortunately, are generally inadequate, even over the continents. In fact, the networks of surface radiation instruments have been designed to monitor insolation not PAR –and deducing PAR from insolation is subject to uncertainty (see above). Furthermore, the satellite estimates are instantaneous whereas the surface measurements are local, making it difficult to compare the two types of data. When the method utilizes coarse resolution pixels (see Eck and Dye, 1991), validation by surface measurements becomes very difficult. One alternative is to compare low resolution PAR estimates to estimates obtained from higher resolution data using a validated satellite method; but the procedure is far from optimum. It is clear, however, that without proper validation strategy, satellite PAR estimates will not find quantitative use in global change studies of the carbon cycle.

Summary and Recommendations

Developing methods for estimating PAR from satellites is a recent activity that has strongly benefited from the work performed on insolation by many investigators. Satellite estimates of insolation can be converted accurately into PAR, which makes it possible to exploit already existing datasets (satellite and

other). From the radiative transfer point of view, the problem of deriving PAR from top-of-atmosphere radiances in the visible is simpler for PAR than insolation because narrow-band to broad-band transformation is not necessary, and cloud absorption does not need to be parameterized (clouds do not absorb in the visible). In situations of partial cloudiness for which plane-parallel theory does not apply, the problem is as complex as for insolation. Although limited comparisons have been made, an inaccuracy smaller than 10% on a monthly time scale appears feasible by the methods reviewed. In view of the existing models of primary productivity, which involve terms other than PAR more difficult to estimate, a 10% inaccuracy is more than sufficient and should allow a correct description of the month-to-month PAR variability and reveal large scale seasonal and interannual phenomena.

Many of the recommendations of previous workshops on surface radiation budget (e.g., Suttles and Ohring, 1986; Sellers et al., 1990) are in order for PAR. Some effort particularly should be put to rigorously specifying the required accuracy on PAR. As suggested by Sellers et al. (1990), sensitivity studies are necessary, but it is unrealistic to expect that they will provide a complete, universal answer; the space and time scales of geophysical phenomena influenced by PAR are too varied. Whatever the phenomenon under study it will always be safe to define the required accuracy so that the variability of PAR over the phenomenon's characteristic space and time scales, generally observable, is described properly.

Regarding the calibration issue, a lot of progress has been made during the last 2-3 years to monitor sensor degradation of meteorological satellites, those used for PAR, after launch (e.g., within the frame of ISCCP, NOAA and GOES pathfinder activities). Despite the numerous studies a consensus sometimes has been difficult to reach on the calibration coefficients to use for some sensors. This underscores the need for instruments that possess on-board calibration capabilities and for detailed, realistic calibration plans prior to launch. In view of the potential of radiometers carried by meteorological satellites for PAR monitoring, it appears in order to equip future versions with a proper calibrator for their solar channels. In the long run, the strategy might prove more economical and rewarding, since costly aircraft calibrations would be downsized,

and scientists would be relieved from tedious, time-consuming calibration tasks they too often have to perform themselves at the expense of other work.

Regarding validation activities, care should be exercised when satellite-derived estimates are compared with in-situ measurements. In general, the two quantities are not the same. On the one hand, satellite-derived values are instantaneous and averaged spatially; on the other hand, surface measurements are local and averaged temporally. The space and time scales at which the comparisons should be made need therefore to be selected rationally, and instrument networks designed accordingly. Using a single instrument is not optimum; dense networks are more appropriate. Such networks were installed during various ISLSCP experiments but covered a limited time period. They should be operated continuously at sites representing world-wide conditions and include measurements of other parameters (e.g., cloud properties) to test individual parameterizations in the models. PAR sensors, which are inexpensive, should also be deployed to complement the networks of pyranometers already in place, at least in representative areas of the globe. Effort should also be made to create a database of PAR measurements from various research experiments and make it available for validation studies. Comparisons of algorithms such as those for insolation should be made (e.g., Whitlock et al., 1990), but with the purpose of understanding the advantages and drawbacks of each algorithm instead of selecting one.

One of the major limitations of the methods is their inability to provide reasonable estimates when plane-parallel theory is not applicable (case of broken clouds, liquid water spatial heterogeneity). Efforts to improve the techniques should therefore focus on situations of cloud heterogeneity. One approach is to perform radiative transfer calculations for realistic cloud fields, determine the cloud parameters that govern departures to plane-parallel theory, and investigate relationships between the governing cloud parameters and observable cloud characteristics (texture, moments, etc.). If this approach proves suitable, current strategies to create long-term, large-scale satellite datasets might have to be reviewed to include those cloud characteristics.

Two other aspects of the methods should also be addressed, namely the presence of snow or ice at the surface and diurnal sampling. Over snow and ice it is not

easy to distinguish clouds, and the methods proposed would likely fail. Efforts should be made to improve the methods in those situations, all the more as the polar oceans cannot be neglected in studies of the global carbon cycle because of their high primary productivity. Regarding diurnal sampling, the success of the satellite methods generally resides in their ability to sample diurnal cloud variability properly. Polar-orbiting satellites do not provide adequate sampling at middle and low latitudes. Statistically obtained correction factors may be used, but they do not offer the solution. The problem may be obviated, however, by complementing data from polar-orbiting and geostationary satellites, as is currently being done to generate ISCCP datasets.

The sensors adapted to PAR monitoring from space are not limited to those used in the algorithms so far proposed. Other instruments, scanners as well as wide-field-of-view radiometers, have not yet been exploited, in particular those of the Earth Radiation Budget Experiment. In fact the current algorithms can be easily modified to become applicable to those sensors. Furthermore, their longevity, careful calibration and characterization, as well as the continuity of the mission well beyond the end of the century (Clouds and Earth's Radiant Energy System, CERES, investigation), make them an ideal tool for studying PAR's inter-annual modes of variability and related questions of climate change. Looking ahead, apart from the future versions of meteorological satellites and the CERES scanner a battery of instruments will be available for PAR monitoring during the Eos era, in particular the MODerate resolution Imaging Spectrometer (MODIS) and the MEdium Resolution Imaging Spectrometer (MERIS). Our prospects are good for an accurate, long-term climatology of PAR over the globe.

Acknowledgments

This work has been supported by the National Aeronautics and Space Administration under grants NAG5-900 and NAGW-1968 and by the California Space Institute. I wish to thank Mamoudou Ba of the California Space Institute for producing the PAR map, John McPherson of the California Space Institute for programming support, Elizabeth Sharp of the California Space Institute and Antarctic Research Center for editing suggestions, Rachel Pinker from the Department of Meteorology of the University of Maryland and Gérard Dedieu of

the Laboratoire d'Etudes et de Recherches en Télédétection spatiale, France, for helpful discussions, and the FIFE information system for technical assistance.

References

Baker, K., and R. Frouin, 1987: Relation between photosynthetically available radiation and total insolation at the ocean surface under clear skies. *Limnol. Oceanogr.*, 32, 1370-1377.

Bishop, J. K., and W. B. Rossow, 1991: Spatial and temporal variability of global surface solar irradiance. *J. Geophys. Res.*, 96, 16839-16858.

Brest, C. L., and Rossow, W. B., 1992: Radiometric calibration and monitoring of NOAA AVHRR data for ISCCP. *Int. J. Rem. Sen.*, 13, 235-273.

Darnell, W. L., W. F. Staylor, S. K. Gupta, and F. M. Denn, 1988: Estimation of surface insolation using sun-synchronous satellite data. *J. Climate*, 1, 820-835.

Dedieu, G., P.-Y. Deschamps, and Y. Kerr, 1987: Satellite estimation of solar irradiance at the surface of the earth and of surface albedo using a physical model applied to Meteosat data. *J. Climate and Appl. Meteor.*, 26, 79-87.

Eck, T. F., and D. G. Dye, 1991: Satellite estimation of incident photosynthetically active radiation using ultraviolet reflectance. *Remote Sen. Environ.*, 38, 135-146.

Frouin, R., and C. Gautier, 1987: Calibration of NOAA-7 AVHRR, GOES-5 and GOES-6 VISSR/VAS solar channels. *Rem. Sen. Environ.*, 22, 73-101.

Frouin, R., and C. Gautier, 1990: Variability of photosynthetically available and total solar irradiance at the surface during FIFE: a satellite description. *Proc. of the Symposium on the first ISLSCP Field Experiment*, Feb. 7-9, 1990, Anaheim, Calif., 98-104. Published by the American Meteorological Society, Boston, Mass.

Gautier, C., Diak, G., and S. Masse, 1980: A simple physical model to estimate incident solar radiation at the surface from GOES satellite data. *J. Appl. Meteor.*, 19, 1005-1012.

Howell, T. A., Meek, D. W., and J. L. Hatfield, 1983: Relationship of photosynthetically active radiation to shortwave radiation in the San Joachim Valley. *Agr. Meteor.*, 28, 157-175.

Morel, A., 1988: Optical modeling of the upper ocean in relation to its biogenous matter content (Case I waters). *J. Geophys. Res.*, 93, 10749-10768.

Möser, W., and E. Raschke, 1984: Incident solar radiation over Europe estimated from Meteosat data. *J. Climate. and Appl. Meteor.*, 23, 166-170.

Pinker, R. T., and J. A. Ewing, 1985: Modeling surface solar radiation: model formulation and validation. *J. Climate and Appl. Meteor.*, 24, 389-401.

Pinker, R. T., and I. Laszlo, 1992: Global distribution of Photosynthetically active radiation as observed from satellites. *J. Climate*, 5, 56-65.

Rao, C. R. N., 1984: Photosynthetically active components of global solar radiation: measurements and model computations. *Arch. Meteor. Geophys. Biokl.*, 34, 353-364.

Sellers, P. J., 1985: Canopy reflectance, photosynthesis, and respiration. *Int. J. Rem. Sen.*, 6, 1335-1372.

Sellers, P. J., S. I. Rasool, and H.-J. Bolle, 1990: A review of satellite data algorithms for studies of the land surface. *Bul. Amer. Meteor. Soc.*, 71, 1429-1447.

Staylor, W. F., 1990: Degradation rates of the AVHRR visible channel for the NOAA6, 7, and 9 spacecraft. *J. Atmos. Ocean. Techn.*, 7, 411-423.

Suttles, J. T., and G. Ohring, 1986: Surface radiation budget for climate applications. *NASA Tech. Memo.* No 1169, 132 pp.

Tarpley, J. D., 1979: Estimating incident solar radiation at the surface from geostationary satellite data. *J. Appl. Meteor.*, 18, 1172-1181.

Whitlock, C. H., W. F. Staylor, G. Smith, R. Levin, R. Frouin, C. Gautier, P. M. Teillet, P. N. Slater, Y. J. Kaufman, B. N., Holben, W. B. Rossow, C. L. Brest, and S. R. Lecroy, 1990: AVHRR and VISSR satellite instrument calibration results for both Cirrus and Marine Stratus IFO periods. *NASA Conf. Proc.*, 3083, 141-145.

Whitlock, C.H., W.F. Staylor, W.L. Darnell, M.D. Chow, G. Dedieu, P.Y. Deschamps, J. Ellis, C. Gautier, R. Frouin, R.T. Pinker, I. Laslo, W.B. Rossow and D. Tarpley, 1990: Comparison of surface radiation budget satellite algorithms for downwelled shortwave irradiance with Wisconsin FIRE/SRB surface-truth data. *Proc. of the 7th Conf. on Atmospheric Radiation*, San Francisco, Jul. 23-27, 1990, Published by the American Meteorological Society, Feb 4-9, 237-242.

Figure Captions

Fig. 1. Primary production as a function of photosynthetically available radiation, PAR. (a) Case of a green canopy with horizontal leaves and a leaf area index ranging from 0.1 to 6 (after Sellers, 1985). (b) Case of a homogeneous, 20°C ocean containing 0.3, 1, 3, and 10 mgm^{-3} of chlorophyll pigments.

Fig. 2. Ratio of photosynthetically available radiation, PAR, and insolation as a function of water vapor amount (top), ozone amount (middle), and aerosol type and visibility (bottom). (After Baker and Frouin, 1987.)

Fig. 3. Ratio of photosynthetically available radiation, PAR, and insolation as a function of cloud optical thickness and sun zenith angle. (After Pinker and Laszlo, 1992.)

Fig. 4. Surface-measured ratio of half-hourly photosynthetically available radiation, PAR, and insolation as a function of satellite-derived instantaneous cloud liquid water content during the First ISLSCP Field Experiment. The ratio varies between 0.25 and 0.75, corroborating theoretical calculations.

Fig. 5. Surface-measured ratio of daily photosynthetically available radiation, PAR, and insolation as a function of satellite-derived daily cloud cover during the First ISLSCP Field Experiment. At this time scale the PAR fraction variability is small, with values ranging between 0.43 and 0.52.

Fig. 6. Monthly photosynthetically available radiation, PAR, derived from METEOSAT data for June 1990. Monthly insolation was first obtained using the method of Dedieu et al. (1987) and PAR was then deduced by taking the ratio of PAR and insolation equal to 0.45.

Fig. 7. Surface-measured and satellite-derived photosynthetically available radiation, PAR, for selected days during the First ISLSCP Field Experiment. Satellite estimates are instantaneous whereas measured values are half-hourly averaged.

Fig. 8. Surface-measured and satellite-derived daily photosynthetically available radiation, PAR, during the second and fourth intensive field campaigns of the First ISLSCP Field Experiment.

Fig. 9. Satellite estimates of monthly photosynthetically available radiation, PAR, versus surface estimates from pyranometer measurements adjusted to PAR. (After Eck and Dye, 1991.)

Fig. 10. Typical error on satellite-derived monthly photosynthetically available radiation, PAR, due to a 10% increase in the calibration gain, g , of the sensor's solar channel. Clouds contain 100gm^{-2} of liquid water, and the clear atmosphere contains 0.3 atm-cm of ozone and aerosols of continental type and optical thickness of 0.22 at 550 nm . Latitude is 39°N . As fractional cloud coverage, N , increases, the error increases in magnitude, reaching -50 Wm^{-2} in June and July.

Fig. 11. Monte Carlo simulations of the spatial distribution of cloud transmittance (in percent) on August 8, 1989 at 13:30 local time over the Konza prairie, Kansas. The clouds are cylindrical of radius 500m , separated by $2,500\text{m}$, and located between $2,000$ and $2,200\text{m}$ (geometrical thickness of 200m). The cloud optical thickness is 12 . When the sun disk is not obscured by clouds, cloud transmittance reaches 113% , indicating that the surface receives more photosynthetically available radiation than in clear sky conditions.

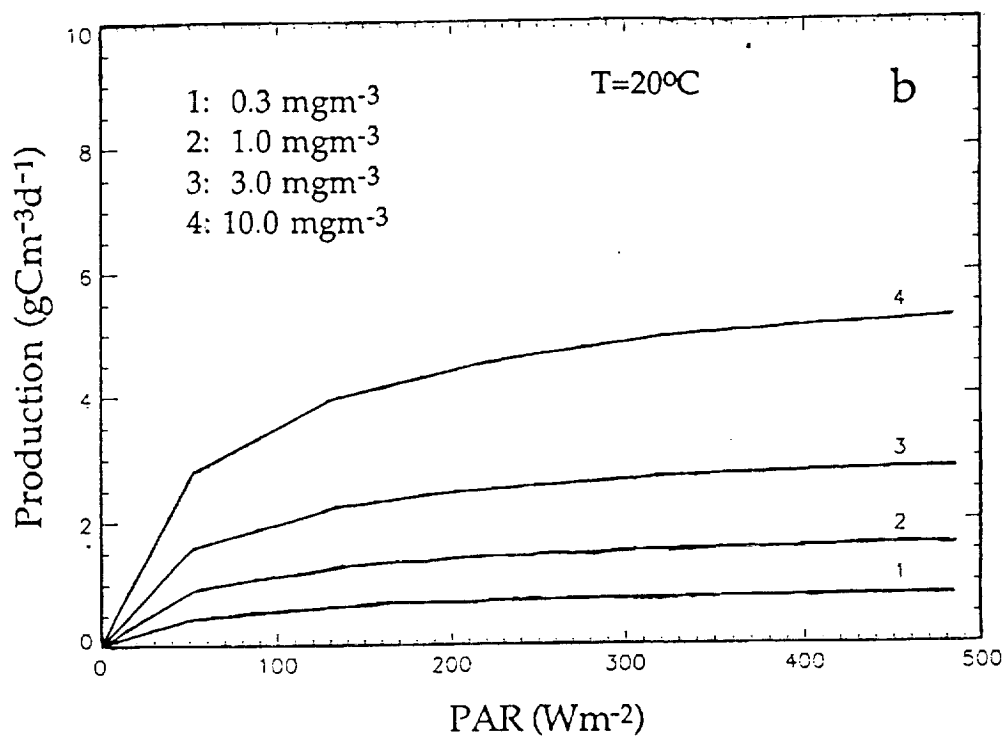
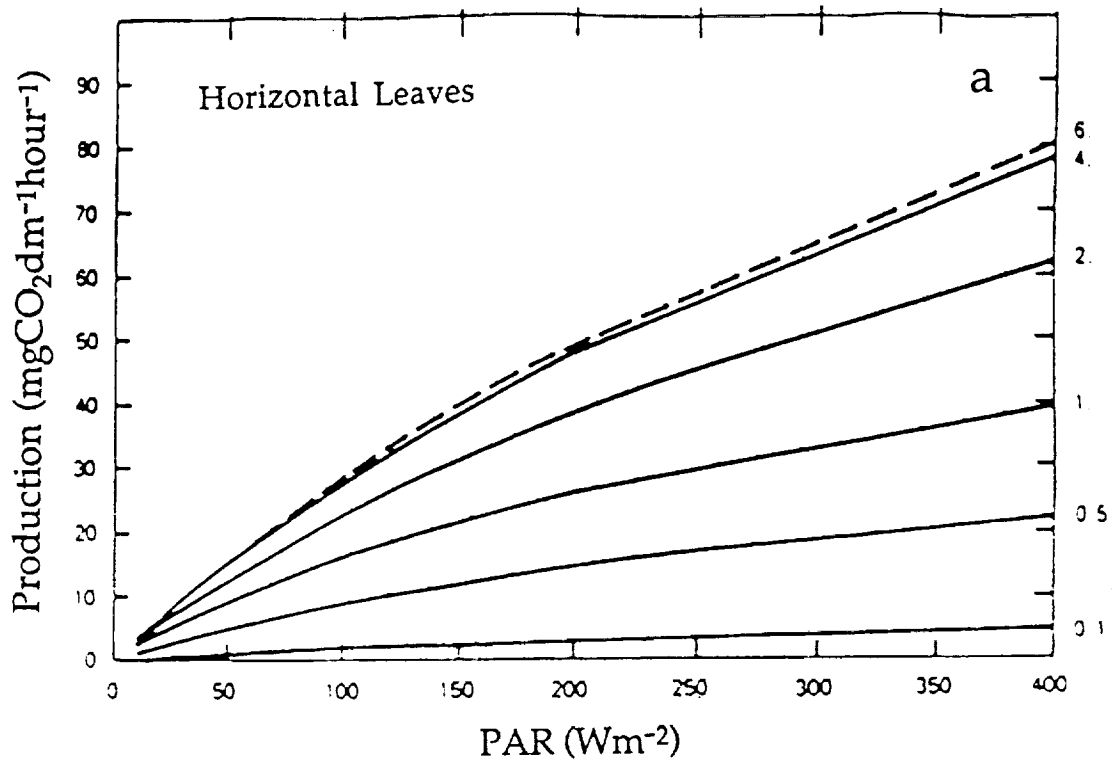


Fig. 1. Primary production as a function of photosynthetically available radiation, PAR. (a) Case of a green canopy with horizontal leaves and a leaf area index ranging from 0.1 to 6 (after Sellers, 1985). (b) Case of a homogeneous, 20°C ocean containing 0.3, 1, 3, and 10 mgm⁻³ of chlorophyll pigments.

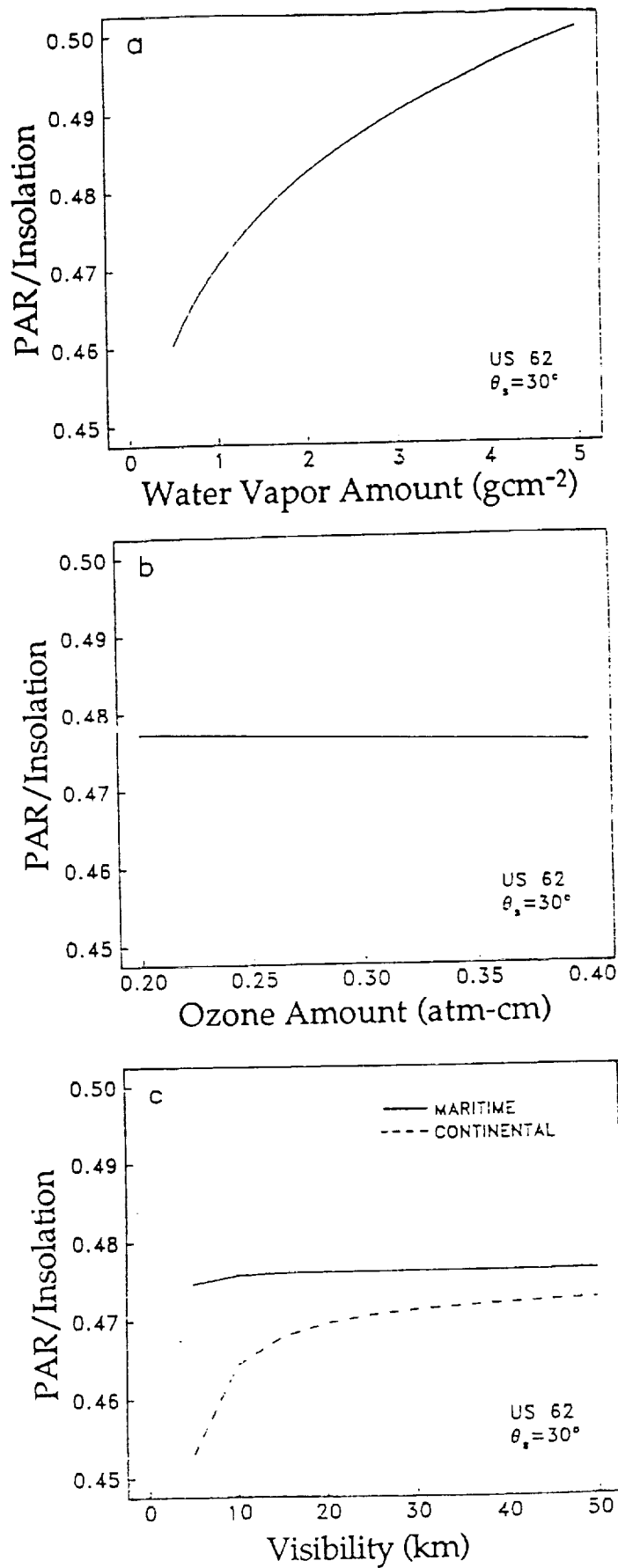


Fig. 2. Ratio of photosynthetically available radiation, PAR, and insolation as a function of water vapor amount (top), ozone amount (middle), and aerosol type and visibility (bottom). (After Baker and Frouin, 1987.)

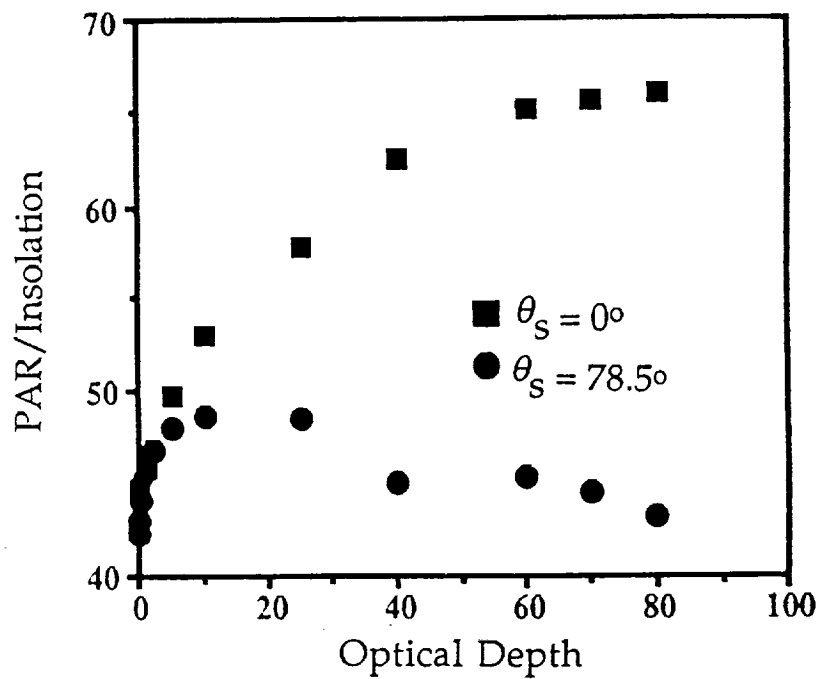


Fig. 3. Ratio of photosynthetically available radiation, PAR, and insolation as a function of cloud optical thickness and sun zenith angle. (After Pinker and Laszlo, 1992.)

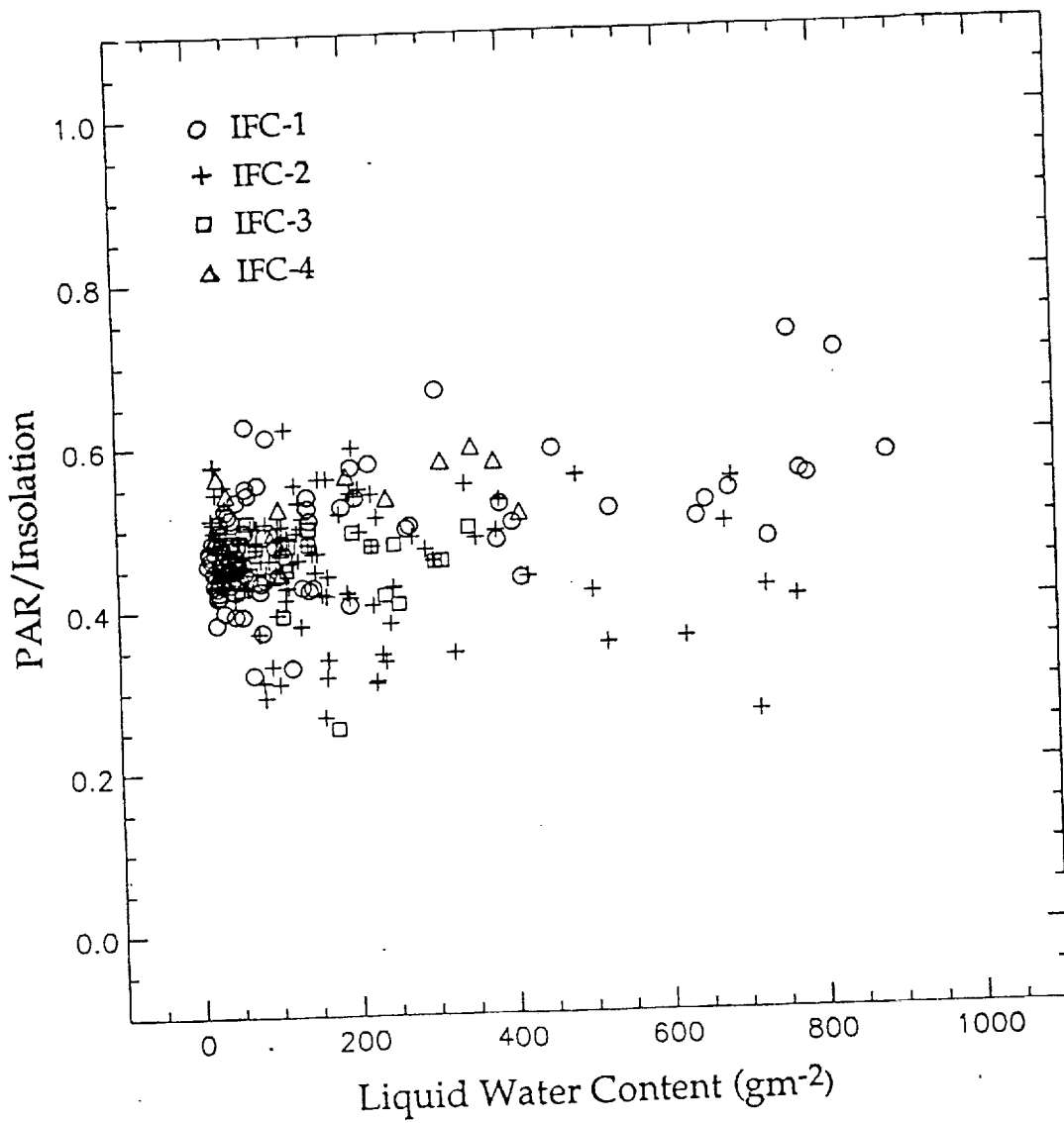


Fig. 4. Surface-measured ratio of half-hourly photosynthetically available radiation, PAR, and insolation as a function of satellite-derived instantaneous cloud liquid water content during the First ISLSCP Field Experiment. The ratio varies between 0.25 and 0.75, corroborating theoretical calculations.

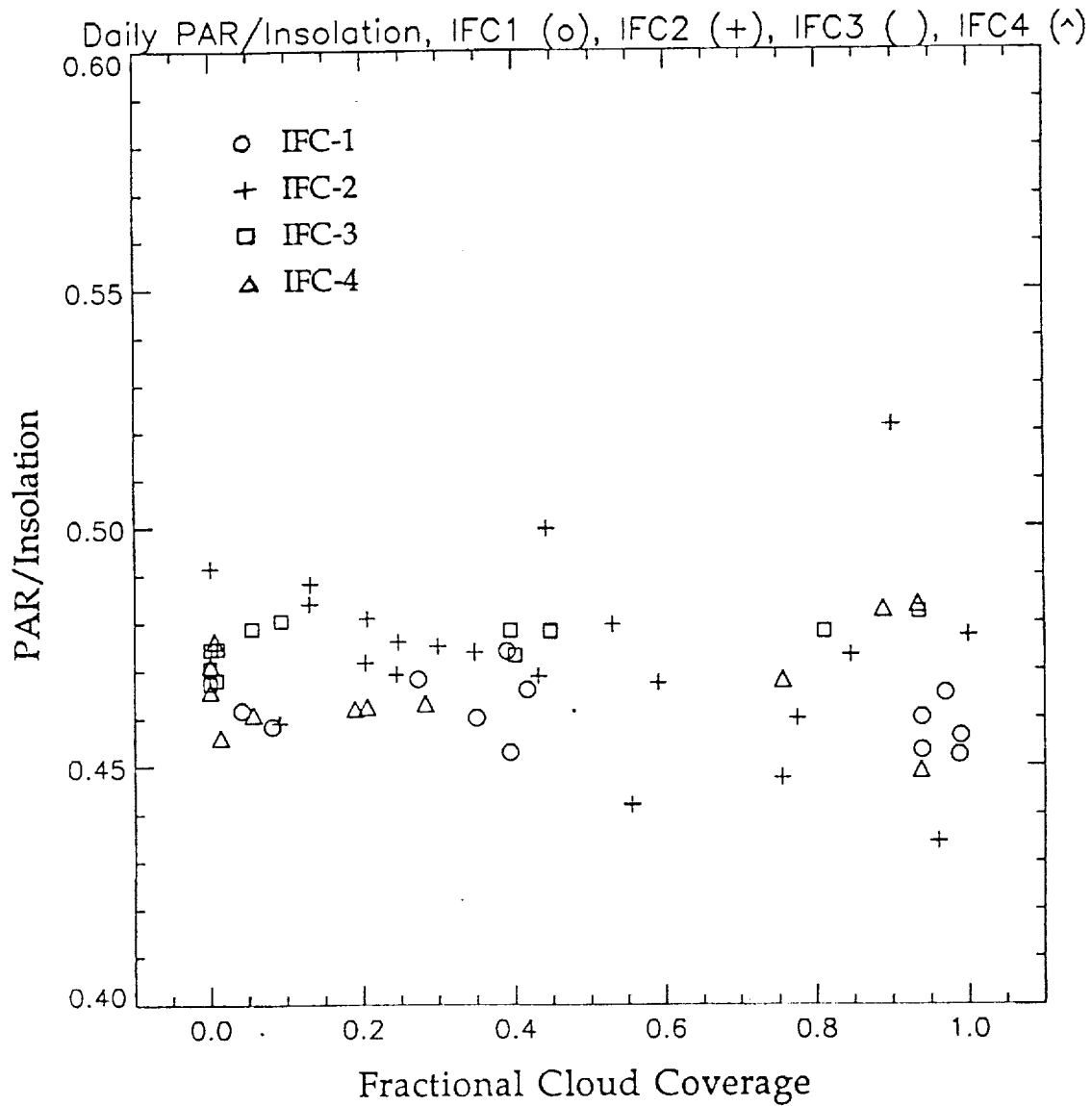
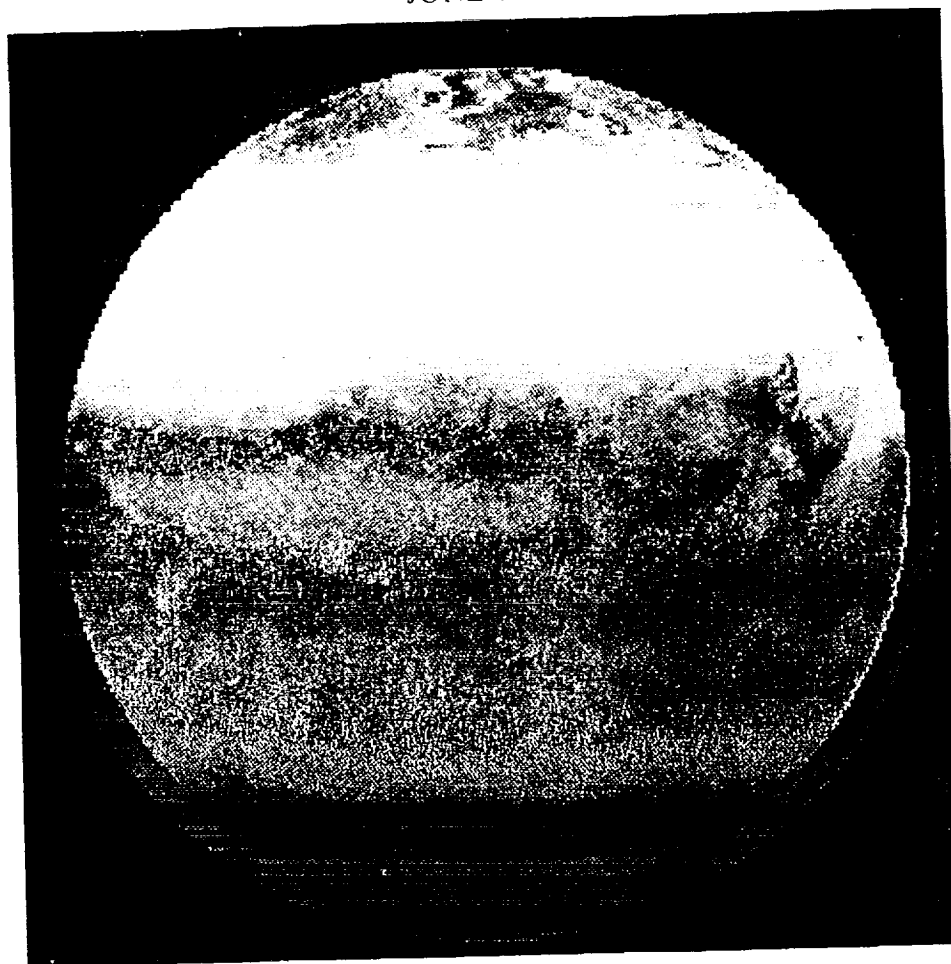


Fig. 5. Surface-measured ratio of daily photosynthetically available radiation, PAR, and insolation as a function of satellite-derived daily cloud cover during the First ISLSCP Field Experiment. At this time scale the PAR fraction variability is small, with values ranging between 0.43 and 0.52.

JUNE 1990



PAR (Wm^{-2})

Fig. 6. Monthly photosynthetically available radiation, PAR, derived from Meteosat data for June 1990. Monthly insolation was first obtained using the method of Dedieu et al. (1987) and PAR was then deduced by taking the ratio of PAR and insolation equal to 0.45.

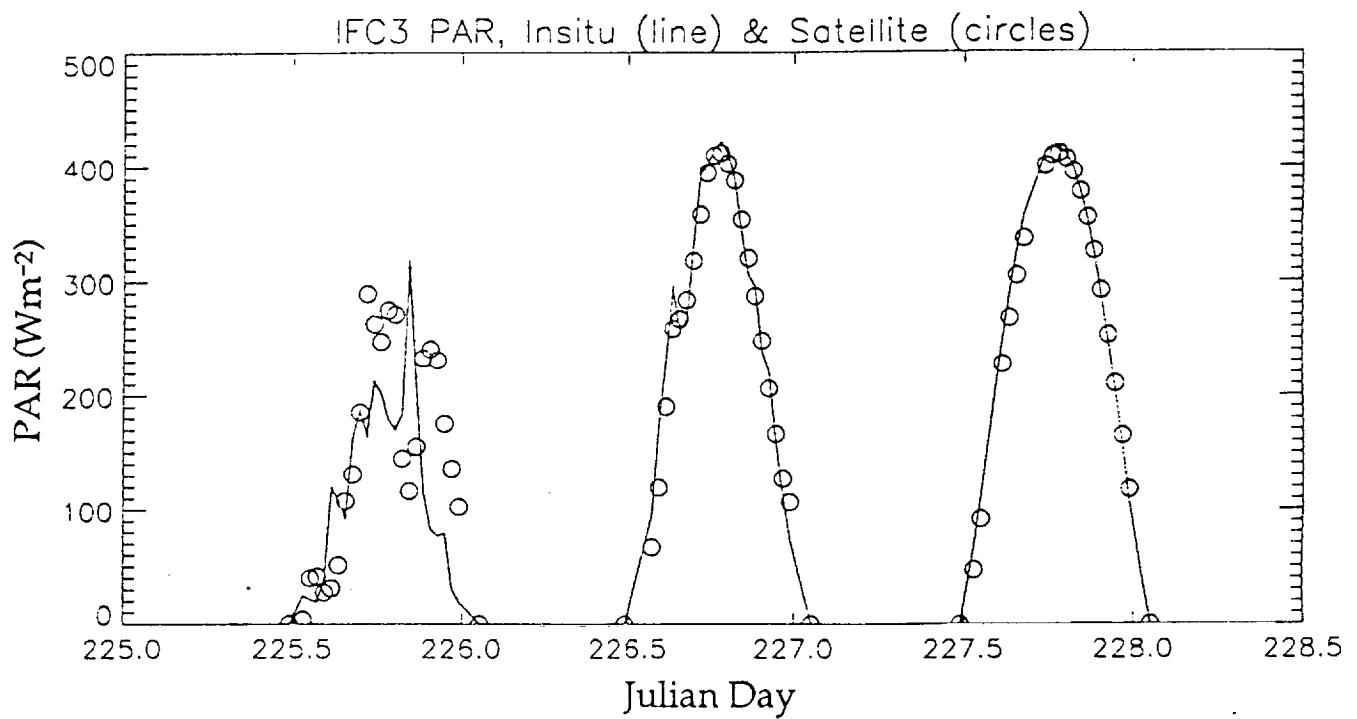
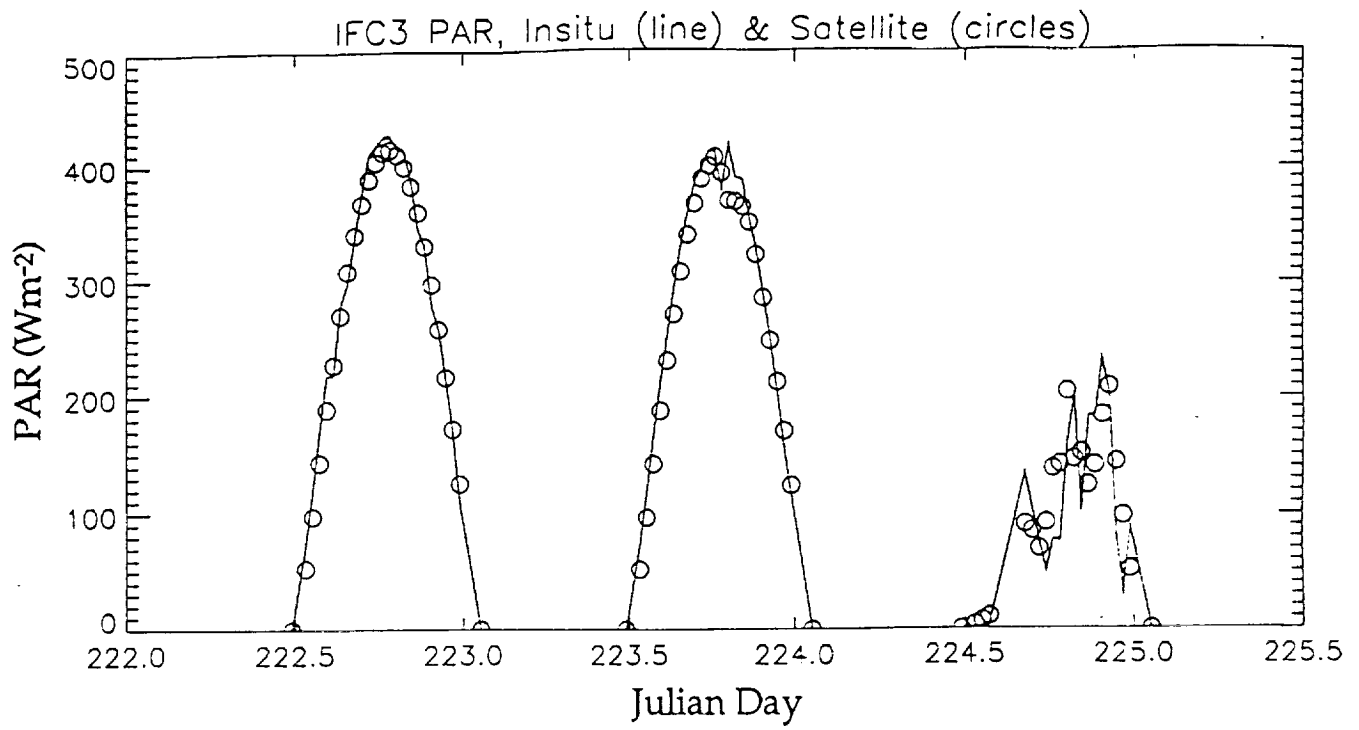


Fig. 7. Surface-measured and satellite-derived photosynthetically available radiation, PAR, for selected days during the First ISLSCP Field Experiment. Satellite estimates are instantaneous whereas measured values are half-hourly averaged.

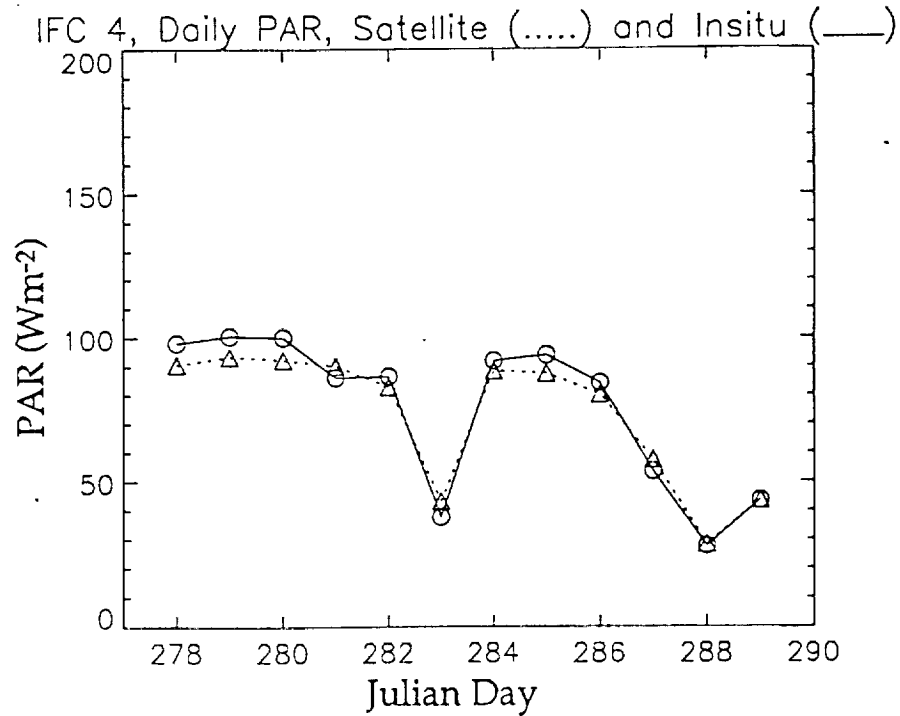
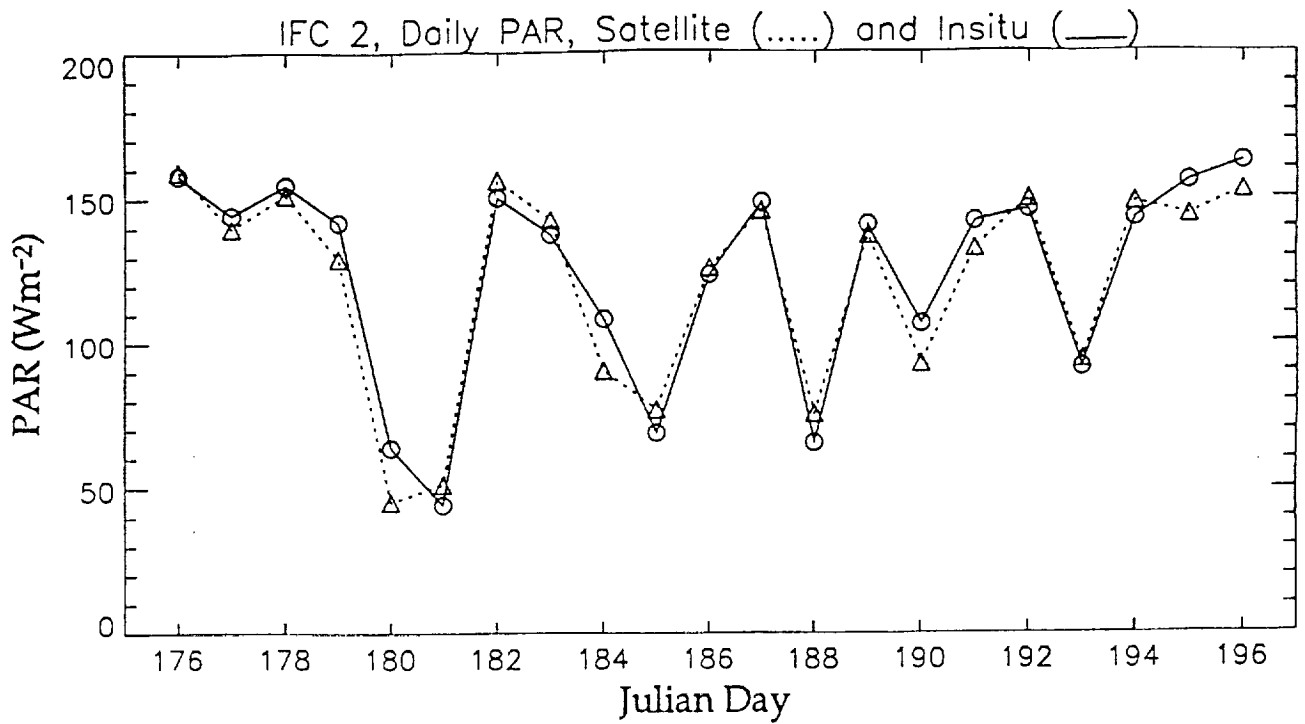


Fig. 8. Surface-measured and satellite-derived daily photosynthetically available radiation, PAR, during the second and fourth intensive field campaigns of the First ISLSCP Field Experiment.

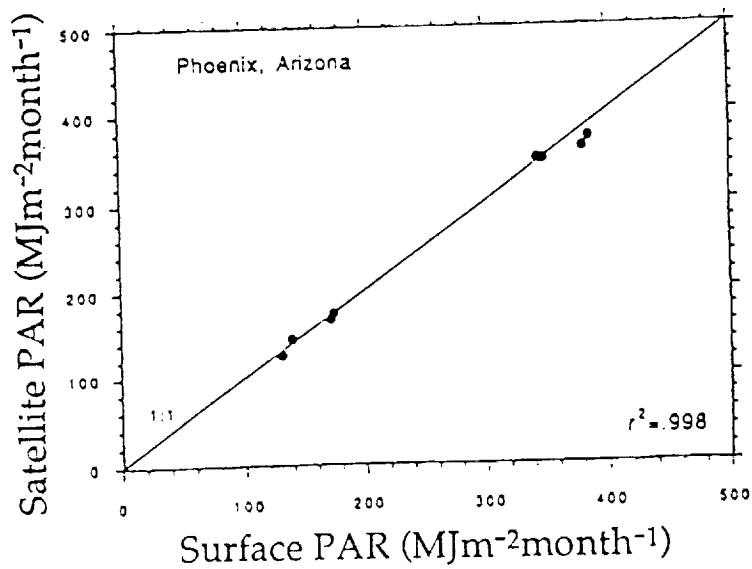
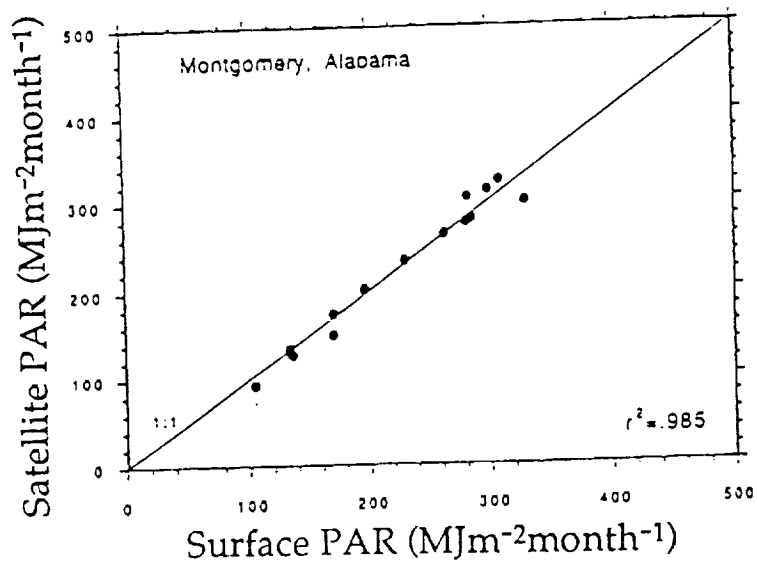
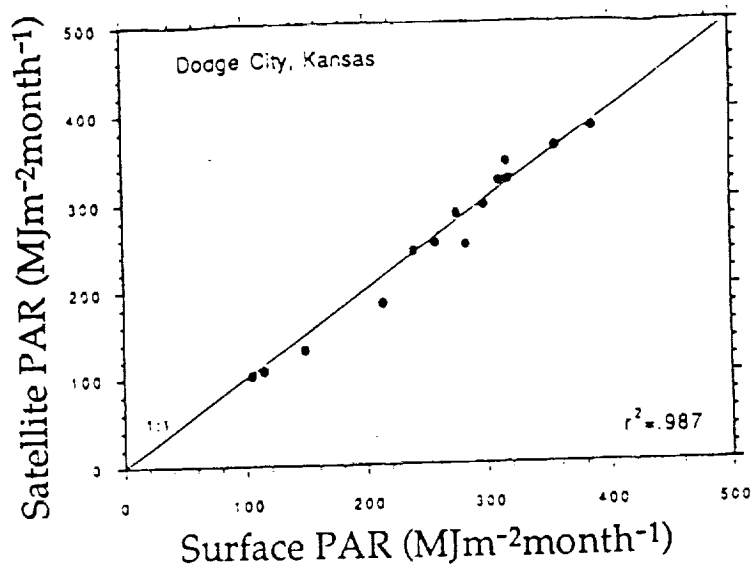


Fig. 9. Satellite estimates of monthly photosynthetically available radiation, PAR, versus surface estimates from pyranometer measurements adjusted to PAR. (After Eck and Dye, 1991.)

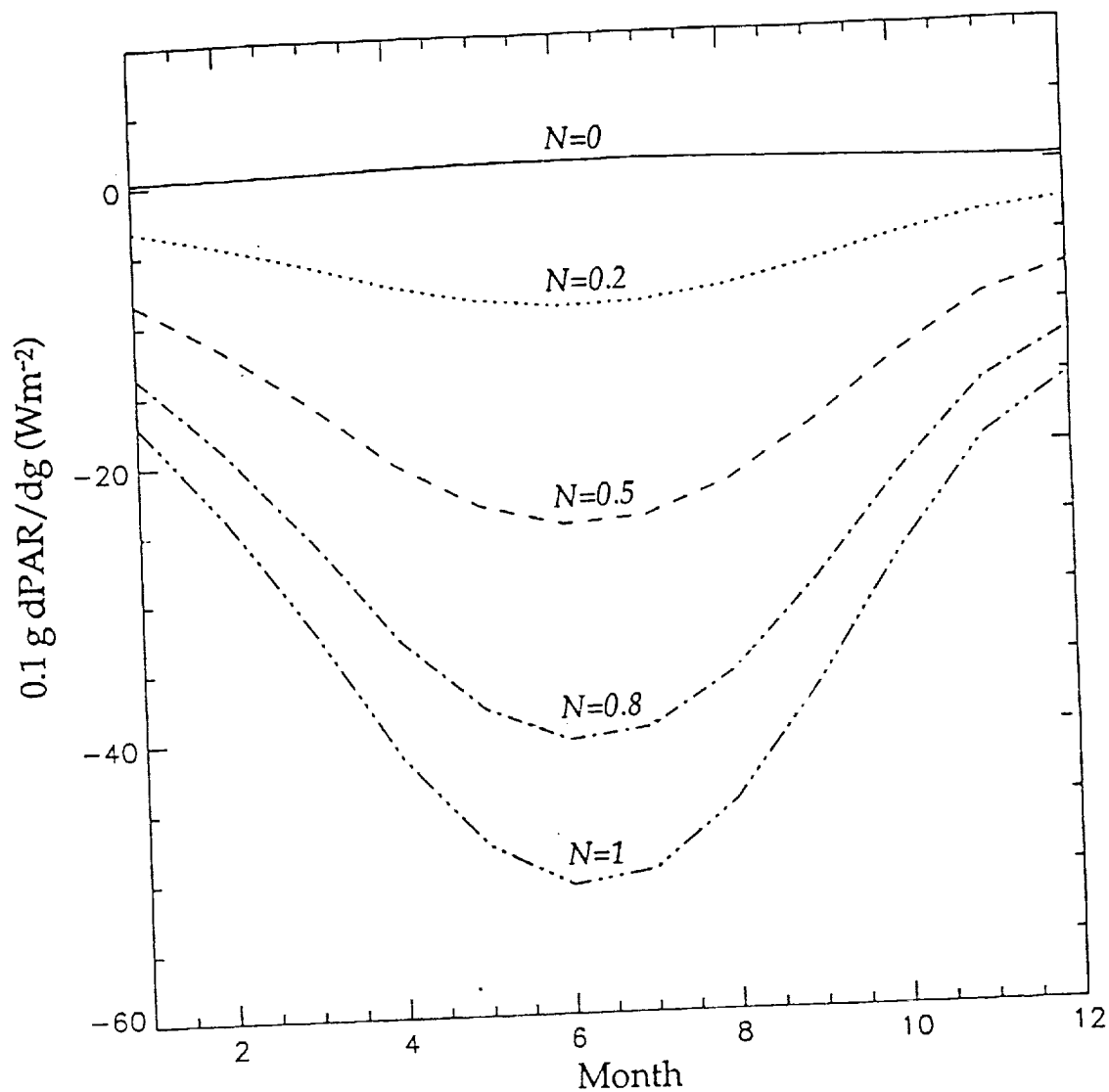


Fig. 10. Typical error on satellite-derived monthly photosynthetically available radiation, PAR, due to a 10% increase in the calibration gain, g , of the sensor's solar channel. Clouds contain 100g m^{-2} of liquid water, and the clear atmosphere contains 0.3 atm-cm of ozone and aerosols of continental type and optical thickness of 0.22 at 550 nm . Latitude is 39°N . As fractional cloud coverage, N , increases, the error increases in magnitude, reaching -50 W m^{-2} in June and July.

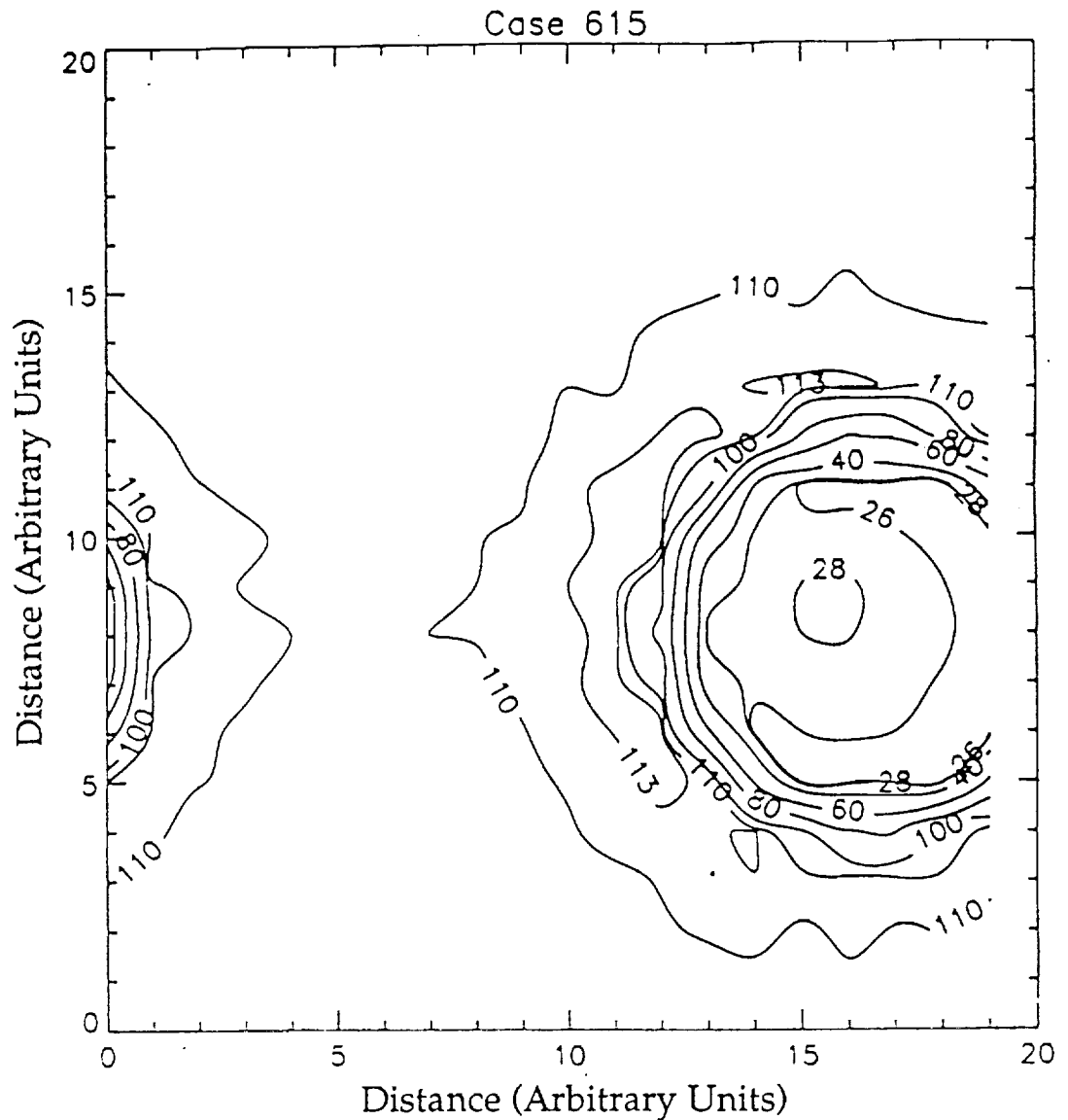


Fig. 11. Monte Carlo simulations of the spatial distribution of cloud transmittance (in percent) on August 8, 1989 at 13:30 local time over the Konza prairie, Kansas. The clouds are cylindrical of radius 500m, separated by 2,500m, and located between 2,000 and 2,200m (geometrical thickness of 200m). The cloud optical thickness is 12. When the sun disk is not obscured by clouds, cloud transmittance reaches 113%, indicating that the surface receives more photosynthetically available radiation than in clear sky conditions.



PREV. ANN
92A13320

Appendix 6

SATELLITE ESTIMATES OF DOWNWELLING LONGWAVE IRRADIANCE
AT THE SURFACE DURING FIFE

F.-M. Bréon, R. Frouin, C. Gautier

Proc. Symp. on the First ISLSCP Field Experiment, Anaheim, CA, February 7-9, 1990, 98-104, Published by the American Meteorological Society

SATELLITE ESTIMATES OF DOWNWELLING LONGWAVE IRRADIANCE AT THE SURFACE DURING FIFE

François-Marie Bréon, Robert Frouin, and Catherine Gautier

California Space Institute A-021
Scripps Institution of Oceanography
La Jolla, California

1. INTRODUCTION

During recent years public and scientific interest in the planet earth's climate system has grown remarkably. This is attributable, in part, not only to an increased concern about possible environmental problems (e.g., global warming due to the famous greenhouse effect), but also to the emergence of technologies enabling new forms of climate study. Meteorological satellites, for instance, now provide global views of the earth's atmosphere and surface, while increasingly powerful computers permit more realistic simulations of atmospheric and oceanic circulations.

One of today's main climate research topics concerns ocean-land-atmosphere interactions on a global scale. This includes studying energy, water, and momentum exchanges at the media's interfaces. Characterizing the energy budget with a reasonable spatial and temporal accuracy is of major importance to various applications, in particular: 1) diagnostic studies of heat transport, cloud forcing, radiative heating; 2) specification of boundary conditions for global circulation models (GCM); 3) amelioration of sub-grid process parameterizations in such models; 4) validation of climate models; and 5) determination of long-term trends (NASA, 1986).

Moreover, since the land surface, unlike the oceans, has a small heat capacity, radiation and water budgets are strongly related: the net heat budget, which is the balance between radiation and the sensible and latent heat fluxes, is close to zero when averaged over time periods longer than a day. The latent heat flux is directly related to the evaporation rate and is consequently determined largely by the sum of the radiation and sensible heat budgets.

The net longwave irradiance flux at the surface, owing to its small variability, is less important than the shortwave, or solar, one. It cannot be neglected, however, particularly in the presence of clouds which decrease surface insolation while increasing

the downward component of the longwave flux. Several methods have been proposed to estimate the downward longwave flux at the surface from satellite measurements (see, for instance, Darnell et al., 1983; Frouin et al., 1988; Gupta, 1989). Although some of them have been used to generate global fields of net longwave flux, few validation studies have been made (WMO-ICSU, 1984). We therefore investigated the performances of two of them, choosing among the most promising ones, by comparing their computations with carefully taken in situ measurements.

In the first part of this paper we describe the data used in this study. The data were collected during the First ISLSCP Field Experiment (FIFE). In analyzing the data quality, we emphasize the difficulty to acquire reliable longwave irradiance measurements and, therefore, validate radiative transfer models. We then present briefly the two methods selected to estimate downward longwave flux at the surface, namely those of Frouin et al. (1988) and Gupta (1989). Finally, the two methods' results are compared and verified against in situ pyrgeometer measurements.

2. DATA

FIFE, an international surface-atmosphere experiment, took place in 1987 at and around the Konza Prairie Long Term Ecological Research (LTER) site near Manhattan, Kansas (Sellers et al., 1988). The FIFE objectives were to gather the necessary data to permit interpretation of satellite observations suitable to infer climatologically significant land surface parameters.

The experimental area is a 15 x 15 km square with various topological features including burned and unburned plateau, slope, and creek (Fig. 1). Although the central portion of the area is studied continuously and additional parameters are

measured throughout the year, the experiment concentrated on four Intensive Field Campaigns (IFCs) corresponding to four different states of the surface vegetation:

First IFC :	"green up"	May 26th to June 6th
Second IFC :	"peak greenness"	June 25th to July 15th
Third IFC :	"dry down"	August 10th to August 21st
Fourth IFC :	"senescence"	October 5th to October 15th

Our study uses 4 different types of data acquired during the IFCs, namely surface measurements, atmospheric soundings, sky photographs, and satellite-derived parameters.

Several surface stations collected radiative flux measurements. At the time of our study, only data from stations 2 and 38 (see Fig. 1) were available through the FIFE information system. These stations were operated by Eric Smith's group (University of Florida) during the four IFCs. A first check of the data was made by comparing hourly measurements from one station to those from the other (Fig. 2). Some of the station 2 measurements are obviously bad (values higher than 450 Wm^{-2}). A plot of the time series of these measurements shows that the unrealistic values are limited in time to the first days of the first IFC. At other times, the two stations' data are well correlated with each other, but exhibit a relative bias (higher measurements at station 2) which is rather small for low flux values (a few Wm^{-2}) but up to 20 Wm^{-2} for the highest fluxes. Since we know with confidence that station 2 provided inconsistent measurements at the beginning of the experiment, we have an objective reason to favor station 38. It is possible, however, that the problems experienced by station 2 did not propagate a bias along the four

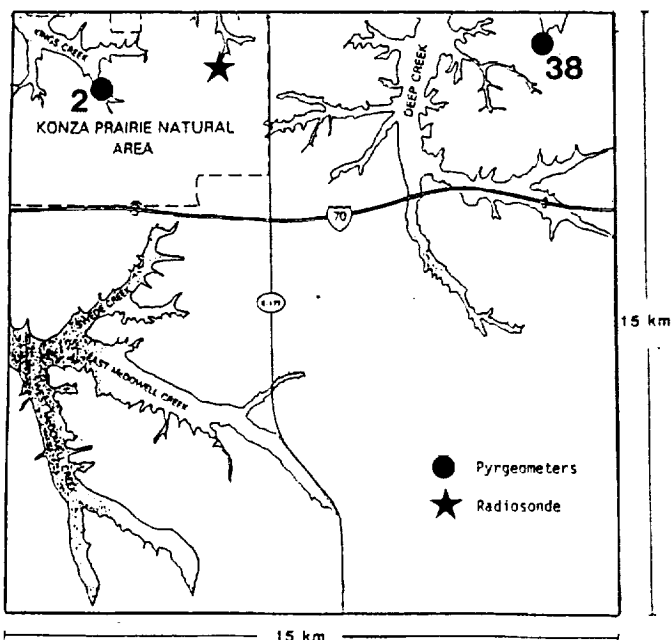


Fig. 1: General presentation of FIFE experimental field. Station 2 and 38 are the two longwave measurement sites used in this study. The black circle indicates the soundings' launch location.

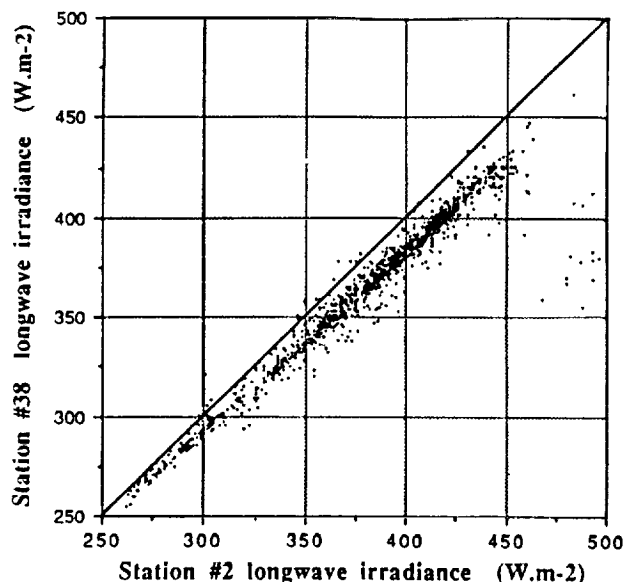


Fig. 2: Comparison of coincident hourly downwelling longwave fluxes measured at station 2 and 38 during the four IFCs of FIFE. The fluxes are in Wm^{-2} .

IFCs. Further discussion with E. Smith convinced us that more work has to be done to favor one station rather than the other. Before the experiment, the two pyrometers had been carefully intercalibrated and gave very close values. The reason for the discrepancy found during the IFCs is still unclear, but a different instrument orientation is suspected (E. Smith, 1989, personal communication).

During the four IFCs there was a strong diurnal cycle of downwelling longwave flux at the surface. The cycle showed a maximum at about 5:00 PM local time and a minimum around sunrise. This does not exactly follow the temperature cycle as could have been expected. However, the development of convective clouds in the afternoon, leading to an increase of the flux, may be responsible for this delayed maximum. The amplitude of the cycle is about 30 Wm^{-2} for IFCs 1 and 3, close to 20 Wm^{-2} for IFC 2 and only 10 Wm^{-2} for IFC 4. The 4 IFCs are not long enough for those figures to be statistically significant; the smaller amplitude for IFC 4 may be explained by its later period in the year, leading to a smaller daily cycle temperature.

Cloudiness was another parameter acquired from the surface. This was done by an uplooking automatic camera. Cloudiness was deduced from the percentage of cloudy areas in the photographs, taking into account the viewing angle of each area relative to the vertical. Since this camera was operating in the visible spectrum, no cloudiness information could be obtained at night. In the study that follows, we considered that the sky was clear when, according to the photographs, less than $1/8$ of the sky was covered by clouds.

The atmospheric measurements used in our study were obtained from radiosondes launched from the experimental site (see Fig. 1). These

measured pressure, temperature, and wet bulb temperature, from which the water vapor mixing ratio was derived. We first had to clean the data: the pressure, which usually decreased smoothly, sometimes showed 50 mb jumps. This problem was resolved by removing corresponding measurements. More bothersome, we found that the water vapor mixing ratio occasionally exhibited negative values! This was the result of improper wet bulb temperature measurements when the air temperature was low; in such cases, the water surrounding the thermometer simply freezes and the wet bulb measurement loses its significance. We overcame this problem by removing all water vapor information for which the wet bulb temperature was negative. The water vapor profile was then extrapolated to higher levels using climatological profiles, taking into account the valid information about the lower layers and the actual temperature profile so that the mixing ratio could not be larger than the saturation level.

The satellite products we used are the pre-processed TIROS-N Operational Vertical Sounder (TOVS) sounding data. The TOVS instrument, a multi-frequency radiometer designed to remotely sense, among other variables, atmospheric temperature and water vapor mixing ratio profiles, has been flying for many years on board the NOAA series satellites (Kidwell, 1981). The TOVS observations were processed with NOAA/NESDIS's operational algorithm (Kidwell, 1981). The TOVS products include surface pressure, surface temperature, air temperature at 15 pressure levels, three layers of water-vapor content, cloud top pressure, and effective cloud amount.

3. METHOD

Two methods that determine downwelling longwave flux at the surface from a description of the atmosphere were selected for this study. These are the method of Frouin et al. (1988), which employs the fairly detailed radiative transfer model designed by Morcrette (Morcrette, 1984; Morcrette and Fouquart, 1985; Morcrette et al., 1986), and a simpler parameterization recently proposed by Gupta (1989).

Morcrette's model uses as input temperature, water vapor and ozone mixing ratio, and cloud amount profiles at levels which can be chosen by the user. The model divides the infrared spectrum into six intervals and explicitly takes into account absorption by the radiatively important atmospheric gases.

To determine the model input parameters, Frouin et al. (1988) proposed various methods. In all the methods, temperature and water vapor mixing ratio are obtained from TOVS data. In the most refined method (method 1), cloud base altitude is deduced from cloud top altitude and liquid water path, assuming a liquid water

distribution within the cloud. In the other methods, simplifying assumptions are introduced which include directly relating liquid water path to cloud geometrical thickness (method 2), fixing the cloud geometrical thickness to its climatological value (method 3), and, finally, parameterizing the cloud effects only as a function of fractional cloud coverage (method 4). In the calculation presented later in this paper, we only employed method 3 using a thickness of 500 m.

The Gupta (1989) scheme, a much simpler one, limits the computational burden. It is a simple parameterization developed using regression techniques applied to a set of atmospheric profiles and the corresponding longwave fluxes at the surface, as determined using a radiative transfer model similar to Morcrette's. Although the Gupta (1989) method can be applied, in principle, to any complete atmospheric description, it has been explicitly designed to use TOVS products; the input parameters are surface temperature, 1000-850 mb and 850-700 mb temperatures, cloud base temperature, total water vapor content, water vapor content below the cloud, and cloud amount. Since cloud base information is not accessible from the TOVS instrument, the method uses the estimated cloud top pressure and assumes a mean cloud thickness of 50 mb; the cloud base temperature and water vapor below the cloud are then obtained from the corresponding profiles. The same assumptions have been used in the study that follows.

One of the goals of this study is to accurately compare longwave flux estimates from the models with in situ measurements. The objective is to estimate how precise the models really are because although model intercomparisons have been performed, careful comparisons with in situ observations have not. When model estimates and measurements show large differences, the differences can be attributed not only to the uncertainty of the model itself, but also to the measurement or to the quality of the input atmospheric profile. To validate a model, we therefore need high quality and reliable longwave radiation measurements and atmospheric profiles. Temperature and water vapor profiles can be obtained with a reasonable accuracy from radiosonde data. This is not the case for the cloud parameters, particularly cloud base pressure and effective cloud emissivity. Therefore, in cloudy conditions, a discrepancy between estimated and measured fluxes will not be conclusive, and we decided to concentrate on clear periods. Clear sky radiosoundings were selected using the information given by the sky camera.

Another goal of the study was to evaluate the Frouin et al. (1988) and Gupta (1989) methods in estimating the longwave flux from satellite observations over the FIFE area.

This includes not only the algorithms themselves, but also the inversion process that retrieves geophysical parameters from TOVS data.

In the evaluation, we included cloudy observations as well as clear ones. Only TOVS observations closer than 200 km from the center of the experimental area were used. In order to keep the more accurate TOVS products, we selected only "class-1" soundings as defined in Gupta's (1989) paper. In other words, the radiative calculations were performed when all the parameters (temperature, water vapor, and cloud parameters) were present in the products.

4. RESULTS AND DISCUSSION

Figure 3 illustrates a comparison between the Morcrette et al. (1986) and Gupta (1989) model outputs when using clear sky radiosoundings acquired during FIFE. The longwave estimates range from 235 to 420 Wm^{-2} . Morcrette's and Gupta's values are very close; the standard deviation of the differences is only 3.5 Wm^{-2} and the correlation coefficient is 0.999. However, a large bias of (15 Wm^{-2}) between the two estimates is observed. This bias is larger than the accuracy required for estimating longwave flux at surface for most scientific applications; it is therefore important to evaluate which model is in fact most accurate. This can be accomplished by comparing a time series of the longwave flux measurements to the values found when applying the two models to the sounding data in clear conditions. Figure 4, which shows an example of such a comparison, was obtained for the third IFC at station 38 using Morcrette's model. Similar comparisons for other IFCs, stations, or models are not presented here but give comparable results. These results show that, in general, the models accurately reproduce the variability of the clear sky flux. In particular, the increase in downwelling longwave flux associated

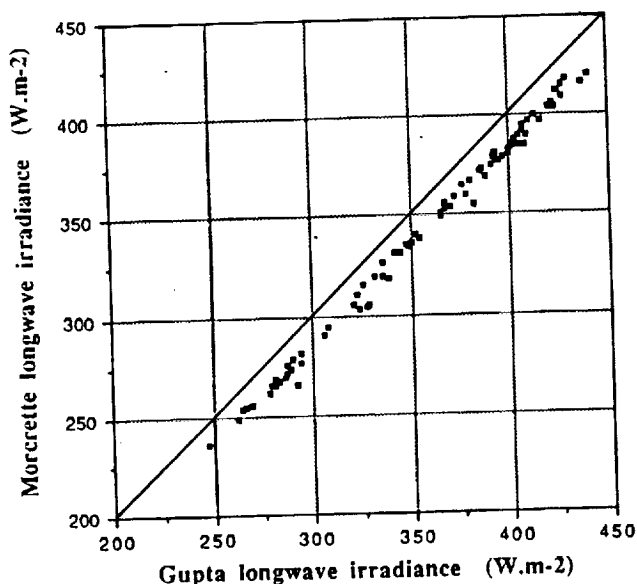


Fig. 3: Comparison between the Morcrette et al. (1986) and Gupta (1989) model clear flux estimates. The input profiles are the FIFE radiosoundings launched during clear periods of the four IFCs. Values are displayed in Wm^{-2} .

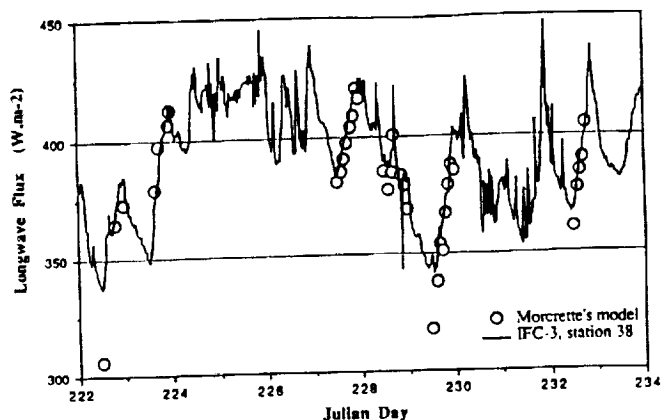


Fig. 4: Time series of in situ-measured longwave fluxes and those estimated by the Morcrette et al. (1986) model using FIFE radiosoundings as an input. The estimates were done only during clear periods, as inferred by the sky-looking camera. Values are in Wm^{-2} . This figure is limited to the third IFC (August 10 to August 21).

with the diurnal variations of air temperature is well-reproduced by the model. It is also interesting to note that the maximum values observed in late afternoon in clear conditions are almost as large as the overall maximum values observed. This suggests that, over land, the cloud effects are no more important in increasing the downwelling longwave flux than the atmospheric temperature (and moisture) effects are. As already mentioned, there is large uncertainty in the measurements themselves. The bias observed between the models is comparable to the one between the measurements. Gupta's model reproduces well the station 2 measurements, while Morcrette's models does the same for station 38. As a consequence, the results do not allow one to conclude which model is more precise.

Figure 5 depicts the time series of downward longwave flux measurements at station 38 (line) and corresponding satellite estimates (open circles) for clear and cloudy conditions. The satellite estimates were obtained with the Frouin et al. (1988) method 3 (Fig. 5a) and the Gupta (1988) method (Fig. 5b). Even though Fig. 5 was obtained for the third IFC, the results are similar for the three other IFCs. Occasionally several satellite estimates are displayed for the same time; they correspond to different satellite soundings during the same satellite pass within the 200 km distance limit. This discrepancy, which can be larger than 20 Wm^{-2} , is mainly due to variable cloudiness parameters. These figures indicate that when using satellite cloud and atmospheric products instead of in situ observations, the estimations of the downwelling longwave radiation degrade significantly. In comparison with the model results presented earlier, it suggests that the TOVS satellite products used are not sufficient for achieving an accuracy of 10 Wm^{-2} . Both methods provide results that are smaller, in general, than the in situ measurements. The reason for this is not understood.

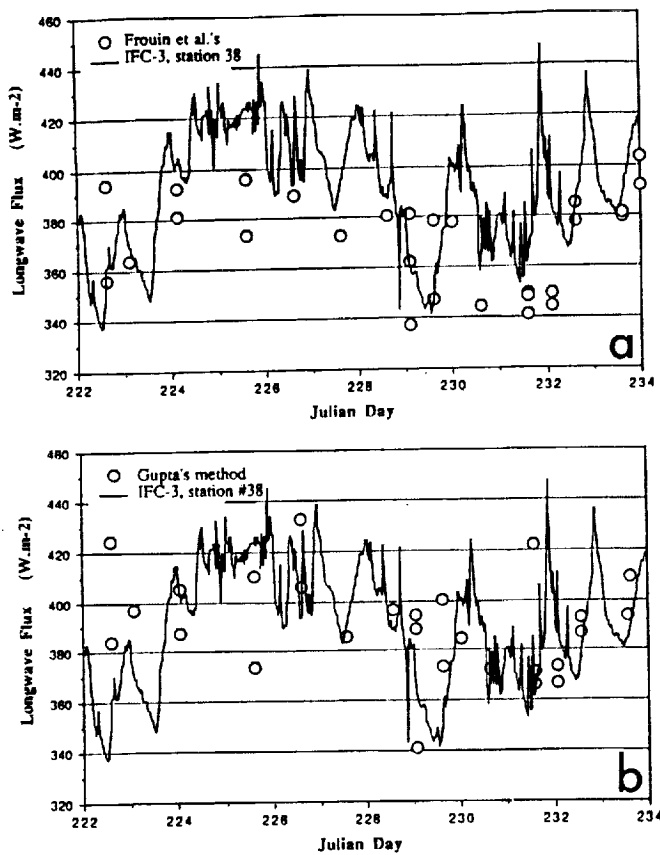


Fig. 5: Time series of in situ measured longwave flux and that estimated by the Frouin et al. (1988) method 3 (Fig. 5a) and the Gupta (1989) model (Fig. 5b) using TOVS retrievals as input. No distinction was made between clear and cloudy retrievals. Values are in Wm^{-2} . This figure is limited to the third IFC (August 10 to August 21).

Investigating the quality of the TOVS products by comparing them to their radiosonde equivalent, we did not detect any bias in the temperature or the water vapor content. We therefore suspect that the cloud parameters were responsible for the bias. The underestimation can possibly result from a lower than actual cloud effective emissivity, which is equivalent to an underestimation of cloudiness and/or cloud emissivity in the TOVS data, or from an overestimated cloud base height. The only cloud parameter we can compare to surface observations is the cloudiness. We attempted to perform such a comparison but the study was not conclusive because either:

- a) the surface-estimated cloudiness displayed a very high temporal variability;
- b) TOVS-based estimates displayed a rather large spatial variability: for the same satellite pass, TOVS retrievals within 200 km of the area often exhibited several order differences in cloudiness; or,
- c) the two types of measurements were not exactly comparable: the camera estimate gives a fractional cloud cover whereas the satellite instrument gives an "effective cloudiness", a product of the cloud cover and the mean cloud emissivity.

5. SUMMARY AND CONCLUSIONS

In this paper we have attempted to compare two methods (i.e., Frouin et al., 1988, and Gupta, 1989) for estimating the downwelling longwave flux at the surface and assess their respective accuracies. Computations with these two models using the same atmospheric temperatures and moisture profiles indicated, that for clear sky conditions, the two model computations are highly correlated. The values, however, present a systematic bias of 15 Wm^{-2} . Since Gupta's parameterization was derived from a radiative transfer model applied to a set of atmospheric profiles, it is likely that the same bias would also be found when this radiative transfer model is compared to that of Morcrette. Additional work needs to be done to understand and explain the systematic difference.

These model computations were then compared with in situ measurements at two nearby locations. The clear sky longwave flux estimates from both models were found to be very consistent with in situ measurements. In this case, differences were of the same order of magnitude as the uncertainty of the measurements themselves. One of our goals in comparing the two models with in situ measurements was to favor one of them, as far as the bias was concerned. Unfortunately, the Gupta (1989) model results were found to be comparable to the station 2 measurements, while the Morcrette model results were found to be comparable to those of station 38. Since we have no reason to have more trust in either dataset, it is impossible, in view of this study, to favor one model or the other. We hope that further work with the in situ measurements at Florida State University will help us understand the differences between the two stations so that we can achieve more solid conclusions regarding the superiority of one model versus the other.

Computations were then performed with the two models under all conditions and using TOVS data as input. Comparisons with in situ measurements indicated that the model computations were much more scattered around the in situ measurements than were the clear sky model estimates with the radiosonde data. This was expected since, to the method's uncertainty, other uncertainties are added: that of the retrieval profile itself and the noise due to the separation between the TOVS sounding and the pyrgeometer sites. More bothersome, however, is the fact that, on average for this small dataset, the flux is underestimated by both satellite-based methods. No explanation is available for this at present.

The general conclusion to the present study is that, once again, it is difficult to definitively quantify the accuracy of radiative transfer models because of the lack of reliable surface measurements. We have shown, however, that the clear sky flux estimates obtained by the two

models we investigated were within the uncertainty of the measurements themselves, which is of the order of 5%. The cloud effect computed by the models, unfortunately, cannot be validated against in situ measurements because of the large uncertainty in the input variables, particularly the cloud parameters.

6. ACKNOWLEDGMENTS

This work was supported by the National Aeronautics and Space Administration under grant NAG5-900 and by the California Space Institute under grant CS89-89. We wish to thank E. Smith for his helpful discussions, K. Shapiro and B. Bloomfield for their editing help, and J. Correa for his technical support.

7. REFERENCES

- Bréon, F.M., R. Frouin and C. Gautier, 1989: In situ measurements and parameterization of downwelling longwave irradiance at the ocean surface. Submitted to *J. Appl. Meteor.*
- Darnell, W. L., S. K. Gupta and W. F. Staylor, 1983: Downward longwave radiation at the surface from satellite measurements. *J. Clim. Appl. Meteor.*, **22**, 1956-1960.
- Frouin, R., C. Gautier and J.J. Morcrette, 1988: Downward longwave irradiance at the ocean surface from satellite data: Methodology and in-situ validation. *J. Geophys. Res.*, **93** (C1), 597-619.
- Gupta, S. H., 1989: A parameterization for Longwave surface radiation from sun-synchronous satellite data. *J. Clim.*, **2**, 305-320.
- Kidwell, K. B., 1981: NOAA polar orbiter data (TIROS-N, NOAA-6 and NOAA-7) users guide. March 1981 (Revised December 1981).
- Morcrette, J.J., 1984: Sur la paramétrisation du rayonnement dans les modèles de la circulation générale atmosphérique. Thèse de Doctorat d'Etat, Université des Sciences et Techniques de Lille, 630, 373 pp.
- Morcrette J.J., and Fouquart Y., 1985: On systematic errors in parameterized calculations of the longwave radiation transfer. *Quart. J. Roy. Meteor. Soc.*, **111**, 691-708.
- Morcrette J.J., Smith L. and Fouquart Y., 1986: Pressure and temperature dependence of the absorption in longwave radiation parameterizations. *Beitr. Phys. Atmosph.*, **59**, 455-469.
- NASA, 1986: Surface radiation budget for climate application. Reference publication 1169.
- Sellers, P.J., F.G. Hall, G. Asrar, D.E. Strebel and R.E. Murphy, 1988: The First ISLSCP Field Experiment (FIFE)". *Bull. AMS*, **69**, 22-27.
- WMO-ICSU, 1984: The intercomparison of radiation codes in climate models. World Climate Research Program Report WCP-93, Geneva, Switzerland.

PREV. ANN
92A 13329

Appendix 7

A DIFFERENTIAL ABSORPTION TECHNIQUE TO ESTIMATE
ATMOSPHERIC TOTAL WATER VAPOR AMOUNTS

R. Frouin, E. Middleton

Proc. Symp. on the First ISLSCP Field Experiment, Anaheim, CA, February 7-9, 1990, 135-139, Published by the American Meteorological Society

A DIFFERENTIAL ABSORPTION TECHNIQUE TO ESTIMATE ATMOSPHERIC TOTAL WATER VAPOR AMOUNTS

Robert Frouin

California Space Institute A-021
Scripps Institution of Oceanography
La Jolla, California 92093

Elizabeth Middleton

Earth Resources Branch
NASA/Goddard Space Flight Center
Greenbelt, Maryland 20771

1. INTRODUCTION

It has long been observed that direct solar radiation is absorbed substantially by water vapor in a cloudless atmosphere, and that the phenomenon is even more pronounced when the observations are conducted in the infrared part of the solar spectrum. Fowle (1912, 1913) first exploited these observations for measuring vertically-integrated (total) atmospheric water vapor amounts. He developed a spectroscopy technique that consists of viewing the sun from the earth's surface through two spectral channels located near the center and outside a near-infrared water vapor band. The ratio of the two voltage outputs, as measured by a radiometer, gives a direct measure of the water vapor amount integrated along the sun-to-surface path. Fowle's differential absorption technique has been subsequently verified and applied in many studies (e.g., Hand, 1940; Foskett and Foster, 1943; Gates, 1956; Siversten and Solheim, 1975; Pitts et al., 1977; and Reagan et al., 1987).

A practical corollary to Fowle's water vapor measuring technique, and this paper's focus, is to view the earth's surface (i.e., measure the solar radiance reflected by the surface) instead of the sun. Although such an extension of the technique is non-trivial, impeded primarily by uncertainties in surface reflectance effects, it is feasible, and its successful implementation would be invaluable to global earth studies. That is, by viewing the surface in place of the sun, this modified technique could be conveniently adapted for aircraft and satellite measuring systems, thus offering the capability to map water vapor amounts over large areas.

The problem in estimating water vapor amounts by viewing the surface in spectral channels centered at the different wavelengths, as in Fowle's technique, is that the ratio of the channels' voltage outputs depends not only on the ratios of the source intensity (the sun) and of the atmospheric transmittance (mostly a function of water vapor abundance) in the two channels, but

also on the ratio of the surface reflectance in the two channels. This ratio is not constant; on the contrary, it varies strongly with surface type and radiation geometry (see, for instance, Bowker et al., 1985). Consequently, applying the current band ratio technique to a radiometer viewing the surface will yield significantly different water vapor amounts depending on the nature and bi-directional properties of the underlying surface.

Our study extends the sun-viewing spectroscopy technique to surface viewing for use with aircraft or satellite-based instruments. We provide appropriate channels in the $0.940 \mu\text{m}$ water vapor band to retrieve total water vapor amount independently of the surface reflectance properties and other atmospheric constituents. The $0.940 \mu\text{m}$ band is selected because it is not saturated, thus sensitive to even large water vapor amounts; furthermore, the spectral reflectance of vegetation in this band is not influenced by leaf water content, and soil moisture content generally shifts the entire reflectance curve. In other words, liquid water absorption by vegetation and soil (also by rocks and minerals) is not expected to affect differentially the spectral signal reflected by the surface.

In the following section, section 2, we describe our technique to minimize surface reflectance effects. We quantify, by performing radiative transfer simulations, the gain in accuracy when employing the proposed instead of the usual channel combination. Section 3 presents a verification of the technique using SE-590 spectrometer measurements and concomitant radiosoundings acquired during FIFE. Section 4 examines, in the case of an airborne or spaceborne instrument, the effect of photons backscattered directly by the atmosphere toward the sensor, which may be a problem over low reflective surfaces, such as the ocean in the presence of vertically-extended aerosols. Finally, Section 5 summarizes the findings and concludes with a discussion of the technique's perspectives in the context of the Earth Observing System (Eos) and future international scientific projects.

2. TECHNIQUE

To eliminate the surface reflectance effect, one may choose two spectral channels, one narrow, the other wide, centered on the same wavelength at the water vapor absorption maximum in the $0.940 \mu\text{m}$ water vapor band. If the surface reflectance depends linearly on wavelength or varies symmetrically with respect to the central wavelength, then it becomes constant when averaged in the narrow and wide spectral channels. In this case, spectral variations in the surface reflectance do not affect estimates of water vapor amount. Indeed, the question arises: does the reflectance of natural and non-natural surfaces exhibit a sufficiently symmetric or linear behavior in the spectral range of the $0.940 \mu\text{m}$ water vapor band?

Using the 5S radiative transfer code (Tanré et al., 1986), we performed simulations of the radiance measured by a radiometer viewing a wide range of surface targets (water, snow, ice, rocks, minerals, vegetation, wet and dry soil, etc.) whose reflectance properties were taken from Bowker et al. (1985). In the calculations, the atmospheric path from the surface to the sensor was considered negligible, corresponding to the radiometer close to the surface. The results, presented in Fig. 1, for a 23 km-visibility US62 atmosphere containing continental aerosols, indicate that variations in the radiance ratio, due to differences in the surface reflectance spectral properties, are substantially reduced when choosing the $0.935\text{--}0.955 \mu\text{m}$, $0.920\text{--}0.970 \mu\text{m}$ channel combination instead of the $0.945\text{--}0.955 \mu\text{m}$, $0.865\text{--}0.875 \mu\text{m}$ combination (the typical combination when viewing the sun).

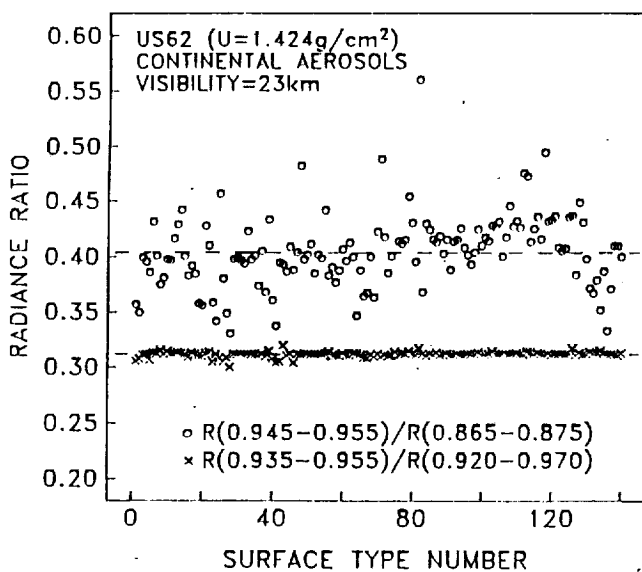


Fig. 1 Simulations for 140 surface targets, including water, snow, ice, bare soil, and dry and wet vegetation, of the radiance ratio in spectral channels centered in the region of the $0.940 \mu\text{m}$ water vapor band. Two channel pairs are considered: $0.945\text{--}0.955 \mu\text{m}$, $0.865\text{--}0.875 \mu\text{m}$ (crosses) and $0.935\text{--}0.955 \mu\text{m}$, $0.920\text{--}0.970 \mu\text{m}$ (open circles).

If we now examine the resulting errors in water vapor amount (Fig. 2), the standard deviation around the actual value (1.4 gcm^{-2} for the selected atmosphere) is reduced from 0.3 to 0.1 gcm^{-2} (by a factor of 3) when using the narrow and wide channel combination. The radiance ratio in these channels, however, is less sensitive to water vapor amount as Fig. 3 demonstrates (the entire depth of the band is not measured in that case); but this should not be a problem since the instrumental noise level in the radiance ratio can be as low as a few thousandths. Note, finally that we have only considered one model atmosphere. Varying the nature and concentration of atmospheric aerosols, however, does not change the radiance ratio significantly (see Table 1).

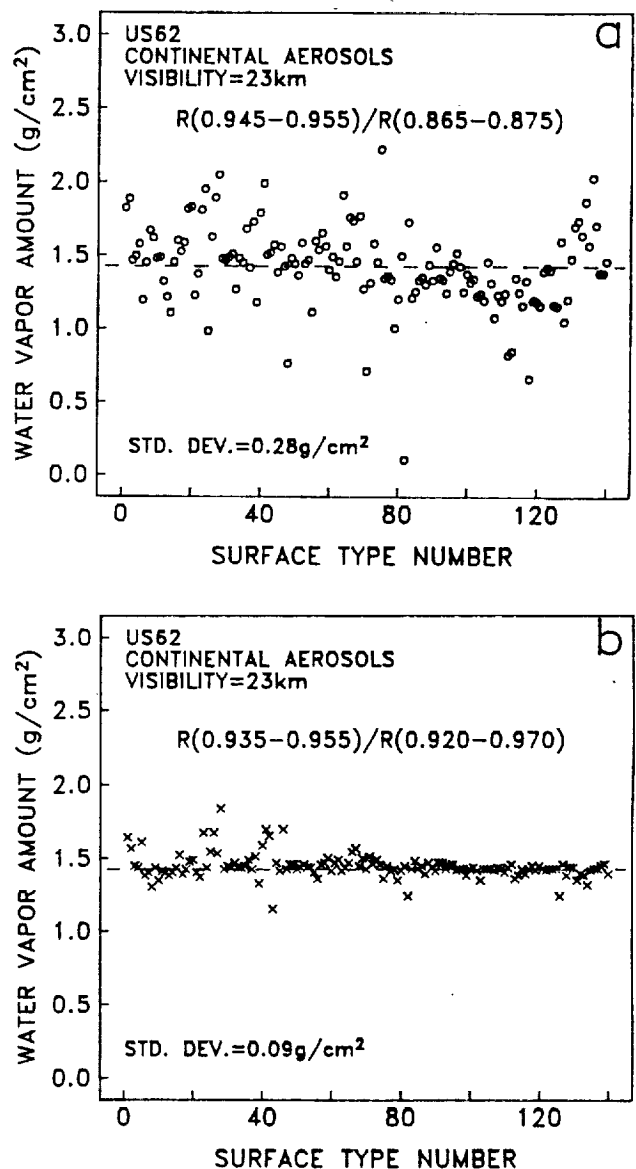


Fig. 2 Simulations of the retrieved water vapor amount for the 140 surface targets, sun geometry, and atmospheric conditions of Fig. 1. The surface is viewed in channels: $0.945\text{--}0.955 \mu\text{m}$ and $0.865\text{--}0.875 \mu\text{m}$ (a), and channels $0.935\text{--}0.955 \mu\text{m}$ and $0.920\text{--}0.970 \mu\text{m}$ (b).

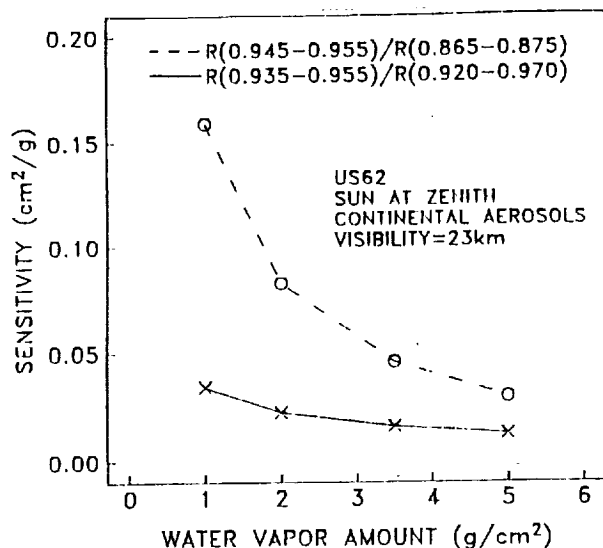


Fig. 3 Sensitivity of the radiance ratio to water vapor amount for channel combinations 0.945-0.955 μm , 0.865-0.875 μm and 0.935-0.955 μm , 0.920-0.970 μm .

Table 1. Radiance ratio for various aerosol models. The values are for a sun at zenith and a Lambertian, perfectly reflecting surface.

Model	$\frac{R(0.945 - 0.955 \mu\text{m})}{R(0.865 - 0.875 \mu\text{m})}$	$\frac{R(0.935 - 0.955 \mu\text{m})}{R(0.920 - 0.970 \mu\text{m})}$
	Atmosphere	
US62, Continental, V=23 km	.4042	.3119
US62, Continental, V=5 km	.4064	.3119
US62, Urban, V=23 km	.4051	.3119
US62, Urban, V=5 km	.4097	.3120
US62, Maritime, V=23 km	.4035	.3119
US62, Maritime, V=5 km	.4040	.3119

3. VERIFICATION

The concept of viewing the surface in narrow and wide spectral channels centered on the same wavelength to eliminate the effect of spectral variations in the surface reflectance has been verified using SE-590 spectrometer data and concomitant radiosonde observations acquired during the 1987 FIFE experiment. Figure 4 shows the location of the SE-590 spectrometer measurements and radiosonde launches, and Table 2 summarizes the dataset collected during FIFE's four intensive field campaigns (IFC's).

The SE-590 spectrometer, which measures in 252 bands from 0.4 to 1.1 μm , collected data at 8 sites. At each site the instrument head was installed approximately 4.5 m above the ground in a relatively uniform and representative area of the site. Many of the measurements were made with the instrument viewing at nadir, but bi-directional datasets were also acquired in the solar principal plane during the second, third, and fourth IFC's at 10° viewing angle increments. To characterize diurnal variations in the surface reflectance, the data were collected at about every 10° change in solar zenith angle.

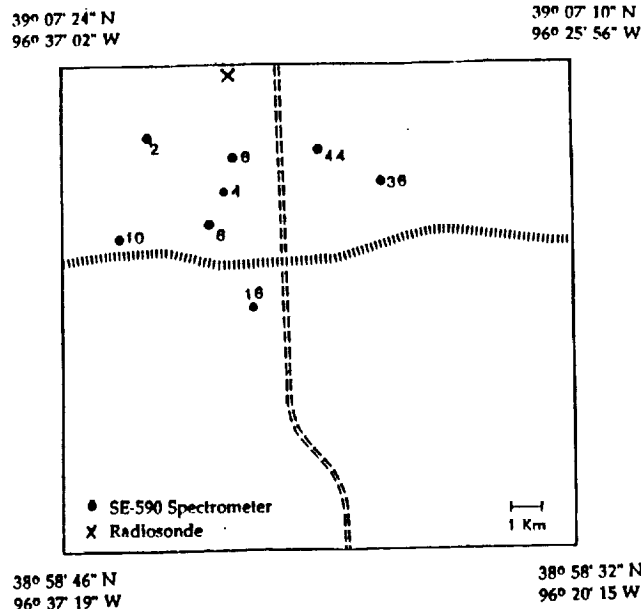


Fig. 4 Map of FIFE area showing SE-590 spectrometer and radiosonde locations.

Table 2. Summary of concomitant SE-590 spectrometer and radiosonde data collected during FIFE. The SE-590 spectrometer measurements were performed at sites 2, 4, 6, 8, 10, 16, 36, and 44 and the radiosondes were launched near site 31 (see Fig. 4 for locations).

Intensive Field Campaign	Number of Field Days	Number of Data Sets	
		SE-590 Spectrometer	Radiosonde
1 (May/June 1987)	8	53	65
2 (June/July 1987)	10	64	48
3 (August 1987)	7	104	50
4 (October 1987)	7	55	48

A total of 276 SE-590 spectra were acquired over 32 field days, and more than 6 radiosondes were launched on average per day within 6 km of the sites. In the preliminary results presented below, however, we only used the data collected at 4 sites (4, 6, 10, and 36) during the four "golden" days (June 6, July 11, August 15, and October 11) of FIFE.

Figure 5 shows the radiance ratio in channels 0.938-0.953 μm and 0.919-0.972 μm deduced from the SE-590 spectrometer measurements as a function of water vapor amount along the optical path calculated from the radiosonde data. The points fit very well the law given by:

$$R = 0.326 \exp\left[-0.177\left(\frac{U}{\cos\theta}\right)^{1/2}\right] \quad (1)$$

where R is the radiance ratio, U is the total water vapor amount, and θ is the solar zenith angle. This law, where the exponential exponent varies as $(U/\cos\theta)^{1/2}$, is expected since the absorption regime is strong in the 0.940 μm water vapor band (see, for instance, Goody, 1964). Using (1) yields $U/\cos\theta$ to $\pm 0.5 \text{ g cm}^{-2}$, which indicates the good stability of the relation between radiance ratio and water vapor amount for varied surfaces and a wide range of

solar zenith angles (the spectral reflectance of the sites varies with radiation geometry). Let us emphasize, however, that only 4 days of data were considered in Fig. 5. More data remain to be analyzed (see Table 2) to corroborate statistically the above results.

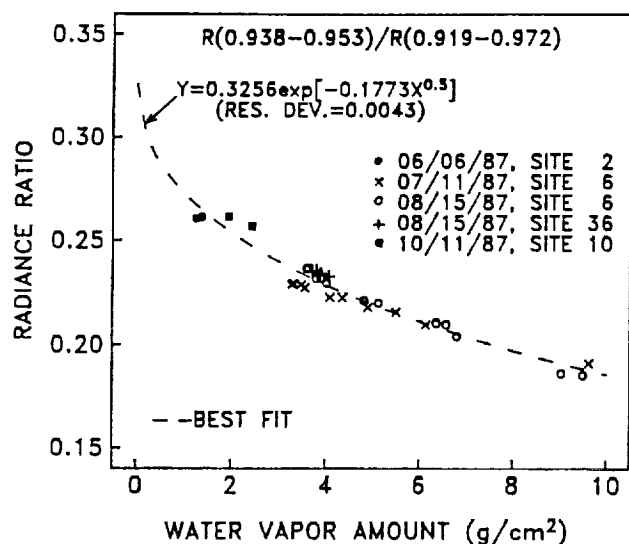


Fig. 5 Radiance ratio in channels 0.938-0.953 μm and 0.919-0.972 μm , computed from SE-590 spectrometer data, as a function of water vapor amount deduced from concomitant radiosonde data.

4. EFFECT OF AEROSOLS

So far we have considered the case of an instrument viewing the surface from just above the ground. In the case of surface viewing from higher altitudes or above the atmosphere, the signal measured by the instrument contains not only photons that have been reflected by the surface, but also photons directly backscattered by the atmosphere. In the presence of aerosols located high in the atmosphere over a low reflecting surface such as the ocean, the contribution of these photons, mostly backscattered by the aerosol layer, may surpass significantly the signal reflected by the surface; it is this signal that contains the water vapor information (the bulk of the atmospheric water vapor is generally encountered within 2 km of the surface). The water vapor amount, in that case, would be underestimated.

To assess qualitatively the underestimation introduced, let us assume that the aerosols are located above the Rayleigh atmosphere. For not-too-horizontal sightings, small aerosol optical thicknesses, and a Lambertian surface, the solar radiance reflected by the surface-atmosphere system can be written simply as:

$$R = R_a^A + \left(R_a^M + \rho T_a \frac{I_0}{\pi} \right) T_g \quad (2)$$

where R_a^A and R_a^M are the signals backscattered by the aerosols and molecules, respectively, ρ is the surface reflectance, I_0 is the extraterrestrial solar irradiance, T_a is the diffuse atmospheric

transmittance, and T_g is the gaseous transmittance. In this formulation, we have neglected the effect of photons that have sustained multiple surface reflections, which is justified for surface targets of low reflectance.

Although extremely simplified, the above modeling retains the essential physics of the problem. The gaseous transmittance does not affect the signal backscattered by the aerosols. When ρ is small, R_a^A may dominate the right-hand side of Eq. (2). As ρ increases, the relative contribution of R_a^A to R decreases and R becomes more sensitive to water vapor amount.

Fig. 6a shows the radiance ratio in the 0.935-0.955 μm and 0.920-0.970 μm channels, computed using Eq. (2), as a function of surface reflectance.

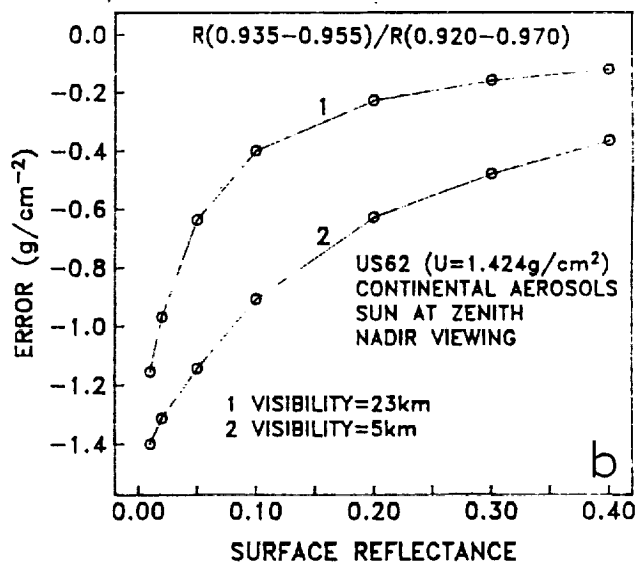
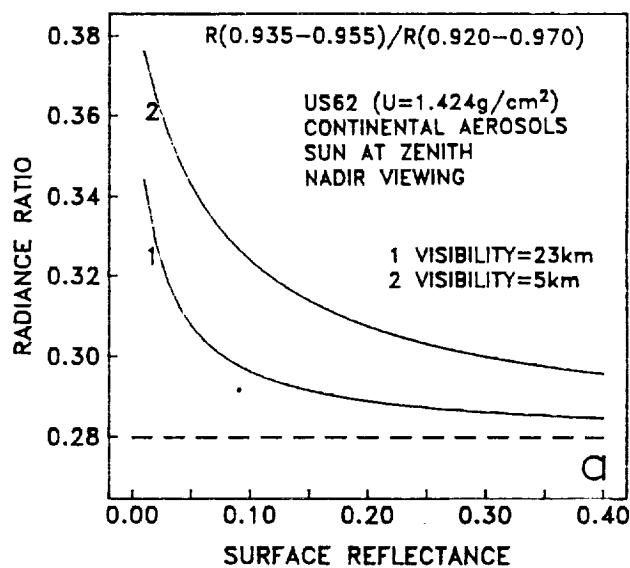


Fig. 6 (a) Radiance ratio in channels 0.935-0.955 μm and 0.920-0.970 μm as a function of surface reflectance for 23 and 5 km visibility atmospheres. The dashed line corresponds to a pure Rayleigh atmosphere. (b) Resulting aerosol-induced error on the retrieved water vapor amount. In the calculations, the aerosols are assumed to be located above the Rayleigh atmosphere, which maximizes the error.

When the reflectance is low ($\rho < 0.1$), the radiance ratio departs substantially from the 0.28 value corresponding to a pure Rayleigh atmosphere (no aerosols), all the more as the visibility decreases. In the 5 km visibility case, the difference reaches 0.09 (32%) for a surface reflectance of 0.01.

The resulting error in water vapor amount is displayed in Fig. 6b. Absolute values below 0.3 gcm^{-2} (21% of the actual value) are only obtained when ρ is above 0.2 and the atmosphere is clear (23 km visibility case). For both model atmospheres, the underestimation reaches over 0.9 gcm^{-2} (63%) when ρ is less than 0.02. The errors, however, should be regarded as upper limits for the aerosol backscattering effect. Tropospheric aerosols are generally located within the boundary layer, which reduces the effect considerably. Radiative transfer calculations for realistic atmospheres are necessary to quantify the error introduced as a function of the relative vertical distribution of aerosols and water vapor.

5. SUMMARY AND CONCLUSIONS

We have shown, from radiative transfer simulations, that viewing the earth's surface in two channels, one narrow, the other wide, centered on the same wavelength at the water vapor absorption maximum near $0.940 \mu\text{m}$ provides accurate atmospheric water vapor amounts independently of the surface reflectance properties. The concept was verified in situ using concomitant SE-590 spectrometer and radiosonde data acquired during FIFE. Under varied radiation geometries and atmospheric conditions, and for several surface targets, the relationship between radiance ratio in the narrow and wide spectral channels and water vapor amount was found to be stable, following an expected exponential law. The SE-590 instrument, however, did not view the surface from above the atmosphere or even above the boundary layer, where most of the water vapor is concentrated, and therefore did not permit verification of the technique in actual conditions of aircraft or satellite viewing. In such conditions, simple physics showed that the effect of photons backscattered directly by the atmospheric aerosols toward the sensor is to lower unacceptably the retrieved water vapor amount when the aerosols are located at high altitudes.

The technique, however, is only suitable in cloudless conditions or, at least, when the sensor views a surface target lit by the sun. Still, compared to satellite microwave techniques, which are applicable under most weather conditions, it has the advantage of simplicity and constitutes a promising alternative over land, where microwave radiometry is not appropriate.

By providing the means of estimating atmospheric total water vapor amounts simply, yet accurately from space, our study is relevant to

international programs, such as the International Land Surface Climatology Project (ISLSCP), for which atmospheric corrections to retrieve land surface parameters require estimates of water vapor amount, and the planned Global Energy and Water Cycle Experiment (GEWEX), whose objectives include establishing an observational basis for predicting water transport in the atmosphere. In this regard, note that the differential absorption concept is applicable to Eos platform's High Resolution Imaging Spectrometer (HIRIS) and Moderate Resolution Imaging Spectrometer (MODIS), instruments that possess channels in the region of the $0.940 \mu\text{m}$ water vapor band.

6. ACKNOWLEDGMENTS

This work was supported by the National Aeronautics and Space Administration under grant NAG5-900 and by the California Space Institute under grant CS87-89. We wish to thank P.Y. Deschamps of the Laboratoire d'Etudes et de Recherches en Télédétection Spatiale, France for helpful discussions; W. Brutsaert of the School of Civil and Environmental Engineering, Cornell University, who collected the radiosonde data; K. Shapiro and B. Bloomfield for technical support.

7. REFERENCES

- Bowker, D.E., R.E. Davis, D.L. Myrick, K. Stacy, and W.T. Jones, 1985: Spectral reflectances of natural targets for use in remote sensing studies. NASA reference publication 1139, 181pp.
- Foskett, L.W., and N.B. Foster, 1943: A spectroscopic hygrometer. *Bull. Amer. Meteor. Soc.*, **34**, 146-153.
- Fowle, F.E., 1912: The spectroscopic determination of aqueous vapor. *Astrophys. J.*, **35**, 149-162.
- Fowle, F.E., 1913: The determination of aqueous vapor above Mount Wilson. *Astrophys. J.*, **37**, 359-372.
- Gates, D.M., 1956: Infrared determination of precipitable water in a vertical column of the earth's atmosphere. *J. Meteor.*, **13**, 369-375.
- Goody, R.M., 1964: Atmospheric radiation, I: Theoretical basis. Clarendon Press, Oxford, 436 pp.
- Hand, J.F., 1940: An instrument for the spectroscopic determination of precipitable atmospheric water vapor and its calibration. *Mon. Wea. Rev.*, **68**, 95-98.
- Pitts, D.E., W.E. McCallum, M. Heidt, K. Jeske, J.T. Lee, D. De Monbrun, A. Morgan, and J. Potter, 1977: Temporal variations in atmospheric water vapor and aerosol optical depth determined by remote sensing. *J. Appl. Meteor.*, **16**, 1312-1321.
- Reagan, J.A., K. Thome, B. Herman and R. Gall, 1987: Water vapor measurements in the 0.94 minor absorption band: Calibration, measurements, and data applications. *Proceedings of IGARSS '87 Symposium*, Ann Arbor, Michigan, May 18-21, 63-67.
- Siversten, S., and J.F. Solheim, 1975: A field instrument for water vapor measurements. *Infrared Phys.*, **15**, 79-82.
- Tanré, D., C. Deroo, P. Duhaut, M. Herman, J.J. Morcrette, J. Perbos and P.Y. Deschamps, 1985: Effets atmosphériques en télédétection-logiciel de simulation du signal satellitaire dans le spectre solaire. *Proc. 3rd Int'l Colloquium on Spectral Signatures of Objects in Remote Sensing*, Les Arcs, France, Dec 16-20.



PREV. ANU.
90A 39746

Appendix 8

DETERMINATION FROM SPACE OF ATMOSPHERIC TOTAL WATER
VAPOR AMOUNTS BY DIFFERENTIAL ABSORPTION NEAR 940 NM:
THEORY AND AIRBORNE VERIFICATION

R. Frouin, P.-Y. Deschamps, P. Lecomte
J. Appl. Meteor, 29, 448-460, 1990

Determination from Space of Atmospheric Total Water Vapor Amounts by Differential Absorption near 940 nm: Theory and Airborne Verification

ROBERT FROUIN,* PIERRE-YVES DESCHAMPS** AND PIERRE LECOMTE

Laboratoire d'Optique Atmosphérique, Université des Sciences et Techniques de Lille, Lille, France

(Manuscript received 28 January 1989, in final form 30 October 1989)

ABSTRACT

A new technique is proposed to estimate atmospheric total water vapor amounts from space. The technique consists of viewing the Earth's surface in two spectral channels, one narrow, the other wide, centered on the same wavelength at the water vapor absorption maximum near 940 nm. With these characteristics, the ratio of the solar radiance measured in the two channels is independent of the surface reflectance and yields a direct estimate of the water vapor amount integrated along the optical path. To test the technique, we designed and built a two-channel radiometer based on the above concept. Airborne experiments carried out with the new device demonstrate the technique's feasibility under clear sky conditions over both sea and land. Over the ocean and in the presence of thick aerosol layers, however, total water vapor amounts may be underestimated by as much as 20%. Compared to satellite microwave techniques, which are applicable under most weather conditions, the proposed technique has the advantage of simplicity and constitutes a promising alternative over land, where microwave radiometry is inappropriate.

1. Introduction

Water vapor is an important constituent of the atmosphere. This is manifested in the ability of water vapor to change phase within atmospheric pressure and temperature ranges, producing clouds and hydrometeors (e.g., rain, snow, hail). When significant amounts of water vapor condense, the latent heat release becomes a source of energy for the maintenance of atmospheric processes. Water vapor also affects atmospheric energetics through radiative interactions.

Previous efforts to obtain water vapor data on a global scale have relied primarily upon radiosondes at hundreds of weather stations scattered around the world. Remote spectroscopy systems operating from space have more recently been deployed, and their major advantage is in obtaining continuous spatial and temporal data from not easily accessible regions (e.g., over the oceans, deserts, and poles).

Microwave measurements near the peak of the 22.235 GHz resonance line from the Nimbus series and Seasat have proved very suitable to derive the ver-

tically integrated (or total) water vapor amount over the oceans under most atmospheric conditions (e.g., Staelin et al. 1976; Chang and Wilheit 1979; Grody et al. 1980; Prabhakara et al. 1981). Typical accuracies of 0.1 to 0.5 g cm⁻² have been reported. The results obtained over land, however, have not been satisfactory, mainly because the surface emissivity in the microwave spectral region depends strongly on soil type and moisture. This strong and variable surface emission camouflages the water vapor information in the measurements.

Infrared measurements in the 6.3 μm rotation-vibration band from Nimbus-6, the NOAA series, GOES-5, and GOES-6 have been used to infer the vertical distribution of water vapor (e.g., Smith and Woolf 1976; Smith 1983), but with degraded accuracy, both in cloudy conditions and near the surface. The inversion techniques employed by these authors have typically yielded a 30% accuracy in the estimated water vapor mixing ratio.

It has long been observed, however, that direct solar radiation is absorbed substantially by water vapor in a cloudless atmosphere and that the phenomenon is even more pronounced when observations are conducted in the infrared part of the solar spectrum. Fowle (1912, 1913) was the first investigator to exploit these observations for measuring atmospheric water vapor amounts. He produced laboratory graphs relating the opacity of near-infrared water vapor bands to water vapor amount. His differential absorption concept has been subsequently verified and applied in many studies (e.g., Hand 1940; Foskett and Foster 1943; Gates 1956;

* Present affiliation: California Space Institute, Scripps Institution of Oceanography, La Jolla, California.

** Present affiliation: Laboratoire d'Etudes et de Recherches en Télédétection Spatiale, Toulouse, France.

Corresponding author address: Dr. Robert Frouin, California Space Institute, Scripps Institution of Oceanography, La Jolla, CA 92093-0221.

Siversten and Solheim 1975; Pitts et al. 1977; Reagan et al. 1987).

Fowle's concept is given further development in the present paper. We intend to demonstrate that it can be extended to the sensing of total water vapor amounts from space. For this purpose, we designed and constructed a radiometer that measures the intensity of the solar radiation reflected by the earth's surface in two spectral channels, one narrow, the other wide, centered on the absorption peak of the 940 nm water vapor band. The ratio of the radiometric signals measured by the two channels is independent of the surface reflectance properties and yields a direct estimate of the water vapor amount along the optical path. We report on the first few flights of this new device.

2. Differential absorption technique

The differential absorption technique consists of viewing a source of radiative energy at two (or more) wavelengths through the same atmospheric path; the wavelengths are chosen so that the absorption coefficients of a given gas, the amount of which is to be measured, are different. In the aforementioned investigations, the technique was applied to water vapor (the gas studied) by viewing the sun (the source) directly through the atmosphere. Instead of viewing the sun, however, one can view the earth's surface from above the atmosphere to estimate the water vapor amount along the optical path. In this case, it is the solar energy reflected by the surface that is measured, and this is done through a double atmospheric path (sun-to-surface and surface-to-sensor); but, a priori, one must know the surface reflectance. Here we derive a technique which requires no a priori knowledge of the surface reflectance.

We first consider the case of a direct path between the sun and the sensor. Denoting the voltage outputs of the radiometer in channels 1 and 2 by V_1 and V_2 , we have the following proportionality:

$$\frac{V_1}{V_2} \sim \frac{I_1 \bar{t}_1}{I_2 \bar{t}_2} \quad (1)$$

where I_1 and I_2 are the source intensities and \bar{t}_1 and \bar{t}_2 are average transmission functions. If channel i ($i = 1, 2$) is characterized by the spectral response $R_i(\lambda)$, t_i is defined as

$$\bar{t}_i = \frac{\int_0^\infty t_i(\lambda) R_i(\lambda) d\lambda}{\int_0^\infty R_i(\lambda) d\lambda} \quad (2)$$

where λ is wavelength and $t_i(\lambda)$ is the spectral atmospheric transmittance. When the two channels are located in a spectral region where atmospheric absorption is essentially due to water vapor, \bar{t}_1/\bar{t}_2 can be expressed as a function of an equivalent amount of water vapor

along the optical path, U^* . Measuring V_1/V_2 , therefore, gives access to U^* .

We now consider a surface target illuminated by the sun. In this case, we have to account for the solar energy reflected by the target, which yields

$$\frac{V_1}{V_2} \sim \frac{I_1 \bar{r}_1 \bar{t}_1}{I_2 \bar{r}_2 \bar{t}_2} \quad (3)$$

where \bar{r}_1 and \bar{r}_2 are average target reflectances. If the channels are selected such that \bar{r}_1/\bar{r}_2 is a constant, V_1/V_2 remains a function of U^* only (I_1/I_2 does not depend on the type of atmosphere encountered), and we can still obtain U^* by measuring V_1/V_2 .

In the present study, the technique employs two channels centered on practically the same wavelength at the absorption peak of the 940 nm water vapor band. The channels have narrow and wide spectral bandwidths, respectively. These characteristics, while differentiating between \bar{t}_1 and \bar{t}_2 for a fixed water vapor path, allow one to eliminate the ratio \bar{r}_1/\bar{r}_2 in (3) ($\bar{r}_1 \approx \bar{r}_2$). We are aware that the region around 940 nm is influenced not only by water vapor absorption, but also, although to a lesser degree, by carbon dioxide, ozone, and aerosol absorption as well as molecular and aerosol scattering. It is assumed, however, that the properties of all the attenuators except water vapor do not vary significantly (or vary linearly) across the channels' bandwidth and, thus, cancel in the ratio. This assumption is justified, as radiative transfer calculations performed with various standard atmospheres demonstrate (see section 3).

Note, furthermore, that (3) neglects the signal back-scattered by the atmosphere toward the sensor, which may not be justified under certain atmospheric conditions (i.e., thick aerosol layers) when the surface reflectance is small. An analysis of this effect will be presented later in the paper, when examining the experimental results (section 5).

Let us now express the average atmospheric transmittance \bar{t}_i . For a homogenous path, two basic random band models can be used (for more details, see Paltridge and Platt 1976):

- 1) the model of Goody (1952)

$$\bar{t}_i \approx \exp \left[-\frac{\bar{S}_i U}{\bar{d}_i} \left(1 + \frac{\bar{S}_i U}{\pi \bar{\alpha}_i} \right)^{-1/2} \right]; \quad (4)$$

- 2) the model of Malkmus (1967)

$$\bar{t}_i \approx \exp \left\{ -\frac{\pi \bar{\alpha}_i}{2 \bar{d}_i} \left[\left(1 + \frac{4 \bar{S}_i U}{\pi \bar{\alpha}_i} \right)^{1/2} - 1 \right] \right\} \quad (5)$$

where \bar{d}_i is the average line spacing, $\bar{\alpha}_i$ is the average Lorentz half-width, and \bar{S}_i is the average line intensity. In these expressions it is assumed that the spectral interval considered is wide compared to $\bar{\alpha}_i$. Since $\bar{S}_i U$

$\gg \pi \bar{\alpha}_i$ in the water vapor bands above 0.7 μm , both (4) and (5) reduce to

$$\bar{t}_i \approx \exp\left[-\frac{(\bar{S}_i U \pi \bar{\alpha}_i)^{1/2}}{\bar{d}_i}\right] \quad (6)$$

For a nonhomogenous path, the pressure and temperature variations along the path (\bar{S}_i depends on temperature and $\bar{\alpha}_i$ depends on temperature and pressure) can be taken into account by scaling U appropriately. A one-parameter scaling approximation (e.g., Goody 1964) is sufficient, since the absorption regime is strong and the effect of tropospheric temperature changes on \bar{S}_i is small. The scaled amount then takes the usual form:

$$U^* = \int_0^{U_i} \left(\frac{P}{P^*}\right)^m \left(\frac{T^*}{T}\right)^n dU \quad (7)$$

where T^* and P^* are the temperature and pressure of the equivalent homogenous path, respectively, and U_i is the water vapor amount integrated along the path. In the major water vapor absorption bands of the shortwave solar spectrum, including the 940 nm band, $m = 0.9$ to 1 and $n = 0.45$ (Selby et al. 1978; Stephens 1984). The procedure to calculate \bar{t}_i is therefore to replace U with U^* in (6) and evaluate \bar{S}_i at temperature T^* and $\bar{\alpha}_i$ at temperature T^* and pressure P^* .

Using the scaling approximation for a vertical atmospheric path characterized by a temperature profile $T = T_0 e^{-z/H_T}$, a pressure profile $P = P_0 e^{-z/H_P}$, and a water vapor density profile $\rho = \rho_0 e^{-z/H_W}$, and taking $T^* = T_0$ and $P^* = P_0$ yields

$$U^* = \rho_0 H_W \left(1 + \frac{m H_W}{H_P} - \frac{n H_W}{H_T}\right)^{-1} \quad (8)$$

Typically, $H_T \approx 30$ km, $H_P \approx 8$ km, and $H_W \approx 2$ km, which gives:

$$U^* \approx 0.8 \rho_0 H_W = 0.8 U_0 \quad (9)$$

where U_0 is the vertically integrated water vapor amount. Thus, U^* is relatively close to U_0 . The factor relating U^* to U_0 , however, is not constant and its changes result mainly from the variability of H_W (the effect of variations in H_T is negligible). Still, the relationship is stable enough to deduce accurately U_0 from U^* , as shown quantitatively in section 3.

The average transmittance \bar{t}_i over a slant path can therefore be expressed as

$$\bar{t}_i \approx \exp[-\bar{\beta}_i (m^* U_0)^{1/2}] \quad (10)$$

where m^* is the equivalent air mass ($1/\cos\theta$ when viewing the sun at zenith angle θ and $1/\cos\theta + 1/\cos\theta'$ when viewing the surface at zenith angle θ' with the sun at zenith angle θ) and $\bar{\beta}_i$ is an average absorption coefficient. Note that atmospheric refraction cannot be neglected at high solar or viewing zenith angles ($\theta, \theta' > 80^\circ$). The resulting increase in air mass, however,

can be easily taken into account using, for instance, Kasten's (1966) approximation formula.

Using (10), the ratio of atmospheric transmittances in the two channels takes the final form

$$\frac{\bar{t}_1}{\bar{t}_2} \approx \exp[-\bar{\beta}' (m^* U_0)^{1/2}] \quad (11)$$

where $\bar{\beta}' = \bar{\beta}_1 - \bar{\beta}_2$. By measuring \bar{t}_1/\bar{t}_2 and knowing $\bar{\beta}'$ and the radiation geometry, it is therefore possible, at least in principle, to derive U_0 from (11).

3. Radiometer

A schematic description of the radiometer is given in Fig. 1, and Table 1 lists the sensor specifications. The radiance passing through the collector is focused on one extremity of an optical fiber. Two condenser lenses form an image of the other extremity of the fiber on the detectors. Using fiber optics was appropriate because the instrument was designed to be flown on an aircraft. The detectors are silicon photodiodes operating at ambient temperature. Two interference filters are mounted in front of the detectors on a rotating wheel driven by a synchronous motor. The spectral response of the filters is shown in Fig. 2. The center wavelength is 938 nm for both filters, and their bandwidths are 13 and 46 nm at half-power points, respectively. These characteristics for the filters ensure that \bar{r}_1/\bar{r}_2 is practically equal to 1 in all conditions (surface type, illumination, and viewing geometry). Also shown in Fig. 2 is the spectral response of the detectors, which is fairly constant over the wavelength range of interest. The temperature dependence of the detector response is small, not exceeding 0.1% per degree Kelvin in the range of temperatures encountered in the troposphere. In addition to the filters, a reference surface is mounted to the wheel so that the detectors view an optically black target at each rotation of the wheel. A timing device permits control of the radiation signals generated by the optical system. The signals from the detectors are amplified and converted by a 12-bit analog-to-digital processor. Two amplifier sensitivities can be selected, and are appropriate for measurements over land (S_1) and sea (S_3), respectively. Once converted to digital format, the signals are fed into a data acquisition unit. The integration time is 0.05 s for each filter and the optical zero.

The differential technique requires only a relative calibration of the radiometric outputs. This calibration was carried out in the laboratory by directing the light collector toward a diffuse target illuminated by a solar simulator. The diffuse target was placed about 30 cm from the solar simulator and the light collector was installed just behind the diffuse target. Typical laboratory conditions were 292 K for air temperature and 80% for humidity. With this experimental setup and these conditions, atmospheric absorption along the optical path was negligible. The procedure was repeated

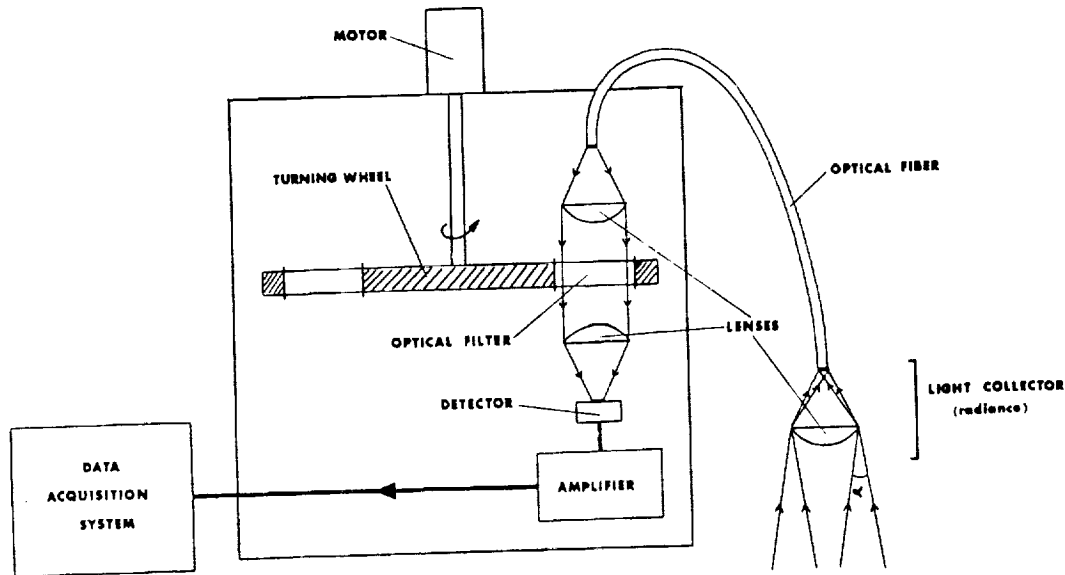


FIG. 1. Radiometer schematic description.

before and after each in situ experiment. The ratio V_1/V_2 was observed to vary little from one calibration to the next, by no more than a few tenths of a percent around the value $1/0.775$.

Figure 3 gives the ratio of the transmission functions, \bar{t}_1 and \bar{t}_2 , for the narrow and wide band channels, respectively, computed with the SS code (Tanré et al. 1985, 1986) for different air masses and atmospheric conditions specified in the code. The salient features

of the SS code are given in the Appendix. In the calculations, the spectral atmospheric transmittance was convoluted with both the spectral response of the interference filters and the spectral response of the detectors. We see that \bar{t}_1/\bar{t}_2 fits fairly well with the law given by (11) and the coefficient β' deduced from the simulation is $0.178 \text{ g}^{-1/2} \text{ cm}$. For a fixed water vapor amount, the dependence of \bar{t}_1/\bar{t}_2 on atmosphere type is negligible. The curve in Fig. 3, which was obtained

TABLE 1. Radiometer characteristics.

Parameter	Value/description
<i>Design Parameters</i>	
Wavelength at half-power points	927-944 nm (narrow), 914-959 nm (wide)
Instantaneous field-of-view (total)	3° (instrument viewing the sun); 11.5° (instrument viewing the surface)
Collecting aperture diameter	3 cm
Rotating wheel (supporting the optical filter)	3 positions (2 filters + a zero); 2 rps
Detector type	photodiodes EG&G (type: HUV 4000)
Detector operating temperature	ambient
Amplifier sensitivity	$S_1: 0.12 \text{ W m}^{-2} \text{ sr}^{-1}/V$; $S_3: 0.46 \text{ W m}^{-2} \text{ sr}^{-1}/V$
Dynamic range	
Narrow-band channel	$0-0.49 \text{ W m}^{-2} \text{ sr}^{-1}$
Broad-band channel	$0-1.84 \text{ W m}^{-2} \text{ sr}^{-1}$
Integration time	0.05 s
Cadence of measurements	1 measurement (2 filters + zero) every 0.5 s
Signal quantizing levels	4096 (12-bit coding)
<i>Noise equivalent radiance</i>	
Narrow-band channel	$S_1: 0.12 \times 10^{-3} \text{ W m}^{-2} \text{ sr}^{-1}$; $S_3: 0.42 \times 10^{-3} \text{ W m}^{-2} \text{ sr}^{-1}$
Broad-band channel	$S_1: 0.46 \times 10^{-3} \text{ W m}^{-2} \text{ sr}^{-1}$; $S_3: 1.61 \times 10^{-3} \text{ W m}^{-2} \text{ sr}^{-1}$
<i>Physical characteristics</i>	
Weight	4 kg
Size	$20 \times 20 \times 24 \text{ cm}$
Power (high/low)	70/25 W

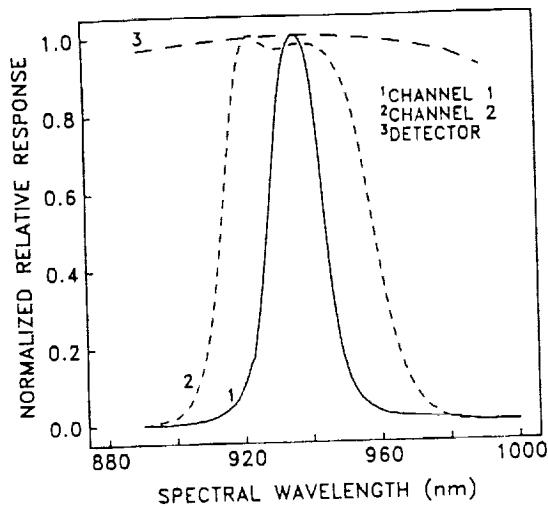


FIG. 2. Spectral response of the interference filters and detectors.

by least-square fitting $\log(\bar{l}_1/\bar{l}_2)$ as a function of $(m^*U_0)^{1/2}$, departs significantly from the simulated points at water vapor amounts above 15 g cm^{-2} . At $m^*U_0 = 17 \text{ g cm}^{-2}$, for instance, the discrepancy in \bar{l}_1/\bar{l}_2 reaches 0.014, which translates into a 10% error on m^*U_0 . Small solar and viewing zenith angles are therefore favored for greater accuracy in the water vapor retrievals. Note also that the radiometer is sufficiently sensitive to \bar{l}_1/\bar{l}_2 variations in the $0\text{--}20 \text{ g cm}^{-2}$ range of water vapor amounts considered in Fig. 3: V_1/V_2 and, hence, \bar{l}_1/\bar{l}_2 , are measured to within a few thousandths.

4. Measurements

a. Ground-based measurements

The two-channel radiometer was used in a sun-viewing configuration from the ground to validate (11) and derive experimentally the coefficient β' . Measurements were made at several locations and various dates in France and Niger: Dinard (48.38°N , 2.03°W) on 20 June 1980; Lille (50.39°N , 3.05°E) on 13 and 15 May 1980; Roscoff (48.43°N , 3.59°W) on 16 September 1980; and Niamey (13.32°N , 2.05°E) on 19, 20, 21, 23, 24, 26, and 29 November and 1, 2, 3, 4, 5, and 7 December 1980. For each day, the data were collected at regular time intervals when $\theta < 80^\circ$ ($1 < m^* < 5$). Radiosonde observations were available for Niamey (one launch per day at 1200 UTC), but not for the other locations. In order to estimate U_0 at those locations, we used 0000 and 1200 UTC radiosonde observations at the nearest launch sites, namely Brest (48.45°N , 4.41°W), Trappes (48.76°N , 2.01°E), and Camborne (50.21°N , 5.31°W) for Dinard and Roscoff, and Uccle (50.80°N , 4.35°E), Crawley (51.08°N , 0.21°W), and Trappes for Lille, and weight-averaged the computed total water vapor amounts according to

distance between the radiosondes and the radiometer. Time differences between radiometer measurements and radiosonde launches were accounted for by linearly interpolating the radiosonde data. The above-described procedure is indeed subject to error, especially since some of the radiosonde sites were located several hundreds of kilometers from the experiment sites. Most of the radiometer data, however, were acquired in Niamey, where radiosondes are launched on a regular basis. Processing the radiosonde data revealed that total water vapor amounts ranged from 1 to 2 g cm^{-2} . This range of U_0 values is small (in a tropical atmosphere, U_0 can exceed 4 g cm^{-2}), but according to theory, \bar{l}_1/\bar{l}_2 is governed by m^*U_0 and not atmosphere type (see Fig. 3). Therefore, calibrating the instrument in the range $1\text{--}2 \text{ g cm}^{-2}$ for U_0 (using m^* from 1 to 5) should also be valid for $U_0 > 2 \text{ g cm}^{-2}$.

Figure 4 shows the ratio of the intercalibrated signals generated in the narrow and wide spectral channels as a function of m^*U_0 , from which β' can be deduced by regression. This was done as for the simulations in Fig. 3. Table 2 gives the values of β' obtained for each day of measurements. The overall mean value of β' is $0.185 \pm 0.14 (1\sigma) \text{ g}^{-1/2} \text{ cm}$. The dispersion of β' , 7.5% (1σ) of the mean value, is due largely to uncertainties in the radiosonde total water vapor amounts [10%–15% errors are frequently reported; for instance, see Richner and Phillips (1982)]. Also, the mean value of β' corresponds fairly well to the value predicted by the 5S code ($0.178 \text{ g}^{-1/2} \text{ cm}$) within the accuracy of this code and experimental uncertainties. We conclude that the two-channel radiometer may derive total water vapor amount with a 15% (1σ) accuracy (a 7.5% uncertainty on β' yields at 15% uncertainty on m^*U_0) using (11),

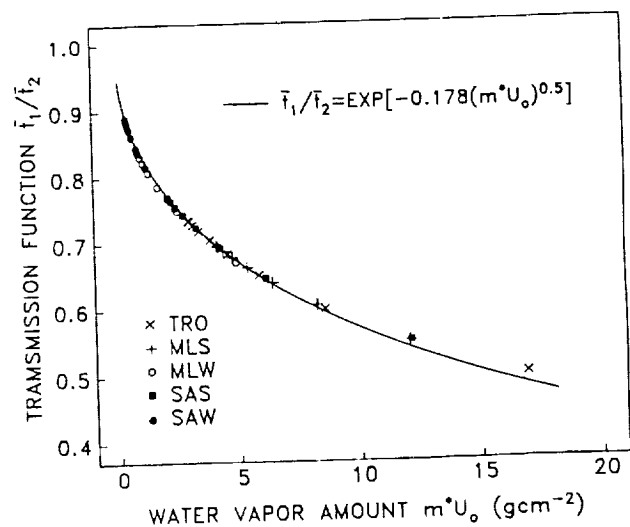


FIG. 3. 5S simulations of the transmission function \bar{l}_1/\bar{l}_2 for different water vapor amounts and atmosphere types (tropical, midlatitude summer, midlatitude winter, subarctic summer, subarctic winter).

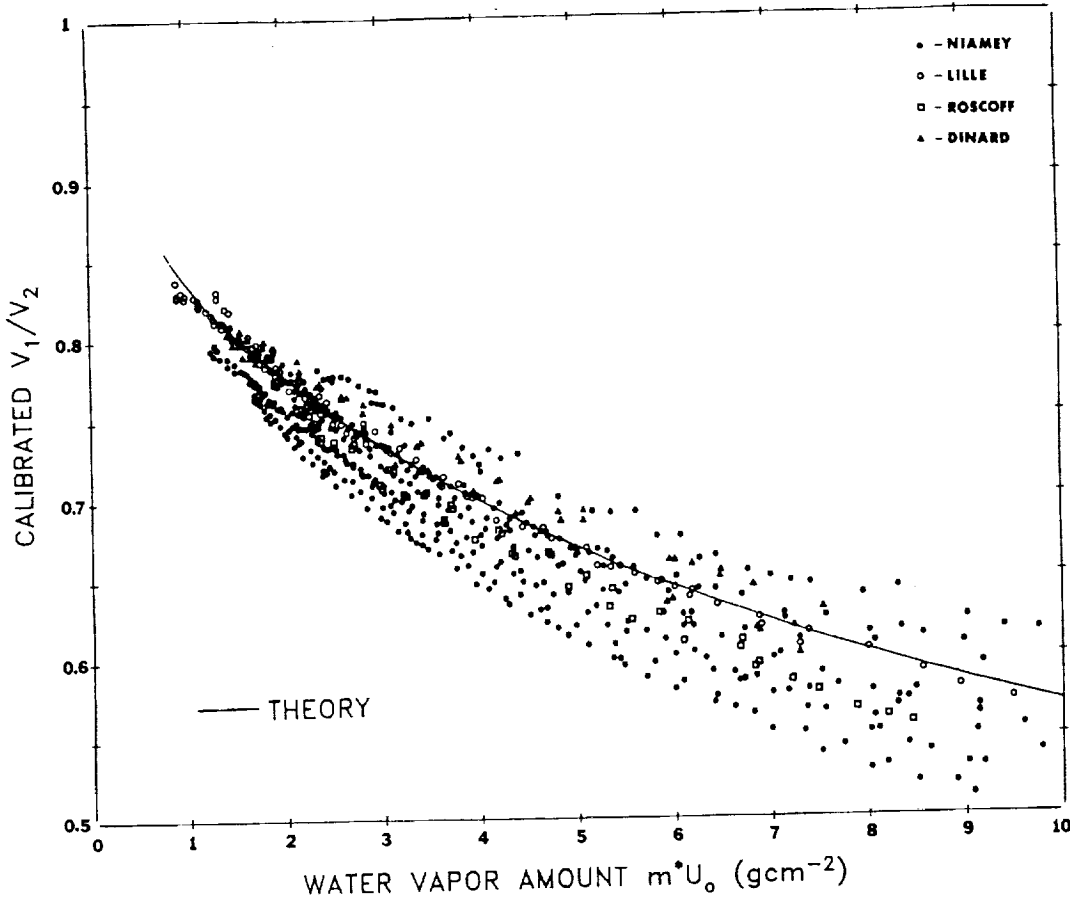


FIG. 4. Ground-based measurements in Lille, Dinard, Roscoff, and Niamey (radiometer viewing the sun): calibrated ratio of voltage outputs V_1 and V_2 as a function of water vapor amount $m \cdot U_0$.

with $\bar{\beta}$ empirically fitted as $0.185 \text{ g}^{-1/2} \text{ cm}$. It is important to emphasize, however, that the 15% accuracy indicated above corresponds to one standard deviation in $\bar{\beta}$ and is therefore valid at the 68% confidence level if we assume a normal distribution of $m \cdot U_0$ values for any V_1/V_2 measurement.

b. Airborne measurements

In order to demonstrate the validity of deriving total water vapor amounts from space by measuring the solar radiation reflected by the Earth's surface, we installed the two-channel radiometer aboard a small aircraft with the light collector viewing the Earth's surface at nadir. Two flights were made on 16 May 1979 and 22 May 1980 over sea and land in the northern part of France. Figure 5 shows the aircraft flight pattern for each day as well as the nearest radiosonde launch sites (Uccle, Trappes, and Crawley), and Table 3 displays the total water vapor amounts at these sites before and after the flights. The aircraft flew over varied surfaces (forest, crops, bare soil, and ocean) whose altitudes did not exceed 100 m above mean sea level.

Figures 6a, 6b, and 6c present the data acquired during the flight of 16 May 1979 at 2800 m altitude over land. The two channels' voltage outputs are plotted as a function of time in Figs. 6a and 6b, respectively, and their calibrated ratio is shown in Fig. 6c. It is striking that each channel output varies rapidly with time, echoing changes in the surface reflectance, while the ratio of these outputs is very independent of the surface properties. This proves quite well that using two channels centered on the same wavelength allows one to eliminate surface reflectance effects. The ratio in Fig. 6c, however, exhibits a few abnormal values. Due to a malfunction of the timing device, the measurement in the narrow band channel was erratically skipped. The problem was corrected prior to the second flight on 22 May 1980.

Figures 7a, 7b, and 7c show the data record for 22 May 1980 when flying at 900 m altitude over land and sea. Again the ratio of the two voltage outputs (Fig. 6c) is quite independent of the surface properties, even when passing from land to sea, and the technique also worked when measuring the small radiation energy reflected by the sea surface.

TABLE 2. Best linear fit between calibrated V_1/V_2 and $\exp[-\beta' \times (m^*U_0)^{1/2}]$ for the different ground-based measurements (instrument viewing the sun). The mean β' value is $0.185 \pm 0.014 \text{ g}^{-1/2} \text{ cm}$.

Location	Date (d/mo/yr)	β' ($\text{g}^{-1/2} \text{ cm}$)	Residual error
Dirard, France (48.38°N, 2.03°W)	22/6/80	0.175	0.008
Lille, France (50.39°N, 3.05°E)	13/5/80	0.117	0.009
	15/5/80	0.165	0.009
Roscoff, France (48.43°N, 3.59°W)	17/9/80	0.189	0.005
Niamey, Niger (13.32°N, 2.05°E)	19/11/80	0.174	0.015
	20/11/80	0.167	0.018
	21/11/80	0.207	0.020
	23/11/80	0.174	0.013
	24/11/80	0.184	0.012
	26/11/80	0.176	0.009
	29/11/80	0.207	0.006
	01/12/80	0.210	0.003
	02/12/80	0.182	0.010
	03/12/80	0.194	0.002
	04/12/80	0.202	0.002
	05/12/80	0.194	0.001
	07/12/80	0.175	0.003

TABLE 3. Radiosonde data used to compute total water vapor amounts along the aircraft flight paths.

Station	Date (d/mo/yr)	Time (UTC)	Water vapor amount U_0 (g cm^{-2})
Crawley	16/5/79	00	2.01
	16/5/79	12	1.94
	22/5/80	00	1.78
	22/5/80	12	1.77
Trappes	16/5/79	00	1.96
	16/5/79	12	1.89
	22/5/80	00	2.27
	22/5/80	12	1.95
Uccle	16/5/79	00	1.87
	16/5/79	12	2.46
	22/5/80	00	2.05
	22/5/80	12	1.78

- When flying at such relatively low altitudes, the water vapor amount along the optical path is not m^*U_0 , with m^* defined in section 2, but

$$U_e = U_0/\cos\theta + U'_0/\cos\theta' \quad (12)$$

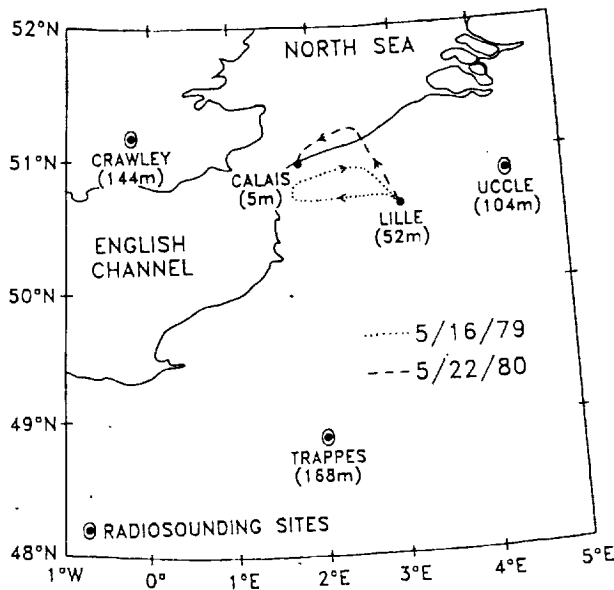


FIG. 5. Aircraft flight pattern for 16 May 1979 and 22 May 1980. The nearest radiosonde launch sites are also shown.

where U'_0 is the water vapor amount along the path from the surface to the flying altitude. Figures 8a and 8b give U_e as a function of time for each flight, deduced from the radiometer measurements and computed from radiosonde observations. The radiosonde data were weight-averaged according to the distance between the launch sites and the aircraft location during the flights, taking into account differences between the altitude of the launch sites and the altitude of the surface viewed by the radiometer. The procedure was performed for times preceding and following the flights, and the resulting water vapor amounts were interpolated linearly with time. As seen in the figures, the agreement between the two types of U_e estimates is fairly good. For the flight of 16 May 1979 (Fig. 8a), the average value of U_e obtained by the differential method is 5.2 g cm^{-2} , and compares with 4.5 g cm^{-2} from the radiosonde data. For the flight of 22 May 1980 (Fig. 8b), the values are 2.2 and 2.6 g cm^{-2} , respectively. These results, however, are not conclusive; they are based on only two flights. Furthermore, uncertainties in the water vapor amounts derived from the radiosonde data may be largely responsible for the discrepancies. A definitive assessment of the method will require more measurements. Perhaps an optimum means of verification would be to install the instrument aboard a helicopter flying above the planetary boundary layer (where most of the water vapor is concentrated) and over surface areas where concurrent high-quality radiosonde observations are made as well as standard sunphotometer measurements.

5. Aerosol contribution to measurement errors

A possible limitation of the method over the ocean should be pointed out. At the very low level of the radiation signal reflected by the sea surface, the aerosol scattering contribution cannot be ignored and may lead to an underestimation of the water vapor amount. Let us assume, for the sake of simplification, that the sur-

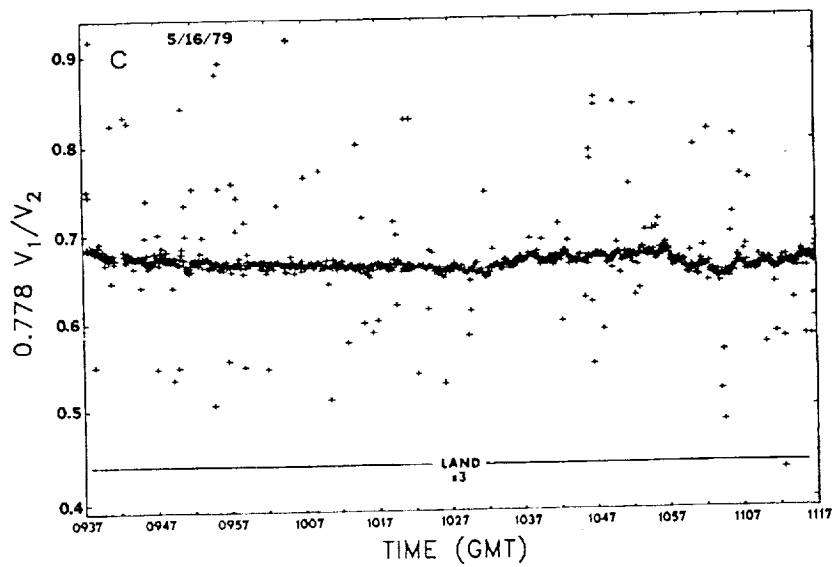
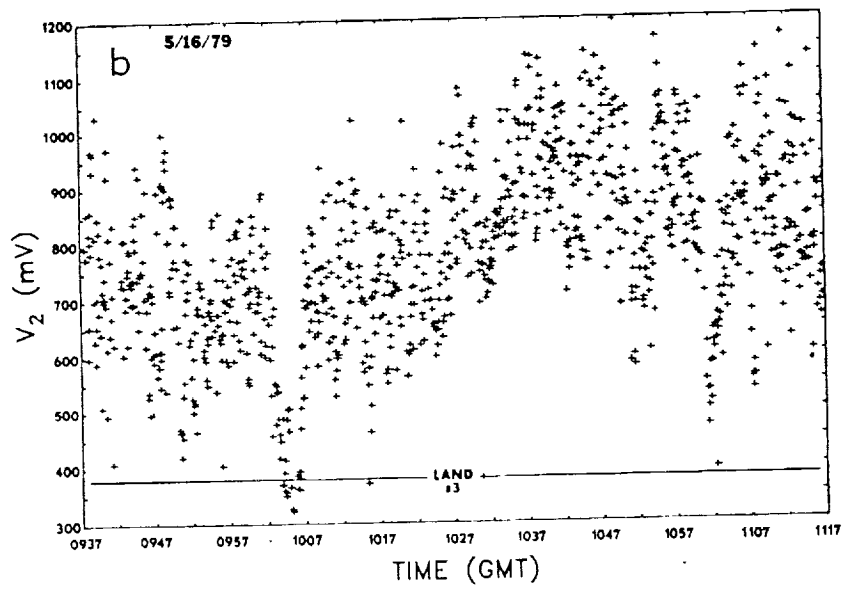
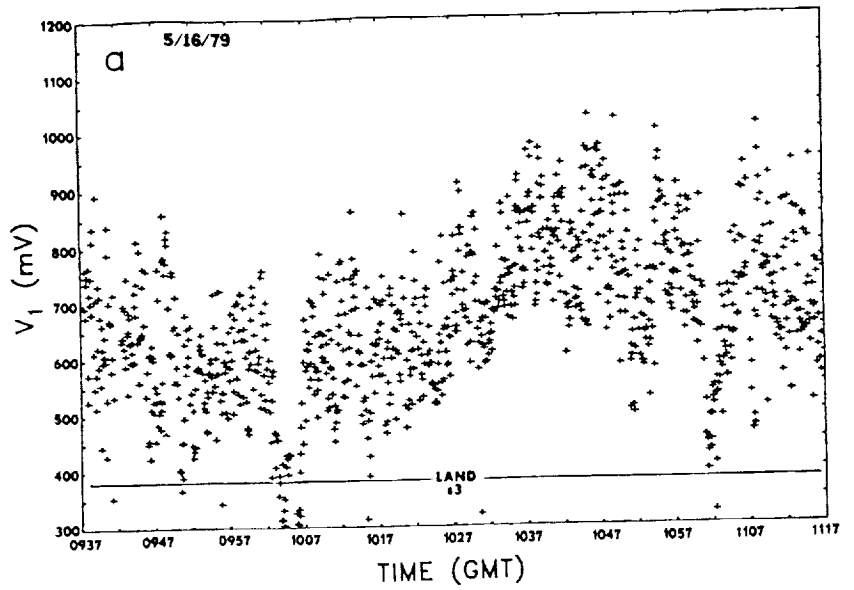


FIG. 6. Flight of 16 May 1979 at 2800 m MSL altitude over land (radiometer viewing the surface): time evolution of the voltage outputs V_1 (a), V_2 (b), and of their calibrated ratio (c).

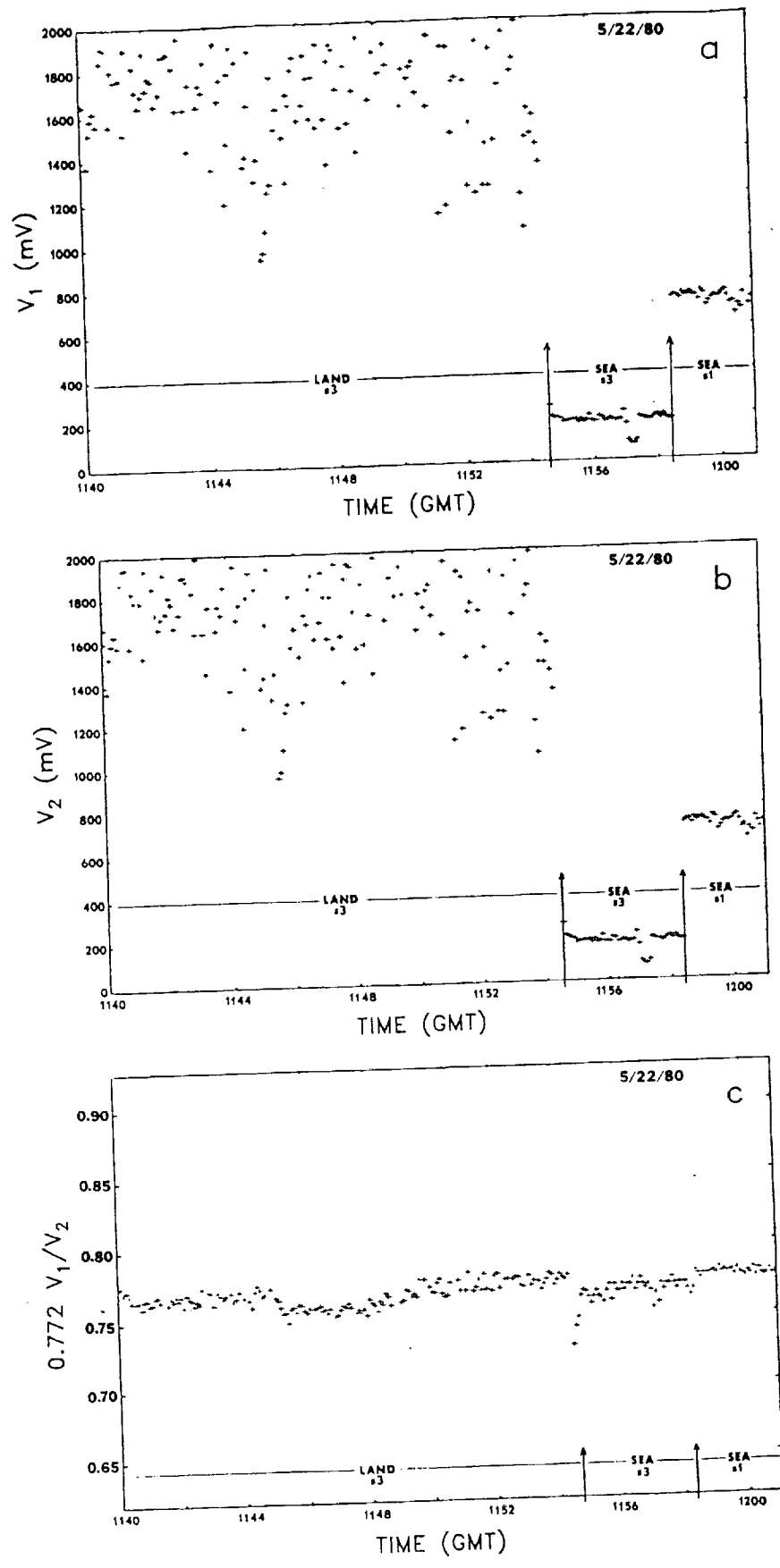


FIG. 7. As in Fig. 5, but for the flight of 22 May 1980 at 900 m MSL altitude over land and sea.

JUNE 1990

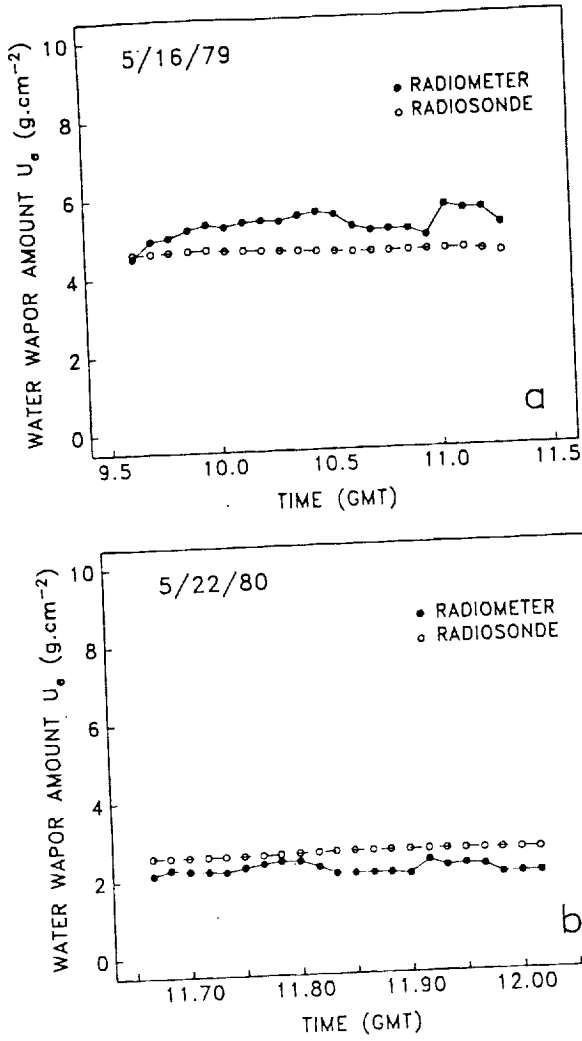


FIG. 8. Time evolution of retrieved and observed water vapor amounts for the flights of (a) 16 May 1979 and (b) 22 May 1980.

face reflectance is null and that the diffuse atmosphere is composed only of aerosols whose concentration decreases exponentially with altitude (optical thickness τ_A , scattering phase function P_A , single scattering albedo $\omega_{0,A}$, scale height H_A). Let us further assume that the aerosol optical properties vary smoothly with wavelength, so that they can be considered equal in the narrow and wide spectral channels. Using the first order scattering approximation, the aerosol atmosphere scatters toward the sensor in channel i the radiance (e.g., Deschamps et al. 1983):

$$L_i = \omega_{0,A} \frac{P_A}{4 \cos \theta'} \frac{I_i}{\pi} \int_0^\infty \bar{i}_i(z, \infty) \frac{d\tau_A(z)}{dz} dz. \quad (13)$$

In this expression, $\bar{i}_i(z, \infty)$ and $d\tau_A(z)/dz$ can be written:

$$\bar{i}_i(z, \infty) \approx \exp\{-\bar{\beta}_i[m^*U(z, \infty)]^{1/2}\} \quad (14)$$

$$\frac{d\tau_A(z)}{dz} = -\frac{\tau_A}{H_A} \exp\left(-\frac{z}{H_A}\right) \quad (15)$$

where $U(z, \infty)$ is the vertically integrated water vapor amount between altitude z and the top of the atmosphere.

Developing the right-hand side of (14) to first order in $U(z, \infty)$ and taking $U(z, \infty) = U_0 \exp(-z/H_W)$ yields

$$\bar{i}_i(z, \infty) \approx 1 - \bar{\beta}_i(m^*U_0)^{1/2} \exp\left(-\frac{z}{2H_W}\right). \quad (16)$$

Although this approximation for $\bar{i}_i(z, \infty)$ is not verified (by definition, water vapor absorption is strong in the 940 nm band), it is sufficient to provide the order of magnitude of the aerosol backscattering effect on the differential method's accuracy.

Substituting (15) and (16) into (13), one can easily evaluate the integral on the right-hand side of (13), which gives

$$L_i \approx \omega_{0,A} \frac{P_A \tau_A}{4 \cos \theta'} \frac{I_i}{\pi} \times \left[1 - \bar{\beta}_i(m^*U_0)^{1/2} \left(\frac{2H_W}{H_A + 2H_W} \right) \right]. \quad (17)$$

Since the ratio of the radiometer voltage outputs in the narrow and wide spectral channels is proportional to L_1/L_2 , we have

$$\frac{V_1}{V_2} \sim \frac{I_1}{I_2} \frac{1 - \bar{\beta}_1 \left[m^*U_0 \left(\frac{2H_W}{H_A + 2H_W} \right)^2 \right]^{1/2}}{1 - \bar{\beta}_2 \left[m^*U_0 \left(\frac{2H_W}{H_A + 2H_W} \right)^2 \right]^{1/2}}. \quad (18)$$

Thus, the total water vapor amount detected is

$$U_{0a} \approx U_0 \left(\frac{2H_W}{H_A + 2H_W} \right)^2. \quad (19)$$

Taking typical values of 0.5 km (e.g., Patterson et al. 1980) and 2 km (e.g., Roll 1965) for H_A and H_W , respectively, over the ocean, we obtain $U_{0a} \approx 0.79U_0$, which indicates that the retrieved total water vapor amount is underestimated by 21%. If H_A is higher or $H_A \approx H_W$, the error becomes unacceptable. One has to point out, however, that (19) gives a superior error limit. As soon as the surface reflectance reaches a few percent, the contribution to L_i of photons reflected by the surface generally surpasses that of photons uniquely backscattered by the atmosphere.

In fact, no noticeable decrease in U_e is observed on 22 May 1980 when passing from land to sea around 11.9 UTC (Fig. 8b). On the contrary, U_e increased from 2.0 to 2.3 g cm⁻². This change may be attributed to the amplifier sensitivity S_3 used over land, which is not adapted to measurement over the ocean. After

switching to the more appropriate sensitivity S_1 , U_e quickly recovered the value of 2.0 g cm^{-2} observed over land.

6. Summary and concluding remarks

From the ground-based measurements, we have first shown that the differential technique can be used to derive total water vapor amounts by viewing the sun through the atmosphere in two channels of different spectral bandwidths centered on the same wavelength near 940 nm. The experiment was calibrated by comparing the ratio of the radiometric outputs generated for the two channels with water vapor amounts deduced from radiosonde observations. The relative accuracy of the water vapor retrievals is 15% (1σ). This value, however, incorporates uncertainties in the radiosonde data (including space and time interpolation errors), so that the actual accuracy is likely to be better, probably around 5%.

The two-channel radiometer was then used in an airborne configuration, measuring the solar radiation reflected by the Earth's surface. In this configuration, the instrument was able to yield a measure of the water vapor amount along the optical path independent of the surface nature, even for the lower radiation signals reflected by the sea surface. In the presence of thick aerosol layers, however, the water vapor amounts derived over the ocean may be underestimated by as much as 20%. One way to remove this limitation, at least partially, is to view the sea surface in the sun glint, which substantially increases the contribution of the signal reflected by the sea surface. Additionally, viewing the sea surface inside and outside the sun glint region would provide information on the ratio of aerosol and water vapor scale heights by giving access to U_0 and U_{0a} [see Eq. (19)].

We conclude by suggesting that the differential absorption technique presented herein can be applied to yield accurate space observations of total water vapor amounts under clear sky conditions over land and sea. Compared to satellite microwave techniques, which are preferred over the ocean since they are applicable in almost all weather conditions, our technique has the advantage of simplicity and would complement the microwave techniques over land where they fail. Interestingly, the Earth Observing System of the 1990s will carry the High Resolution Imaging Spectrometer (HIRIS), an instrument that possesses adequate channels to exploit our differential absorption concept.

Acknowledgments. This work was supported by the Centre National d'Etudes Spatiales, the Centre National de la Recherche Scientifique, and the California Space Institute. The authors gratefully acknowledge C. Verwaerde for realizing the electronics of the radiometer, J. Y. Balois for his help in taking the measurements, C. Deroo for her programming support, B.

Bloomfield for editing suggestions, and R. Markworth for typing the manuscript. One of us, R. Frouin, wishes to thank E. Maes for his assistance in pre- and postflight operations at the Lille-Bondues airport.

APPENDIX

The 5S Code

The Simulation of the Satellite Signal in the Solar Spectrum (5S) code (Tanré et al. 1985, 1986) computes the solar radiation backscattered to space by the Earth-atmosphere system as it may be observed by a satellite sensor. Given a Lambertian ground target, the code estimates the target's apparent reflectance by taking into account the effects of gaseous absorption, scattering by molecules and aerosols, and spatial inhomogeneities in the surface reflectance. The input parameters, namely, solar and viewing geometries, atmosphere model, surface reflectance, and spectral band, can either be specified from standard conditions or user-defined. In addition to apparent reflectance, the code provides gaseous transmittance and irradiance at the surface, as well as the various components of the satellite signal. Complementary results are also available; exact calculations at selected wavelengths, in particular, allow one to assess the code accuracy.

Based on Tanré et al. (1979), the satellite signal is expressed as a function of the successive orders of radiation interactions in the coupled surface-atmosphere system. If ρ is the reflectance of the target, and ρ_e that of its environment, the apparent reflectance is written as

$$\rho^*(\theta, \theta', \phi) = t_g(\theta, \theta') \left\{ \rho_a(\theta, \theta', \phi) + \frac{[e^{-\tau/\cos\theta} + t_d(\theta)]}{1 - \rho_e S} [\rho e^{-\tau/\cos\theta'} + \rho_e t_d(\theta')] \right\} \quad (\text{A1})$$

where θ and θ' are the sun and satellite zenith angles, respectively, ϕ the relative azimuth between sun and satellite directions, τ the atmospheric optical thickness, t_g the gaseous transmittance, t_d the atmospheric diffuse transmittance, and S the spherical albedo of the atmosphere. The first term enclosed by the curly brackets represents the contribution of photons backscattered to space without surface reflection, whereas the second term characterizes photons that have sustained one or multiple surface reflections. Absorption by atmospheric gases is considered as a single multiplicative factor dependent on the direct paths sun-to-surface and surface-to-sensor. Decoupling absorption and scattering processes are justified since, on the one hand, ozone is located at altitudes where molecules are rarefied, and on the other, water vapor and carbon dioxide absorption occur above 850 nm where molecular scattering is negligible, and first and second orders of aerosol scattering (predominantly forward) reconstitute almost all

of the diffuse radiation. According to Tanré et al. (1986), the error introduced by separating the two processes is smaller than one percent, except for grazing incidence or observation directions ($\cos\theta, \cos\theta' < 0.1$).

The atmospheric functions t_d and S are approximated by analytical formulas determined empirically from exact radiative transfer computations performed for a wide range of model atmospheres. Table A1 shows the disparity between 5S and exact calculations of the total atmospheric diffuse transmittance, $e^{-\tau/\cos\theta} + t_d(\theta)$, for various solar zenith angles and wavelengths. Calculations were made for two atmospheres, clear and hazy. The differences are small, generally less than 1%, but may reach over 2% (hazy atmosphere, $\theta = 60^\circ$).

The gaseous transmittance, t_g , is computed from two exponential random band models, that of Goody (1964) for water vapor, and of Malkmus (1967) for oxygen, ozone, and carbon dioxide. The spectral resolution, 20 cm^{-1} , is sufficient (contains enough spectral lines) to apply the random band models confidently. Figure A1 compares the gaseous transmittance in the spectral region of the 940 nm water vapor band computed using the 5S code and with a well-known code, LOWTRAN-6 (Kneizys et al. 1983). For the tropical and midlatitude summer atmospheres considered, the agreement is good near the peak water of vapor absorption, but notable differences exist in the wings of the band. We recall here that for computational efficiency, LOWTRAN-6, unlike 5S, neglects the influence of temperature on the molecular absorption coefficient, and approximates molecular line absorption by a one parameter band model. Nevertheless, integration over the wavelength range of the narrow and wide band-passes considered in the present study provides very similar results with both codes.

TABLE A-1. Comparison between 5S and exact calculations of the total atmospheric diffuse transmittance.

Wavelength (nm)	$\theta = 15^\circ$		$\theta = 60^\circ$	
	5S	Exact	5S	Exact
<i>Clear atmosphere</i>				
450	.877	.873	.755	.753
550	.930	.928	.841	.839
650	.954	.953	.885	.883
850	.973	.973	.926	.924
1600	.988	.989	.966	.963
2200	.992	.993	.976	.975
<i>Hazy atmosphere</i>				
450	.810	.806	.648	.633
550	.866	.864	.721	.705
650	.895	.895	.766	.750
850	.926	.927	.819	.806
1600	.963	.964	.899	.890
2200	.973	.976	.925	.921

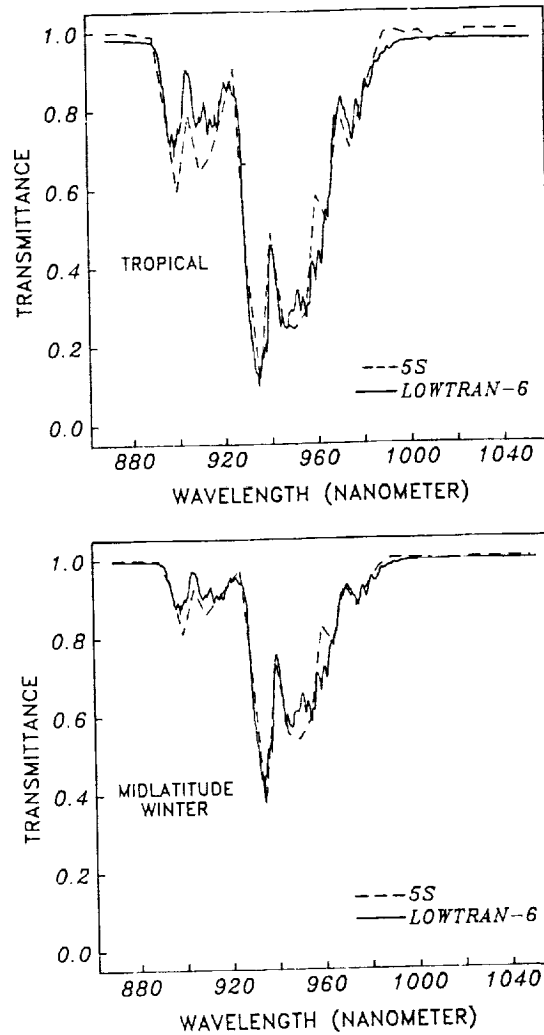


FIG. A-1. Gaseous transmittance along a vertical path sun-to-surface computed with 5S and LOWTRAN-6 for tropical and midlatitude winter atmospheres.

REFERENCES

Chang, A. T. C., and T. T. Wilheit, 1979: Remote sensing of atmospheric water vapor, liquid water and wind speed at the ocean surface by passive microwave techniques from the NIMBUS-5 satellite. *Radio Sci.*, **14**, 793-803.

Deschamps, P. Y., M. Herman, and D. Tanré, 1983: Modélisation du rayonnement réfléchi par l'atmosphère et la terre, entre 0,35 et 4 μm . ESA Rep. 4393/80/F/DD(SC), Eur. Space Agency, 165 pp.

Foskett, L. W., and N. B. Foster, 1943: A spectroscopic hygrometer. *Bull. Amer. Meteor. Soc.*, **24**, 146-153.

Fowle, F. E., 1912: The spectroscopic determination of aqueous vapor. *Astrophys. J.*, **35**, 149-162.

—, 1913: The determination of aqueous vapor above Mount Wilson. *Astrophys. J.*, **37**, 359-372.

Gates, D. M., 1956: Infrared determination of precipitable water in a vertical column of the earth's atmosphere. *J. Meteor.*, **13**, 369-375.

Goody, R. M., 1952: A statistical model for water vapour absorption. *Quart. J. Roy. Meteor. Soc.*, **78**, 165-169.

—, 1964: *Atmospheric Radiation, I: Theoretical Basis*. Clarendon Press, 436 pp.

- Grody, N. C., A. Gruber and W. C. Shen, 1980: Atmospheric water content over the tropical Pacific derived from the NIMBUS-6 scanning microwave spectrometer. *J. Appl. Meteor.*, **19**, 986-996.
- Hand, J. F., 1940: An instrument for the spectroscopic determination of precipitable atmospheric water vapor and its calibration. *Mon. Wea. Rev.*, **68**, 95-98.
- Kasten, F., 1966: A new table and approximation formula for the relative optical air mass. *Arch. Meteor. Geophys. Bioklimatol.*, **B14**, 206-223.
- Kneizys, F. X., E. P. Shettle, W. O. Gallery, J. H. Chetwynd, Jr., L. W. Abreu, J. E. A. Selby, S. A. Clough and R. W. Fenn, 1983: Atmospheric transmittance/radiance: computer code LOWTRAN 6. *Envir. Res. Pap. No. 846*, AFGL-TR-83-0187, Hanscom AFB, Massachusetts, 200 pp.
- Malkmus, W., 1967: Random Lorentz band model with exponential-tailed S-1 line intensity. *J. Opt. Soc. Am.*, **57**, 323-329.
- Paltridge, G. W., and C. M. R. Platt, 1976: *Radiative Processes in Meteorology and Climatology*. Elsevier Scientific, 318 pp.
- Patterson, E. M., C. S. Kiang, A. C. Delany, A. F. Wartenburg, A. C. D. Leslie and B. J. Huebert, 1980: Global measurements of aerosols in remote continental and marine regions: Concentrations, size distributions, and optical properties. *J. Geophys. Res.*, **85**, 7361-7376.
- Pitts, D. E., W. E. McCallum, M. Heidt, K. Jeske, J. T. Lee, D. De Monbrun, A. Morgan and J. Potter, 1977: Temporal variations in atmospheric water vapor and aerosol optical depth determined by remote sensing. *J. Appl. Meteor.*, **16**, 1312-1321.
- Prabhakara, C., D. Chang and T. C. Chang, 1981: Remote sensing of precipitable water over the oceans from NIMBUS-7 microwave measurements. *J. Appl. Meteor.*, **21**, 59-68.
- Reagan, J. A., K. Thome, B. Herman and R. Gall, 1987: Water vapor measurements in the 0.94 micron absorption band: calibration, measurements, and data applications. *Proceedings of IGARSS 87 Symposium, Ann Arbor, Michigan*, 63-67.
- Richner, H., and P. D. Phillips, 1982: The radiosonde intercomparison: SONDEX, Spring 1981, Payenne. *Pure Appl. Geophys.*, **120**, 852-1198.
- Roll, H. U., 1965: *Physics of the Marine Atmosphere*. Academic Press, 426 pp.
- Selby, J. E. A., F. X. Kneizys, J. H. Chetwynd and R. A. McClatchey, 1978: Atmospheric transmittance/radiance computer code LOWTRAN-4. AFGL-TR-0053 *Envir. Res. Paper No. 587*, 79 pp.
- Siversten, S., and J. F. Solheim, 1975: A field instrument for water vapor measurements. *Infrared Phys.*, **15**, 79-82.
- Smith, W. L., 1983: The retrieval of atmospheric profiles from VAS geostationary radiance observations. *J. Atmos. Sci.*, **40**, 2025-2035.
- , and H. M. Woolf, 1976: The use of eigenvectors of statistical covariance matrices for interpreting satellite sounding radiometer observations. *J. Atmos. Sci.*, **33**, 1127-1140.
- Staelin, D. H., W. H. Ledsham, R. L. Pettyjohn, P. W. Rosenkranz, R. K. L. Poon and J. W. Waters, 1976: Microwave sensing of atmospheric temperature and humidity from satellites. *Space Research XVI*, M. J. Rycroft, Ed., Akademie-Verlag.
- Stephens, G. L., 1984: A review of the parameterizations of radiation for numerical weather prediction. *Mon. Wea. Rev.*, **112**, 826-867.
- Tanré, D., M. Herman, P. Y. Deschamps and A. Deleffe, 1979: Atmospheric modeling for measurements of ground reflectances, including bidirectional properties. *Appl. Opt.*, **18**, 3587-3596.
- , C. Deroo, P. Duhaut, M. Herman, J. J. Morcrette, J. Perbos and P. Y. Deschamps, 1985: Effets atmosphériques en télédétection-logiciel de simulation du signal satellitaire dans le spectre solaire. *Proc. Third Int. Colloq. on Spectral Signatures of Objects in Remote Sensing, Les Arcs, France*, 315-319.
- , —, —, —, —, —, and —, 1986: Simulation of the Satellite Signal in the Solar Spectrum (5S). Internal Report, Laboratoire d'Optique Atmosphérique, Université de Lille, France, 267 pp.

PREV. ANN.
92N 11474

Appendix 9

OPTIMUM COMBINATIONS OF VISIBLE AND NEAR-INFRARED
REFLECTANCES FOR ESTIMATING THE FRACTION OF
PHOTOSYNTHETICALLY AVAILABLE RADIATION ABSORBED BY PLANTS

A. Podaire, P.-Y. Deschamps, R. Frouin, A. Asrar
*Proc. 5th Int. Col. on Physical Measurements and Signatures in Remote
Sensing, Courchevel, France, January 14-18, 1991, ESA SP-319, 405-408*

OPTIMUM COMBINATIONS OF VISIBLE AND NEAR-INFRARED REFLECTANCES FOR ESTIMATING THE FRACTION OF PHOTOSYNTHETICALLY AVAILABLE RADIATION ABSORBED BY PLANTS

A. Podaire¹, P.Y. Deschamps², R. Frouin³, G. Asrar⁴

¹ Centre National d'Etudes Spatiales; ² Laboratoire d'Optique Atmosphérique;
³ California Space Institute, Scripps Institution of Oceanography;
⁴ National Aeronautics and Space Administration

ABSTRACT

A useful parameter to estimate terrestrial primary productivity, that can be sensed from space, is the daily-averaged fraction of photosynthetically available radiation (PAR) absorbed by plants. To evaluate this parameter, investigators have relied on the fact that the relative amount of radiation reflected by a vegetated surface in the visible and near-infrared depends on the fraction of the surface covered by the vegetation and, therefore, correlates with absorbed PAR. They have used vegetation indices, namely normalized difference and simple ratio, to derive absorbed PAR, even from coarse spatial resolution sensors such as the Advanced Very High Resolution Radiometer (AVHRR) aboard the NOAA satellites. The problem with normalized difference and simple ratio is first, they are non-linear functions of radiance or reflectance and, therefore, cannot be readily applied to heterogeneous targets, second, they are used in generally non-linear relationships, which make time-integrals of the indices not proportional to primary productivity, and third, the relationships depend strongly on the type of canopy and background. To remove these limitations, we propose linear combinations of visible and near-infrared reflectances at optimum (one or two) viewing zenith angles.

Keywords: radiation, plants, primary production.

1. INTRODUCTION

Land primary productivity, or the rate at which materials from the atmosphere and soils are accumulated into biomass through photosynthesis, is of great importance. The reasons are numerous and have been discussed extensively in the literature (see, for instance, Ref. 1). Basically, the major portion of human food is provided by plants growing over land. Land primary productivity also affects the environmental context in which man and societies develop. In addition to its key role in sustaining human populations and structuring communities, land primary productivity governs to a large extent the seasonal oscillations of atmospheric carbon dioxide and impacts the water and energy available to the atmosphere. Anthropogenic changes, such as those linked to the destruction of major vegetation systems, have potential implications on climate. If we are to truly understand the interactions between the terrestrial biosphere and the atmosphere and their effects on climate, we need to know the geographic distribution and temporal variability of land primary productivity over the globe.

To achieve this goal, satellite observations are essential. A promising technique for sensing primary productivity from space, at least in the case of light-limited situations, incorporates the fact that the growth rate of many plants is close to proportional to the rate at which radiant solar energy is absorbed by the foliage (Ref. 2):

$$PP = \epsilon f_{PAR} PAR \quad (1)$$

where PAR is the incident photosynthetically active radiation, practically the solar radiation reaching the canopy in the 0.4-0.7 μ m spectral interval, f_{PAR} is the fraction of PAR intercepted by

the canopy, and ϵ is an efficiency factor for carbon fixation that depends slightly on plant type, temperature, and available soil water. For various canopies (mostly crops), ϵ has been found to lie between 1.1 and 1.4 g C per MJ of PAR (Ref. 3).

Photosynthetically active radiation represents a nearly constant fraction of total insolation (e.g. Ref. 4), and total insolation can be retrieved accurately from satellite observations (e.g., Refs. 5, 6, 7, 8). Direct satellite estimates of PAR can also be obtained, as recent studies demonstrate (e.g., Ref. 9).

The absorbed fraction of PAR can be estimated from vegetation indices, the most commonly used being simple ratio, SR and normalized difference, ND . These indices are defined by:

$$SR = \frac{R_N}{R_V} \quad (2)$$

$$ND = \frac{R_N - R_V}{R_N + R_V} \quad (3)$$

where R_V and R_N are upwelling radiances in the visible and near-infrared (for instance radiances in channels 1 and 2 of the Advanced Very High Resolution Radiometer aboard NOAA satellites), respectively. Instead of radiances, reflectances are also used. That SR and ND are sensitive to f_{PAR} results from the characteristic spectrum of sunlight reflected by leaves, which is distinct from that of sunlight reflected by soils. Chlorophyll pigments absorb a large fraction of the light which reaches them in the visible, but not in the near-infrared where scattering by the chloroplasts is effective. This is not the case of soils, whose reflectance increases more linearly with wavelength in the visible and near-infrared. It follows that the relative amount of radiation reflected by a vegetated surface in the visible and near-infrared depends on the fraction of the surface covered by vegetation and, therefore, correlates with f_{PAR} .

Several theoretical studies have predicted how SR and ND relate to f_{PAR} (e.g., Refs. 2, 10, 11, 12, 13). Kumar (Ref. 2) suggested a near-linear relationship between SR and f_{PAR} . Asrar et al. (Ref. 10) and Sellers (Refs. 11, 12) showed that f_{PAR} should vary non-linearly with SR , but almost linearly with ND . Choudhury (Ref. 13) found that the relationships between f_{PAR} and vegetation indices are generally non-linear. Soil reflectance changes, in particular, appeared to significantly affect the linearity of the relationships.

Experimental studies (e.g., Refs. 2, 14, 15, 16, 17) have also provided disparate results and, therefore, did not resolve the apparent theoretical controversy. Kumar (Ref. 2), for instance, observed that SR is linearly related to f_{PAR} for sugar beet, which supported their theoretical analysis, yet Steven et al. (Ref. 14) reported an exponential relationship. In short, the observations indicate that the relationships between f_{PAR} and vegetation indices depend strongly on the type of canopy and underlying surface, as pointed out by Choudhury (Ref. 13).

That the interdependence of f_{PAR} and vegetation indices is linear or non-linear is an important issue because linearity implies that the time-integral of SR and ND should also be linearly related to primary production (e.g., Refs. 11, 12, 18). Even though serious doubts exist about the linearity of the relationships, especially when considering various ecosystems and climates, Tucker et al. (Ref. 19) and Goward et al. (Refs. 20, 21) have reported agreement between ND time-integrals obtained from AVHRR data over the Senegalese Sahel and North and South American biomes, respectively, and published production rates.

Using SR or ND for estimating f_{PAR} has several limitations. First, as mentioned above, the relationships are generally non-linear, which makes SR and ND time-integrals not proportional to primary production. Second, SR and ND are non-linear functions of radiance. Since vegetation is highly heterogeneous spatially, sub-pixel variability is likely to introduce uncertainties in SR and ND , particularly when the sensor spatial resolution is coarse (case of AVHRR). For such sensors, which have the advantage of frequent global coverage, applying relationships established for homogeneous canopies is not satisfactory. Third, satellite-derived SR and ND may reduce to some extent the effects of sensor calibration uncertainties and atmospheric interference, yet they depend on atmospheric composition, in particular aerosol and water vapor amounts, and viewing geometry (e.g., Ref. 22). Even time series of maximum AVHRR vegetation indices over a several-day period, which correspond to minimum atmospheric contamination, remain relatively noisy, and it has not yet been possible to identify whether the noise is due to residual variations in the atmospheric contribution or to variable directional surface properties. We need to address these limitations if we are to remotely sense f_{PAR} from space accurately.

Our objective, therefore, and the purpose of this paper, is to define optimum combinations of visible and near-infrared reflectances that: a) relate linearly to f_{PAR} ; b) can be used independently of the type of foliage and substrate; c) eliminate the effects of sub-pixel spatial heterogeneity; and d) improve the accuracy of f_{PAR} estimates when compared to SR and ND .

2. METHODOLOGY

Instead of using radiance ratios, we express f_{PAR} as a linear combination of visible and near-infrared radiances or, equivalently, reflectances. This procedure, when applied to a coarse resolution sensor such as AVHRR, should eliminate or, at least, substantially reduce sub-pixel variability effects. Linear combinations of reflectances, known as "greenness" transformations, have been used for many years to study vegetation parameters, in particular by Hatfield et al. (Ref. 15) and Asrar et al. (Ref. 17). These authors found that greenness obtained by combining reflectances measured by a Barnes Modular Multispectral Radiometer (MMR) in two visible and two near-infrared bands is a much more linear predictor of f_{PAR} than simple ratio and normalized difference. They did not favor greenness, however, because of the smaller sensitivity of this index to f_{PAR} and the strong dependence of the relationship between f_{PAR} and greenness upon solar zenith angle and canopy geometry. If known (e.g., from theoretical calculations), the dependence upon solar angle or, more generally, radiation geometry, should not be a problem because solar and viewing angles can be determined exactly. The problem is to eliminate the effects of variable canopy geometry and soil reflectance in the relationships. Given a sun position, this may be possible for specific viewing angles.

Our approach, therefore, is to simulate for varied soil and canopy parameters, namely leaf optical properties, soil reflectance, leaf area index (LAI), and leaf inclination distribution function (LIDF), above-canopy visible and near-infrared reflectances as well as f_{PAR} and daily averaged (weighted by incident radiation) f_{PAR} . The simulations are performed with the SAIL canopy reflectance model (Ref. 23). Various radiation geometries (solar and viewing zenith angles, relative azimuth angle) are considered, as well as direct and diffuse fractions of incident solar radiation. The absorbed fraction of PAR, f_{PAR} , is computed as a function of solar zenith angle and f_{PAR} as a function of latitude and season. From the reflectances, simple ratio and normalized difference are derived.

We focus on \bar{f}_{PAR} since this parameter rather than f_{PAR} is required in

primary productivity models. In addition, since the sensors potentially useful to monitor land primary productivity from space are, or will be carried by heliosynchronous satellites (AVHRR on the NOAA series, the POLarization and Directionality of the Earth Reflectance instrument, POLDER, on ADEOS, and the MODerate resolution Imaging Spectrometer, MODIS, on EOS) and, therefore, offer the possibility of viewing the same target under one or several geometries during a several-day period, we attempt to estimate \bar{f}_{PAR} from single or multi-angle combinations of visible and near-infrared reflectances. Indeed, the multi-angle approach is only suitable when the characteristics of the surface target do not change significantly over the several-day period.

Thus, we regress \bar{f}_{PAR} at each latitude and month during the year against simple ratio, normalized difference, and visible and near-infrared reflectances. One and two viewing geometries are considered for the combinations of reflectances. The regression statistics, namely correlation coefficient, regression coefficients, and residual error of estimate are analyzed to determine the solar and viewing angles that minimize the effects of variable LIDF and soil reflectance. The improvement in the predicting power of the linear combinations is also assessed.

3. RESULTS

To illustrate our theoretical approach and show the promise of linear combinations, Figs. 1, 2, and 3 display selected results obtained with the SAIL model. The calculations were performed for LAIs of 0.01, 0.05, 0.1, 0.2, 0.5, 1, 2, and 5, erectophile, spherophile, and planophile canopies, soil reflectances of 0.1, 0.2, 0.3, and 0.4, and typical leaf optical properties (reflectance and transmittance of 0.1 and 0.001, respectively, in the visible, and 0.45 and 0.4 in the near-infrared). The soil reflectance was assumed white spectrally, and the various LIDFs were considered conjointly in the regressions. A US 62 standard atmosphere (Ref. 24) containing continental aerosols (Ref. 25) was overlying the canopy. We see in Fig. 1 (bottom) that the influence of the background on the \bar{f}_{PAR} versus ND relationships is substantial, especially at moderate LAIs, but is reduced considerably when using linear combinations of reflectances (Fig. 2, bottom). In this case, the points corresponding to a same LAI are generally more aligned with the best fit line. The result is a drastic improvement in the \bar{f}_{PAR} residual error. For the solar and viewing geometries of Figs. 1 and 2, bottom, the residual error is reduced from 0.058 to 0.033. When using ND the minimum residual error is obtained for a nadir viewing (Fig. 1, top), but when using linear combinations it is preferable to view the canopy at a 45° zenith angle (Fig. 2, top). The \bar{f}_{PAR} residual error can be further reduced by combining linearly visible and near-infrared reflectances at two viewing zenith angles (Fig. 3). Using reflectances at nadir and 60° from zenith, for instance, reduces the \bar{f}_{PAR} residual error to 0.026 (Fig. 3, bottom). Smaller residual errors can even be obtained when the second viewing zenith angle is as far as possible from nadir (Fig. 3, top).

The above results, however, are only valid for a sun at 60° of zenith in July and at 45° latitude. For a sun closer to zenith, the minimum \bar{f}_{PAR} residual error is encountered at higher viewing zenith angles when using ND , for instance at 45° when the sun is at 30° from zenith. In the case of uni-angle linear combinations, the minimum at 45° (Fig. 3, top) moves to 60° when the sun zenith angle decreases to 30°. The picture is more complex with multi-angle combinations because of the many angular possibilities. In general, for a particular sun configuration, several viewing zenith angle pairs provide similar good results (\bar{f}_{PAR} residual error around 0.020). For a sun at 30° from zenith, for instance, viewing at nadir, 15°, or 30° from zenith and at 75° from zenith gives residual errors ranging from 0.019 to 0.021. The regression coefficients, however, are quite sensitive to the viewing geometries selected.

4. DISCUSSION

The results presented in section 3, although encouraging, should be interpreted with caution. No hasty generalization can be made at this point. First, the SAIL model has often showed weaknesses when compared to measurements; it does not predict a hot spot and is only appropriate for agricultural plants that form a layer-type canopy. More accurate canopy reflectance models may be used, at least to provide a reference. Second, the background reflectance

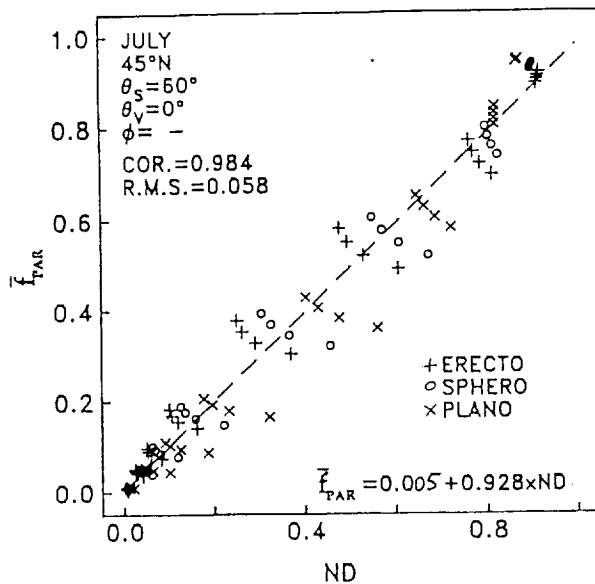
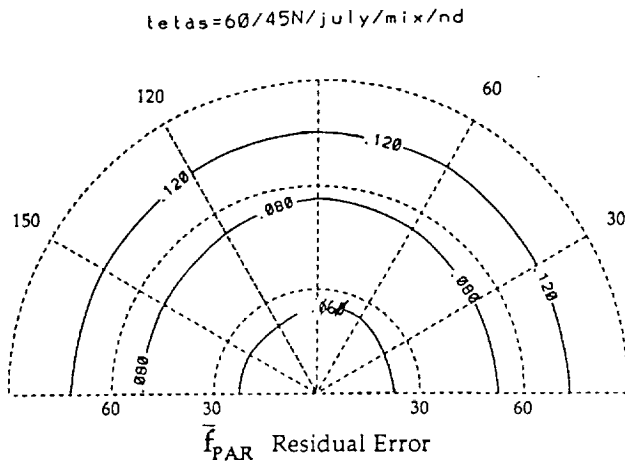


Fig. 1 Top: \bar{f}_{PAR} residual error as a function of viewing geometry for a sun at 60° from zenith in July at $45^\circ N$. In the calculations, \bar{f}_{PAR} estimated from normalized difference, ND, is compared to \bar{f}_{PAR} obtained with the SAIL model. Bottom: scatter plot of \bar{f}_{PAR} versus ND for a nadir viewing. Variable soil reflectance results in points aligned rather perpendicularly to the best fit line (dashed line), especially at moderate LAIs \bar{f}_{PAR} and ND values around 0.5), which indicates that the relationship between \bar{f}_{PAR} and ND is not only non-linear, but also strongly depends on the type of background.

may vary with wavelength in the visible and near-infrared, as is the case with most soils (e.g., Ref. 27) and leaf litter (Ref. 28). The canopy may also be composed of living as well as dead leaves or, more generally, leaves of different optical properties. Calculations, therefore, should include more realistic situations. Still, our study strongly suggests that linear combinations at specific viewing angles may be much more accurate in predicting \bar{f}_{PAR} than indices that are non-linear functions of radiances or reflectances.

The relationships established theoretically, the gain in \bar{f}_{PAR} residual error when using preferential viewing geometries, the ability of the linear combinations to reduce soil and LIDF dependence, etc., remain to be verified using in situ measurements. Unfortunately, few data sets exist that contain concomitant \bar{f}_{PAR} and reflectance measurements at various viewing angles. The results, therefore, may not be statistically significant. A dedicated experiment to establish and verify the validity of the SAIL-based data fits, therefore, appears necessary.

One should further emphasize that surface reflectances observed from space are inherently subjected to instrument noise and are

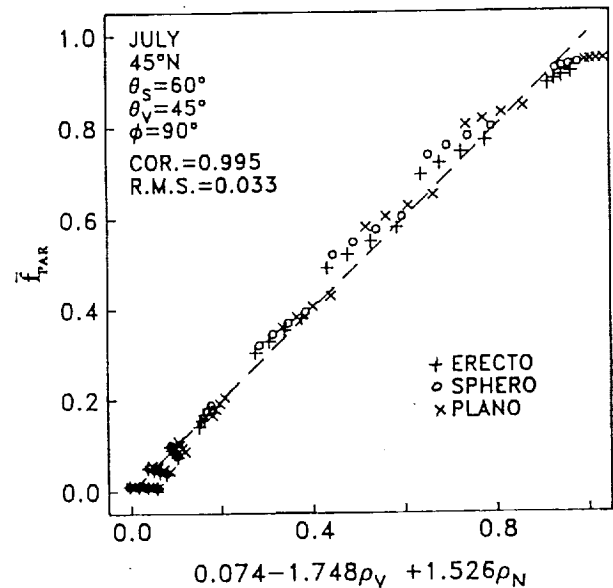
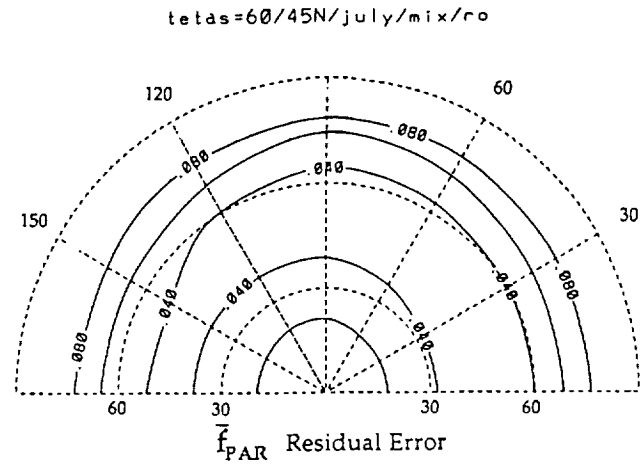


Fig. 2 Same as Fig. 1, but linear combinations of visible and near-infrared reflectances (single viewing geometry), ρ_v and ρ_n , respectively. Compared to Fig. 1, the \bar{f}_{PAR} residual error is substantially reduced when viewing around 45° from zenith. Points corresponding to a same LAI, but different soil reflectances, are now more aligned along the best fit line.

contaminated by the atmosphere. Consequently, it will be necessary in the comparisons of the various estimators' performance to include the effects of instrument noise and atmospheric interference, which act differentially on simple ratio, normalized difference, and linear combinations. This can be done by simulating the top of atmosphere reflectances corresponding to the surface reflectances, correct those reflectances for atmospheric effects assuming typical atmospheric characteristics, and translate the effects of uncertainties in these characteristics into above-canopy reflectance uncertainties. The procedure is then to introduce the above canopy reflectance uncertainties in the regression datasets, as well as typical instrument noise.

Our investigation should be viewed in the context of future spaceborne radiometers, in particular MODIS on EOS and POLDER atmosphere reflectances for atmospheric interference, are particularly adapted to monitor \bar{f}_{PAR} and, therefore, primary productivity from linear (uni- and multi-angle) combinations of reflectances. This should lead, during the EOS era, to a better characterization of terrestrial primary productivity on a global scale.

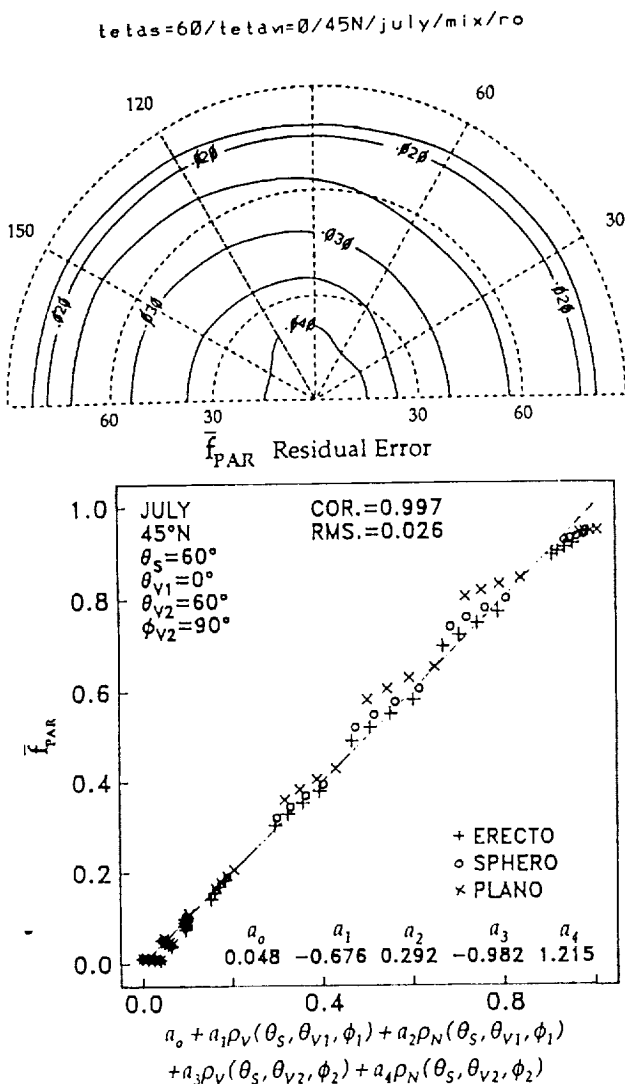


Fig. 3 Same as Fig. 2, but two viewing geometries. Compared to Fig. 2, the \overline{I}_{PAR} residual error is further reduced when reflectances at nadir and 60° from zenith are linearly combined.

5. ACKNOWLEDGMENTS

This work has been supported by the National Aeronautic and Space Administration under grants NAG5-900 and NAGW-1968 and by the California Space Institute under grant CS76-90. We wish to thank F. Hall, K. Huemmrich, and E. Middleton of NASA Goddard Space Flight Center and B. Blad and E. Walter-Shea of the University of Nebraska for helpful discussions, M. Ba for technical support.

6. REFERENCES

- Lieth H., 1975: Modeling the primary productivity of the world. In "Primary productivity of the biosphere" H. Lieth and R.H. Whittaker eds. Springer-Verlag New York/Heidelberg/ Berlin.
- Kumar, M. and J.L. Monteith, 1981: Remote sensing of crop growth. In "Plants and Daylight Spectrum", H. Smith, Ed., Academic, New York, 133-144.
- Monteith, J. L., 1977: Climate and the efficiency of crop production in Britain. *Phil. Trans. Roy. Soc. London*, B281, 277-294.
- Baker, K. S., and R. Frouin, 1987: Relation between photosynthetically available radiation and total insolation at the ocean surface under clear skies. *Limnol. Oceanog.*, 32, 1370-1377.
- Tarpley, J. D., 1979: Estimating incident solar radiation at the surface from geostationary satellite data. *J. Appl. Meteor.*, 41, (4), 1172-1181.
- Gautier, C. G. Diak and S. Masse, 1980: A simple physical model to estimate incident solar radiation at the surface from GOES satellite data. *J. Appl. Meteor.*, 19, 1005-1012.
- Pinker, R. T., and J.A. Ewing, 1985: Modeling surface solar radiation: Model formulation and validation. *J. Clim. and Appl. Meteor.*, 24, (5), 389-401.
- Dedieu, G., P. Y. Deschamps and Y.H. Kerr, 1987: Satellite estimation of solar irradiance at the surface of the earth and of surface albedo using a physical model applied to Meteosat data. *J. Clim. and Appl. Meteor.*, 26, (1), 79-87.
- Frouin, R. and C. Gautier, 1990: Variability of photosynthetically available and total solar irradiance at the surface during FIFE. *Symposium on the First ISLCP Experiment-FIFE*, Feb. 7-9, 1990 Anaheim, CA.
- Asrar, G. M. Fuchs, E.T. Kanemasu and J.L. Hatfield, 1984: Estimating absorbed photosynthetic radiation and leaf area index from spectral reflectance in wheat. *Agron. J.*, 6, 300-306.
- Sellers, P. J., 1985: Canopy reflectance, photosynthesis and transpiration. *Int. J. Rem. Sens.*, 6, 1335-1372.
- Sellers, P. J., 1987: Canopy reflectance, photosynthesis, and transpiration. II. The role of biophysics in the linearity of their interdependence. *Rem. Sens. Environ.*, 21, 143-183.
- Choudhury, B. J., 1987: Relationships between vegetation indices, radiation absorption, and net photosynthesis evaluated by a sensitivity analysis. *Rem. Sens. Environ.*, 22, 209-233.
- Steven, M. D., P.V. Biscoe, and K.W. Jaggard, 1983: Estimation of sugar beet productivity from reflection in the red and infrared spectral bands. *Int. J. Remote Sens.*, 4, 325-334.
- Hatfield, J. L., G. Asrar, and E.T. Kanemasu, 1984: Intercepted photosynthetically active radiation estimated by spectral reflectance. *Remote Sens. Environ.*, 14, 65-75.
- Gallo, K. P., C.S.T. Daughtry, and M.E. Bauer, 1985: Spectral estimation of absorbed photosynthetically active radiation in corn canopies. *Remote Sens. Environ.*, 17, 221-232.
- Asrar, G. E. T. Kanemasu, G.P. Miller, and R.L. Weiser, 19887: Light interception and leaf area estimates from measurements of grass canopy reflectance. (IEEE). *Trans. Geosciences and Remote Sensing*, GE-24, 76-82.
- Tucker, C. J., and P.J. Sellers, 1986: Satellite remote sensing of primary production. *Int. J. Remote Sensing*, 2, 1395-1416.
- Tucker, C. J., C.L. Vanpraet, M.J. Sharman and G. Van Ittersum, 1985: Satellite remote sensing of total herbaceous biomass production in the Senegalese Sahel: 1980-1984. *Remote Sens. of Environ.*, 17, 233-249.
- Goward, S. N., C.J. Tucker, and D.G. Dye, 1985: North American vegetation patterns observed with the NOAA-7 advanced very high resolution radiometer. *Vegetation*, 64, 3-14.
- Goward, S. N., D.G. Dye, A. Kerber, and V. Kalb, 1987: Comparison of north and south American biomes from AVHRR observations. *Geocarto International*, 1, 27-39.
- Holben, B. N., and R.S. Fraser, 1984: Red and near-infrared sensor response to offnadir viewing. *Int. J. Remote Sensing*, 5, 145-160.
- Verhoef, W., 1984: Light scattering by leaf layers with application to canopy reflectance modeling: The SAIL model. *Rem. Sens. Environ.*, 16, 125-141.
- Mc Clatchey, R.A., R.W. Fenn, J.E.A. Selby, F.E. Voltz, and J.S. Garing, 1971: Optical properties of the atmosphere. AFCRL 71-0279, Environ. Res. Paper 354, 108 pp.
- WCP-55, 1983: Report of WMO (CAS)/Radiation Commission of IAMAP Meeting of Experts on Aerosols and their Climatic Effects, Williamsburg, Virginia, March 28-30, 1983.
- Stoner, E.R., and M.F. Baumgardner, 1981: Characteristic variations in reflectance of surface soils, *Soil Sci. Soc. Am. J.*, 45(6), 1161-1165.
- Hall, F.G., and K.F. Huemmrich, 1990: Use of narrow-band spectra to estimate the fraction of absorbed photosynthetically active radiation. *Remote Sens. Environ.*, 29, 47-53.



92A13935

Appendix 10

CLOUD RADIATIVE FORCING VARIABILITY DURING FIFE

F.-M. Bréon, R. Frouin, C. Gautier

Proc. Symp. on the First ISLSCP Field Experiment, Anaheim, CA, February 7-9, 1990, 173-179, Published by the American Meteorological Society

CLOUD RADIATIVE FORCING VARIABILITY DURING FIFE

François-Marie Bréon
Robert Frouin
Catherine Gautier

California Space Institute A-021,
Scripps Institution of Oceanography
La Jolla, CA 92093

1. INTRODUCTION

Spurred by the possible consequences of the so-called greenhouse effect, or the trapping of longwave radiation within the atmosphere by water vapor, carbon dioxide, and trace gases, public awareness and scientific interest in the planet Earth's climate system has grown considerably during recent years.

General Circulation Models (GCMs) have been trying to identify pertinent climate changes. Predictions of global changes, however, vary widely. For a doubling of carbon dioxide concentration, for instance, the predicted mean temperature increase ranges from about 1°C to 4°C. It is now believed that the main factor of uncertainty is cloud feedback: changes in the Earth's climate may drive variations in cloud parameters (height, liquid water content, brokenness, distribution) that could amplify or cancel out the greenhouse effect.

Clouds affect climate in many ways; however, their main effect regarding climate research, of particular interest in this study, is on radiative exchanges occurring within the surface/atmosphere system. Except for some pathological cases of very high surface albedo (Kobayashi, 1989), clouds increase the Earth's system albedo which, by reducing the solar radiation absorbed by the surface, leads to a cooling of the Earth. On the other hand, clouds trap terrestrial radiation within the troposphere, reducing the amount of longwave flux escaping to space, and thereby causing a warming of the surface. The net cloud radiative forcing is therefore a difference between the two effects, which are of the same order of magnitude. Its sign and amplitude depend on cloud characteristics, in particular height and water content (Somerville, 1984).

Current cloud forcing predictions are of poor quality for the following reasons: 1) we still cannot correctly predict the occurrence of clouds under given atmospheric conditions and 2) the radiative effect of a cloud, given its liquid water

content and height characteristics, is subject to uncertainties, even though the radiative transfer through a vertically inhomogeneous atmosphere is now well understood (Fleateau and Stephens, 1988).

Given this situation, it is important to conduct observations of cloud radiative forcing and understand what parameters drive the main variations. Parameterizing cloud forcing from variables that are well predicted by GCMs when compared to present climate is a key objective. The study presented in this paper evaluates a set of radiative flux surface measurements, concomitant with other meteorological observations, so as to derive the cloud radiative forcing at the surface. The forcing is then analysed in terms of variability and relation to other meteorological parameters.

In the first part of this paper we describe the data used in this study, which were collected during the First ISLSCP Field Experiment (FIFE). We then present the methods that are used to process these data and characterize the cloud radiative forcing at the surface. This forcing's variability is finally examined as a function of cloudiness and atmospheric changes.

2. DATA

The First ISLSCP Field Experiment (FIFE), an international surface-atmosphere experiment, took place in 1987 at and around the Konza Prairie Long Term Ecological Research (LTER) site near Manhattan, Kansas (Sellers et al., 1988). The FIFE objectives were to gather the necessary data to permit interpretation of satellite observations suitable to infer climatologically-significant land surface parameters.

The experimental area was a 15 x 15 km square with various topological features including burned and unburned plateau, slope, and creek (Fig. 1). Although the central portion of the area is studied continuously and additional parameters were measured throughout the year,

the experiment concentrated on four Intensive Field Campaigns (IFCs) corresponding to four different states of surface vegetation:

First IFC :	"green up"	May 26th to June 6th
Second IFC :	"peak greenness"	June 25th to July 15th
Third IFC :	"dry down"	Aug. 10th to Aug. 21st
Fourth IFC :	"senescence"	Oct. 5th to Oct. 15th

Our study uses 4 different types of data acquired during the IFCs, namely surface radiative measurements, atmospheric soundings, sky photographs, and conventional cloud observations.

Several surface stations collected radiative flux measurements. We selected stations 2 and 38 (see Fig. 1) and acquired the radiation data from the FIFE information system. These stations were operated by Eric Smith's group (Florida State University) during the four IFCs. The surface measurements were compared with other stations and with radiative models outputs using atmospheric profiles (Bréon et al, 1990a). A bias was found in the longwave measurements, but was later corrected (E. Smith, personal communication), so that we can expect an accuracy at least equal to the manufacturer's specifications (within a few percentile).

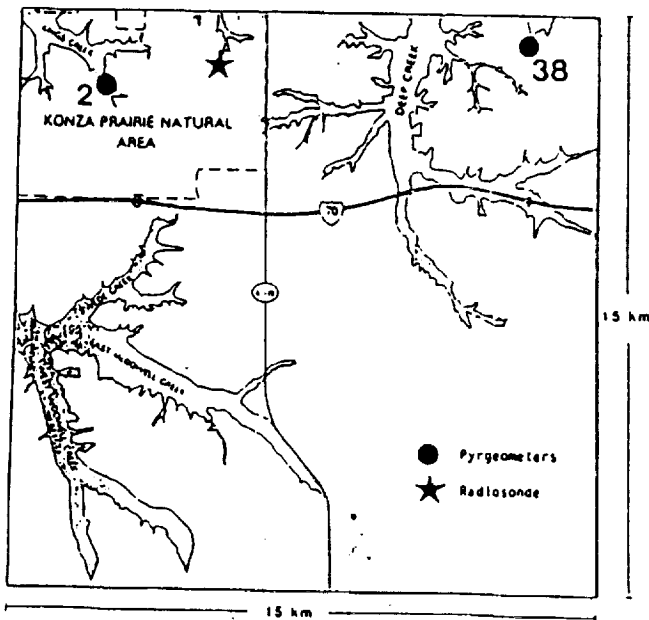


Fig. 1: General presentation of the FIFE experiment field. Station 2 and 38 are the two surface radiation measurement sites used in this study. The black star indicates the location of the soundings.

Fractional cloud cover was another parameter observed from the surface. Within the FIFE area, observations were made with an uplooking automatic camera. Cloudiness was deduced from the percentage of cloudy areas in the photographs, taking into account the viewing angle of each area relative to the vertical. Since the camera was operating in the

visible spectrum, no cloudiness information could be obtained at night. Another limitation of the camera is that no information on cloud thickness or height could be provided.

In the immediate vicinity of the FIFE area, two stations (MHK and FRI) collected standard meteorological data. We acquired their cloud observations through the FIFE information system. These observations consisted of hourly estimates of three, or less, cloud layers giving their height and fractional cover in octas. In order to use the data in our particular study, we classified them in three atmospheric layers: low, mid-level, and high, with limits at 900 and 3000 meters. For each layer and each day, a mean cloudiness was computed, assuming a random overlap if several cloud layers were found within the same atmospheric layer. Fig. 2 presents a comparison of the mean cloudiness as found during the 4 IFCs by the two stations.

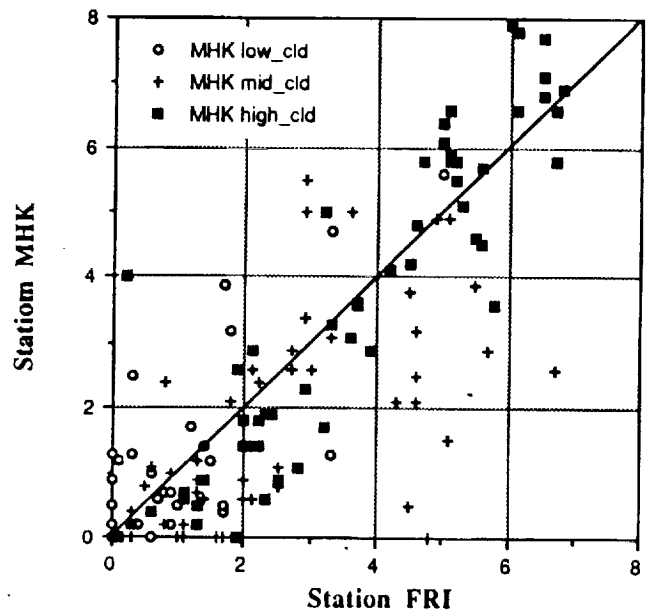


Fig. 2: Comparisons between the daily cloud amount estimates from two nearby meteorological stations for the three cloud layers (less than 900 meters, between 900 and 3,000 meters, more than 3,000 meters). Values are given in octas.

The scatter is rather large, even though the two stations are close to one another (about 10 kilometers) and are located in a similar surface environment. It is interesting to note, however, that the correlation between the two estimated cloudiness datasets, increases from low to high clouds. With the levels chosen, mean cloudiness results mostly from high clouds (altitude greater than 3000 m) that can produce overcast skies on a daily average. Most low cloudiness values are less than 2 octas but reached 5.5 octas on one occasion.

The atmospheric measurements used in our

study were obtained from radiosondes launched from the experimental site (see Fig. 1). These measured pressure, temperature, and wet bulb temperature, from which the water vapor mixing ratio was derived. Pre-processing and extrapolation of the profiles is described in Bréon et al. (1990a).

3. METHOD

To derive the cloud radiative forcing from the surface observations, one must first estimate the downwelling irradiance in the absence of clouds. The two spectral intervals, shortwave and longwave, need different methods.

The "clear" longwave flux was computed using Morcrette's radiative transfer model (Morcrette, 1984; Morcrette and Fouquart, 1985; Morcrette et al., 1986), with the FIFE soundings of temperature and water vapor mixing ratio as input. Ancillary data, namely ozone profile, carbon dioxide concentration, and temperature and water vapor profiles in the upper layers of the atmosphere, had to be set to their climatological value since no other information was available. Although necessary, these data have little effect on the results. After comparison with other radiative transfer models (WMO, 1984) and validation with in-situ observations (Bréon et al., 1990b), it is believed that accuracy of models such as Morcrette's is better than 10 W m^{-2} . During the FIFE experiment, there was an average of 6 soundings per day, during day-time, which provided a time step sufficient to follow the longwave flux variability. "Clear" longwave fluxes could therefore be interpolated from one sounding to the next.

Main variations of the shortwave irradiance at the surface are driven by the solar zenith angle and cloud parameters (amount, optical thickness). Other parameters, such as the water vapor profile and the ozone content, have a second order effect and can be set to their climatological value. Effects of aerosols, although small in many cases, can be large. During FIFE, aerosol turbidity measurements were too sporadic to establish their variability since they were taken only during clear days. We therefore estimated an ad-hoc atmospheric visibility for each of the IFCs by adjusting our shortwave irradiance estimates to the measurements obtained during clear periods, as seen by the clear-sky camera. Computations were done with an half hour time step, using a parameterization developed by Frouin et al. (1988) from the radiative transfer model of Tanré et al., (1979).

From the "clear" flux values obtained by the two radiative transfer models, it was easy to

determine the cloud effect. The longwave effect is simply the difference between the measurement and the "clear" flux estimate. The shortwave estimate is defined differently because we have to compensate for the large diurnal cycle of the shortwave irradiance. We define the shortwave cloud effect by the formula:

$$CL_{eff} = (1 - \frac{SW_{obs}}{SW_{clear}})SW_{daily} \quad (1)$$

where SW_{obs} is the instantaneous shortwave flux measured at the station, and SW_{clear} and SW_{daily} are the instantaneous and daily-integrated "clear" shortwave flux as estimated by the model, respectively. This formulation allows one to cancel out most of the diurnal variability for a constant cloudiness. It is obviously not usable for night period, when SW_{clear} is equal to zero. When doing time averages, however, we did not simply average CL_{eff} but gave each instantaneous value a weight proportional to the shortwave "clear" flux estimate. This method allows one, in case of variable fractional cover and non-continuous measurement, to obtain the statistically best possible estimate of a time average.

Net cloud radiative forcing at the surface is the difference between the longwave and shortwave cloud effects. On a daily time scale, a negative value corresponds to a net cooling of the surface (shortwave forcing is larger than the longwave forcing); a positive value indicates that longwave heating overcomes shortwave cooling.

4. RESULTS AND DISCUSSION

Because of the notably variable cloudiness, as well as the uncertainties on each of the parameters, time series of the instantaneous cloud radiative forcings are extremely variable, especially close to the sunrise and sunset when SW_{clear} values are small. Fortunately, when doing time averages, these values are given a low weight and the uncertainty is therefore reduced. Similarly, the uncertainty is statistically reduced when averaging several observations taken at the same local time. We therefore chose not to present instantaneous values, from which information is difficult to distinguish from the noise, but rather the daily cycles and the day-averaged values.

Table 1 gives, for most days of the FIFE experiment, a daily average of the various measurements and estimates presented above. "Mod" refers to the model estimates of clear sky radiative fluxes, "obs" to the observations, and "cl_eff" to the cloud effect. "N_obs" gives the number of half-hourly values that were used in

Tab. 1: Daily averages of radiative parameters and cloudiness during the four FIFE IFCs. SW refers to the shortwave irradiance and LW to the longwave irradiance. Clear sky estimates from a model are denoted "mod", observations "obs" and cloud effects "cl_eff". Radiative flux parameters are given in Wm^{-2} . "Cloudiness" is the cloud amount given in percent from the sky camera observations, Low_neb, Mid_neb and High_neg are the cloudiness, in octas, obtained from nearby meteorological stations for three cloud layers as defined in the text.

Date	SWmod	LWmod	SWobs	LWobs	Cld. am.	SWcl_eff	LWcl_eff	TOTcl_eff	Nobs	Low_Neb	Mid_Neb	High_Neb
28-May	354.1	341.9	228.7	384.1	91.0	117.9	42.1	-75.8	14	1.1	4.2	6.7
29-May	354.8	335.2	248.6	375.8	84.9	100.0	40.6	-59.4	17	2.5	4.2	5.1
30-May	355.6	349.3	316.4	367.1	29.3	37.0	17.8	-19.2	16	0.1	2.0	4.2
31-May	356.3	363.1	315.9	377.1	50.4	38.1	14.0	-24.1	20	0.0	1.4	4.7
1-Jun	357.0	356.9	331.5	374.2	25.2	24.0	17.3	-6.7	20	0.7	0.7	2.0
2-Jun	357.6	355.0	76.8	392.5	83.7	264.6	37.5	-227.1	22			
3-Jun	358.2	300.8	351.8	324.6	39.1	6.1	23.7	17.7	28			
4-Jun	358.8	320.6	353.3	334.6	0.9	5.2	14.1	8.9	19	0.0	0.5	0.1
5-Jun	359.4	331.7	355.6	347.0	4.3	3.5	15.4	11.8	19	0.0	0.2	2.5
6-Jun	336.3	319.7	352.3	340.4	0.1	-16.1	20.7	36.8	9	0.0	0.0	1.5
25-Jun	355.8	337.4	346.2	355.3	12.4	9.1	18.0	8.9	17	2.3	1.6	1.2
26-Jun	355.7	314.3	323.3	345.8	16.2	30.6	31.5	0.9	30	0.0	1.0	2.2
27-Jun	355.5	326.9	348.9	359.8	44.4	6.3	32.9	26.6	9	0.0	3.2	2.3
28-Jun	355.3	361.9	323.7	369.5	42.3	29.8	7.7	-22.2	9	0.0	2.5	4.7
1-Jul	354.5	354.6	331.5	361.5	30.8	21.8	6.9	-14.9	19	0.0	2.3	2.0
2-Jul	354.2	361.3	291.1	375.5	49.5	59.4	14.2	-45.2	30	0.0	1.5	4.4
3-Jul	353.8	376.3	225.8	390.5	64.2	120.8	14.2	-106.6	30	0.5	1.0	5.2
4-Jul	353.4	372.1	125.2	393.5	79.9	215.6	21.3	-194.3	15	0.3	2.8	5.9
5-Jul	353.0	375.9	332.3	376.6	38.2	19.5	0.8	-18.7	12	1.4	2.8	4.1
6-Jul	352.5	410.1	316.6	413.8	29.1	33.9	3.7	-30.2	18	0.8	1.1	1.0
7-Jul	352.0	388.8	125.9	413.4	85.6	213.3	24.6	-188.7	19	0.7	2.7	5.5
8-Jul	351.5	375.4	287.6	384.5	73.2	60.3	9.1	-51.2	27	0.8	3.3	6.4
9-Jul	350.9	399.0	260.3	407.0	74.8	85.5	8.0	-77.5	28	0.3	1.8	6.9
10-Jul	350.3	399.7	304.3	403.8	55.8	43.5	4.1	-39.4	28	0.8	0.9	5.5
11-Jul	326.0	396.3	293.3	401.8	21.0	33.1	5.4	-27.7	28	0.0	1.0	3.3
11-Aug	304.7	395.3	297.6	393.3	7.9	6.7	-1.9	-8.6	17	0.0	1.3	0.9
13-Aug	301.7	401.9	120.5	427.6	92.9	171.1	25.7	-145.4	19	5.3	4.9	5.3
14-Aug	300.1	414.8	276.9	414.3	54.7	22.0	-0.4	-22.4	22	1.4	3.7	1.8
15-Aug	298.6	401.4	311.2	401.8	2.6	-12.0	0.4	12.4	14	0.0	0.7	0.5
16-Aug	296.9	387.5	300.1	387.0	5.2	-3.0	-0.4	2.5	21	0.1	1.7	1.7
17-Aug	295.3	365.5	303.1	370.5	1.7	-7.4	5.0	12.4	26	0.0	1.3	0.3
18-Aug	293.6	363.8	266.9	380.4	41.0	25.3	16.5	-8.8	22	1.1	5.0	3.4
19-Aug	292.0	387.7	248.6	389.7	30.0	40.9	2.0	-38.9	27	0.1	3.2	1.7
20-Aug	290.2	398.1	286.4	402.0	13.1	3.6	3.9	0.4	24	0.0	0.5	1.8
21-Aug	267.5	392.4	272.8	398.6	2.9	-5.4	6.2	11.6	20	0.0	0.0	0.8
6-Oct	214.0	275.2	214.8	286.5	0.0	-0.8	11.3	12.1	23	0.0	0.0	0.9
7-Oct	211.7	269.1	209.1	279.5	4.1	2.4	10.4	7.9	23	0.0	0.4	1.9
8-Oct	209.4	274.8	221.9	292.0	4.9	-11.7	17.3	29.0	6	0.0	0.0	5.1
10-Oct	204.8	232.2	76.6	325.8	99.1	120.8	93.6	-27.2	9	1.4	4.3	7.0
11-Oct	202.6	243.1	199.2	274.7	22.8	3.1	31.5	28.4	6	0.3	2.4	2.1
12-Oct	200.3	283.9	191.0	302.8	18.8	8.7	18.9	10.2	14	0.0	0.0	2.1
13-Oct	198.0	292.6	177.4	322.7	48.6	19.4	30.0	10.7	22	0.0	0.0	3.7
14-Oct	195.8	313.8	111.7	355.2	65.6	79.0	41.3	-37.7	21	0.0	2.4	6.3
15-Oct	193.5	306.0	172.5	341.7	82.2	19.8	35.7	15.9	7	1.5	4.7	5.5

the averaging. "Cloudiness" is the fractional coverage from the sky camera (in per cent), and the three last columns give, in octas, the mean cloudiness of the three layers defined above, as observed by the meteorological stations.

Unexpectedly, for a few days, the longwave or the shortwave cloud effect took negative values. The negative values for the longwave cloud effect are $-1.9 W m^{-2}$ and $-0.4 W m^{-2}$ (twice), which is negligible and could be attributed to either the measurement or the model estimate. For two of these cases, cloudiness is very low, as expected since no cloud effect is computed. In the third case, however, cloudiness is larger than 50% and, therefore, we would have

expected a larger longwave cloud effect. One notices the high value of the estimated "clear" flux found for that particular day (May 14). A careful analysis of the soundings showed that May 14 was exceptionally humid, which in turn explains the high value of the longwave irradiance, and the absence of a discernable longwave cloud effect.

Seven days (out of 44) showed a negative shortwave cloud effect. The values decrease to $-16 W m^{-2}$ and are only found for very low mean cloudiness (less than 5%). These erroneous value can be explained by model and measurement uncertainties when the actual shortwave irradiance is very close to the

theoretical "clear flux" (clear days). One of the major uncertainties for the modeled "clear" flux is the effect of aerosols. It is possible that the actual visibility was higher than that modeled for some of these days, leading to a higher "clear" flux.

The largest shortwave cloud effect is found on June 2, with an absolute value of 264 W m^{-2} (less than 24% of the clear sky radiation reaches the ground). Instantaneous observations showed a very variable insolation with values constantly low and reaching extremely low levels. During a half hour period centered on local noon, for instance, only 1% of the clear sky irradiance was measured. A detailed analysis of other meteorological observations showed a very high cloudiness during most of the day and gusty winds frequently changing directions. This strongly supports the presence of Cb type clouds. Surprisingly, despite the obvious presence of very thick clouds, no rain was reported for that day over the site. It is possible, however, that very localized rainfall occurred, but did not reach the measurement station.

The largest longwave cloud effect (94 W m^{-2}) is more than twice the value of the second largest (42 W m^{-2}). It is found on October 10, an overcast day with a very low boundary layer temperature: An average of 4°C of surface air temperature during daytime was measured, to be compared to about 15°C on average during the IFC. This low temperature leads to a record-low "clear" flux and explains the magnitude of the cloud effect. The shortwave cloud effect for this day is also one of the largest reported. Both effects partially compensated each other leading to a -27 W m^{-2} net cloud forcing.

Net cloud radiative forcing ranges are from -227 W m^{-2} to 37 W m^{-2} , most days showing negative values. The few positive values are obtained for small mean cloud fractions. The highest negative values result mainly from the shortwave component.

Correlations of radiative forcing with cloudiness values were done using the sky camera and the meteorological reports (Fig. 3a,b,c). Using the sky camera, we found a correlation of 0.62, 0.31 and 0.49 with the shortwave, longwave, and net cloud radiative forcing, respectively. Using the observations from the meteorological stations, we found an even lower correlation. This shows, that cloud amount is not the only parameter driving the radiative forcing. Another parameter governing shortwave cloud forcing is liquid water content, but this parameter was not measured. On the other hand, we know that the longwave flux should be more sensitive to the low cloudiness than to total cloudiness. We therefore correlated

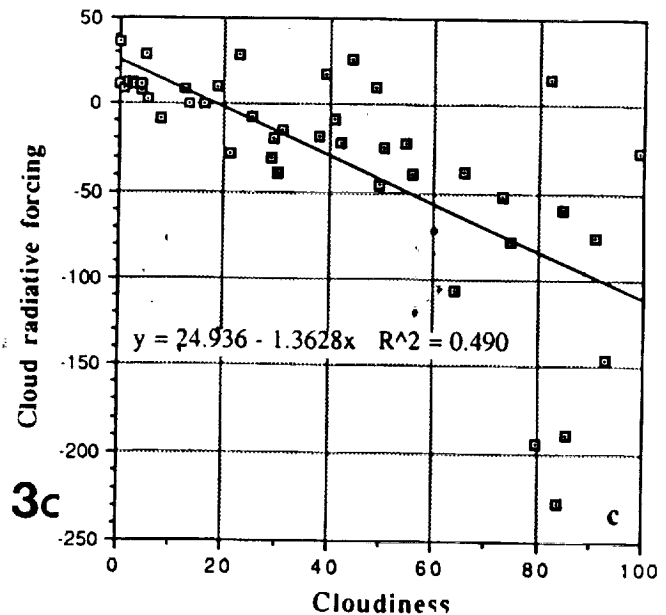
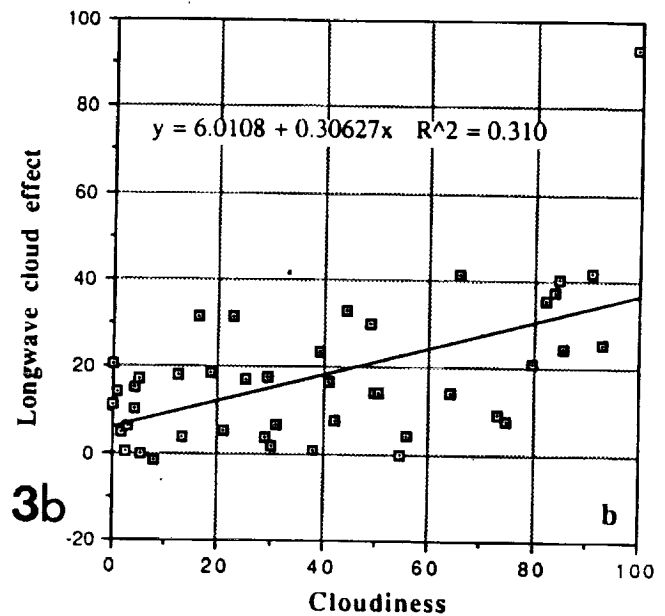
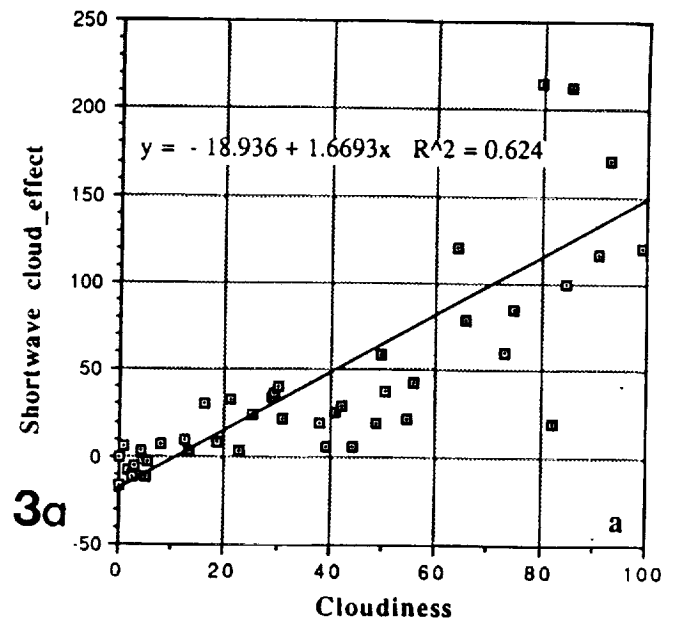


Fig. 3: Cloud forcing (in Wm^{-2}) as a function of cloud amount (in %) as seen by the sky camera. The cloud forcing is given for the shortwave (Fig. 3a), the longwave (fig. 3b) and the net (fig. 3c).

longwave radiative forcing with low cloudiness; but, once again, the results were rather disappointing.

Fig. 4 shows the average diurnal cycle of the shortwave, longwave, and net cloud radiative forcing as a function of day fraction. No values are given at night since the shortwave cloud forcing has no meaning. Sunrise and sunset occur approximately at day fractions 0.5 and 1.1, respectively. It is clear that the three quantities, which are not independent, show a diurnal cycle. The longwave radiative forcing has an amplitude of about $15 W m^{-2}$, with a minimum around local noon. The cycle of the shortwave cloud radiative forcing is even larger: it is minimum at sunset and sunrise but remains rather constant during a large part of the day. Note that, owing to our definition of the shortwave cloud radiative forcing, the shortwave cloud effect in Fig. 3 is not directly related to the actual amount of incoming radiation. As mentioned above, the accuracy of the shortwave radiative forcing is lower for low solar zenith angles than during the rest of the

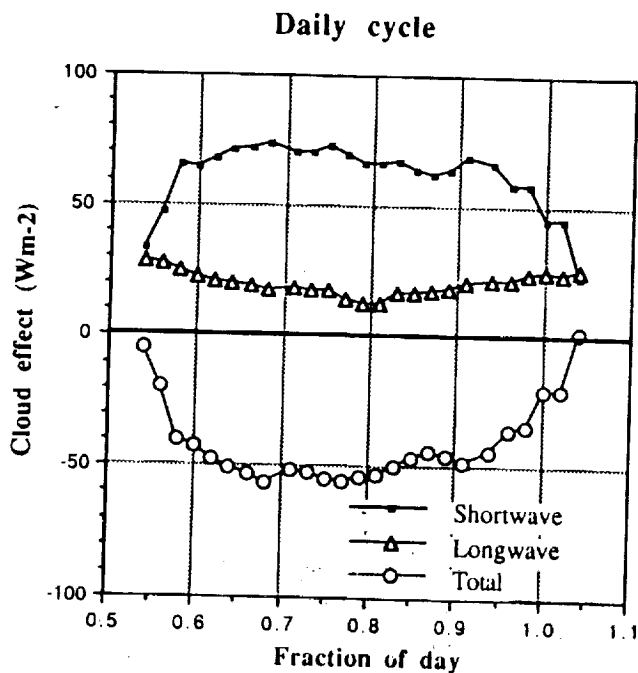


Fig. 4: Daily cycle of the cloud radiative forcings (in Wm^{-2}) during FIFE. Sunrise and sunset occur when the fraction of day is about 0.5 and 1.1 respectively.

day, but we believe that the large cycle is not entirely due to uncertainties. The net cloud radiative forcing exhibits an even larger cycle, enlarged by the longwave component.

5. SUMMARY AND CONCLUSIONS

During FIFE, a large set of meteorological measurements was taken. "Clear" longwave and shortwave fluxes at the surface were computed using atmospheric soundings and radiative transfer models. Coincident radiative flux measurements were used to derive the surface cloud radiative forcing for both components.

Both shortwave and longwave cloud forcings show a very large temporal variability due, for the most part, to the changing cloudiness, and to measurements and computational uncertainties.

Daily values of the cloud radiative forcings were analyzed and compared to cloud parameters obtained from a sky camera situated on the FIFE site and from conventional meteorological observations in the immediate vicinity. The advantage of the sky camera was its immediate proximity to the surface radiative observations, but the stations near the FIFE area also gave information on cloud height, another important factor governing longwave cloud radiative forcing variability.

No dominant correlation between either components of the cloud radiative forcing and cloudiness were found using the sky camera data. This is explained by the fact that forcings are a function, not only of cloudiness, but also of cloud liquid water content (mainly for the shortwave) and cloud base height (for the longwave). We expected that more results could be drawn from the conventional cloud observations which enabled distinction between low cloudiness and cirrus; once again, however, the correlation was very low. One reason for this is the poor spatial coherency of the cloudiness, especially for low clouds, as was shown by comparing two similar observations about 10 km apart.

Surface cloud radiative forcing showed a rather large diurnal cycle with a minimum at local noon for the longwave component and two pronounced minimum at sunrise and sunset for the shortwave component. These cycles, if confirmed by other studies, should be taken into account when evaluating radiation budgets from space using heliosynchronous satellites.

One main deficiency of this study was the limited number of days during which observations were made. To provide convincing results on the mean radiative effect of clouds, at least one year of observations is needed. The measurements should include radiative fluxes, cloudiness, cloud base height, cloud optical thickness, as well as temperature and water profiles, and should be done within a

very limited area. Such measurements are planned within the Atmospheric Radiation Measurement Program of the Department Of Energy (DOE, 1990), which, therefore, should be useful to cloud radiative forcing studies.

6. ACKNOWLEDGMENTS

This work was supported by the National Aeronautics and Space Administration under grant NAG5-900 and by the California Space Institute under grant CS89-89. We wish to thank M. Petrie and B. Bloomfield for their editing assistance, and J. Correa for his technical support.

7. REFERENCES

- Bréon, F.M., R. Frouin and C. Gautier, 1990a: Satellite estimates of downwelling longwave irradiance at the surface during FIFE. Preprint of the AMS conference, Anaheim California, pp 92-97.
- Bréon, F.M., R. Frouin and C. Gautier, 1990b: In situ measurements and parameterization of downwelling longwave irradiance at the ocean surface. Accepted in *J. Appl. Meteor.*
- DOE, 1990: Atmospheric Radiation Measurement Program Plan. Report DOE/ER-401. Available from the National Technical Information Service, U.S. Department of commerce, Springfield, Virginia 22161.
- Fleteau, P.J., and G.L. Stephens, 1988: On the fundamental solution of the radiative transfer equation. *J. Geophys. Res.*, 93, 11037-11050.
- Frouin, R., D.W. Lingner, C. Gautier, K.S. Baker and R.C. Smith: A simple analytical formula to compute clear sky total and photosynthetically available irradiance at the ocean surface. *J. Geophys. Res.*, 94 (C7), 9731-9742.
- Kobayashi, T., 1989: Radiative properties of finite cloud fields over a reflecting surface. *J. Atm. Sci.*, 46, 2208-2214.
- Morcrette, J.J., 1984: Sur la paramétrisation du rayonnement dans les modèles de la circulation générale atmosphérique. Thèse de Doctorat d'Etat, Université des Sciences et Techniques de Lille, 630, 373 pp.
- Morcrette J.J., and Fouquart Y., 1985: On systematic errors in parameterized calculations of the longwave radiation transfer. *Quart. J. Roy. Meteor. Soc.*, 111, 691-708.
- Morcrette J.J., Smith L. and Fouquart Y., 1986: Pressure and temperature dependance of the absorption in longwave radiation parameterizations. *Beitr. Phys. Atmosph.*, 59, 455-469.
- NASA, 1986: Surface radiation budget for climate application. Reference publication 1169.
- Sellers, P.J., F.G. Hall, G. Asrar, D.E. Strebel and R.E. Murphy, 1988: The First ISLSCP Field Experiment (FIFE)". *Bull. AMS*, 69, 22-27.
- Somerville, R.C.J., and L.A. Remer, 1984: Cloud optical thickness feedbacks in the CO₂ climate problem. *J. Geophys. Res.*, 89, 9668-9672.
- Tanré, D., M. Herman, P.Y. Deschamps and A. Delcèffe; 1979: Atmospheric modeling for space measurements of ground reflectances, including bidirectional properties, *Appl. Opt.*, 18, 3587-3596.
- WMO-ICSU, 1984: The intercomparison of radiation codes in climate models. World Climate Research Program Report WCP-93, Geneva, Switzerland.